The Physical Properties of Intermediate-Velocity Gas at High Galactic Latitudes

Dissertation
zur
Erlangung des Doktorgrades (Dr. rer. nat.)
der
Mathematisch-Naturwissenschaftlichen Fakultät
der
Rheinischen Friedrich-Wilhelms-Universität Bonn

von
Tobias Röhser
aus
Bayreuth

Bonn, Januar 2016

Dieser Forschungsbericht wurde als Dissertation von der Mathematisch-Naturwissenschaftlichen Fakultät der Universität Bonn angenommen und ist auf dem Hochschulschriftenserver der ULB Bonn `http://hss.ulb.uni-bonn.de/diss_online` elektronisch publiziert.

1. Gutachter:	Privat-Dozent Dr. Jürgen Kerp
2. Gutachter:	Prof. Dr. Thomas H. Reiprich
Tag der Promotion:	31.05.2016
Erscheinungsjahr:	2016

Contents

Abstract

The accretion of matter onto galactic disks, the formation of molecular clouds, and the formation of stars are of major importance for the evolution of galaxies over cosmic times. During their lifetimes, high-mass stars inject large amounts of energy and momentum into the interstellar medium (ISM) of galaxies, driving galactic fountains and outflows of material into their halos. Such extra-planar gas clouds, the intermediate-velocity clouds (IVCs), have been discovered in spectroscopic surveys of atomic hydrogen (HI) in our Galaxy. IVCs are thought to be related to a Galactic fountain process.

In this thesis we present an observational study of Galactic IVCs and their molecular content. By the combination of HI and far-infrared (FIR) dust emission, we infer the distribution of molecular material within IVCs. A detailed study of two individual IVCs and their transition from atomic to molecular gas is conducted and the first global analysis of molecular gas within IVCs is performed. New all-sky HI and FIR surveys constitute an exceptional database for such a study of the Galactic ISM.

The two particular IVCs of interest approach the Galactic disk and are indistinguishable as measured by the Effelsberg-Bonn HI Survey (EBHIS). However, the one is a rare molecular IVC, while the other is a purely atomic IVC. Because of their similarities and differences, we suggest that the two objects are at different stages in the transition from atomic to molecular clouds at the disk-halo interface. This transition is thought to be driven by the bulk motion of the clouds through the surrounding medium, which causes ram pressure that perturbs and condenses the infalling IVCs. At the leading front the pressure is enhanced, which accelerates the formation of molecular hydrogen. These processes are not apparent in EBHIS data suggesting that the accumulation of gas and the H_2 formation occur on angular scales well below the angular resolution limit of EBHIS.

We conducted dedicated high-resolution observations of the two IVCs using the Westerbork-Synthesis Radio Telescope (WSRT) for the HI and the IRAM 30 m telescope for measurements of carbon monoxide ^{12}CO(1→0) emission, the main tracer of molecular hydrogen. The atomic IVC is not detected in ^{12}CO(1→0) emission and the HI gas appears to be diffusely and smoothly distributed, lacking high-column density cores. The molecular IVC harbours a rich atomic and molecular clumpy substructure. The atomic and molecular small-scale structures appear to be connected. Most of the ^{12}CO(1→0) emission originates from the eastern edge of the molecular cloud, which we propose to be the leading front, where the strongest ram-pressure interactions are expected to occur.

An analogy between infalling IVCs and turbulent colliding flows of atomic gas is put forward. The action of dynamical and thermal instabilities causes the formation of dense and cold cores, in which the formation of H_2 is much faster. Ram pressure is thought to move the warm neutral medium into the thermally unstable regime, from which it rapidly cools down to the thermally stable cold medium. In this sense the HI-H_2 transition within IVCs appears to be a natural step during the late phases of the Galactic fountain cycle in the disk-halo interface region.

The first global analysis of the molecular content within the high-Galactic IVC sky is conducted towards the northern and southern Galactic hemispheres. In total 206 molecular IVC (MIVC) candidates are identified that include the previously known objects except for a single one. While on the northern Galactic hemisphere there are large IVC complexes, no similar IVC structures are detected south. The almost complete lack of MIVC candidates with positive radial velocities in the local standard of rest suggests different physical processes within out- and inflowing gas.

The derived physical and kinematical properties of the IVC samples are consistent with the expectations from a Galactic fountain process. A large fraction of fountain ejecta within our Galaxy may not be observable as atomic IVC gas. Extrapolating from the local IVC population, the global Galactic fountain inflows may be an important contribution to the required accretion rate of the Milky Way.

CHAPTER 1

Introduction

In a galaxy the space between the stars is filled with the interstellar medium (ISM), a mixture of gas and dust grains, pervaded by radiation, cosmic rays, and magnetic fields. The interplay between ionisation and recombination, heating and cooling, formation and dissociation determines locally in which state the gas is found. The gas can be ionised, atomic, or molecular, which is reflected by different temperatures and densities of the gas. Detailed descriptions of the physical properties and the mechanisms that govern the state and structure of the ISM are given by Draine (2011), Cox (2005), or Ferrière (2001).

The ISM is a complex system in which energy and momentum is continuously changed and redistributed. This is determined mostly by the young and high-mass stars in a galaxy. These stars are hot and luminous and emit most of their radiation in the visible and UV regime, which is able to ionise the ISM. They can launch powerful winds that push away nearby gas and dust. At the end of their life, high-mass stars explode in supernovae releasing large amounts of momentum and energy back into the ISM. In addition, the ISM is enriched with metals[1] that have been formed in the interiors of the exploding stars. Hence, young and high-mass stars have a large impact on the ISM in their local vicinity.

The cycle of matter from the ISM into stars and back into the ISM has been recognised in the last decades by extensive observational and theoretical work (for recent reviews see Kennicutt & Evans 2012; McKee & Ostriker 2007). To understand the process of star formation in the Milky Way, one studies almost the entire electromagnetic spectrum. Different steps in the star formation process are observable only in certain regimes of the electromagnetic spectrum.

In our Galaxy the bulk of the baryonic[2] gaseous mass is found in hydrogen (for a recent review see Kalberla & Kerp 2009). Atomic hydrogen is easily observable by its emission of the HI 21 cm line in the radio regime. Molecules form only in the densest parts of the ISM where star formation may happen. Typically, molecular line transitions have energies in the radio and infrared (IR) regime. Dust grains are agglomerates of silicates, carbonaceous materials, and other metals (Draine 2003). Dust absorbs stellar light by which the grains get some temperature and emit a black-body-like emission spectrum that peaks in the IR. Stars themselves can be observed in the visible light, while high-mass ones radiate also significantly in the UV. X-ray emission is emitted from the hottest gas, which is created by supernova explosions and stellar coronae. Gamma rays and cosmic rays contribute significantly to the ionisation within the densest molecular clouds (for a recent review on cosmic rays in galaxies see Grenier et al. 2015), affecting the chemistry within the gas and the gravitational collapse of the cloud, since ions are coupled to magnetic fields.

[1] In astronomy all elements larger than helium are referred to as metals.

[2] Baryonic matter is everything that is built out of quarks like all the atoms and molecules that we are made of. According to the most recent measurements, only ∼2% of the energy density in our Universe is in the form of baryonic matter (Planck Collaboration XIII 2015). The rest is in the unknown forms of Dark Matter and Dark Energy.

Stars form only in the densest and coldest environments where the gravitational collapse of small gaseous cores is possible (Kennicutt & Evans 2012). However, most of the gas in the ISM of the Milky Way is not in this condition (Draine 2011, his Table 1.2): About 20% of the total hydrogen is in the form of ionised hydrogen (H^+), comparable to the amount of molecular hydrogen (H_2); the remaining 60% is atomic hydrogen (HI). The co-existence of ionised, atomic, and molecular species in the Milky Way and its halo is referred to as the multiphase ISM. Hence, for the understanding of the ISM and the initial stages of star formation, which are the assembly of gas from the diffuse ISM into dense structures, the study of HI emission is of large importance.

Since its formation, the Milky Way has formed stars, with a maximum rate ∼10 Gyr ago (redshift $z \simeq 1.9$) when the star formation rate was a factor 2–3 higher than the current rate (Wyse 2009; Madau & Dickinson 2014). Today, the Milky Way forms stars at a rate of $1.9 \pm 0.4\,M_\odot\,yr^{-1}$ (Chomiuk & Povich 2011). In order to sustain this star formation activity over such long timescales, a continuous accretion of material onto the star-forming disk is required with about the same amount as the star-formation rate (Putman et al. 2012). Models of the chemical evolution of our Galaxy indicate that the accreted material has to be of low metallicity in order to match the observations of stellar compositions of small stars, which is known as the G-dwarf problem (e.g. Caimmi 2008).

Hence, galaxies like the Milky Way have to attain new low-metallicity material from the outside. The halo medium and its atomic halo clouds, observable by their HI emission, are thought to be key in order to account for most of the accretion (Putman et al. 2012). Putman et al. state that there are numerous fuelling sources for spiral galaxies like the Milky Way. However, many questions remain concerning the continuity of these sources and the mechanisms that convert infalling ionised and atomic fuel into molecular gas for star formation. Most of this material is observed by HI emission, which is discussed in the following Section.

1.1 The HI sky

By observing HI emission in spectroscopic surveys over the entire sky, the spatial and kinematic distribution of atomic hydrogen is revealed. HI 21 cm emission is a hyperfine-structure emission line of the ground state of atomic hydrogen. The Doppler shift of the HI line relative to its rest frequency of 1.420 . . . GHz gives the radial velocity component of the emitting gas with respect to the observer.

Several large-scale single-dish HI surveys have been conducted in the past that have contributed significantly to the understanding of the ISM and the global structure of our Galaxy. Most notable is the Leiden-Argentine Bonn (LAB) Survey (Kalberla et al. 2005), which is a composite of the Leiden Dwingeloo Survey (Hartmann & Burton 1997) and the Villa Elisa Survey (Arnal et al. 2000; Bajaja et al. 2005). The LAB survey is the first coherent all-sky survey of Galactic HI emission with a precise correction for stray radiation[3].

The successors of the two constituent surveys of LAB are the Parkes Galactic All-sky Survey (GASS, McClure-Griffiths et al. 2009; Kalberla et al. 2010; Kalberla & Haud 2015) and the Effelsberg-Bonn HI Survey (EBHIS, Winkel et al. 2016; Kerp et al. 2011; Winkel et al. 2010). Both, GASS and EBHIS use modern digital equipment and larger dishes. GASS and EBHIS have a significantly better angular resolution than the LAB survey allowing a much more detailed study of the Galactic HI distribution (see Sects. 2.1 and 2.2 for more details of the HI surveys).

[3] Stray radiation is an emission component that enters the receiving system of a telescope through its side lobes (Kalberla et al. 1980). A side lobe is a directional sensitivity not in the pointing direction of the telescope. When the telescope observes in one direction, bright emission in the direction of side lobes may contribute to the measured signal. The relative contribution of stray radiation is largest at high Galactic latitudes and has to be removed.

In the Milky Way most of the HI is associated with a rotating thin disk with a scale height of ~400 pc for the warm HI at the location of the Sun (see Kalberla & Kerp (2009) for a recent review of the HI distribution of the Milky Way). Surrounding the inner disk, there is a rotating thick disk component that connects to the Galactic halo. Towards the outer Galaxy, the disk is strongly warped and flaring, extending further into the halo.

The observed radial velocities of the gas clouds are used to differentiate between HI clouds that follow Galactic rotation or not. Different authors use different velocity criteria in the local standard of rest (LSR[4]) to distinguish between disk and halo. A clear separation between Galactic disk and halo is not possible since the disk has no clear boundary but smoothly connects to the halo. At high Galactic latitudes, a simple LSR velocity criterion is sufficient to identify halo clouds, since Galactic rotation is not as important there as in the Galactic disk (e.g. Wakker 1991). In order to separate the disk and halo also at low Galactic latitudes, Wakker (1991) introduces the deviation velocity $v_{\rm dev}$, which compares the observed radial LSR velocity to the minimum or maximum velocity allowed by a simple model of Galactic rotation. In this way the position-dependent differential Galactic rotation is taken into account. Depending on the observed velocities, one distinguishes between different types of halo clouds. Such a classification scheme is convenient, however, it does not necessarily reflect physical properties of the halo clouds. Since only the radial velocity component of the 3D velocity vector is observable, projection effects due to the orientation of the 3D velocity vector relative to the line-of-sight can strongly influence the classification of halo clouds.

1.1.1 Intermediate-velocity clouds

HI halo clouds with observed radial velocities of $20\,{\rm km\,s^{-1}} \leq |v_{\rm LSR}| \leq 100\,{\rm km\,s^{-1}}$ are classified loosely as intermediate-velocity clouds (IVCs). This is the definition for IVCs that we will use here, since we are only looking at objects with high Galactic latitudes of $b > 20°$. A precise velocity distinction cannot be made since in the spectra many IVCs continuously connect to the local disk gas.

Typically, IVCs have distances $D \lesssim 2\,{\rm kpc}$ and metallicies close to solar (Wakker 2001; Richter et al. 2001c; Albert & Danly 2004; Wakker 2004; Richter 2006; Wakker et al. 2008). Commonly, IVCs contain dust and emit in the far-infrared (FIR), although the dust grains appear to be smaller and hotter compared to grains in the Galactic disk (e.g. Planck Collaboration XXIV 2011). Smaller and hotter grains are interpreted as evidence for dust destruction and dust shattering in shocks, which can give insight in the history and origin of the gas. The HI mass in the largest IVC structures is $0.5 - 8 \times 10^5\,{\rm M_\odot}$ (Putman et al. 2012), which is uncertain due to the distances and problems with the separation between IVC and disk gas.

Altogether, these properties suggest that most of the IVCs consist of material that has been enriched with metals from stellar nucleosynthesis within the Galactic disk. This processed material is expelled by stellar feedback into the halo where it cools down and forms atomic gas clouds. This is commonly referred to as the Galactic fountain process (Shapiro & Field 1976; Bregman 1980). In Sect. 1.2, we discuss the Galactic fountain in more detail since it is important for the understanding of the IVC phenomenon in general, which is central in this work presented here.

There appear to be more IVCs with negative than with positive radial velocities, also when the deviation velocity is used, and more IVCs on the northern than on the southern hemisphere (Wakker 2004; Putman et al. 2012). Most of the IVCs are distributed in large complexes like the Intermediate-Velocity

[4] The local standard of rest (LSR) is a particular velocity frame used in astronomy. The LSR velocity quantifies the motion of objects relative to the mean motion of material within the solar neighbourhood. The Sun is assumed to follow a perfect circular orbit around the Galactic centre. The barycentre of our Solar System, e.g. the centre of mass, is typically used as the spatial reference point.

(IV) Arch and IV Spur on the northern hemisphere (see Fig. 1.1).

Concerning the molecular abundances, one can distinguish between two types of IVCs. On the one hand there are purely atomic IVCs with a tiny H_2 column density of $N_{H_2} = 10^{14} - 10^{16}\,\mathrm{cm}^{-2}$, which is inferred by UV absorption spectroscopy (Richter et al. 2003; Wakker 2006). This is a few orders of magnitude less than typical HI column densities of IVCs (compare with Fig. 1.1). Given the relatively high detection rate of H_2 within IVCs in absorption studies, Richter (2006) argues that cold and dense atomic gas clumps of typical spatial sizes of ~0.1 pc should be present in most IVCs. On the other hand there are a few molecular intermediate-velocity clouds (MIVCs) with significant molecular fractions such that carbon monoxide ^{12}CO(1→0) emission is detectable (Magnani & Smith 2010). The detection of molecular hydrogen in IVCs, in particular the large molecular fractions in MIVCs, requires dust for the formation of molecular hydrogen (Gould & Salpeter 1963). More details on the formation of molecules are given in Sect. 1.4.

The class of MIVCs is special because these clouds have larger heights z above the Galactic disk as compared to the majority of molecular material in our Galaxy (Magnani & Smith 2010). In the solar neighbourhood, the molecular disk material has a typical scale height of $z \simeq 81$ pc (Cox 2005). However, the MIVCs Draco, IVC 135+54, and IVC 210 have vertical heights of $z = 339^{+201}_{-134}$ pc (Gladders et al. 1998), $z = 285 \pm 75$ pc (Benjamin et al. 1996), and $z \simeq 350$ pc (Röhser et al. 2014). Hence, MIVCs constitute a distinct class of molecular clouds in the Milky Way. The origin of these clouds and the requirements for their formation are still not understood well.

In the context of gas accretion onto the Milky Way disk, the formation of molecular material at the disk-halo interface during the fountain cycle is of major importance: only cold atomic or molecular gas can feed star formation (Putman et al. 2012). If the material is heated and ionised, it is converted into the hot and tenuous Galactic halo medium. That is why MIVCs are objects of most interest for the accretion of cold and dense gas from the Galactic halo onto the disk: located within the disk-halo interface region, MIVCs contain cold gas and fall down onto the disk due to gravity.

1.1.2 High-velocity clouds

A different class of HI halo clouds are high-velocity clouds (HVCs), which are identified by their large radial velocities of $|v_{\mathrm{LSR}}| > 100\,\mathrm{km\,s}^{-1}$. The first detection of HI emission at such anomalous velocities goes back to Muller et al. (1963). Typically, HVCs have distances of $5\,\mathrm{kpc} \leq D \leq 50\,\mathrm{kpc}$, which are significantly larger than for the IVCs (e.g. Wakker 2001, 2004; Richter 2006; Wakker et al. 2008). The metallicities of most HVCs are 0.1–0.3 solar indicating a different origin than for the IVCs (Bregman 2004). So-far no HVC has been found with primordial metal abundances, indicating that most HVCs, if not all, contain some processed and metal-enriched material.

No HVC has been detected in the FIR (Wakker & Boulanger 1986; Peek et al. 2009; Williams et al. 2012). This is related to the low dust abundances due to the low metallicities and gas column densities in the Galactic halo. In addition, dust grains emit in the FIR because of the absorption of radiation, which heats up the grains. Since HVCs are located at large distances ($D \gtrsim 5\,\mathrm{kpc}$), the radiation field from the Galactic disk is weaker accordingly (Wolfire et al. 1995a). There could be dust within HVCs but it may be too cold to emit in the FIR to be detected. Molecular hydrogen has been found in HVCs only towards the Magellanic Stream (Richter et al. 2001b). This is consistent with the widely accepted model that the Magellanic Stream is tidally stripped material from the Magellanic Clouds (e.g. Nidever et al. 2008; Putman et al. 2012). The lack of detections of H_2 in HVCs in general points towards the low abundance of dust grains and the lack of dense gas in these objects.

The distribution of HVCs (Fig. 1.2) exhibits, similar to IVCs, large complexes in addition to smaller and isolated compact HVCs with angular sizes of less than 2° (Braun & Burton 1999). The Magellanic

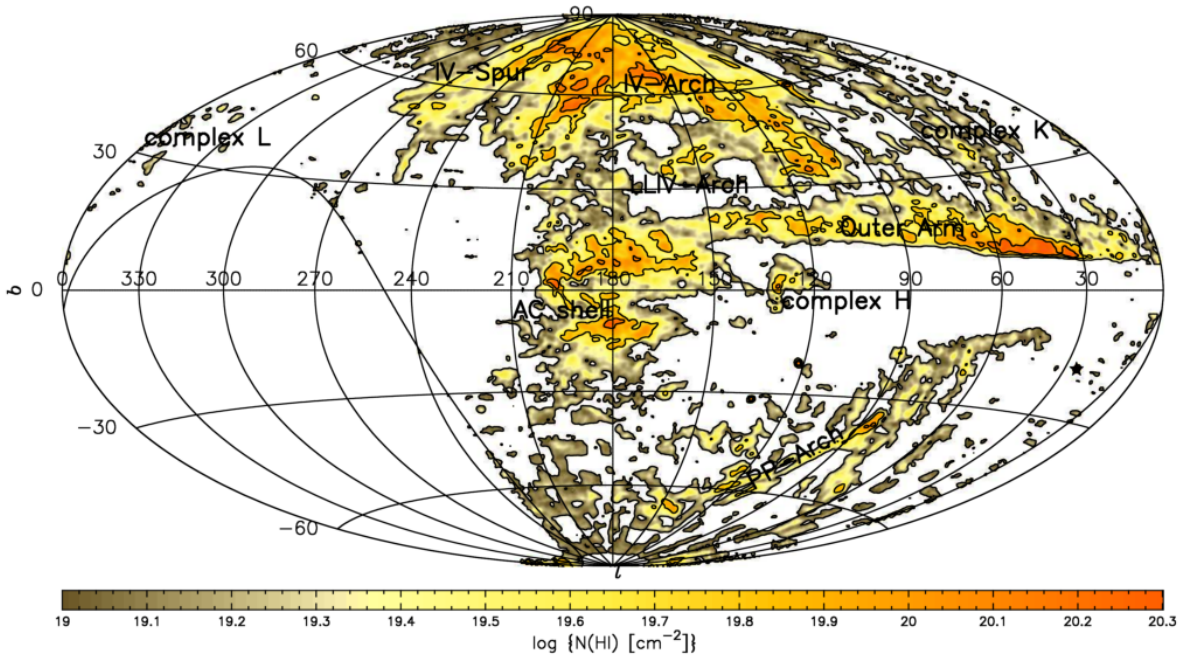

Fig. 1.1: Map of Galactic IVCs in Galactic coordinates l and b as compiled by Wakker (2004). The map is derived from the Leiden-Dwingeloo Survey (Hartmann & Burton 1997) showing all IVC gas with deviation velocities of $-90\,\mathrm{km\,s^{-1}} \leq v_{\mathrm{dev}} \leq -30\,\mathrm{km\,s^{-1}}$. The different complexes are labelled according to the literature. The colours encode the HI column density N_{HI} of the IVC gas. Image credit Wakker (2004).

System covers large fractions of the southern Galactic hemisphere, consisting of the Large and Small Magellanic Clouds (LMC and SMC), the Magellanic Stream (MS), and the Leading Arm (LA). Since the Magellanic System contains lots of low-metallicity gas that spreads within the local velocity regime (e.g. Nidever et al. 2010), this material is considered specially in our study of the IVC sky on the southern Galactic hemisphere.

The observable HI emission of HVCs is just a portion of the entire HVC phenomenon: Absorption-line observations indicate that the ionised gas mass of HVC complexes is similar to the neutral gas mass (Putman et al. 2012), suggesting that HI HVCs are embedded in extended ionised material (Ben Bekhti et al. 2012; Lehner et al. 2012). Furthermore, the halo is filled with low-column density atomic gas that is below the detection threshold of HI emission surveys (Richter 2006). With a simple approach, Putman et al. (2012) estimate an accretion rate of HVCs onto the Galactic disk of about $\sim 0.08\,\mathrm{M_\odot\,yr^{-1}}$. Hence, HVCs alone likely cannot account for the required accretion rate in our Galaxy.

There are many HVCs that show an elongated structure, some of which exhibit gradients in velocity and HI column density that result into a cometary appearance, the head-tail HVCs (Brüns et al. 2000). Such a morphology is commonly interpreted as a signature for the interaction between the cloud and the surrounding halo medium through which the clouds move with large relative velocities. Such interactions are critical in the context of the survival of HVCs in the Galactic halo (Putman et al. 2012). According to hydrodynamical simulations, HVCs should not survive more than a few 100 Myr because of their motion through the halo, which causes the action of gas instabilities, like Kelvin-Helmholtz instabilities, that ablate material from the clouds' rims causing for instance head-tail structures (Heitsch & Putman 2009). When clouds get disrupted, they should become part of the ionised halo medium.

There are several scenarios for the origin of HVCs (see e.g. Bregman 2004; Putman et al. 2012):

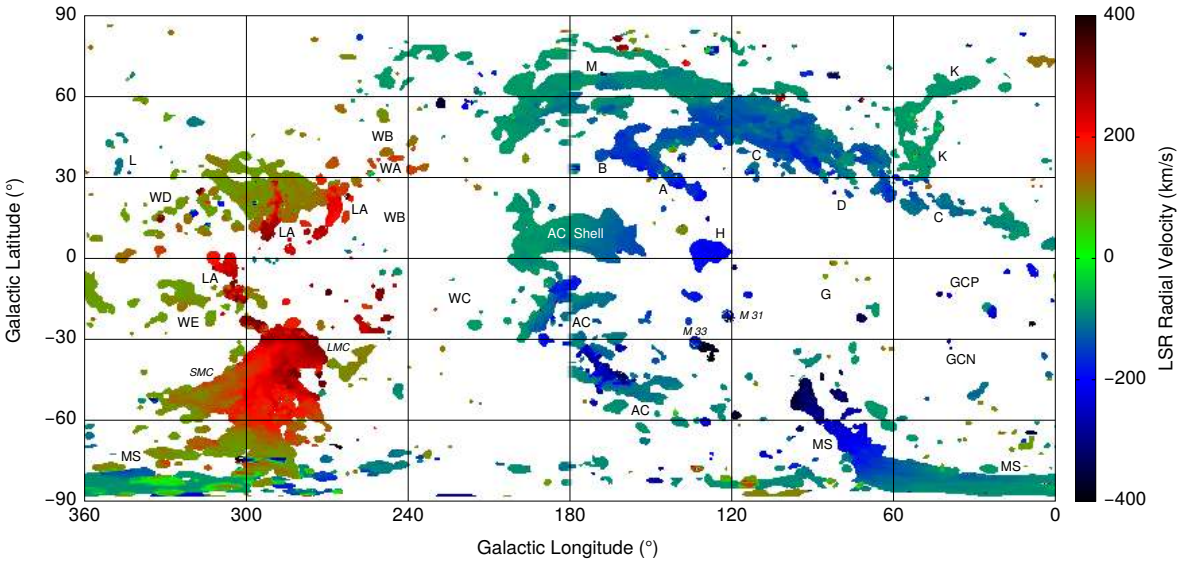

Fig. 1.2: All-sky map of Galactic HVCs in Galactic coordinates as compiled by Westmeier (2007). The map is derived from the LAB Survey (Kalberla et al. 2005) using a simple model of Galactic rotation and applying a deviation velocity criterion of $v_{\rm dev} > 65\,{\rm km\,s^{-1}}$. The different complexes are labelled according to their designations in the literature. The colours encode the radial velocity of the HVC gas. Image credit Westmeier (2007).

accretion from the intergalactic medium along cosmic filaments; tidal interactions between the Milky Way and other dwarf galaxies; ram-pressure stripping of gas from satellite galaxies because of the motion through the ambient hot halo (Grcevich & Putman 2009). In addition, strong Galactic fountains may be able to eject material to such large absolute velocities and distances. Recent simulations by Fraternali et al. (2015) claim that the HVC complex C could be the result of clustered supernovae in a Galactic spiral arm.

Around other spiral galaxies, analogues of Galactic HVCs are detected within ~50 kpc in projected distance (Thilker et al. 2004; Pisano et al. 2007; Westmeier et al. 2007). Many HI features in galactic halos appear to be related to accretion from satellite galaxies and tidal interactions with companion galaxies (Putman et al. 2012). Sancisi et al. (2008) find that about 50% of the field galaxies show evidence for external influences and large HI halo features. About 25% of the field galaxies show extraplanar HI emission with masses comparable to the Magellanic Stream (Putman et al. 2012). However, Heald (2015) states that the observable HI gas in emission has likely a low contribution to the total accretion rate onto galaxies. According to Giovanelli & Haynes (2015), no study of galaxies could identify enough accretion of gas that is sufficient to sustain their current star formation rate.

These works consider galaxies in the local universe. In the cosmological context of galaxy formation and evolution, the damped Lyman-α systems are gas-rich and star-forming galaxies (for a review see Wolfe et al. 2005). Damped Lyman-α systems are identified as strong absorption features in the spectra of distant quasars[5]. The intervening gaseous material along the line-of-sight to the quasar is thought to be associated with galaxies in the early universe, which contain most of the neutral gas at redshifts $1.6 < z < 5.0$ (Wolfe et al. 2005). Damped Lyman-α systems appear to host a multiphase ISM, which is regulated by radiative and hydrodynamic processes. In the framework of hierarchical structure for-

[5] Quasars are extremely luminous galaxies in the early universe. These objects are powered by the accretion of matter onto a supermassive black-hole.

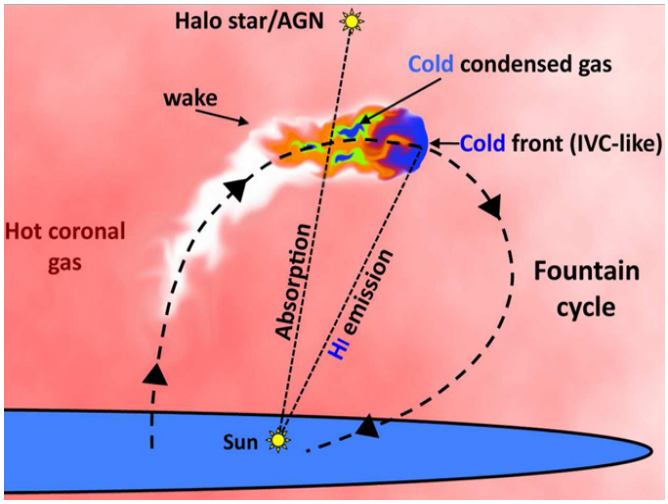

Fig. 1.3: Schematic view of the Galactic fountain cycle taken from Fraternali et al. (2013). Gas is ejected from the Galactic disk (blue disk) into the halo that is filled with hot and ionised gas (red). The ejected material cools and condenses, forming atomic clouds that are observable in HI emission. Eventually, the fountain ejecta fall back onto the disk. Image credit Fraternali et al. (2013).

mation these young galaxies are part of the early galaxy formation that is characterised by the merging of galaxies and the inflow of matter (Madau & Dickinson 2014). These processes are thought to be shaping the structure and evolution of galaxies even today.

1.2 Galactic fountains

One of the driving mechanisms of the evolution of galaxies is the fountain process. This is also one of the most important scenarios for the origin of the observable IVC sky of the Milky Way (Bregman 2004). The Galactic fountain describes a disk-wide phenomenon that is established by the joint effect of stellar feedback onto the ISM (Shapiro & Field 1976; Bregman 1980; Putman et al. 2012). Material is lifted into the halo, mostly as ionised gas, where it can cool and form neutral clouds, which mix with low-metallicity halo material. Because of the gravitational pull of the disk, these halo clouds fall back onto the disk eventually. A schematic view of the fountain cycle is shown in Fig. 1.3.

Stars form in the ISM and disperse their surroundings due to feedback processes. Especially high-mass stars emit lots of radiation, ionising and heating the surrounding gas. The gas may buoyantly rise up into the halo, or the gas and dust may be pushed away by stellar winds and supernovae.

In simulations of Galactic fountains, Melioli et al. (2008, 2009) find that the combined power of 100 supernovae of type II[6] are able to eject material to scale heights of up to $|z| \simeq 2\,\mathrm{kpc}$. The gas returns back to the disk mostly in the form of cool and atomic clouds. Simulations by de Avillez (2000) and others sketch the same picture: supernovae disrupt the disk locally and sustain a thick gaseous disk out to $|z| = 2 - 4\,\mathrm{kpc}$. Within the thick disk these ejecta cool down and form clouds that show similar morphologies and kinematics like the observed IVCs.

For violent star-forming events, like in star-burst dwarf galaxies, the combined effect of clustered supernovae may lead to a galactic wind that removes material from the gravitational potential of the galaxy altogether. This wind ejects material and magnetic fields into the intergalactic medium (Veilleux et al. 2005; Melioli et al. 2015).

Further observational support for the link between star formation and the existence of halo material is given by Ford et al. (2010), who identify small disk-halo clouds that appear to be linked to star

[6] Type II supernovae are core-collapse supernovae of high-mass stars with initial masses of more than $8\,\mathrm{M}_\odot$ (e.g. Poelarends et al. 2008).

formation sites in the spiral arms of our Galaxy. The goals of the Hydrogen Accretion in Local Galaxies Survey (HALOGAS, Heald et al. 2011) are to study the distribution and kinematics of extraplanar HI gas in nearby galaxies with deep observations using the Westerbork-Synthesis Radio Telescope (WSRT). Recent results show that thick disks with scale heights of $|z| \simeq 3\,\mathrm{kpc}$ are found typically in star-forming galaxies (Gentile et al. 2013). Hence, when a galaxy harbours sufficient star-formation activity, a gaseous thick disk is expected (Zschaechner et al. 2012; Heald 2015). For the halo of NGC 891, that extends up to $|z| \simeq 5\,\mathrm{kpc}$, Oosterloo et al. (2007) argue that its properties are explained well by a galactic fountain process and the accompanying ionised outflow, subsequent cooling of the ejecta, and cold inflow. All these observations indicate a connection between star formation activity, galactic fountains, and existing halo-material (see also the review on galactic winds by Veilleux et al. 2005).

Since we study the FIR emission of potential fountain ejecta in this thesis, the existence and survival of dust grains during the fountain cycle is important. It is clear that dust grains are transported from the galactic thin disks into the thick disks and halos (e.g. Howk 2012). However, it is still obscure to what degree the properties of the grains are changed by the energetic driving processes (Jones & Nuth 2011). For example, the grain-size distributions within IVCs appear to be changed such that more smaller grains are present (e.g. Weiß et al. 1999; Planck Collaboration XXIV 2011). Grains are efficiently eroded and shattered by collisions between gas and dust particles (Jones et al. 1994, 1996; Guillet et al. 2009, 2011). Jones & Nuth (2011) suggest that the clumping of the gas may protect dust grains within shocks.

For the transportation of dust grains into the halo, radiation pressure may be of large importance, which is the force exerted onto grains by radiation (e.g. Murray et al. 2005, 2010, 2011; Coker et al. 2013). Such radiative-driven ejections are thought to be less destructive than wind- or shock-driven processes, sustaining more cold and neutral gas within the ejecta (Murray et al. 2011). Even before any supernova goes off in a star-forming region, radiation pressure is able to lift cold and neutral gas several hundreds of parsecs above the disk (Nath & Silk 2009; Murray et al. 2011). In this way radiation pressure appears to alleviate the problems of dust destruction in outflows into the halo. In addition, in the galaxy M 82 the existence of large amounts of extra-planar dust and molecular gas as traced by CO emission may be explained (Coker et al. 2013; Leroy et al. 2015). Recent studies also find that cosmic rays alone can drive outflows that are slower but denser and colder than those of thermal supernova-driven ones (Girichidis et al. 2015).

The material that is transported into the halo will eventually fall back onto the disk. At the disk-halo interface region a significant amount of material may cool to form dense clouds, which are accreted (Marinacci et al. 2010; Joung et al. 2012; Marasco et al. 2012). These objects would be part of the observable IVC population.

MIVCs, which contain cold, dense, and molecular gas, may be an important link connecting the gaseous halos to the star-forming disks. However, only a few of these objects are known (Magnani & Smith 2010). These IVCs all show infalling radial velocities and are located within a few hundreds of parsecs of the Galactic disk indicating that these clouds are in the final stages of the accretion process. They have significant molecular fractions indicating large amounts of cold and dense gas. These properties suggest that molecular IVCs are ideal candidates for the accretion of cold and molecular material for the next generation of stars in the Milky Way. In order to allow for the existence of cold and dense material, the gas has to be able to efficiently cool, which is discussed in the next Section.

1.3 Heating, cooling, and the phases of the interstellar medium

Constantly, energy and momentum is injected into the ISM. Depending on the specific environmental conditions, the gas either heats up or cools down striving for a balance and equilibrium. The cooling ca-

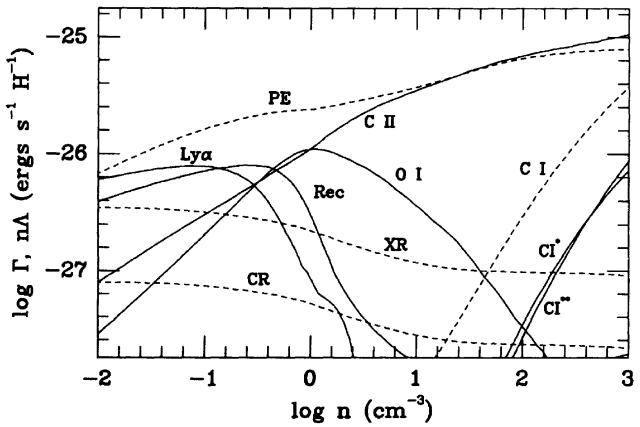

Fig. 1.4: Heating and cooling efficiencies in the ISM taken from Wolfire et al. (1995a). The dashed lines give heating efficiencies Γ and the solid lines cooling efficiencies $n\Lambda$. Depending on the particle density different processes are important. The photoelectric emission (PE) of electrons from dust grains is the dominating heating source for all considered particle densities. Fine-structure emission lines are dominating the cooling for particle densities of $n \gtrsim 1\,\mathrm{cm}^{-3}$. Image credit Wolfire et al. (1995a).

pabilities of gas are very important for the potential existence of molecular material. There are different heating and cooling mechanisms in the ISM that dominate for different particle densities. Wolfire et al. (1995a) calculate the cooling and heating efficiencies for a range of densities (Fig. 1.4). Depending on the degree of ionisation and the efficiency of heating and cooling, one distinguishes between different phases of the ISM. A full description of heating and cooling in the ISM can be found in Wolfire et al. (1995a), Kalberla & Kerp (2009), and Draine (2011).

Heating The most efficient heating mechanism for a wide range of volume densities is the photoelectric emission (PE) of electrons from the surfaces of dust grains (Fig. 1.4). These free electrons heat the gas by coulomb scattering with other free electrons.

Cooling The emission of fine-structure lines, mostly by ionised carbon CII at $158\,\mu$m and neutral oxygen OI at $63\,\mu$m, are most important for the cooling of the ISM in the atomic phases with densities $n \gtrsim 1\,\mathrm{cm}^{-3}$ and gas temperatures $10\,\mathrm{K} \lesssim T_{\mathrm{gas}} \lesssim 10^4\,\mathrm{K}$ (Fig. 1.4). At these temperatures, the fine-structure levels are efficiently populated by collisions. The ISM is also transparent for this radiation in the FIR allowing the energy to leave the emitting medium.

Phases of the ISM The ISM is described by a number of different phases that are in approximate pressure equilibrium with each other: the cold phase is surrounded by a warmer medium which is encompassed by a hot and ionised phase (e.g. McKee & Ostriker 1977; Cox 2005; Snow & McCall 2006). These phases exist because of the different importance of the heating and cooling processes for various densities and the accompanying changes in ionisation. One divides the ISM into the hot-ionised medium (HIM), warm-ionised medium (WIM), warm-neutral medium (WNM), cold-neutral medium (CNM), and molecular medium (MM).

The atomic medium is differentiated in two regimes, the WNM and CNM. These two phases naturally arise from the dependencies of the heating and cooling functions on density leading to a characteristic S-shape in the density-pressure diagram (Wolfire et al. 1995a, their Fig. 3a). The atomic gas is stable when it can balance itself against energy input. At low densities only warm gas (WNM), at high densities only cold gas (CNM) exists. In between, classically the atomic medium is unstable and should not exist. Any over-density within the gaseous medium should re-expand due to its enhanced temperature in order to stay in pressure equilibrium, unless the cooling is efficient and rapid enough. However, observations of the ISM find that a large fraction of the atomic medium is in between the two stable atomic phases

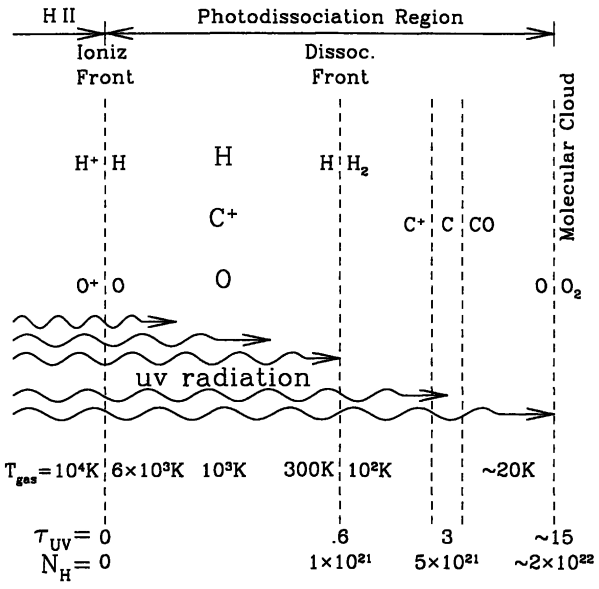

Fig. 1.5: Schematic view of the transition region from atomic to molecular gas taken from Draine & Bertoldi (1999). The chemistry of the photodissociation region (PDR) is governed by the attenuation of the UV radiation field for larger optical depths $\tau_{\rm UV}$. Image credit Draine & Bertoldi (1999).

(Heiles & Troland 2003). The existence of a large fraction of thermally unstable gas is direct evidence for the dynamical and turbulent ISM (e.g. Saury et al. 2014).

The efficient cooling by fine-structure lines leads to short cooling times of the CNM of $t_{\rm cool} \simeq 10^5$ yr, while for the WNM $t_{\rm cool} \simeq 10^7$ yr (e.g. Kalberla & Kerp 2009). These cooling times reflect also the spatial length-scales on which CNM and WNM exist. Generally, CNM is clumpy and structured on scales of a few parsecs while the WNM is diffuse and smoothly distributed over tens or hundreds of parsecs (e.g. Kalberla & Kerp 2009).

The cooling of the gas is important for the formation of molecular material, consequently also for the existence of MIVCs. Dense and cold structures must be formed from the atomic medium, allowing the efficient formation of molecules in these condensations. The relevance and the physics of simple interstellar molecules are described in the next Section.

1.4 Molecules in the interstellar medium

Molecules are abundant in the ISM. However, the binding energy of even simple molecules is low, suggesting that molecules can only reside in regions of low ionising radiation fields, which are found in dense and cold environments (e.g. Snow & McCall 2006).

The structure of the transition region from atomic to molecular gas is shown in Fig. 1.5 schematically. The chemistry of the photodissociation region (PDR) is determined by the attenuation of the UV radiation field (Draine & Bertoldi 1999). Near $N_{\rm H} = 1 \times 10^{21}$ cm^{-2} atomic hydrogen turns molecular, while the transition from atomic carbon to carbon monoxide (CO) occurs around $N_{\rm H} = 5 \times 10^{21}$ cm^{-2}.

Despite the importance of molecules as observational diagnostics (Sect. 1.4.4), molecules act as coolants of the ISM in dense environments (Juvela et al. 2001). Even simple molecules like CO, H_2, H_2O, or O_2 offer a large number of electronic, rotational, and vibrational transitions by which energy can be radiated away providing significant cooling of molecular clouds (Goldsmith & Langer 1978). The most abundant molecule H_2 has a special role as a precursor to a rich interstellar chemistry.

1.4.1 Formation

The gas-phase formation of H_2 is inefficient in the ISM of the Milky Way (Glover 2003). Instead, most H_2 and other molecules form on the surfaces of dust grains, which act as reaction catalysts (e.g. Gould & Salpeter 1963; Hollenbach & Salpeter 1971; Herbst & van Dishoeck 2009). Hydrogen atoms hit the grain surface and stick to it. This provides time for the reaction with another hydrogen atom to form H_2 on the surface. The H_2 formation rate depends on many parameters like the collision rate between hydrogen atoms and dust grains, the probability that atoms stick on the grain surface, their mobility and lifetime on the surface, and the probability that the formed molecule is ejected into the gas phase (Shull & Beckwith 1982).

According to Hollenbach et al. (1971) the equilibrium formation timescale for H_2 depends on the gas density n by

$$t_{H_2} \simeq \frac{10^9\,\mathrm{yr}}{n\,[\mathrm{cm}^{-3}]}. \tag{1.1}$$

For a dense gas with $n = 100\,\mathrm{cm}^{-3}$, typical for diffuse molecular clouds, the formation timescale is $t_{H_2} \simeq 10^7$ yr. This is in conflict with the apparent short lifetimes of molecular clouds, which require that large amounts of H_2 should be formed within a few Myr (Hartmann et al. 2001). Non-equilibrium processes like turbulence, and dynamical and thermal instabilities allow a much more rapid H_2 formation (e.g. Audit & Hennebelle 2005; Heitsch et al. 2005; Glover & Mac Low 2007). Still, achieving chemical equilibrium abundances takes a lot of time which indicates that the formation of molecular clouds is a non-equilibrium and transient process (Glover & Mac Low 2007; Vázquez-Semadeni et al. 2005).

Molecular hydrogen is the most abundant gas-phase molecule in the universe, while carbon monoxide, the second most abundant molecule, has a typical fractional abundance of 10^{-4} relative to H_2 in dense molecular clouds (Herbst & van Dishoeck 2009). There are several formation routes for CO in the diffuse molecular ISM (Snow & McCall 2006; Draine 2011, p. 377). All of these formation channels require the presence of H_2 as a prerequisite for the formation of CO.

1.4.2 Shielding

Molecules are easily destroyed by the ambient UV radiation field (e.g. Herbst & van Dishoeck 2009). Considering the most abundant molecules, H_2 and CO have binding energies of ~4.5 eV (e.g. Stecher & Williams 1967) and ~11.09 eV (e.g. van Dishoeck & Black 1988).

Depending on the optical depth of the medium, the photodissociating emission is attenuated, which leads to a shielding effect. One can distinguish between different shielding mechanisms (van Dishoeck & Black 1988): 1) self-shielding: the absorption of a line grows with increasing column density until saturation is reached; 2) mutual shielding: absorption lines of different species overlap with each other, e.g. from different isotopes or atomic and molecular species; 3) dust grains attenuate the radiation field.

Self-shielding is the most important process for the attenuation of the UV radiation field at the initial formation of molecular clouds. Once H_2 has formed, it absorbs UV radiation and hinders the radiation to penetrate deeper into the cloud. Self-shielding of H_2 starts to be efficient at H_2 column densities of only $\sim 10^{14}\,\mathrm{cm}^{-2}$ (Draine & Bertoldi 1996; Lee et al. 1996).

1.4.3 Excitation and level population

For the emission of, e.g., the rotational line ^{12}CO(1→0), the molecules have to get excited to the first energy level in order to allow the emission of photons by radiative deexcitation. Generally, radiative and collisional excitation in combination establish the relative level populations. For large particle densities,

like in molecular clouds, excitation by collisions with electrons, other atoms, or molecules within the gas phase is the dominant excitation mechanism (e.g. Draine 2011).

One defines a critical density $n_{\rm crit}$ for a particular collision partner and energy state as the density at which the rate of collisional deexcitations equals the rate of radiative deexcitations. When a particular transition is subthermally excited, equivalent to densities lower than the critical density, radiative processes dominate the population levels of the molecule. In such cases not all molecules are excited to radiate but may be invisible (e.g. Liszt et al. 2010).

1.4.4 Observations

Due to their complexity, molecules offer a large number of energy levels that lead to complicated electronic, vibrational, and rotational spectra. Generally, electronic transitions have energies in the UV or visible regime, while vibrational transitions are found at IR wavelengths, and rotational lines in the radio regime (e.g. Snow & McCall 2006). The emission from molecules is a useful probe for the physical conditions within the medium. For instance, information on the temperature and density, the time-evolution of the sources, and their kinematics can be gained (Herbst & van Dishoeck 2009; Snow & McCall 2006).

Molecular hydrogen H_2 is the most abundant molecule in the universe. However, it is symmetric causing a vanishing permanent dipole moment. Only much weaker quadrupole line transitions are allowed. Hence, the direct observation of H_2 is difficult and other tracers are used to infer the distribution of molecular hydrogen. The first direct observations of H_2 in absorption (Carruthers 1970) were possible only with the advent of UV satellites. Today, instruments like the Cosmic Origins Spectrograph (COS, Osterman et al. 2011) on-board the Hubble Space Telescope allow to conduct high-sensitivity spectroscopy in the UV range towards distant stars and quasars probing the physical conditions in the intervening absorbing gas.

However, such observations are not well suited to study the distribution of the molecular gas on large scales in our Galaxy, especially spectrally close to the strong absorption of the Milky Way (e.g. Fig. 3 of Richter et al. 2001a). Hence, a tracer for molecular gas is required that allows the efficient mapping of the molecular material on large scales. The most commonly used tracer for H_2 is CO, which is easily observable due to its electric dipole moment because the constituting atoms have different masses. Its lowest rotational emission lines are in the millimetre regime, which can be observed from the ground[7].

One adopts a conversion factor between the integrated ^{12}CO(1→0) line emission $W_{^{12}\mathrm{CO}(1\rightarrow0)}$ and the H_2 column density $N_{\mathrm{H_2}}$ by

$$X_{\rm CO} = \frac{N_{\mathrm{H_2}}}{W_{^{12}\mathrm{CO}(1\rightarrow0)}}. \tag{1.2}$$

For the Milky Way an average $X_{\rm CO} = 2 \times 10^{20}\,\mathrm{cm^{-2}}\,(\mathrm{K\,km\,s^{-1}})^{-1}$ is inferred from observations and numerical models (Bolatto et al. 2013). However, due to the sensitivity of CO chemistry to local conditions, the occurrence and distribution of CO is different than that of H_2 (e.g. Liszt & Pety 2012). There are regions where H_2 can exist but CO does not. Hence, the correspondence between H_2 and CO is expected to vary significantly across an individual cloud.

The formation of H_2 and CO in different environments leads to the existence of H_2 that is not traced by CO. This molecular gas is commonly referred to as CO-dark gas (Grenier et al. 2005; Wolfire et al. 2010). By modelling the PDR in molecular clouds, Wolfire et al. (2010) find fractions of CO-dark H_2 gas of typically ∼0.3, which is a significant amount of the total hydrogen content of molecular clouds. Generally, $X_{\rm CO}$ depends strongly on environmental conditions (Shetty et al. 2011a,b; Feldmann et al.

[7] Observatories for mm and sub-mm wavelength are located typically at high altitudes to reduce the effects of the atmosphere (see Sect. 2.6).

2012). Although CO emission maps are easily obtained, one has to be careful in the conversion between CO emission and H_2 column density.

Emission maps of CO lines reveal the distribution and kinematics of molecular gas. Dame et al. (2001) present a composition of individual ^{12}CO(1→0) surveys of our Galaxy providing a complete coverage in the Galactic plane. However, the high Galactic latitudes are not covered in large-scale CO surveys. One reason for this is that there is simply not as much molecular gas and only selected clouds at high latitude are associated with molecular gas and CO emission (Magnani et al. 1985). Recently, the all-sky distribution of CO was measured by the *Planck* satellite (Planck Collaboration I 2014) as a by-product (Planck Collaboration XIII 2014). By modelling the total FIR emission, the integrated ^{12}CO(1→0) emission is inferred. These maps have a limited sensitivity at high Galactic latitudes. For instance, the molecular IVC that we study in Chapters 3 and 4 is not detected in CO emission by *Planck*. Hence, a different method for the inference of molecular hydrogen is required on large scales at large Galactic latitudes, which is described next.

1.5 The correlation between gas and dust in the interstellar medium

One of the important discoveries of the Infrared Astronomical Satellite (IRAS, Neugebauer et al. 1984) is the detection of the IR cirrus and the existence of a linear correlation between the hydrogen column density and the FIR emission from dust (Boulanger & Perault 1988; Boulanger et al. 1996). This correlation indicates a good mixture between gas and dust. In other words, the observed FIR emission I of a gas cloud is directly related to the total amount of hydrogen N_H by two linear parameters. At frequency ν one writes

$$I_\nu = R_\nu + \epsilon_\nu \times N_\mathrm{H} \simeq R_\nu + \epsilon_\nu \times (N_{\mathrm{H}^+} + N_\mathrm{HI} + 2N_{\mathrm{H}_2}). \tag{1.3}$$

The total hydrogen column density N_H is the sum of the ionised hydrogen column density N_{H^+}, the atomic hydrogen column density N_HI, and the molecular hydrogen column density N_{H_2}. The offset R_ν is not an instrumental effect but related to the cosmic infrared background (for a recent review see Lagache et al. 2005), which originates from extragalactic IR galaxies unrelated to the Milky Way. The dust emissivity ϵ_ν, that is associated with the different species of hydrogen, is assumed to be similar. The column density of ionised hydrogen is usually negligible in HI clouds that form molecular hydrogen (e.g. Lagache et al. 2000). The offset R_ν and the dust emissivity ϵ_ν can be fitted directly from the correlation data for data points where the amount of H_2 is assumed to be minor. Different authors report thresholds between $N_\mathrm{HI} = 1 - 5 \times 10^{20}\,\mathrm{cm}^{-2}$ up to which the correlation is linear and no H_2 is present (e.g. Savage et al. 1977; Reach et al. 1994; Lagache et al. 1998; Gillmon et al. 2006; Gillmon & Shull 2006; Planck Collaboration XXIV 2011; Röhser et al. 2014; Lenz et al. 2015).

The direct observables in Eq. (1.3) are the FIR intensity I_ν and the HI column density N_HI, easily accessible by all-sky surveys (Sect. 2.1-2.4). If a cloud contains significant amounts of H_2, this contribution of hydrogen is missing from the HI-FIR correlation, resulting in the FIR excess, which is a steepening of the correlation towards larger column densities (Désert et al. 1988). The FIR emission strength is directly related to the total amount of hydrogen. By subtracting the contribution from atomic hydrogen to the FIR emission, the residual FIR emission is the contribution from dust mixed with molecular hydrogen. By rearranging Eq. (1.3) to

$$N_{\mathrm{H}_2} \simeq \frac{1}{2}\left(\frac{I_\nu - R_\nu}{\epsilon_\nu} - N_\mathrm{HI}\right), \tag{1.4}$$

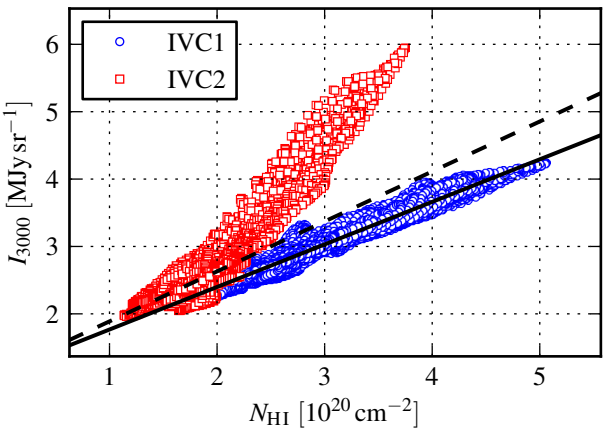

Fig. 1.6: Exemplary HI-FIR correlations for different amounts of molecular hydrogen taken from Röhser et al. (2014). The FIR intensity at 3000 GHz is plotted against the HI column density for two clouds IVC 1 (blue circles) and IVC 2 (red squares). The linear fits of Eq. 1.3 to the data are shown as the solid black line for IVC 1 and as the dashed black line for IVC 2. For IVC 2 the fit is performed up to $N_{\rm HI} = 2 \times 10^{20}\,{\rm cm}^{-2}$, up to which H_2 is expected to be negligible. Image credit Röhser et al. (2014).

one can derive the distribution of molecular hydrogen from surveys of the HI and FIR emission with estimates of R_ν and ϵ_ν.

An example of the HI-FIR correlation is shown in Fig. 1.6 for two IVCs with different amounts of molecular hydrogen. In this Figure, the FIR intensity at 3000 GHz is plotted against the HI column density for the two clouds IVC 1 (blue) and IVC 2 (red). This Figure is taken from Röhser et al. (2014), which is presented in Chapter 3 later. The linear fits of Eq. (1.3) to the data are shown as the solid black line for IVC 1 and as the dashed black line for IVC 2. For IVC 2 the fit is performed up to $N_{\rm HI} = 2 \times 10^{20}\,{\rm cm}^{-2}$, up to which H_2 is expected to be negligible. For IVC 1 a single linear function is able to model the correlation reasonably well, despite some intrinsic scatter. For IVC 2, up to $N_{\rm HI} \simeq 2 \times 10^{20}\,{\rm cm}^{-2}$ a similar correlation is valid, which steepens significantly for larger HI column densities. This is the FIR excess that can be converted to a column density of H_2 by inserting the fitted linear parameters in Eq. (1.4). The detection of ^{12}CO(1→0) emission at the location of the FIR excess proves the existence of molecular material within the cloud (Désert et al. (1990), also Chapter 4).

In this scheme some assumptions are made, most importantly there can be clouds along the lines-of-sight with different dust-to-gas ratios. One can compensate for this by adding more emission components with different slopes ϵ_ν^i to the HI-FIR correlation to model the observed emission appropriately (e.g. Lenz et al. 2015). The emission strength of the dust may vary intrinsically, which is usually found to be insignificant for the diffuse ISM (Planck Collaboration XXIV 2011). There are indications that the dust may change its emission properties due to grain coagulation and the formation of ice mantles within dense and cold regions of molecular clouds (e.g. Ormel et al. 2011). However, these effects are thought to be negligible for the diffuse ISM with particle densities below $\sim$1000 cm^{-3}. Furthermore, for large HI column densities HI gets optically thick (e.g. Braun 2012), which leads to a similar effect as the FIR excess since the HI column densities are underestimated. However, the optical thickness is only relevant for $N_{\rm HI} > 10^{21}\,{\rm cm}^{-2}$ (Fig. 10 of Strasser & Taylor 2004). In IVCs, the HI column densities are typically significantly less (e.g. compare with Fig. 1.1).

An important advantage of the inference of molecular hydrogen from the FIR dust emission, rather than from CO emission, is that the FIR dust emission traces the complete amount of H_2. Hence, FIR emission traces also the CO-dark gas (Wolfire et al. 2010).

Reach et al. (1998) present the most recent study of the FIR excess emission on global scales in our Galaxy, which is why we discuss their data, methods, and results in more detail. Reach et al. use data in the FIR at 60 − 240 μm with a spatial resolution of 42′ from the Diffuse Infrared Background Experiment (DIRBE) on-board the Cosmic Background Explorer satellite (COBE, Boggess et al. 1992). For the HI, they use two different surveys: for the northern hemisphere the Leiden-Dwingeloo Survey (Hartmann

& Burton 1997) with a beam size of 36′ and beam-by-beam sampling, for the southern hemisphere the Parkes 60 ft telescope 21 cm line data (Cleary et al. 1979) with an angular resolution of 48′, which suffers from data artefacts and severe under-sampling. The insufficient sampling means that not the entire HI emission is measured, leading to biases in the derived HI column densities.

Reach et al. (1998) correlate the HI column density integrated between $-100\,\mathrm{km\,s^{-1}} \leq v_{\mathrm{LSR}} \leq 100\,\mathrm{km\,s^{-1}}$ to the FIR emission at each individual FIR frequency and subtract the FIR emission associated with the atomic medium. In this way they exclude many of the HVCs, however, they do not consider the HI emission from the Magellanic Stream that stretches across the velocity interval. The correlation is performed in regions with a radius of 10° on a regular grid with spacings of 10°. In each of these cells the pixel-to-pixel correlation is performed and the slope and offset of the HI-FIR correlation is computed. Reach et al. (1998) apply an upper threshold of $N_{\mathrm{HI}} = 3 \times 10^{20}\,\mathrm{cm^{-2}}$ for the fitting.

According to Reach et al. (1998) the correlation works very well in most cells. In some regions the fitting procedure fails where large molecular clouds or bright dust emission is located, which most likely lead to insufficient data points with $N_{\mathrm{HI}} < 3 \times 10^{20}\,\mathrm{cm^{-2}}$. In these cases the slopes and offsets are interpolated from neighbouring cells. The authors note that the slope and offset are degenerated in the fitting with an apparent anti-correlation.

Reach et al. (1998) speak of FIR excess-clouds in case of significant excess at both 100 μm and 240 μm. In their Table 4, they compile the list of detected FIR excess clouds. In addition, maps of the FIR excess emission are presented above $|b| = 20°$ in various angular projections. Typically, FIR excess objects show lower dust temperatures than the average atomic ISM, indicating that these clouds are associated with molecular hydrogen rather than subject to enhanced dust luminosity due to heating.

The authors compare their FIR-excess clouds to the known high-latitude molecular clouds, most of which are the Magnani-Blitz-Mundi clouds (MBM, Magnani et al. 1985, 1996), and to the study on FIR excess conducted by Désert et al. (1988). Reach et al. (1998) recover all high-latitude molecular clouds from Magnani et al. (1996) as FIR excess clouds. However, about half of the excess clouds identified by Désert et al. (1988) are not confirmed. This is attributed to the different data sets used by Désert et al. (1988). For about half of the Reach et al. (1998) excess clouds, Onishi et al. (2001) detect ^{12}CO(1→0) counterparts. Onishi et al. report on a higher detection rate for cold than for warm excess clouds.

The study by Reach et al. (1998) is in a sense the basis from which we advance in this thesis. There are major improvements possible, which allow a better analysis of the global HI-FIR correlation. In particular, their analysis does not distinguish between different gaseous components like low-velocity clouds (LVCs) and IVCs.

1.6 Motivation and outline of this thesis

While the existence of atomic and molecular IVCs (AIVCs and MIVCs) is known for a long time, their evolution in the Galactic halo and their importance for our Galaxy is still unclear. The few known MIVCs are a puzzling phenomenon since these low-mass clouds are observed in an unusual environment of low density. Generally, the amount of molecular material in the lower Galactic halo is difficult to quantify. Likewise, the importance of MIVCs for the accretion of cold material onto the star-forming disk is unclear.

The uncertain role of MIVCs in Galactic evolution is also related to the fact that to-date there is no coherent study of the molecular content of IVCs. Previous studies of the HI-FIR correlation either focussed on the global correlation of the total HI gas and dust, which is dominated by the disk material, ignoring the kinematic information, or on individual small objects. Sensitive large-scale CO surveys are available only for the Galactic disk and low latitudes. Searches for CO emission towards the Galactic

poles are too sparsely sampled to detect the full amount of molecular material (Hartmann et al. 1998).

In this work, we use the most recent HI and FIR surveys, EBHIS (Winkel et al. 2016; Kerp et al. 2011; Winkel et al. 2010) and GASS (McClure-Griffiths et al. 2009; Kalberla et al. 2010; Kalberla & Haud 2015), from the *Planck* satellite (Planck Collaboration I 2014), and the Improved Reprocessing of the IRAS Survey (IRIS, Miville-Deschênes & Lagache 2005) to study IVCs and their molecular content in the Milky Way halo. These surveys provide a much better angular resolution, sensitivity, and frequency coverage in the FIR as compared to previous data sets. The goals are to understand the evolution of IVCs at the disk-halo interface and their transition from atomic to molecular clouds better.

For two particular IVCs, an atomic and a molecular one, we carried out high-resolution observations in HI and CO. The HI observations were conducted with the Westerbork-Synthesis Radio Telescope (WSRT). As a radio interferometer, the WSRT provides superior angular resolution as compared to a single-dish telescope. The ^{12}CO(1→0) emission of the MIVC was mapped with the Institut de Radioastronomie Millimétrique (IRAM) 30 m telescope.

Since the data is key in this work, we present the above-mentioned data sets thoroughly in Chapter 2. The technical details of the instruments, the measurement strategies, and the data reduction are described in detail for our own observations.

In Chapters 3 and 4, the transition from atomic to molecular IVCs is studied in large detail for the pair of atomic and molecular IVCs that are located close to each other at high Galactic latitudes. In Chapter 3[8], their environment is analysed and their physical properties are determined from single-dish HI data complemented with FIR data. Furthermore, the idea of the dynamical nature of the transition from atomic to molecular clouds is presented and validated with the data at hand.

In Chapter 4[9], we elaborate on these results and present more details of the gaseous structures of the two IVCs by analysing their high-resolution HI and CO observations. The high angular resolution enables us to compare the different small-scale structures within the atomic and molecular IVC, respectively. Since molecules require shielding, the different spatial and spectral properties are expected to reflect the different chemical states as well. The dynamical aspect of the transition from atomic to molecular clouds is discussed further. In addition, our multi-frequency data set allows the estimation of the X_{CO} conversion factor and its variations over the MIVC.

In Chapter 5, we study the molecular abundances in IVCs on large scales using a general approach. The aim is in particular to search for additional MIVCs, which were not detected in former studies using previously existing data. Since molecules form in small and dense structures, such objects may have been simply overlooked in former studies due to the lack of angular resolution of the HI data. In addition, the all-sky perspective gives a view of the general environmental conditions of AIVCs and MIVCs. The question arises, if the formation of MIVCs requires special conditions or if it is a natural part within the Galactic fountain cycle during the final accretion phase. Statistical properties of the global IVC population are presented and interpreted within the Galactic fountain model. The sample of MIVCs allows for the first time to constrain the total molecular mass in IVCs and the corresponding accretion rate onto our Galaxy.

[8] Published in "A dynamical transition from atomic to molecular intermediate-velocity clouds", T. Röhser, J. Kerp, B. Winkel, F. Boulanger, and G. Lagache, A&A, 564, A 71, 2014.

[9] Submitted to the journal A&A as "High-resolution HI and CO observations of high-latitude intermediate-velocity clouds", T. Röhser, J. Kerp, N. Ben Bekhti, and B. Winkel.

CHAPTER 2

Data sets

In this Chapter all data sets are presented, which are used in this work. The quality and the properties of the data are key for the results obtained in Chapters 3–5. In the following the all-sky HI and FIR data are discussed first, then the high-resolution HI and CO observations. The most important characteristics of these data sets are listed in Table 2.1 on page 20.

2.1 The Parkes Galactic All-sky Survey

The Parkes Galactic All-sky Survey (GASS, McClure-Griffiths et al. 2009; Kalberla et al. 2010; Kalberla & Haud 2015) is a survey of the Galactic HI emission on the whole southern hemisphere for declinations $\delta \leq 1°$. The GASS complements the HI Parkes All-Sky Survey (HIPASS, Barnes et al. 2001), which is a blind extragalactic HI survey on the southern hemisphere out to a redshift of ∼0.04. GASS was performed between January 2005 and November 2006 with the Parkes 64 m radio telescope (Australia) using its 21 cm multi-beam receiver system that consists of 13 individual feed horns. For GASS the sky was surveyed twice, with scanning direction along Right Ascension and Declination. The effective spatial resolution of the survey is ∼14.4′ with full Nyquist sampling (Shannon 1949).

A wideband correlator was used that provided a bandwidth of 4.5 MHz divided into 2048 channels. This corresponds to a spectral resolution of $\Delta v \simeq 1.0\,\mathrm{km\,s^{-1}}$ and a channel spacing of $\sim 0.82\,\mathrm{km\,s^{-1}}$ at 21 cm wavelength[1]. For all measured data the spectral setting covers a velocity range of $|v_{\mathrm{LSR}}| \lesssim 468\,\mathrm{km\,s^{-1}}$. The rms brightness temperature noise is ∼57 mK.

In the first data release (McClure-Griffiths et al. 2009) the survey and the initial data reduction is presented including the bandpass correction, flagging of radio-frequency interference[2] (RFI), brightness

[1] Spectrometers transform a time-dependent voltage into frequency-dependent power (e.g. Klein 2006). Today, most commonly digital auto-correlators are used that apply a Fourier transform after the digitisation of the signal with some time resolution. In the simplest case, the digitisation function is a rectangular response pattern in time. After Fourier transformation of the digitised voltage signal, the equivalent frequency response function, a sinc function, exhibits strong side lobes that cause spectral sensitivity of spectral channels to signals outside the frequency width of the channels (e.g. compare with Fig. 8 of Klein et al. 2012). In order to reduce this spectral leakage, one applies some window function that modifies the response pattern such that the side lobes are reduced. This leads to an effective spectral resolution that is lower than the actual channel spacing.

[2] Radio-frequency interference (RFI) is artificial man-made signal that contaminates the measured emission from a radio-astronomical source (e.g. International Telecommunication Union - Radiocommunication 2013). RFI shows temporal, spatial, or spectral structure. RFI signals are caused by Radio or TV broadcasts, mobile communications, radar systems, navigation satellites, etc. Especially due to the increasing applications of mobile and wireless communication, the RFI situation near human civilisation is more and more problematic for radio-astronomical measurements. Radio-astronomical observatories are extremely sensitive, which is why even weak RFI sources may lead to corrupted data. There are three main principles how to deal with RFI (e.g. Fisher 2002): 1) minimising the signals that enter the measurement in the first

data set	ν [GHz]	FWHM	$\Delta v \left[\mathrm{km\,s^{-1}}\right]$	σ	Ref.
GASS	1.42	14.4′	0.82	57 mK	(1)
EBHIS	1.42	10.8′	1.29	90 mK	(2)
Planck	353	$4.82 \pm 0.02'$	–	$0.012\,\mathrm{MJy\,sr^{-1}}$	(3)
Planck	545	$4.68 \pm 0.04'$	–	$0.015\,\mathrm{MJy\,sr^{-1}}$	(3)
Planck	857	$4.33 \pm 0.06'$	–	$0.016\,\mathrm{MJy\,sr^{-1}}$	(3)
IRIS	3000	$4.30 \pm 0.20'$	–	$0.06 \pm 0.02\,\mathrm{MJy\,sr^{-1}}$	(4)
WSRT mIVC	1.42	$49.1'' \times 17.9''$	1.03	$1.7\,\mathrm{mJy\,(beam)^{-1}}$	(5)
WSRT aIVC	1.42	$75.1'' \times 23.0''$	1.03	$1.3\,\mathrm{mJy\,(beam)^{-1}}$	(5)
FTS ^{12}CO(1→0) mIVC	115.27	23.0″	0.53	0.20 K	(5)
FTS ^{13}CO(1→0) mIVC	110.20	24.1″	0.53	0.10 K	(5)
VESPA ^{13}CO(1→0) mIVC	110.20	24.1″	0.13	0.15 K	(5)
VESPA ^{13}CO(1→0) mIVC	110.20	24.1″	0.30	0.08 K	(5)
FTS ^{12}CO(1→0) aIVC	115.27	23.0″	0.53	0.17 K	(5)

References: (1) McClure-Griffiths et al. (2009); (2) Winkel et al. (2016); (3) Planck Collaboration I (2011); (4) Miville-Deschênes & Lagache (2005); (5) Röhser et. al (subm.), Chapter 4.

Table 2.1: Characteristics of the different data sets used in this thesis. The columns list (from left to right) the data set, the corresponding frequency ν, the angular resolution FWHM, the channel width Δv for spectral data, the average noise σ, and the corresponding reference. The molecular cloud is abbreviated by "mIVC", the atomic cloud by "aIVC" (see Sects. 2.5 and 2.6 for details).

calibration, and imaging.

In the second data release (Kalberla et al. 2010), the correction for stray radiation is performed. Stray radiation is an emission component that enters the receiving system of a telescope through its side lobes (Kalberla et al. 1980). A side lobe is a directional sensitivity not in the pointing direction of the telescope. When the telescope observes in one direction, bright emission in the direction of side lobes may contribute to the measured signal. The relative contribution of stray radiation is largest at high Galactic latitudes and has to be removed. Furthermore, Kalberla et al. (2010) remove remaining instrumental baselines and RFI signals. About 0.5% of all telescope records were flagged. In the third data release (Kalberla & Haud 2015) more instrumental effects and more RFI are removed such that additional ∼1.5% of the telescope records of the second release were discarded.

2.2 The Effelsberg-Bonn HI Survey

The Effelsberg-Bonn HI Survey (EBHIS, Winkel et al. 2016; Kerp et al. 2011; Winkel et al. 2010) is a survey of atomic hydrogen on the whole northern hemisphere for declinations $\delta \geq -5^\circ$ using the Effelsberg 100 m telescope (Germany). The regular observations started at the end of 2008 and in April 2013 the first coverage was completed. Observations are still ongoing in order to obtain a second coverage. The survey utilises the seven-beam 1.4 GHz receiver that is combined with state-of-the-art digital Fast Fourier Transform (FFT) spectrometers (Stanko et al. 2005; Klein et al. 2012). This modern hardware offers a large spectral bandwidth, which allows to cover the extragalactic HI emission out to a redshift of ∼0.07 and the Galactic HI in one observation with a sufficient spectral resolution for Galactic

place; 2) removing RFI from the measured data in real time during observations; 3) removing RFI from the measured data after the observations are completed, e.g. by manual flagging or software-based signal processing.

HI science. Furthermore, the spectrometers provide a high data rate, which is important for the removal of time-dependent RFI.

The spectral capabilities of the new digital spectrometers are exceptional in comparison to the hardware used for the southern Galactic counterpart of EBHIS, the GASS (Sect. 2.1), which only covers the HI emission of the Milky Way within $|v_{\rm LSR}| \lesssim 468\,{\rm km\,s^{-1}}$. For EBHIS, a bandwidth of 100 MHz is spread over 16384 individual channels. The resulting velocity resolution is $\Delta v \simeq 1.45\,{\rm km\,s^{-1}}$ with a channel spacing of $\sim$1.29 km s^{-1} over the velocity range of $|v_{\rm LSR}| \lesssim 600\,{\rm km\,s^{-1}}$ for the Galactic part of EBHIS. The rms brightness temperature noise of the data is ~90mK with an effective spatial resolution $\sim 10.8'$ with full Nyquist sampling. The first coverage was mapped in on-the-fly (OTF) mode along Right Ascension, while for the second coverage OTF scans are performed along Declination. For the observations the sky is divided into fields with sizes of $5^\circ \times 5^\circ$.

The main features of the data reduction are described in Winkel et al. (2010), while the first data release and the final data reduction are presented in Winkel et al. (2016). Lots of effort is put into the detection and removal of RFI from the data, the proper estimation of baselines, the correction for stray radiation, and consistency checks of the final data. For the stray-radiation correction the antenna pattern[3] including its near- and far-side lobes are required. The modelling of the antenna pattern, however, turned out to be difficult for the Effelsberg 100 m telescope because of details in the telescope design. Multiple reflections are possible between the apex roof, the primary focus, and the support legs of the primary focus, which are difficult to model leading to complex stray-radiation contributions.

The calibration of the EBHIS data is consistent with that of other data sets, notably the Leiden-Argentine-Bonn (LAB) Survey (Kalberla et al. 2005) and with GASS (Sect. 2.1). Together, EBHIS and GASS provide a new all-sky spectral HI data base, which will be the state-of-the-art for the coming decades improving on the angular resolution of LAB and its insufficient spatial sampling (Kerp et al. 2011).

2.3 The *Planck* satellite

The *Planck* satellite (Planck Collaboration I 2011) was a survey instrument of the European Space Agency targeting frequencies between 30 GHz and 857 GHz. The satellite was designed to scan the entire sky every six months continuously with an effective aperture of 1.5 m. The main science goal of *Planck* was to measure the Cosmic Microwave Background (CMB), its spatial anisotropies, and polarisation. While the main focus of the mission was on cosmology, *Planck* provided a detailed picture of the Galactic dust emission as well due to its wide frequency coverage.

The *Planck* satellite was launched on 14 May 2009 into the second Lagrange point. The satellite contained two instruments, the Low Frequency Instrument (LFI) and the High Frequency Instrument (HFI). The HFI offered six frequency bands at 100, 143, 217, 353, 545, and 857 GHz. The three highest frequency bands are dominated by Galactic dust emission, which are of main interest for our work. *Planck* covered these frequencies in order to allow the extraction of the CMB by the modelling and subtraction of the foreground dust emission. Since August 2009 until February 2012 *Planck* covered the entire sky almost five times with both instruments (Planck Collaboration I 2014). In mid-January 2012 the on-board supply of coolant ran out for the HFI marking the end of the HFI surveys. Until October 2013 the satellite continued operations.

During survey observations, the satellite was spinning continuously at one revolution per minute around the axis between Sun and satellite, pointing away from to the Sun. The solar panels were directed

[3] The antenna pattern describes the sensitivity of a telescope depending on the direction. In optical astronomy the antenna pattern is called point spread function.

always towards the Sun and shielded the cooled instrumentation (Tauber et al. 2010). The telescope had an angle of 85° with respect to the spin axis, covering more and more parts of the sky as the Earth and the satellite moved around the Sun.

The HFI contained 52 bolometer detectors that were cooled to 0.1 K in order to minimise thermal noise from the detectors (Lamarre et al. 2010). Bolometer detectors contain an absorber that transforms incoming radiation into heat, the amount of which is measured by the change in electrical resistivity that corresponds to a change of voltage at the bolometer's output. The absorber is thermally connected to a thermal sink that dissipates the heat in some finite time, which is determined by the heat capacity of the bolometers and the thermal conductance. This bolometer time constant has to be compatible with the envisaged scanning speed of the satellite in order to sample the sky emission at sufficient rates. Bolometers are only sensitive to the total radiation along individual lines-of-sight, which is an important limitation as compared to spectral line observations.

The Planck Collaboration offers all-sky maps of the total FIR emission in each observing band. In addition, sophisticated data products are derived from the survey data, such as an all-sky map of the integrated ^{12}CO(1→0) emission (Planck Collaboration XIII 2014) or an all-sky model of the thermal dust emission (Planck Collaboration XI 2014).

Whenever we use a frequency map measured by the *Planck* satellite, we refer to the frequency maps with a correction for zodiacal emission[4] (Planck Collaboration XIV 2014), but without a CMB subtraction. The CMB contributes significantly in all frequency bands from *Planck* up to 353 GHz, the higher frequency bands are dominated by dust emission (e.g. Planck Collaboration XXX 2014). All frequency maps up to and including 353 GHz are made public in units of differential CMB temperature[5] $\mathrm{K_{CMB}}$, which are converted into MJy sr^{-1} by applying the conversion factors given in Planck Collaboration IX (2014, their Table 6). No colour corrections are made (Planck Collaboration IX 2014).

2.4 The Infrared-Astronomical Satellite

The Infrared Astronomical Satellite (IRAS, Neugebauer et al. 1984) was a joint mission of the Netherlands Agency for Aerospace Programs, the US National Aeronautics and Space Administration, and the UK Science and Engineering Research Council. IRAS was designed to conduct the first all-sky survey between 12 μm and 100 μm from space with cooled detectors.

IRAS, launched on 26 January 1983, provided the first all-sky coverage of this wavelength regime, which is dominated by the dust emission in the Milky Way. The sensitivity goal was to reach the level of fluctuations in the zodiacal light. The satellite carried a telescope with an aperture of 0.57 m with mirrors that were cooled to less than 10 K. The 62 detectors in the focal plane of the mirror were cooled

[4] Zodiacal emission is the IR emission from small dust particles within the Solar System (Kelsall et al. 1998; Planck Collaboration XIV 2014). These grains absorb stellar light and emit thermal radiation. All-sky surveys over timescales of years allow to study the distribution of these interplanetary dust particles because any point on the celestial sphere is observed multiple times by different lines-of-sight through the interplanetary dust distribution. Most of the zodiacal emission originates from dust located near the ecliptic plane. The correction of the zodiacal light is important since it contributes to the total IR sky brightness about 2/3 in the near-IR at a few μm, 90% or more in the mid-IR at tens of μm, and ~20% in the far-IR at hundreds of μm (Kelsall et al. 1998).

[5] The HFI maps are calibrated by two different schemes depending on frequency (Planck Collaboration VIII 2014): 1) The CMB dipole is used for the frequencies below 353 GHz, 2) Uranus and Neptune for 545 GHz and 857 GHz. That is why the maps are published in different units. For the conversion from differential CMB temperature $\mathrm{K_{CMB}}$ to MJy sr^{-1}, one calculates

$$\Delta T_{\mathrm{CMB}}\ [\mathrm{K_{CMB}}] = \frac{\Delta I_\nu \left[\mathrm{MJy\,sr^{-1}}\right]}{(d\,B_\nu/d\,T)_{T_0}}$$

with the black-body spectrum B_ν and the CMB temperature $T_0 = 2.7225$ K.

to less than 3 K. During normal survey operations, the contamination from sources like the Sun or the Earth was less than a few percent of the zodiacal emission.

IRAS was brought into a sun-synchronous 900 km altitude near-polar orbit with an inclination of 99° relative to Earth's equator. During one day, the satellite completed about 14 orbits that precessed roughly by one degree per day such that the satellite remained close to the plane of the terminator[6]. The satellite rotated with 3.85° min^{-1} scanning the sky. In November 1983 the cryogenic coolant ran out and the satellite stopped the survey operations. Until this point 72% of the sky were covered with three or more hours, 95% of the sky with two or more hours, and 98% with one or more hours.

Despite the scientific success of the IRAS mission, the latest data version still suffers from problems with calibration, zero level, and measurement stripes (Miville-Deschênes & Lagache 2005). In preparation of the *Planck* mission (Sect. 2.3), Miville-Deschênes & Lagache (2005) worked on these issues and presented the Improved Reprocessing of the IRAS Survey (IRIS). In addition to the correction of residual instrumental effects, the missing stripes of the IRAS survey are filled also with low-resolution (42 arcmin) data from the Diffuse Infrared Background Experiment (DIRBE, Hauser et al. 1998) onboard the Cosmic Background Explorer (COBE, Boggess et al. 1992).

Together with the *Planck* FIR data, the FIR frequencies at 353, 545, 857, and 3000 GHz trace the peak and Rayleigh-Jeans part of the black-body-like emission from large dust grains within the diffuse ISM (e.g. Draine & Li 2007). This is the spectral regime in which we are most interested. At higher frequencies the IR emission is dominated by small grains that are heated stochastically to high temperatures (e.g. Boulanger & Perault 1988; Draine & Li 2001). An ensemble of large grains, on the contrary, attains roughly an equilibrium temperature and can be described by a single temperature that depends on the strength of the radiation field and the corresponding heating (e.g. Draine 2011, page 295).

2.5 Observations with the Westerbork-Synthesis Radio Telescope

As part of the high-resolution study presented in Chapter 4, we mapped the HI emission in the central parts of the two clouds of interest with the Westerbork Synthesis Radio Telescope (WSRT, Netherlands) at higher angular resolution as compared to EBHIS. The data and its analysis is presented in Chapter 4. Due to limited space we give more information about the observations and the data reduction here. In Appendix B the principles and most important aspects of radio interferometry are explained briefly.

2.5.1 Scientific goal

The comparison of the two clouds that are presented in Chapter 3 reveals that these two objects have very similar HI properties in EBHIS data. However, the two clouds of interest are very different in the FIR, which points towards the different nature of the clouds: one is molecular, the other purely atomic. These opposing chemical states should be imprinted in the gas phase also, e.g., by cold small-scale structures, which could not be inferred from EBHIS data. This suggests that the clouds should be largely differing on spatial scales unresolved by EBHIS and *Planck*.

The HI observations with the WSRT aim at characterising the different chemical nature of the two clouds by differences in the atomic small-scale structures. These observations are not supposed to provide a complete mapping of the two clouds of interest. For this an extensive mosaicing with several pointings for each cloud would be required. The WSRT data is complemented by the CO observations with the IRAM 30 m telescope (Sect. 2.6).

[6] The plane of the terminator is the moving zone on a planetary body that separates the illuminated day side and the dark night side.

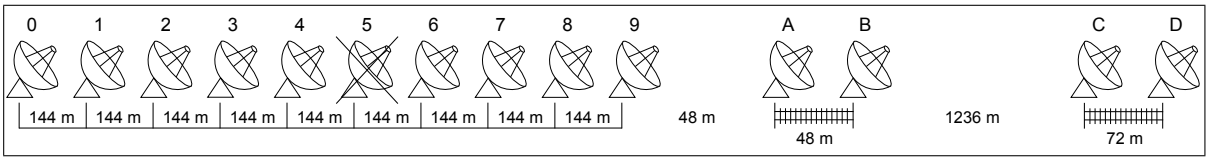

Fig. 2.1: Sketch of 2x48 configuration of the WSRT. Antenna 5 was not available for the observations. Antennas A, B, C, and D are movable on rail tracks, antennas A and B within 300 m, antennas C and D within 180 m.

2.5.2 Observational set-up

The WSRT is a radio interferometer that contains 14 identical radio dishes with a diameter of 25 m each that are spread on an east-west axis over a maximum distance of 2.7 km. Ten of these dishes are fixed on the ground with a separation of 144 m, while four dishes are movable on rail tracks on one side of the fixed array (Fig. 2.1). The different configurations change the properties of the observed data, suitable for a particular science goal. Because of construction work, antenna number 5 was not available for our observations.

A radio interferometer has two important parameters, which have to be considered for designing the observations. 1) The entire array has an instantaneous field-of-view, which is determined by the angular resolution of an individual antenna as given by the Rayleigh criterion (Sect. B.1). For a 25 m dish and an observing wavelength of 21 cm, the field-of-view is $\sim 0.6^\circ$. Hence, the entire array sees a circle with a diameter of FWHM $\simeq 0.6^\circ$ on the sky at any time with a reduced sensitivity at the edges of the field-of-view. 2) The actual angular resolution of the radio interferometer depends on the longest distance between two individual antennas within the array (Sect. B.2). For the WSRT, at an observing wavelength of 21 cm the maximum angular resolution in the east-west direction is $\sim 13''$.

The aim of our observations is to study the small-scale HI structures within the two targets and not to obtain a complete mapping of the two clouds in HI. That is why the smaller molecular cloud is observed with a single pointing of the WSRT (a circle with $\sim 0.6^\circ$), while the atomic cloud is covered with two pointings that are positioned onto the brightest HI emission as measured by EBHIS. The two HI column density maps in Fig. 2.2 show the integrated HI emission from EBHIS of the two target clouds in colour and the 857 GHz FIR emission as measured by *Planck* in black contours, starting at 0.5 MJy sr^{-1} in steps of 0.5 MJy sr^{-1}. The white circles mark the locations and sizes of the WSRT pointings that were observed.

The array configuration 2x48 was used, for which the antenna-pairs 9A and AB are separated by 48 m (Fig. 2.1). The other two movable antennas are positioned at distances of 1332 m and 1404 m from antenna 9. The advantages of this configuration are that both shortest and largest antenna separations are uniformly covered, reducing the average side-lobe levels. Each array-pointing was observed for 12 h in addition to 1 h of calibration scans. Such a long observation time is required especially for an east-west interferometer in order to fill the (u, v)-plane as fully as possible (Sect. B.5).

The L-band 21 cm receiver system was used for performing spectroscopy of the HI line, providing a total bandwidth of 2.5 MHz over 1024 spectral channels for both horizontal and vertical polarisations. Applying natural weighting (Sect. B) and Hanning smoothing[7], a 1σ noise level of ~ 2.2 mJy/beam for the line and ~ 0.1 mJy/beam for the continuum emission was expected. The final velocity resolution after Hanning smoothing is ~ 1 km s^{-1}, which is better than for the EBHIS data (Table 2.1).

[7] Hanning smoothing is a common method in order to reduce ringing artefacts in the final spectra, for instance from bright and narrow RFI. The smoothing is done by applying a triangular smoothing kernel that averages three neighbouring channels. The central channel is given a weight of 0.5 and the two outer channels a weight of 0.25 to preserve the flux. This reduces the spectral resolution of the data, but diminishes RFI ringing and enhances the sensitivity of the data.

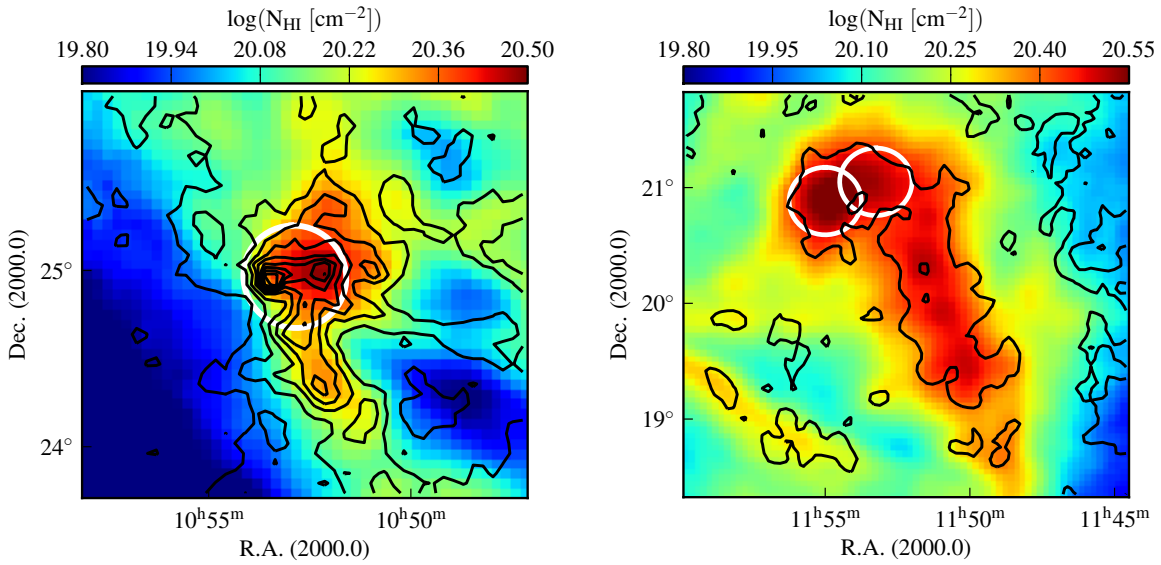

Fig. 2.2: HI column density maps from EBHIS of target clouds superimposed with WSRT pointings as white circles. The molecular cloud (*left*) was observed with one pointing, while the atomic cloud (*right*) was covered with two pointings. The black contours indicate the FIR emission at 857 GHz as measured by the *Planck* satellite starting at 0.5 MJy sr^{-1} in steps of 0.5 MJy sr^{-1}.

The observations were conducted by the WSRT staff on 12–14 June 2013 from noon to midnight. At the beginning of each observation session the standard calibration source 3C147 was observed for 30 min, followed by 12 h of science observations, followed by the standard calibration source 3C286 for another 30 min.

2.5.3 Data preparation and calibration

The data is prepared and calibrated with the software package Multichannel Image Reconstruction, Image Analysis, and Display (MIRIAD, Sault et al. 1995). The preparation and calibration steps are 1) removal of bandpass edges, 2) flagging, 3) calibration, and 4) continuum subtraction.

Bandpass trimming A bandpass is part of the receiving system of each antenna. The measurement has a finite bandwidth, which is centred on the desired frequency, in our case at the 21 cm line. All emission that is spectrally too far off should be suppressed. Otherwise it may affect the receiver chain, e.g., like bright RFI outside the band. At the edges of the spectra, the data cannot be used anyway, hence it is cut off. For this we select channels 100–900 for the further analysis. This is illustrated for the calibration source 3C147 in Fig. 2.3, where the measured un-calibrated amplitudes are plotted against the spectral channels. The original raw data is shown with all 1024 channels. The vertical black lines encompass the extracted channels. The wiggles and curves in the spectra show a combination of the bandpass shape and the frequency-dependent system temperature[8] $T_{\rm sys}$. In the middle of the spectra, some absorption features are observed that are associated with the calibration source.

Flagging The auto-correlations of each antenna are flagged, which are not used for the data but only cross-correlations. In addition, neighbouring antennas may block each other for sources at low eleva-

[8] The system temperature $T_{\rm sys}$ quantifies the total power received by a radio telescope. See Sect. 2.6.4 for more details.

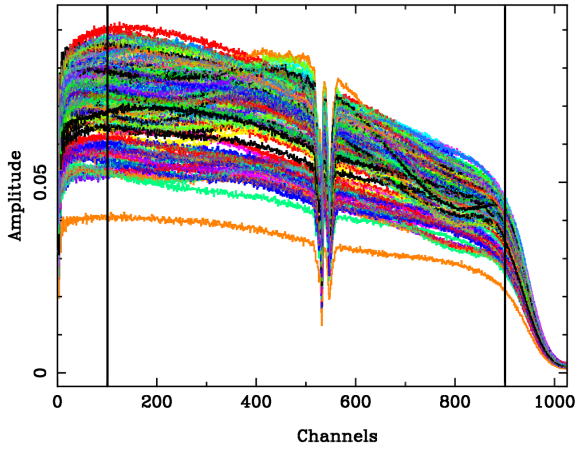

Fig. 2.3: Bandpass trimming for calibration source 3C147. The channel number is plotted against the un-calibrated amplitude of the cross-correlations. The original raw data is shown, from which channels 100–900 are selected as indicated by the vertical black lines. Each different spectrum corresponds to the measurement of a particular pair of antennas. The wiggles and curves of the spectra are due to the combination of instrumental properties of the bandpass and the frequency-dependent system temperature. The features in the middle of the spectra are absorption features associated with the calibration source.

tions (compare with Fig. 2.1), which is called shadowing. Furthermore, RFI contaminations and other data defects have to be removed, both along frequency and time, in order to improve the final data quality.

For radio interferometers, RFI is not as big of a problem as for single-dish observations (e.g. Roshi & Perley 2003). A radio interferometer is phased up in the direction of the phase centre, towards which the array is most sensitive. Any sources, including RFI, that originate from outside the phase centre are not coherently integrated and consequently averaged out. The filtering of a radio interferometer is more effective for increasing frequency and angular resolution. Nevertheless, the dynamic range and sensitivity of the measurements are affected by RFI since they contribute to the system temperature.

Since for our observations the RFI contamination is small, we do the RFI flagging manually. An example is shown in Fig. 2.4 for the baseline of antennas 0 and 6 (Fig. 2.1) of the observations of the molecular cloud. We look at waterfall-plots, showing for each baseline separately the time against the spectral channels of the observations. In grey scales the intensity of the measured signal is given. On the left the un-flagged data is shown, on the right the data after manual flagging. The data consists mostly of noise with a faint signal from the science target near channel 420 where we do not flag any data because one cannot be sure if this is RFI or real signal. There is some RFI confined to a few channels but spreading over the entire time of observation. Short RFI bursts in a number of different spectral channels are evident at the beginning and end of the observations. In addition, there are a few time intervals that show enhanced noise, probably due to instabilities in the receiver system. The flagged data is indicated by the red boxes.

The overall data quality is good. In Table 2.2 we list the relative amounts of flagged data for each observation, divided into each pointing and each observed source (calibration sources 3C147 and 3C286, science targets). For the calibration scans no shadowing occurred, while for the science observations 6% or 7% of the total data have to be flagged due to shadowing. This is likely related to the long observation time of 12 over which the source is near the horizon at the start or end of the observation.

The RFI contamination is 3–4% for the science observations, indicating similar RFI conditions and a similar detection completeness during data reduction. For the calibration scans the RFI is significantly worse. Sometimes up to 40% of the data has to be flagged because antennas 9 and 13 showed unusual behaviour, e.g. brighter or dimmer amplitudes, and were flagged partially or completely. This is still acceptable for the calibration sources, which are very bright targets. Also, no individual channel was removed completely.

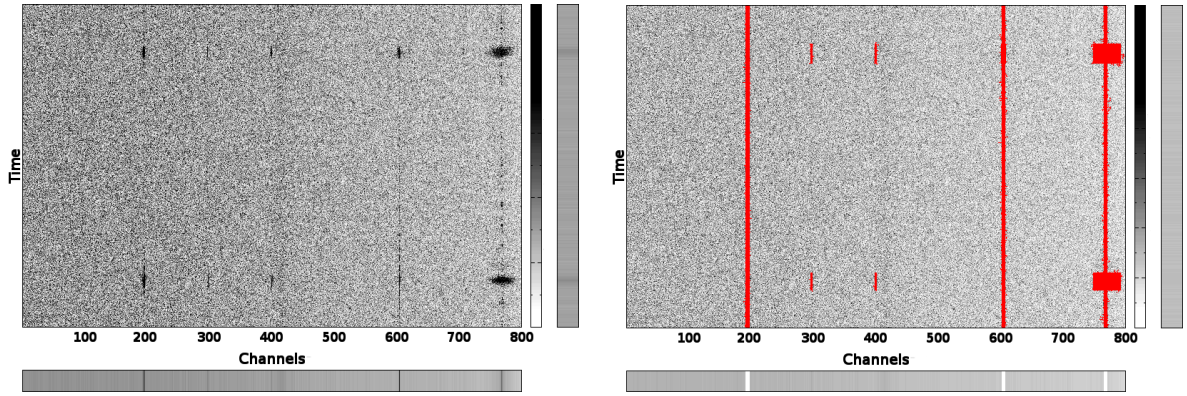

Fig. 2.4: Example of flagging for baseline 0–6 for the molecular cloud. The waterfall-plot shows the spectral channels on the x-axis against the time of the observations on the y-axis. In grey scales the amplitudes are given. On the left the un-flagged data is shown, on the right the data after manual flagging. The data consists mostly of noise with a faint signal near channel 420 where the science target is located. There are some bright features confined to a few channels but spreading over the entire time of observation. Short RFI bursts in a number of different spectral channels are evident at the beginning and end of the observations. The flagged data is indicated by the red boxes.

	3C147		3C286		science target	
pointing	shadowing	RFI	shadowing	RFI	shadowing	RFI
molecular cloud	0%	34%	0%	4%	6%	3%
atomic cloud (a)	0%	39%	0%	41%	7%	4%
atomic cloud (b)	0%	10%	0%	12%	7%	3%

Table 2.2: Amount of flagged data in the WSRT observations. Sources for flagging are shadowing and RFI. The number of flagged auto-correlations is the same for all observations. For shadowing, the flags are given relative to the total amount of cross-correlation data. For RFI, the percentage is relative to the remaining data after flagging of the shadowing.

Calibration The observed standard calibrators 3C147 and 3C286 are well known sources with known flux and angular structure. Before and after each of the three science observations, these two sources were observed. 3C147 has a flux density of ~22 Jy and is brighter than 3C286 with ~15 Jy, but 3C147 is slightly resolved by the WSRT. Hence, 3C147 is used for the bandpass, for which brighter sources are better suited since the signal-to-noise ratio is larger, and 3C286 is used for the flux and phase calibration. For the phase calibration unresolved point sources are better (Sect. B.3).

In order to remove the bandpass shape, one has to mask absorption or emission signals from the spectra (compare with Fig. 2.3), otherwise these would be incorporated into the bandpass solution. The bandpass calibration is done with the MIRIAD-task *mfcal*, which simultaneously calibrates the bandpass, amplitudes and phases of 3C147. The bandpass solution is interpolated into the masked channels. The resulting calibrated amplitudes are constant at ~22 Jy with noise of ~0.2 Jy.

With the MIRIAD-task *gpcopy*, the bandpass solution is copied from 3C147 to 3C286 before its amplitudes and phases are calibrated. The calibrated data of 3C286 shows no phase structures and just a small scatter around zero within $\sim\pm1^\circ$.

We have thus determined the bandpass shape, amplitude calibration, and phase corrections. These parameters are now transferred to the science observations. The bandpass solution is taken from 3C147 and the amplitudes and phases from 3C286. After each calibration, the data is inspected again for RFI,

but no additional data has to be flagged.

The calibration scheme with the primary and secondary calibrator is simpler as compared to the CO-observations with the IRAM 30 m telescope (Sect. 2.6). This is because at 21 cm the atmosphere has only a small influence on the measurements, which does not require to continuously monitor and subtract atmospheric effects and variations. Nevertheless, there are atmospheric and also instrumental variations that cause residual amplitude and phase errors in the science observations. The phase calibration is improved later by applying self-calibration (Sect. B.6). Any residual amplitude or phase errors lead to structures in the noise of the final data.

Continuum subtraction Our observations are spectral line observations of HI 21 cm emission. However, this line emission is superimposed on top of a continuous emission component, the radio continuum, which originates from thermal and non-thermal emission processes in which we are not interested. Over the relatively small bandwidth of 2.5 MHz of our observations the continuum varies only slightly.

This continuum emission is subtracted from the visibility data for each of the three pointings separately using the MIRIAD-task *uvlin*. In the channels that are free of HI emission a polynomial of second order is fitted in order to capture the weak frequency-dependency of the continuum. We obtain two data products: the pure continuum emission and the pure HI line emission. The former is used for the self-calibration later, while both are imaged in the next step.

2.5.4 Imaging

The imaging of the visibility data is done with the software package Common Astronomy Software Applications (CASA, McMullin et al. 2007). The reason for this is that our science data is complicated and difficult to image as we will make clear in the following. CASA offers some sophisticated methods to deal with these issues.

Any radio-interferometric observation is incomplete due to the limited number of baselines, which are provided by the array during observations, and the inhomogeneous sampling of the (u, v)-plane. When the inverse Fourier transform of the visibilities is computed, the dirty image is obtained. For a sparse sampling of the (u, v)-plane, the dirty image is of low quality because of severe imaging artefacts (Fig. 2.5, left). A large fraction of the features in our dirty images is actually not real but a result of the incomplete data. In this form, the data is not usable for any science application. The dirty continuum image shows nicely the side-lobe-structure expected for our observations. The bright continuum point-sources are surrounded by ellipses of signals with a particular aspect ratio and spacing (Fig. 2.5, left). These features should be removed as complete as possible.

The clean-method is applied, which diminishes this issue of incompleteness and side-lobes by iteratively building a model of the source emission, providing additional information that is filled in. In a traditional clean-algorithm, a source is modelled as the sum of many point sources (Högbom 1974). Point sources are a good approach for continuum data but not for our science targets, that show extended emission. This was clear after the first attempts utilising such a traditional algorithm, which could not produce satisfying results for our science targets.

In all the following imaging and cleaning steps, for all three pointings the same imaging parameters are used: 1) Briggs's weighting (Briggs et al. 1999) with a robust parameter of 2 is applied, which is close to natural weighting of the data (Sect. B). Natural weighting improves the sensitivity at loss of angular resolution. 2) The images are created with a pixel size of $5''$, which is less than 1/3 of the minor axis of the final image resolution (Table 2.1). 3) The image size is set to 1024×1024 pixels, which for the given pixel size fully covers the extent of two primary beams of the WSRT.

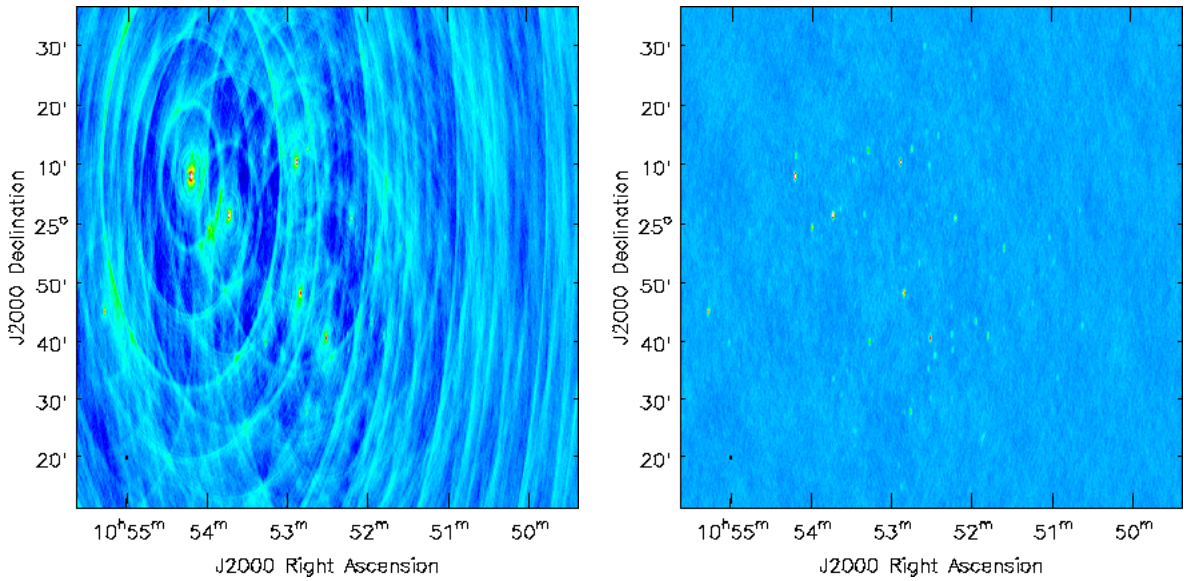

Fig. 2.5: Dirty (*left*) and cleaned (*right*) continuum image for the molecular cloud. The dirty image is dominated by elliptical beam-structures surrounding bright point sources. These beam-structures are removed mostly in the cleaned image.

As the first step of the imaging, we iteratively clean the continuum images of each of the three pointings. Masks are set around the true emission sources at the centre of the side-lobe-structures. Only within these masks the clean-algorithm searches for new model components. Source models are derived, convolved with the dirty beam, and subtracted from the image, iteratively removing the image artefacts (Fig. 2.5, right). After each iteration the masks are widened to encompass more and more pixels of the point sources until the entire image is cleaned. Since we apply self-calibration later on the cleaned continuum image, we are careful that the source model does not contain components from side-lobe emission. This would otherwise lead to bad results in the self-calibration. The continuum image is cleaned down to a flux density of 3×10^{-4} Jy, which is $\sim 2\sigma$ of the noise amplitude. The noise of the cleaned continuum is close to the expected noise limit for the observations.

Then, the first multi-scale cleaning of the line emission is performed down to a level of $\sim 3\sigma$, equivalent to 6×10^{-3} Jy. The noise of the dirty line cube is close to the expected noise limit. The cleaning is done interactively over multiple iterations, during which we manually set mask-polygons around regions that most likely contain real emission. This is done very conservatively and slowly over many iterations in order to avoid cleaning of the side-lobes as much as possible. In Fig. 2.6 one spectral channel of the observations of the molecular cloud is shown for two subsequent iterations during cleaning. For each iteration the side-lobes are reduced and a lower cleaning threshold is set.

After the first set of cleaned images of continuum and line emission are obtained, these images could be used for the scientific analysis already. However, we try self-calibration that improves the data quality further. During self-calibration the science observations themselves are used for the phase calibration. So far the calibration was drawn only from the two calibration sources. The idea is that additional phase solutions are derived on the shortest possible time-intervals, which are determined by the signal-to-noise of the data. The self-calibration is done with the CASA-task *gaincal* applied onto the source model of the cleaned continuum image. This source models contains only relatively bright point sources that are suitable for calibrating the phases, similar to the phase calibrator 3C286.

During the first self-calibration, several time-intervals of 120, 60, 30, 15, and 10 min are tested and

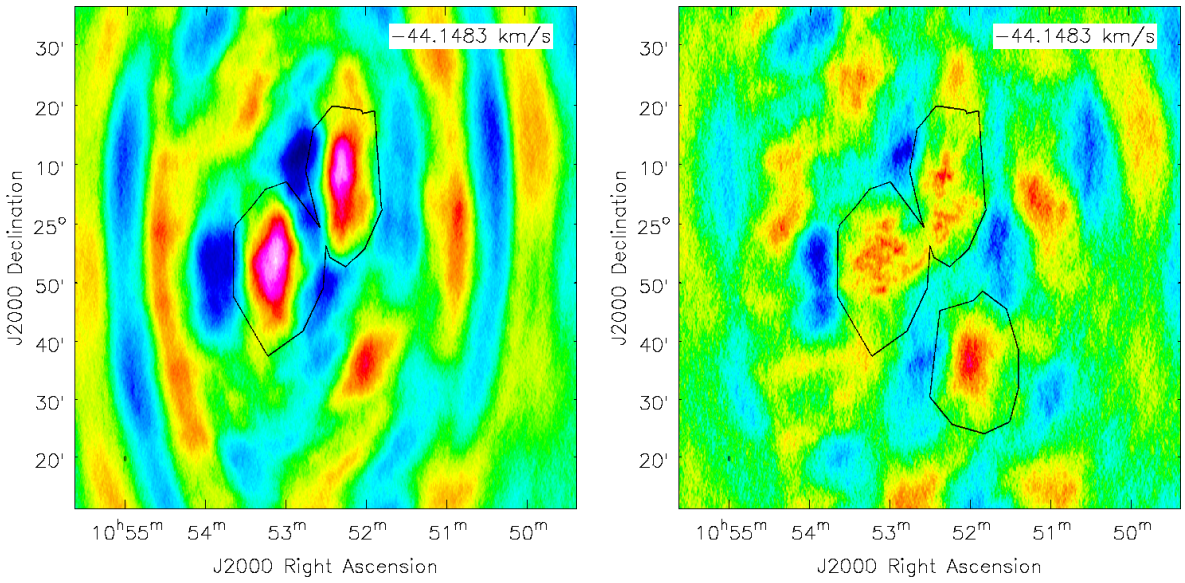

Fig. 2.6: Example masking for cleaning of line emission of the molecular cloud. The two plots show the same velocity channel at $-44.1483\,\mathrm{km\,s^{-1}}$ for two subsequent iterations of the interactive multi-scale cleaning process. In colour the dirty (*left*) and cleaned maps (*right*) are shown, where the black contours give the polygon-masks that encompass true sources of emission. The cleaning is continued for several iterations.

the best one is picked from the final images. The criteria for this decision are the noise-levels in the cleaned continuum images, the peak brightness of point-sources, and the number of failed phase solutions because of too low signal-to-noise. With a better calibration the noise should go down in the cleaned images because residual structures in the noise are removed. Furthermore, point sources should get brighter because the emission is more phased up. Residual phase errors disperse any point-source slightly.

These criteria suggest that the best first self-calibration is achieved for a time-interval of 30 min. The derived phase solutions are significant, for a few baselines the corrections are up to ∼30°. This set of new phase solutions is applied to the original calibrated visibility data. With this new and slightly improved phase solutions the entire imaging process is repeated.

From these new cleaned continuum and line images a second self-calibration is attempted on the new continuum source-model trying to improve the phases even more. The same procedure is applied as for the first self-calibration. The best second self-calibration is achieved for a shorter time-interval of 15 min, although the differences in the final cleaned images are minor. For the molecular cloud, the final line-cube is cleaned down to 4.75×10^{-3} Jy corresponding to $\sim 2.4\sigma$.

Finally, the cleaned line cube is corrected for the primary beam of the WSRT, which is the primary-beam sensitivity of an individual 25 m antenna. The primary-beam correction is done by dividing the emission by the sensitivity of the dish that decreases for larger distances from the pointing centre. This results in strongly enhanced noise towards the edges of the primary beam. Outside, no useful information is obtained by the interferometer. Only after the primary-beam correction the true measured line emission is obtained. For the analysis in Chapter 4 we always use the primary-beam corrected data. In Fig. 2.7 we show two velocity channels of our final self-calibrated, cleaned, and primary-beam-corrected HI line cubes for the molecular cloud. It is evident that the cleaning is not perfect, however, we were not able to improve the result any further. The most important parameters of the resulting line-cubes are listed in Table 2.1.

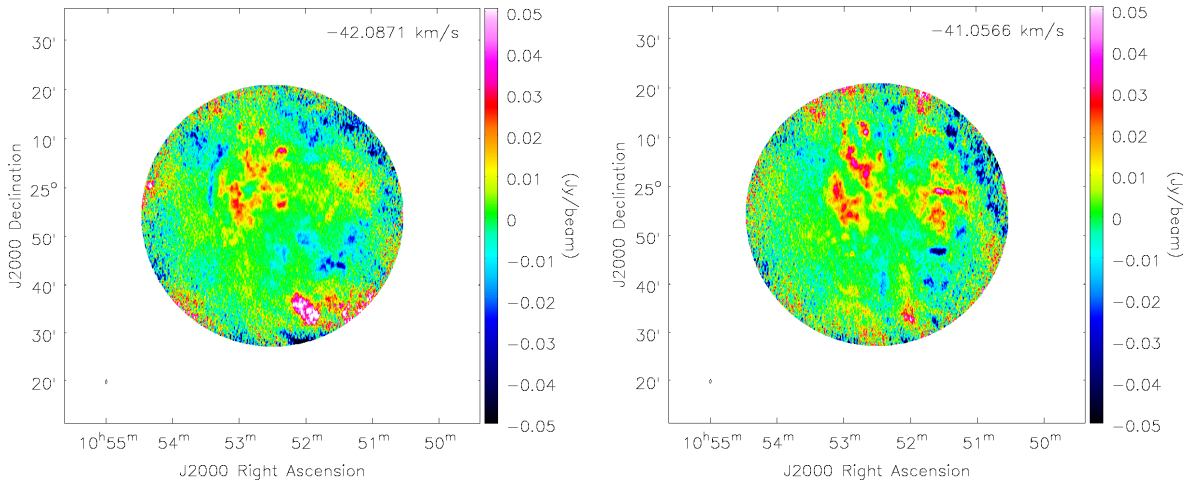

Fig. 2.7: Two velocity channels of the final self-calibrated, cleaned, and primary-beam corrected HI line emission for the molecular cloud. The correction for the primary-beam of the array enhances the data and the noise at the edges of the field.

For the atomic cloud the same methods are applied. The two pointings are imaged and cleaned separately and combined afterwards into one mosaic-image. A better result could be achieved if the two pointings were combined into one image that is cleaned together. However, the cleaning of the combined mosaic image did not converge.

In general, the cleaning of all three observations was very tedious and difficult because of the high side-lobe levels and the fairly extended HI emission covering basically the entire field-of-view. This is evident from Fig. 2.2, where the WSRT pointings are positioned on the peaks of the HI emission. The clouds extend beyond the measured regions, which would require large mosaic-observations to cover the entire emission. This emission likely creates side-lobe structures within the field-of-view that cannot readily be cleaned. Still, after extensive trial and error, the final data cubes have some residual side-lobes and clean-artefacts in them. This is also related to the clean-algorithms, which require proper masking to differentiate between artefact and source emission.

2.5.5 Short spacing correction

A radio interferometer is only sensitive to certain angular scales on the sky, which are determined by the different baselines that are sampled during an observation. Fundamentally, the shortest baselines are never sampled because the dishes of the array cannot be put arbitrarily close together. These shortest baselines correspond to the large angular scales on the sky, on which diffuse gas can be detected. More extended spatial scales of a source are filtered out by the radio interferometer (Sect. B.7).

In order to fill in this missing information one can combine radio-interferometric and single-dish observations, known as the short spacing correction (SSC). For this we use EBHIS data, which is spatially and spectrally re-gridded onto the final imaged interferometric data cubes. The interferometric data is spectrally smeared to match the velocity resolution of EBHIS. The combination is performed using the method by Faridani et al. (2014), who combine the science-ready interferometric data directly in the image domain with the single-dish data. Any residual image artefacts are of course problematic for this combination method, since these will influence the final image. However, as compared to other combination methods the procedure of Faridani et al. (2014) is clear and predictable.

In the final cleaned interferometer maps negative emission is still present, which is unphysical. Before

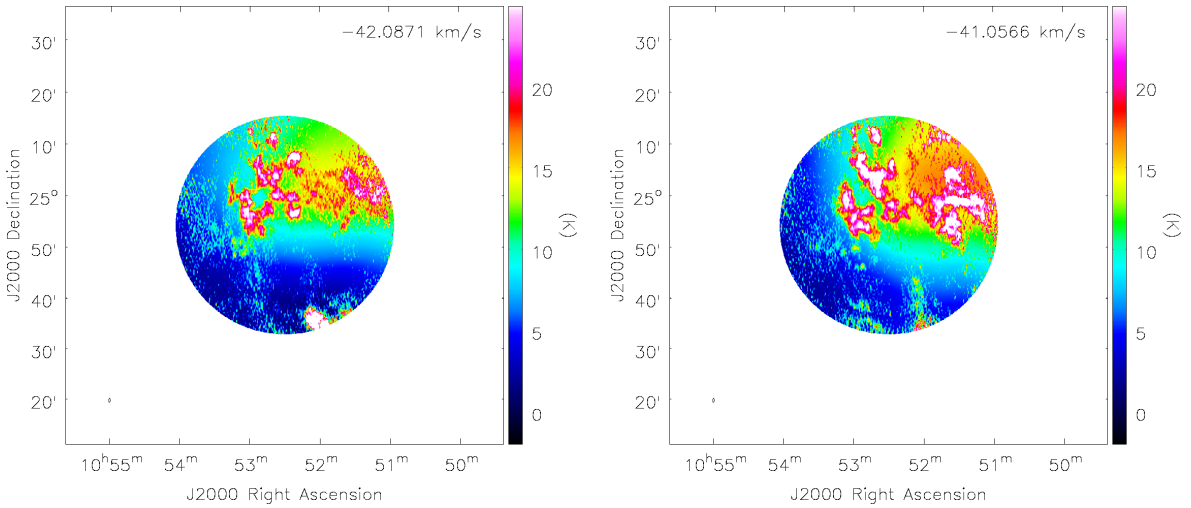

Fig. 2.8: Two velocity channels of combined EBHIS and WSRT HI data for the molecular cloud. The primary beam out to a sensitivity level of 0.25 is used for the combination. This reduces the extent of the field-of-view (compare with Fig. 2.7). In the bottom-left the angular resolution of the WSRT data is shown.

the cubes are combined, we set these values to zero. The primary-beam corrected data is used. Because of the strong amplification of the noise towards the edges of the field-of-view of the WSRT, we do not use the entire primary beam but only those regions down to a primary-beam sensitivity level of 0.25. This is a trade-off between residual noise-amplification and loss of coverage.

The resulting combined EBHIS and WSRT HI data cubes are shown in Fig. 2.8 for two exemplary velocity channels. The maps illustrate the different scales that are probed by either the single-dish telescope or the radio interferometer. The EBHIS data reveals a smooth and diffuse HI distribution on top of which small-scale structures measured by the WSRT are superimposed. These small clumps have a much larger brightness temperature than the diffuse emission.

In addition to the difficult and imperfect cleaning that cause problems in the short spacing correction, there is emission outside the primary beam of the WSRT. This emission may be smeared into the WSRT pointing because of the comparably large beam of the Effelsberg 100 m telescope. However, there is no way to compensate for these issues, other than to obtain a full mosaic of the clouds that would allow a proper cleaning and combination of the targets.

2.6 Observations with the 30 m telescope of the Institut de Radioastronomie Millimétrique

As part of the high-resolution study presented in Chapter 4, we observed two IVCs with the 30 m telescope of the Institut de Radioastronomie Millimétrique (IRAM, Spain) in order to map the emission of ^{12}CO(1→0) within the two clouds. Some details of the data are presented in Chapter 4. Due to limited space, we give more information about the observations here.

The ^{12}CO(1→0) emission line has a rest frequency of ∼115.27 GHz (equivalent to ∼2.6 mm), which is observable from the ground. However, the atmosphere not only attenuates incoming signals but also emits brightly itself with changes on timescales of minutes. For mm-observations most important is water vapour, oxygen, and ozone (e.g. Wilson et al. 2009, pages 173, 176). To good approximation, the atmospheric pressure decreases exponentially with increasing height above the ground. Water vapour

has a scale height of ~2 km (e.g. Wilson et al. 2009, page 174), which is why ground-based observatories for the mm- and sub-mm-regime are built at high altitudes of 3 km or more. For example, the IRAM 30 m telescope is located on the Pico Veleta in the Spanish Sierra Nevada at an altitude of 2850 m. Nevertheless, at such altitudes the influence of the atmosphere is still a challenge and weather conditions can significantly affect the quality of the observations.

2.6.1 Scientific goal

The emission of ^{12}CO(1→0) is commonly used as a tracer for molecular hydrogen in the ISM. Thus, the purpose of the CO observations is to cover the cloud of interest and its molecular content as completely as possible within the granted observation time. This allows the detailed comparison of HI, FIR, and CO emission with the goal to map the transition from atomic to molecular gas within the cloud. The CO data is complementary to the high-resolution HI data that we obtained also (Sect. 2.5). Furthermore, the correlation of HI and FIR emission gives independent information on molecular hydrogen as well. This allows to deduce the conversion factor X_{CO} across the cloud at the angular resolution of the FIR data.

We were granted 27 h of observation time. These observations were scheduled between 31 May 2014 and 02 June 2014 in three shifts of nine hours each, starting in the afternoon. However, the first and second day were lost due to bad weather, including wind and snow. On the third day we could observe most of the time. We were granted additional six hours of unallocated telescope time in the evening of 03 June 2014. Because of the bad weather conditions, our project was kept in the observation schedule. Fortunately, we got additional 56 hours of observation time between 28 August and 04 September 2014 between morning and late afternoon. In total 89 h of observing time was given to us.

2.6.2 Observational set-up

We decided to map the ^{12}CO(1→0) emission line because of three main reasons: 1) In a low-density environment, the most abundant isotope ^{12}CO is useful for the mapping of the bulk of molecular gas (e.g. Bolatto et al. 2013). High-density tracers like ^{13}CO or even ^{12}C^{18}O (e.g. Pineda et al. 2008) are likely only sparse and emit weakly. 2) The ground transition ^{12}CO(1→0) is required as the tracer for the molecular hydrogen in the form of the canonical X_{CO} conversion factor (e.g. Bolatto et al. 2013). For higher line transitions like the ^{12}CO(2→1) line, one has to make assumptions about the level populations in order to convert ^{12}CO(2→1) into ^{12}CO(1→0). In addition, the level populations are expected to be such that most of the ^{12}CO is in the lowest excited states because of the lack of strong heating or pumping sources. 3) There is a multi-beam receiver for observations of the ^{12}CO(2→1) at ~230.54 GHz available at the IRAM 30 m telescope, which would enhance the expected sensitivity for a given observation time significantly as compared to a single-pixel detector. However, the observations are more difficult at these high frequencies as compared to the ground transition ^{12}CO(1→0) at 115.27 GHz. On the one hand the angular resolution of the telescope is better by a factor of ~2 requiring more precise pointing and focussing (Sect. 2.6.3). On the other hand the atmospheric conditions have a larger impact on the observational data and sensitivity for 230 GHz than for 115 GHz (e.g. Pety et al. 2009), which promote ^{12}CO(1→0) observations for the backup schedule also[9].

[9] The different atmospheric influences at 115 GHz and 230 GHz are not primarily determined by resonant line transitions of H_2O, O_2, or O_3, but by the dry and wet continuum, which are broadband continuum-like atmospheric opacities (e.g. Pardo et al. 2001; Pety et al. 2009, and references therein). The dry continuum is caused by collisionally-induced transient dipole moments of symmetric molecules with electric multipole moments, like N_2 or O_2, creating transient absorption opacity. The wet continuum is due to overlap of the far-wings of higher-frequency H_2O lines. At 115 GHz the atmospheric opacity is dominated by the dry continuum, at 230 GHz by the wet continuum. Hence, observations near 230 GHz suffer more severely from larger amounts of water in the atmosphere.

Hence, the Eight Mixer Receiver (EMIR, Carter et al. 2012) was used to map the ^{12}CO(1→0) line. EMIR is a single-pixel receiver, which was combined with the Fast Fourier Transform Spectrometer (FTS, Klein et al. 2012) as a backend. The FTS offers a spectral channelwidth of either 50 kHz or 195 kHz. Since the observations aim to map the angular extent of the clouds as largely as possible, we chose the wide mode with 195 kHz, by which the sensitivity of the observations increases at the loss of spectral resolution. The spectral setting corresponds to a velocity resolution of ∼0.53 km s^{-1}.

EMIR provides four frequency bands that cover the four atmospheric windows. The ^{12}CO(1→0) line is located within the E090-band that ranges between 83 − 117 GHz. The system offers a total bandwidth of 16 GHz in both horizontal and vertical linear polarisations separated in two sidebands each (lower and upper). These two 8 GHz outputs are split in two blocks of 4 GHz and connected to the FTS resulting in four frequency blocks (lower-outer, lower-inner, upper-inner, upper-outer). It would be possibly to combine the E090-band with the E230-band, in which the ^{12}CO(2→1) line is located, in order to simultaneously observe the two lowest rotational lines of ^{12}CO. However, we decided against this option since it would have reduced the sensitivity of our main measurement, the ^{12}CO(1→0) line. The sensitivity loss is due to the design of the optics and mirrors that redirect the incoming photons. With the single-pixel receiver the sensitivity of ^{12}CO(2→1) maps would be poor anyway.

With the local oscillator, the spectral bandwidth of 16 GHz was tuned such that both the ^{13}CO(1→0) transition at 110.20 GHz and the ^{12}CO(1→0) transition at 115.27 GHz were observed simultaneously. Since EMIR allows in principle 32 GHz of instantaneous bandwidth, which was not used by the E090 band, we additionally connected the Versatile Spectrometer Array[10] (VESPA) for high-resolution spectroscopy with 50 kHz centred on the ^{13}CO(1→0) line. Unfortunately, VESPA cannot be set on the ^{12}CO(1→0) line simultaneously with FTS. The angular resolution of the 30 m dish is 21.8″ for the ^{12}CO(1→0) line and 22.8″ for the ^{13}CO(1→0).

2.6.3 Performing the observations

We conducted the observations ourselves at the telescope. The targets were mapped in OTF mode. The OTF stripes were positioned such that the data fulfils Nyquist sampling, meaning the OTF scans are separated by $\Delta\theta\,[\mathrm{rad}] \leq \lambda/2D$, where λ is the observing wavelength and D the telescope diameter[11] (e.g. Mangum et al. 2007). For the ^{12}CO(1→0) line at 2.6 mm and a dish with $D = 30$ m, a spacing of $\Delta\theta \simeq 8.9''$ is required. We chose a separation of 8″ in either Right Ascension or Declination, which is above the Nyquist frequency. The scanning direction was either along Right Ascension or Declination with a measurement dumped every 1 s. This is about the frequency required for Nyquist-sampling along the scanning direction when the IRAM 30 m telescope scans with its maximum speed of ∼11″ s^{-1}, which was never exhausted. Usually we scanned with 5″ s^{-1} or less.

The scans were performed with position switching. By regularly observing an OFF-position, a region of the sky without CO emission, for a few seconds in between ON-source OTF scans, the atmospheric emission only is measured, which is used to remove the bandpass and the atmospheric contribution later during data reduction. All OFF-positions were checked before the actual OTF-measurements were started that the OFF-positions do not contain any CO emission. Since our target clouds are located at high Galactic latitudes, it is easy to find positions near the targets that are devoid of CO emission.

A typical observing session consisted of these steps:

- The operator prepares the receiver and backend, such that they are tuned to the right frequencies.

[10] http://www.iram.fr/IRAMFR/TA/backend/veleta/vespa/index.htm

[11] This is true for 1D signals. For 2D maps one has to sample the underlying distribution also in the diagonal sense, which requires $2\sqrt{2}$ samples for a single beam. For OTF scans this is not completely required, since the scanning direction is usually denser sampled.

- The pointing of the telescope is corrected for any positional offset between the expected and the actual pointing-direction of the telescope. This is done by measuring cross-scans over a bright point-source like a quasar or a planet. Note that some planets may be slightly resolved depending on the observing wavelength and the planetary constellation at time of observation (e.g. Kramer 1997). The pointing should be done as close as possible to the science target because the atmosphere may change away from the sources rendering the pointing corrections inaccurate and long movements of the telescope may cause an improper pointing again.
- Similarly, the focus of the telescope has to be corrected, otherwise the main-beam of the telescope would be larger than necessary. One of the mirrors in the telescope-optics is moved by a few mm in order to find the maximum intensity from a bright point-source, like quasars or planets.
- Before the science observations are started, it is recommended to observe a reference source and check if the system works fine. In our case the line calibrator IRC+10216 was used.
- The observations of the science target always switch between a reference OFF-position and the target OTF-scans, typically every 1–2 min. Every ∼10 min a calibration is performed. The frequency with which OFF-scans and calibrations are performed is a trade-off between data quality and ON-source time. The pointing is corrected every 2 h and the focus every 4 h. During sunrise or sunset the pointing and focussing should be repeated more often because of the changing temperature of the telescope.

Due to the difficult weather situation in the first days of our observations, the initially planned homogeneous coverage of the targets was not possible. We switched more frequently to OFF-positions requiring shorter OTF-scans. Hence, the targets were covered by multiple smaller fields. With each observing session the coverage was extended. We did not know beforehand where and how much emission is located within the targets and how much of the clouds could be observed within the given time.

The target sources rose from elevations of about 20° in the beginning of the observations to their culmination point around 80° elevation and down again. The mean elevation of the two sources during the observations was about 60°, which is good since at higher elevations the line-of-sights have shorter lengths through the atmosphere. The average atmospheric zenith-opacities during the observations were $\tau \simeq 0.2 - 0.3$ at 115 GHz.

In total we covered the molecular cloud of interest with a field of about $25' \times 35'$ comprising 223481 individual spectra, including 1728 additional spectra kindly provided to us by Jorge L. Pineda, also measured with the IRAM 30 m telescope. The central part of the atomic IVC was covered with 24946 spectra corresponding to a field of $10' \times 15'$.

2.6.4 Calibration

In order to explain the calibration of observations in the radio- and mm-regime, the measurements of radio telescopes have to be explained first. The following can be found in standard textbooks on radio astronomy and in the calibration memo for the IRAM 30 m telescope (Kramer 1997).

The flux density S_ν at frequency ν of some source is related to the measured power of a telescope by the effective antenna area A_{eff}:

$$P_\nu = \frac{1}{2} A_{\mathrm{eff}} S_\nu. \tag{2.1}$$

A_{eff} is smaller than the geometrical area of the telescope because of several fundamental limitations, e.g. a tapering-function, diffraction causing a side-lobe pattern, surface imperfections of the dish, or blockage of the dish by a secondary reflector.

In the Rayleigh-Jeans limit of the black-body radiation, e.g. $h\nu \ll k_B T$, any measured brightness or power can be assigned to a temperature. The flux density S_ν of a source and its measured power P_ν can be related to the temperature of a resistor that would produce the same noise power by

$$S_\nu = \frac{2\,k_B}{A_{\text{eff}}} T_A, \tag{2.2}$$

where k_B is the Boltzmann constant and T_A is the antenna temperature. In radio astronomy the brightness B_ν of a source is converted into the brightness temperature T_B, which is the temperature a black-body would have in order to emit the observed intensity:

$$B_\nu \simeq \frac{2\,k_B \nu^2}{c_0^2} T_B, \tag{2.3}$$

where c_0 is the speed of light in the vacuum. By integrating the intensity or equivalently brightness temperature over all solid angles Ω, one obtains the flux density S_ν. We can relate the brightness temperature T_B (the astronomical signal) to the antenna temperature T_A (the telescope response) by

$$T_A = \frac{A_{\text{eff}} \nu^2}{c_0^2} \int \mathrm{d}\Omega\, T_B(\Omega). \tag{2.4}$$

However, this is not the output of a real measurement. Instead, a telescope measures the system temperature[12] T_{sys}, which is the sum of many different contributions:

$$T_{\text{sys}} = T_{\text{receiver}} + T_A = T_{\text{receiver}} + T_{\text{source}} + T_{\text{atmosphere}} + T_{\text{ground}} + ... \tag{2.5}$$

The task of the calibration is now to translate the output of the receiving system into the system and antenna temperature in order to calibrate the astronomical signal. For mm-observations a special treatment of the atmospheric contribution to the antenna temperature is mandatory.

The determination of the receiver noise T_{receiver} is usually done by the hot-cold method. If the receiving system is linear, one can write the output counts C of the system for two different known temperatures T_{hot} and T_{cold} as

$$C_{\text{hot}} = G \times (T_{\text{hot}} + T_{\text{receiver}}) \tag{2.6}$$

$$C_{\text{cold}} = G \times (T_{\text{cold}} + T_{\text{receiver}}) \tag{2.7}$$

with the gain factor G of the receiver. These equations can be solved for the receiver temperature. The hot and cold load are typically realised by one absorber at room temperature and one cooled down with liquid nitrogen. These two measurements determine the receiver noise T_{receiver}.

The next step is to quantify the contribution from the atmosphere to the measured antenna temperature. For this the hot-sky calibration is used. Together one speaks of the hot-cold-sky calibration.

The receiver counts C are measured towards a sky position without astronomical emission (OFF position). However, the telescope does not measure T_{sky} directly. Instead, T_{sky} is modified by the

[12] The system temperature T_{sys} is essential for the expected noise ΔT in a radio astronomical observation. For given bandwidth $\Delta\nu$ and integration time τ, the noise is calculated by the radiometer formula:

$$\Delta T \simeq \frac{T_{\text{sys}}}{\sqrt{\Delta\nu\,\tau}}.$$

forward efficiency $F_{\rm eff}$ of the telescope, which is the ratio of the power that is received in the forward direction relative to the total power. Additional emission is entering the sky measurement from the ground and the receiver cabin also.

By fitting an atmospheric model (Pardo et al. 2001) to the observed counts, the atmospheric opacity and the amount of precipitable water vapour is deduced for the measured atmospheric pressure and temperature at the observatory. With these quantities the radiative transfer through the atmosphere can be solved, including the atmospheric absorption and emission.

The final calibration step is to relate the count rates of the science target and the blank sky $\Delta C_{\rm source} = C_{\rm source} - C_{\rm sky}$ to the hot load and the empty sky $\Delta C_{\rm cal} = C_{\rm hot} - C_{\rm sky}$. This can be written as the forward-beam brightness temperature $T'_{\rm A}$:

$$T'_{\rm A} = K \, \frac{\Delta C_{\rm source}}{\Delta C_{\rm cal}}. \tag{2.8}$$

The calibration factor K incorporates results from previous calibration steps, like the atmospheric properties. The gain factor G and the receiver noise $T_{\rm receiver}$ cancel. Thus, any time-variations in the receiver system are calibrated out. The full derivation of K is shown in Kramer (1997, his Eq. 8).

The temperature $T'_{\rm A}$ is the brightness temperature of a source that fills the entire forward beam pattern of the telescope within a solid angle of 2π. For the conversion into the main-beam brightness temperature $T_{\rm mb}$, which is the brightness of the same source filling only the primary beam of the telescope, the antenna temperature $T'_{\rm A}$ is multiplied by the ratio of forward $F_{\rm eff}$ to main-beam efficiency $B_{\rm eff}$.

2.6.5 Data reduction and gridding

The data measured by the IRAM 30 m is calibrated by an automated online data processing (ODP) system during observations. However, in the standard ODP-approach only a simple and fast reduction-pipeline is applied in order to avoid a pile-up of data during the observations for large data rates, e.g., for OTF-mapping. We improve this calibration with the Multichannel Imaging and Calibration Software for Receiver Arrays (MIRA)[13] afterwards.

In OTF-mapping an OFF-measurement is done, followed by the OTF-stripes, followed by another OFF-measurement within 1–2 minutes. We use time-weighted reference signals from the OFF-positions. This weights the OFF-measurements before and after an OTF-scan with the elapsed time of the scan. In this way the first OFF-measurement has initially a large weight that decreases with the elapsed time of the OTF-scan. Likewise the weight of the OFF-measurement after the OTF-scan is increased with time. This scheme ensures that the OFF-measurements are given more weight that are closer in time to a measurement of the OTF-scan.

Since we are interested only in a small part of the total measured bandwidths, we cut out 300 spectral channels from the total spectrum centred on each the ^{12}CO(1→0) and ^{13}CO(1→0) using the Continuum and Line Analysis Single-dish Software (CLASS)[14]. These 300 channels cover still a much broader frequency range than required for the emission. Enough emission-free channels are required for the fitting of baselines. In addition, the primary beam efficiency of 0.78 of the telescope at 115 GHz is corrected. Since the observations consist of multiple small fields that are centred on different central coordinates, the spatial locations of the spectra on the sky are re-arranged such that all spectra have spatial offsets relative to a single central position. Furthermore, the noise in each spectrum is estimated. These noise values are used in order to assess the quality of the different observations. The full spectral resolution of the backends (FTS and VESPA) is kept and, finally, the spectra are written to text files for

[13] http://www.iram.fr/IRAMFR/GILDAS/doc/html/mira-html/mira.html
[14] http://www.iram.fr/IRAMFR/GILDAS/doc/html/class-html/class.html

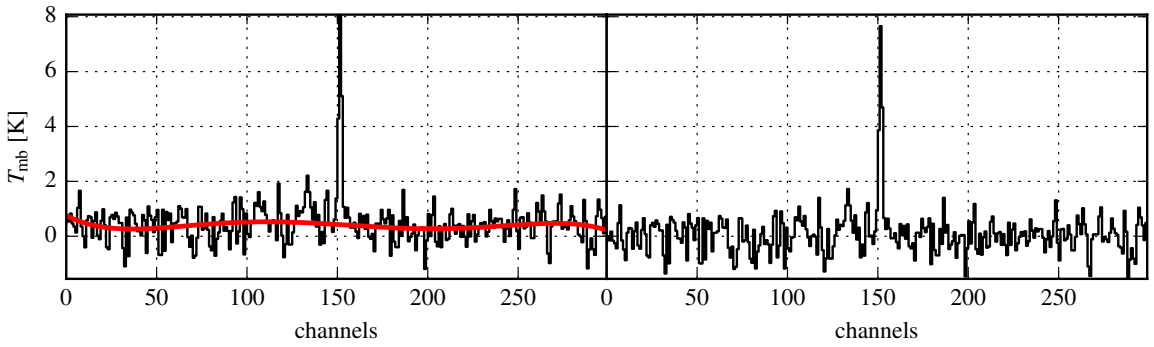

Fig. 2.9: Example of baseline correction for a spectrum from ^{12}CO(1→0) FTS data. In the left part the spectrum is shown after calibration, temperature scaling and OFF-subtraction. There is some emission near channel 150, which is masked out for the baseline-polynomial fit of fifth order. The fitted baseline is plotted in the left part as the red line. One can see that the red line is well above zero showing some wiggles that are residual bandpass features. In the right part, the same spectrum is shown with the subtracted baseline.

both backends and both observed transitions.

The emission of the detected target cloud is confined to about 20 channels near the centre of the remaining spectra. A polynomial of fifth order is fitted to the emission-free channels in each spectrum separately and subtracted from the entire spectrum with python[15]-scripts. In Fig. 2.9 an example of a spectrum before (left) and after (right) the baseline correction is shown. The spectrum is quite flat even before the baseline correction, since the spectrum is shown after the calibration removing most of the bandpass shape. In the middle of the spectrum there is some emission in a few channels. These channels are masked from the fifth-order polynomial baseline fit. The fitted baseline is shown as the red line in the left part of Fig. 2.9. The baseline is off-set from zero and shows some wiggles, which may be caused by a frequency-dependent T_{sys}. In the right part of Fig. 2.9, the baseline is subtracted resulting in a flatter and zero-centred spectrum.

For all individual subfields and spectra, the data reduction is the same. Kindly, Jorge L. Pineda provided additional ^{12}CO(1→0) and ^{13}CO(1→0) data for one of our targets also measured with the IRAM 30 m telescope, but with older hardware. Nevertheless, this data is also used. For this, the reference position of the data is changed to match the same central coordinates. Furthermore, the spectra are spectrally smoothed and re-gridded to match our spectral setting.

Three fields suffer from very bad weather conditions that make the calibration uncertain and cause large noise values, which is why we do not use this data in the final data cube. In addition, one data set of the ^{12}CO(1→0) line from J. Pineda shows some strong negative features. This data is also not used. All remaining baseline-corrected spectra (223841 for ^{12}CO(1→0), 225758 for ^{13}CO(1→0)) are then gridded to FITS[16] data cubes, one data cube for each target, each spectral line, and each backend.

The pixel size of the final data cubes is set to 8″, which is the spatial distance of the OTF-scans. The data cubes are gridded with a Gaussian kernel of 1/3 of the beam-size for each line respectively. So-far we only have spectra at specific sky coordinates and no maps. The gridding process re-samples these measured spectra on a single cartesian grid involving proper averaging of spectra. The size of the kernel determines the spatial distance up to which observed spectra contribute to a given pixel, calculating weights that depend on the distance to the pixel. As the result the angular resolution of the final data is

[15] http://www.python.org/
[16] http://fits.gsfc.nasa.gov/

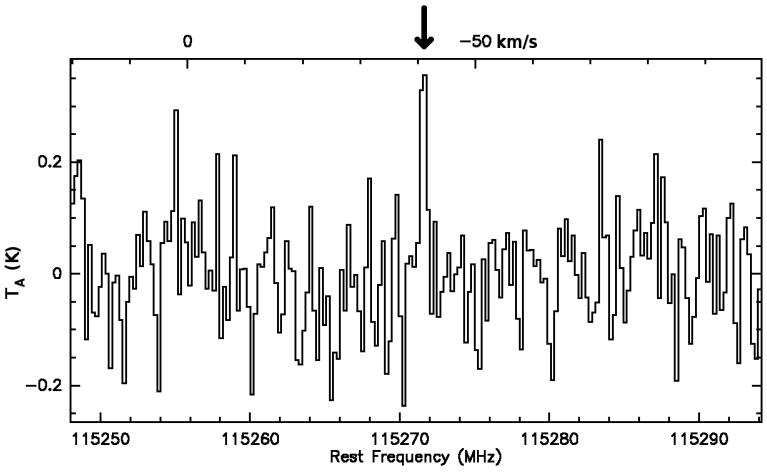

Fig. 2.10: OFF-position measurement with weak ^{12}CO(1→0) emission from FTS. The black arrow indicates a weak emission feature near $\sim$−40 km s^{-1} that affects the data reduction.

decreased slightly.

For ^{13}CO(1→0) from VESPA, data cubes with two different spectral resolutions are gridded, one high resolution cube with 0.125 km s^{-1} and a lower resolution one with 0.3 km s^{-1}. The spectral resolution of the ^{13}CO(1→0) data from Jorge L. Pineda is $\sim$0.21 km s^{-1}, which is not combined with the data of the full VESPA resolution.

During the inspection of the final data cubes we noted that four fields with one particular OFF-position show some slight negative features near the line emission of the target. It turns out that this particular OFF-position is not completely free of signal, which was not recognised during the initial inspection. In Fig. 2.10 the calibrated OFF-position measurement is shown after averaging over the two polarisations. The black arrow marks weak emission near a radial velocity of $\sim$−40 km s^{-1}. This emission feature is subtracted during the calibration of the data causing slight negative features in the affected channels. For ^{13}CO(1→0) the emission is not detected. We add the calibrated OFF-measurement for the respective polarisation back to all spectra in the four affected fields before the baseline is fitted and the spectra are gridded. This mostly removes these negative features from the final data cubes.

2.6.6 Data products

An overview of the properties of the IRAM data is given in Table 2.1. The given noise value is the median of the position-dependent noise maps (Fig. 2.11).

The actual data and its analysis are presented in Chapter 4. Here, we additionally show noise maps of the two targets for FTS ^{12}CO(1→0) in Fig. 2.11. Note that the two noise maps have completely different sizes. The noise is computed for each position individually, revealing the position-dependent noise structure for the molecular cloud (Fig. 2.11, left). The structured noise is the result of the inhomogeneous coverage of the target consisting of lots of individual sub-fields with small overlaps and with different noise properties. This is because the fields were measured over several days with different daytime, weather conditions, and sometimes also different scanning speeds, split in two observing sessions in spring and summer. Within a single field, the noise is more or less homogeneous. At the edges of neighbouring fields, the maps overlap, which results into stripes of lower noise. The deepest observations, equivalent to the lowest noise, are obtained towards the region of the cloud with brightest ^{12}CO(1→0), which is where the data from Jorge L. Pineda is located (the small dark field that is slightly tilted with the bottom-right corner at (R.A, Dec.) $\simeq$ ($10^{\rm h}\,53^{\rm m}, 24^\circ\,55'$).

For the atomic IVC (Fig. 2.11, right) the OTF-mapping is a detection experiment. The observations

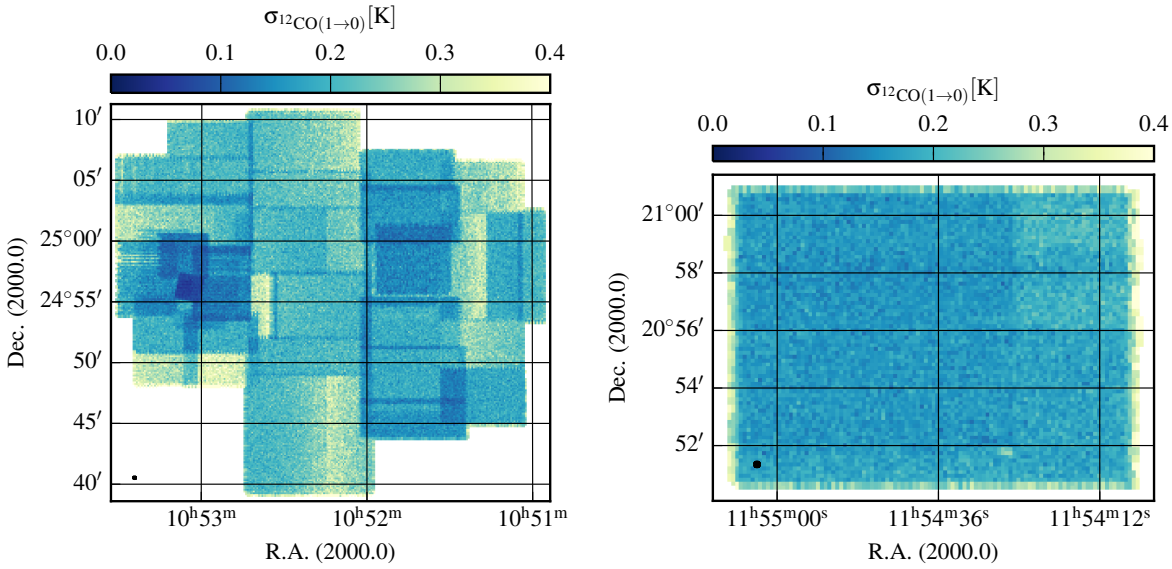

Fig. 2.11: Noise maps of ^{12}CO(1→0) line data cubes from FTS for the molecular (*left*) and atomic cloud (*right*). In the bottom-left of each map the corresponding beam-size of the telescope is shown as the black circle.

consist of two different fields, which have similar noise, indicating similar conditions for the two measurements. The median noise values are very similar for both cloud.

The data quality is good, despite the varying noise in the data of the molecular cloud. The data is sensitive enough to detect numerous small clumps of molecular gas spread across the measured regions (Chapter 4). For the atomic cloud no CO emission is detected, even when the data is spatially and spectrally smoothed.

CHAPTER 3

A dynamical transition from atomic to molecular intermediate-velocity clouds

The content of this Chapter is published in the article entitled "A dynamical transition from atomic to molecular intermediate-velocity clouds", T. Röhser, J. Kerp, B. Winkel, F. Boulanger, and G. Lagache, A&A, 564, A 71, 2014, bibliographic code 2014A&A...564A..71R. For consistency with the rest of the text, we made some minor adjustments to the published version.

Abstract

Towards the high Galactic latitude sky, the far-infrared (FIR) intensity is tightly correlated to the total hydrogen column density which is made up of atomic (HI) and molecular hydrogen (H_2). Above a certain column density threshold, atomic hydrogen turns molecular. We analyse gas and dust properties of intermediate-velocity clouds (IVCs) in the lower Galactic halo to explore their transition from the atomic to the molecular phase. Driven by observations, we investigate the physical processes that transform a purely atomic IVC into a molecular one. Data from the Effelsberg-Bonn HI Survey (EBHIS) are correlated to FIR wavebands of the *Planck* satellite and IRIS. Modified black-body emission spectra are fitted to deduce dust optical depths and grain temperatures. We remove the contribution of atomic hydrogen to the FIR intensity to estimate molecular hydrogen column densities. Two IVCs show different FIR properties, despite their similarity in HI, such as narrow spectral lines and large column densities. One FIR bright IVC is associated with H_2, confirmed by ^{12}CO(1→0) emission; the other IVC is FIR dim and shows no FIR excess, which indicates the absence of molecular hydrogen. We propose that the FIR dim and bright IVCs probe the transition between the atomic and molecular gas phase. Triggered by dynamical processes, this transition happens during the descent of IVCs onto the Galactic disk. The most natural driver is ram pressure exerted onto the cloud by the increasing halo density. Because of the enhanced pressure, the formation timescale of H_2 is reduced, allowing the formation of large amounts of H_2 within a few Myr.

3.1 Introduction

The Infrared Astronomical Satellite (IRAS) showed that, up to a certain threshold, the HI 21 cm emission correlates linearly with the far-infrared (FIR) dust continuum at high Galactic latitudes (Low et al. 1984; Boulanger & Perault 1988; Boulanger et al. 1996). Despite this linear relationship, previous studies towards high Galactic latitudes (e.g. Désert et al. 1988; Reach et al. 1998) find excess FIR radiation associated with molecular gas, which is traced by carbon monoxide (CO) emission (Magnani et al.

1985). Several of these objects show radial velocities relative to the local standard of rest (LSR) between $30\,\mathrm{km\,s^{-1}} \leq |v_{\mathrm{LSR}}| \leq 90\,\mathrm{km\,s^{-1}}$ that are difficult to account for with a simple model of Galactic rotation. These clouds are classified as intermediate-velocity clouds (IVCs) and, as a subcategory, molecular intermediate-velocity clouds (MIVCs).

Intermediate-velocity clouds are thought to originate from a Galactic fountain process (Bregman 2004). Typically they show up with metal abundances close to solar, a traceable dust content, and distances below 5 kpc (Wakker 2001). Commonly, IVCs emit in the FIR (e.g. Planck Collaboration XXIV 2011). Towards many IVCs a diffuse H_2 column density of $N_{H_2} = 10^{14} - 10^{16}\,\mathrm{cm^{-2}}$ is inferred by interstellar absorption line measurements (Richter et al. 2003; Wakker 2006); however, only a few MIVCs are known (Magnani & Smith 2010). Dynamical processes resulting from the motion of IVCs through the halo and their descent onto the Galactic disk are thought to play a major role in the process of H_2 formation in IVCs (Odenwald & Rickard 1987; Désert et al. 1990; Gillmon & Shull 2006; Guillard et al. 2009). The transition between the atomic and the molecular phase happens at a total hydrogen column density of $N_{\mathrm{H}} = 2.0 - 5.0 \times 10^{20}\,\mathrm{cm^{-2}}$ (Savage et al. 1977; Reach et al. 1994; Lagache et al. 1998; Gillmon et al. 2006; Gillmon & Shull 2006; Planck Collaboration XXIV 2011).

In this paper we study the gas and dust properties of IVCs and their transition from the atomic to the molecular phase by correlating the HI distribution to the FIR dust emission at high Galactic latitudes. We are interested in the conditions required for the transition from HI to H_2 in IVCs at the disk-halo interface.

We use data from the new Effelsberg-Bonn HI-Survey (EBHIS, Winkel et al. 2010; Kerp et al. 2011), the *Planck* Satellite (Planck Collaboration I 2014), and IRIS (Miville-Deschênes & Lagache 2005). Our field of interest has a size of $25 \times 25\,\mathrm{deg^2}$ centred on Galactic coordinates $(l, b) = (235°, 65°)$. This area is located between the intermediate-velocity (IV) Arch and IV Spur, which are two large structures in the distribution of IVCs (Wakker 2004). In Planck Collaboration XXX (2014) this field is used also in the analysis of the cosmic infrared background.

Section 3.2 gives the properties of our data in HI and the FIR. Section 3.3 describes the HI-FIR correlation in more detail. Section 3.4 presents the observational results inferred from the HI, the FIR, and their correlation for the entire field, while Sect. 3.5 gives results for two particular IVCs within the field. Section 3.6 discusses a dynamically driven HI-H_2 transition with respect to the two IVCs and Sect. 3.7 summarises our results.

3.2 Data

Table 3.1 gives the main characteristics of the different data sets. In the FIR we use data at 353, 545, and 857 GHz from *Planck* and 3000 GHz from IRIS. These frequencies probe the peak of the FIR dust emission.

The Effelsberg-Bonn HI-Survey (EBHIS, Winkel et al. 2010; Kerp et al. 2011) is a new, fully sampled survey of the northern hemisphere in HI 21 cm line emission above declinations of $-5\,°$. FPGA-based spectrometers (Stanko et al. 2005) allow one to conduct in parallel a Galactic and extragalactic survey out to redshifts of $z \simeq 0.07$. The angular resolution is approximately $10.8'$, and with a channel width of $1.3\,\mathrm{km\,s^{-1}}$ the rms noise is less than 90 mK. The data is corrected for stray radiation, which is especially important for studies of the diffuse ISM at high Galactic latitudes.

The *Planck* satellite covers the spectral range between 25 and 1000 GHz (Planck Collaboration I 2014). The High Frequency Instrument (HFI) has bolometer detectors that offer six bands centred on 100, 143, 217, 353, 545, and 857 GHz.

We use the *Planck* maps that are corrected for zodiacal emission (Planck Collaboration XIV 2014),

Survey	ν [GHz]	FWHM [′]	Average noise	Ref.
EBHIS	1.42	10.8	$\lesssim 90\,\mathrm{mK}$	1
Planck	353	4.82	$0.012\,\mathrm{MJy\,sr^{-1}}$	2
	545	4.68	$0.015\,\mathrm{MJy\,sr^{-1}}$	2
	857	4.33	$0.016\,\mathrm{MJy\,sr^{-1}}$	2
IRIS	3000	4.30	$0.06\,\mathrm{MJy\,sr^{-1}}$	3

References: (1) Winkel et al. (2010); (2) Planck Collaboration I (2014); (3) Miville-Deschênes & Lagache (2005).

Table 3.1: Properties of the HI and FIR data. The columns list (from left to right) the survey, the corresponding frequency, the angular resolution, the average noise, and a reference.

but no CMB emission is subtracted. The 353 GHz data is transformed from the original $\mathrm{K_{CMB}}$ units to $\mathrm{MJy\,sr^{-1}}$ by applying the conversion factor given in Planck Collaboration IX (2014). No colour correction is done for any FIR frequency.

Infrared dust continuum data is available from the Infrared Astronomical Satellite (IRAS) at 12, 25, 60, and 100 μm (Neugebauer et al. 1984). The four IRAS wavelengths have been revised in the Improved Reprocessing of the IRAS Survey (IRIS, Miville-Deschênes & Lagache 2005). They preserve the full angular resolution and perform a thorough absolute calibration. In recent data products the stripe of missing data in IRAS is filled with observations from DIRBE of lower angular resolution.

3.3 Methods

We correlate the HI column density N_{HI} to the FIR intensity I_ν at frequency ν. The quantitative correlation of two different data sets like HI and the FIR demands a common coordinate grid with the same angular resolution. Hence we convolve the FIR maps with two-dimensional Gaussian functions that have a spatial width given by the full width half maximum (FWHM) fulfilling $\mathrm{FWHM^2_{HI}} = \mathrm{FWHM^2_{Gauss}} + \mathrm{FWHM^2_{FIR}}$.

At high Galactic latitudes the HI-FIR correlation is linear (e.g. Boulanger et al. 1996) and it can be written as

$$I_\nu = R_\nu + \epsilon_\nu \times N_{\mathrm{HI}}, \tag{3.1}$$

where ϵ_ν is the dust emissivity per nucleon. A general offset R_ν accounts for emission that is not associated with the Galactic gas distribution, for example the cosmic infrared background. The values of each pixel of the HI and FIR maps are plotted against each other. With standard least-squares techniques the linear parameters and their statistical errors are estimated.

In order to exclude point sources from the fit, we apply a first fit to reject all data points that deviate by more than 3σ from this initial estimate. In a second step, we reject all pixels in which more HI emission is in IVCs between $-60\,\mathrm{km\,s^{-1}} \leq v_{\mathrm{LSR}} \leq -20\,\mathrm{km\,s^{-1}}$ than in the local gas with $-20\,\mathrm{km\,s^{-1}} \leq v_{\mathrm{LSR}} \leq +20\,\mathrm{km\,s^{-1}}$. We do this because of the generally lower dust emissivities of IVCs compared to local gas (Planck Collaboration XXIV 2011), which is expected to bias the fit.

We only quote errors on the emissivities that represent statistical uncertainties. These uncertainties are lower than the true errors (Planck Collaboration XXIV 2011) since we do not consider effects like the cosmic infrared background or residual zodiacal emission.

Equation (3.1) can be generalised by adding more HI components with different dust emissivities. As Peek et al. (2009) show, this superposition can easily produce false estimates for a FIR dim cloud behind

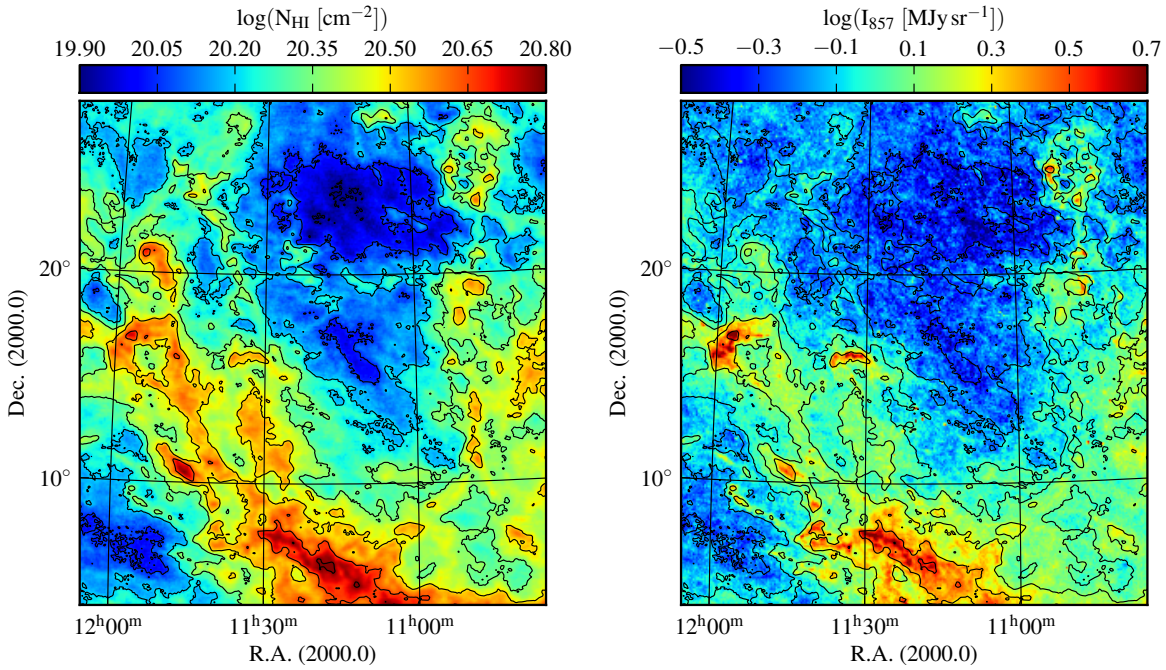

Fig. 3.1: *Left*: Column density map of EBHIS integrated between $-100\,\mathrm{km\,s^{-1}} \leq v_{\mathrm{LSR}} \leq +100\,\mathrm{km\,s^{-1}}$. *Right*: Corresponding unsmoothed *Planck* map at 857 GHz. In both figures the black contours mark N_{HI} at the levels of the colour bar tick labels of the column density map.

a bright local foreground. In this paper we concentrate on two bright IVCs which completely dominate the emission along their lines of sight. Thus, a superposition of several components is not required in order to model their FIR brightness.

The emissivity ϵ_ν in Eq. (3.1) depends on the dust-to-gas ratio, but also on gas and dust properties. Deviations from a linear behaviour are mostly due to local variations of the amount of neutral atomic gas where significant amounts of the hydrogen are in either ionised or molecular forms. These species will be missing from the HI-FIR correlation. Above an empirical threshold of $N_{\mathrm{HI}} = 2 \times 10^{20}\,\mathrm{cm^{-2}}$, molecular hydrogen steepens the correlation (e.g. Planck Collaboration XXIV 2011), which can be inferred without tracer molecules like CO (Reach et al. 1998). This steepening is not due to HI absorption, since opacity corrections are relevant for $N_{\mathrm{HI}} > 10^{21}\,\mathrm{cm^{-2}}$ (Strasser & Taylor 2004) which is much more than the column density observed with EBHIS in Galactic cirrus clouds.

3.4 Analysis of the entire field

In this Section we present the analyses of the entire field: first the HI-FIR correlation, second the modified black-body fitting, and third the estimation of molecular hydrogen column densities from the FIR emission.

3.4.1 Global correlation of gas and dust

The HI column density map integrated across $-100\,\mathrm{km\,s^{-1}} \leq v_{\mathrm{LSR}} \leq +100\,\mathrm{km\,s^{-1}}$ and the corresponding *Planck* data at 857 GHz are shown in Fig. 3.1 for the entire studied field. From these maps the close correlation between gas and dust is evident. The field is located near a region of low N_{HI} which is

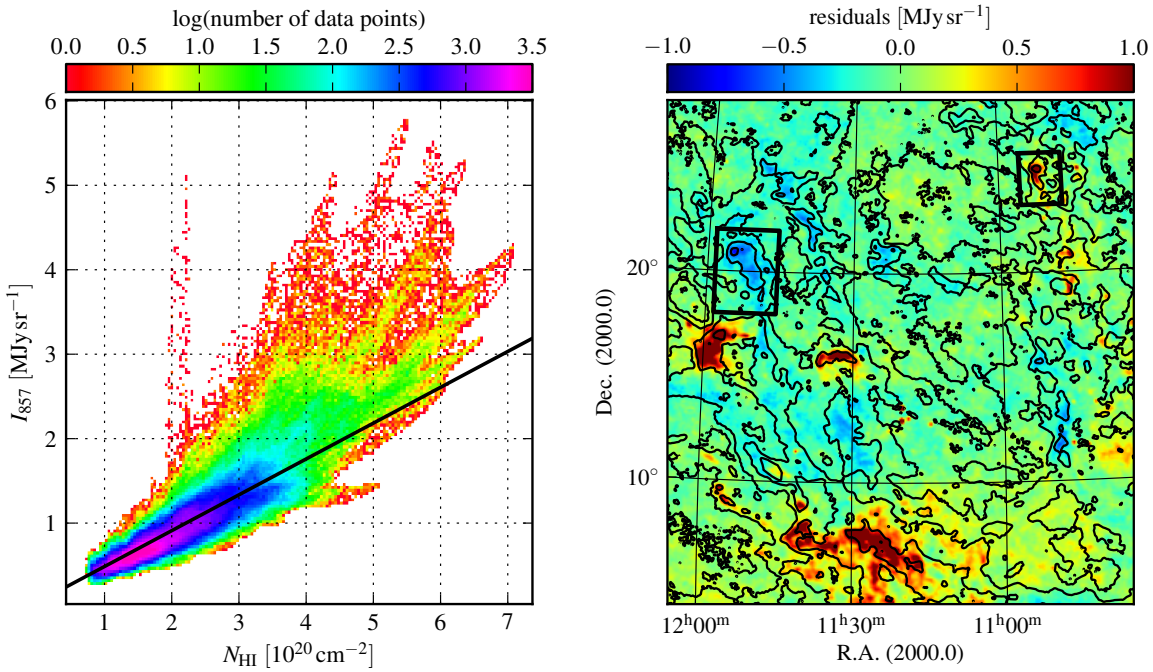

Fig. 3.2: *Left*: Correlation plot N_{HI} vs. $I_8$57 for the entire field. The black solid line is our best fit of Eq. (3.1) to the data below $N_{HI} = 2 \times 10^{20}$ cm^{-2}. *Right*: Residual map at 857 GHz. The residuals are derived by subtracting for each pixel the FIR sky brightness calculated from Eq. (3.1) using the linear-fit parameters. The black contours denote N_{HI} as in Fig. 3.1. The black rectangles mark the locations of two HI clouds (IVC 1 on the left, IVC 2 on the right), which are presented in more detail in Sect. 3.5.

ν [GHz]	$\epsilon_\nu^{\text{total}} \left[\frac{\text{MJy sr}^{-1}}{10^{20}\text{ cm}^{-2}}\right]$	$\epsilon_\nu^{\text{IVC 1}} \left[\frac{\text{MJy sr}^{-1}}{10^{20}\text{ cm}^{-2}}\right]$	$\epsilon_\nu^{\text{IVC 2}} \left[\frac{\text{MJy sr}^{-1}}{10^{20}\text{ cm}^{-2}}\right]$
353	0.0505 ± 0.0002	0.0333 ± 0.0004	0.050 ± 0.003
545	0.1577 ± 0.0002	0.0789 ± 0.0005	0.185 ± 0.005
857	0.4243 ± 0.0006	0.239 ± 0.001	0.56 ± 0.01
3000	0.5597 ± 0.0007	0.631 ± 0.001	0.74 ± 0.02

Table 3.2: Dust emissivities across the entire field, IVC 1, and IVC 2. The values are derived by fitting Eq. (3.1) to the HI-FIR correlation plots (Figs. 3.2, 3.7).

surrounded by the IV Arch and Spur. From the bottom towards the north-east there are large amounts of local gas that is part of high-latitude HI-shells probably directly connected to Loop I and the North Polar Spur (Puspitarini & Lallement 2012).

We create HI-FIR correlation plots (Fig. 3.2, left for 857 GHz) and use Eq. (3.1) to fit dust emissivities, which are listed in Table 3.2 (second column). The correlation parameters are estimated for $N_{HI} \leq 2.0 \times 10^{20}$ cm^{-2} which is the empirical threshold for the HI-H_2 transition found in other studies and also for one particular IVC within the field (Sect. 3.5.2).

There is a large scatter around a linear relation (Fig. 3.2, left). Many clouds in the field have a FIR excess, but some also have a deficiency in brightness. We obtain a residual map (Fig. 3.2, right) by subtracting in each pixel the FIR intensity that is expected from Eq. (3.1) using the fitted linear parameters. In particular we find two IVCs with completely different FIR emission despite their similarity in

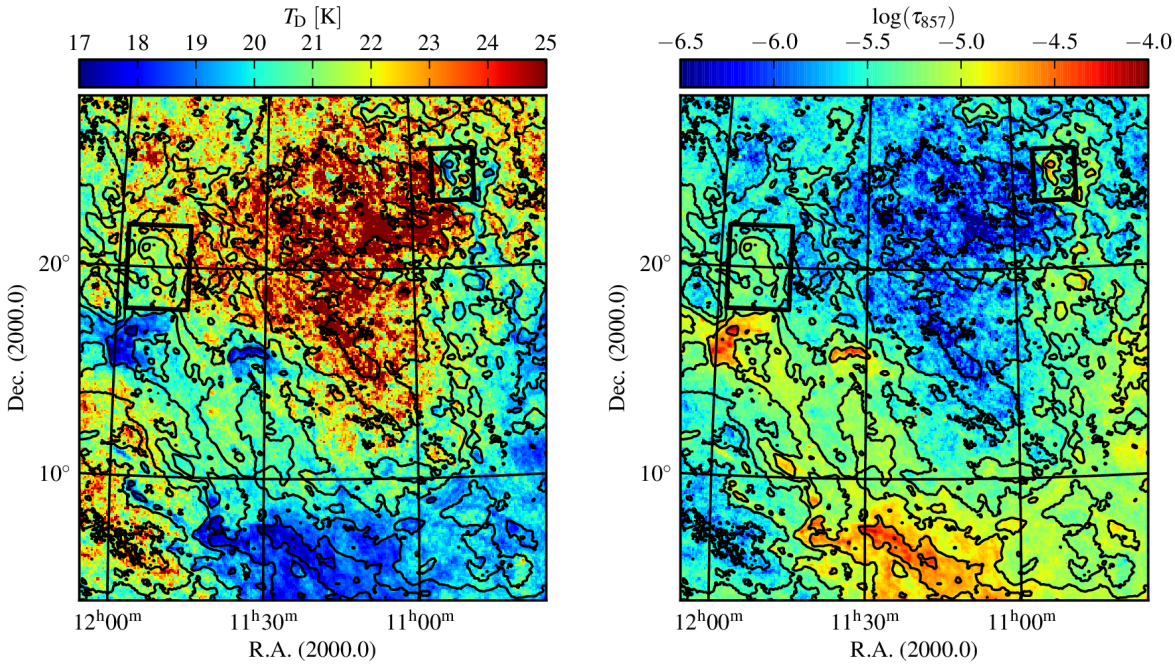

Fig. 3.3: Maps of dust temperature T_D (*left*) and dust optical depth τ_{857} (*right*) at the resolution of the 353 GHz data. Black contours mark N_{HI} as in Fig. 3.1.

HI. These two clouds are marked by the black boxes in Fig. 3.2 (right). Section 3.5 gives a detailed description of these two IVCs.

3.4.2 Maps of dust temperature and optical depth

Our FIR data probes the thermal dust emission. We fit modified black-body spectra of the form

$$I_\nu(\tau_{857}, \beta, T_D) = \tau_{857} \times \left(\frac{\nu}{\nu_0}\right)^\beta \times B_\nu(T_D). \tag{3.2}$$

Parameters are the dust optical depth τ_{857}, which we choose at 857 GHz; the dust temperature T_D; and the spectral index β of the power law emissivity $(\nu/\nu_0)^\beta$. We normalise the dust emission spectrum to $\nu_0 = 857$ GHz. From Planck Collaboration XXIV (2011) we adopt $\beta = 1.8$. Furthermore, we smooth the FIR data to the lowest resolution, which is the 353 GHz map. The noise values given in Planck Collaboration I (2014) and Miville-Deschênes & Lagache (2005) are used as weights for the modified black-body fits.

There may be offsets in the FIR data that are not related to the Galactic gas distribution. These are corrected for by subtracting offsets that are estimated in Planck Collaboration XIX (2011), where reference pixels with $N_{HI} \leq 2.0 \times 10^{19}$ cm^{-2} are used to infer the smooth background FIR radiation.

By fitting Eq. (3.2) in each pixel independently, we derive maps of dust temperature T_D and dust optical depth τ_{857} (Fig. 3.3). The dust temperatures have a median value of 21.2 K. The dust optical depths cover about two orders of magnitude. Both T_D and τ_{857} correlate to gaseous structures.

In Fig. 3.4 (left, middle) we compare dust temperatures to dust optical depths and HI column densities. In general, low dust temperatures are associated with large optical depths and vice versa (Fig. 3.4, left).

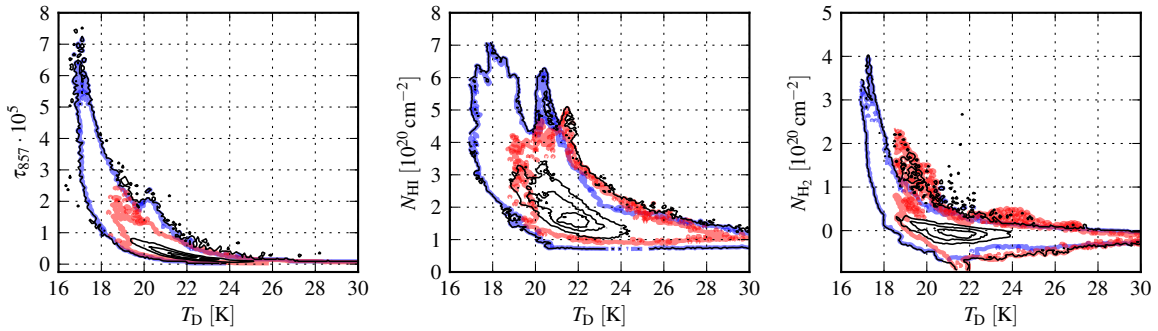

Fig. 3.4: Dependence of dust optical depth τ_{857} (*left*), HI column density N_{HI} (*middle*), and H_2 column density N_{H_2} (*right*) on dust temperature T_D. The $T_D - \tau_{857}$ plot is done for FIR data at the resolution of the 353 GHz data while the other two plots are for FIR data smoothed to the EBHIS resolution. The black contours show the number density distribution of all data points. The blue contour traces the pixels that contain more HI between $-20\,\mathrm{km\,s^{-1}} \leq v_{\mathrm{LSR}} \leq +20\,\mathrm{km\,s^{-1}}$ than in the IVC range $-60\,\mathrm{km\,s^{-1}} \leq v_{\mathrm{LSR}} \leq -20\,\mathrm{km\,s^{-1}}$, whereas the red contour traces pixels that have more HI in the IVC regime. In Sect. 3.4.3 we describe how we derive an H_2 map from the FIR excess emission. Negative N_{H_2} are a result of the derivation.

A similar correlation exists between T_D and N_{HI} (Fig. 3.4, middle). The IVC gas appears to contain warmer dust grains compared to local structures confirming previous studies (e.g. Planck Collaboration XXIV 2011). This is related to the Galactic fountain origin of IVCs by which dust grains are shattered and the number of very small grains is increased (see e.g. Jones & Nuth 2011 for a discussion of the destruction and survival of dust grains in the ISM in general).

We note that the fitted dust temperatures do not reflect the actual dust temperatures (Planck Collaboration XXIV 2011). A simple modified black body is an average over the line of sight and its parameters are biased towards regions of bright emission. Nevertheless, spatial variations of this fitted dust temperature are related to changes in the spectral energy distribution.

3.4.3 Estimation of the molecular hydrogen column density

The thermal dust emission acts as a tracer of the total gas column density. The linear HI-FIR correlation covers the range where hydrogen is neutral, whereas the FIR excess emission traces H_2. Thus, maps of molecular hydrogen column density can be calculated from the total FIR emission (e.g. Dame et al. 2001).

3.4.3.1 FIR emission and molecular hydrogen

We assume that the excess emission is solely due to H_2. Any influences due to H^+ are considered to be negligible and changes of the dust-to-gas ratio or emissivity properties of the grains are omitted. The simple HI-FIR correlation in Eq. (3.1) is generalised to account for H_2:

$$I_\nu = R_\nu + \epsilon_\nu \times N_{\mathrm{H}} = R_\nu + \epsilon_\nu \times (N_{\mathrm{HI}} + 2N_{\mathrm{H_2}}). \tag{3.3}$$

Solving for N_{H_2} yields

$$N_{\mathrm{H_2}} = \frac{1}{2}\left(\frac{I_\nu - R_\nu}{\epsilon_\nu} - N_{\mathrm{HI}}\right). \tag{3.4}$$

In each pixel of the map we calculate N_{H_2} from the total HI column density and the 857 GHz data smoothed to the EBHIS resolution of 10.8′. For the correlation parameters, we use the values derived

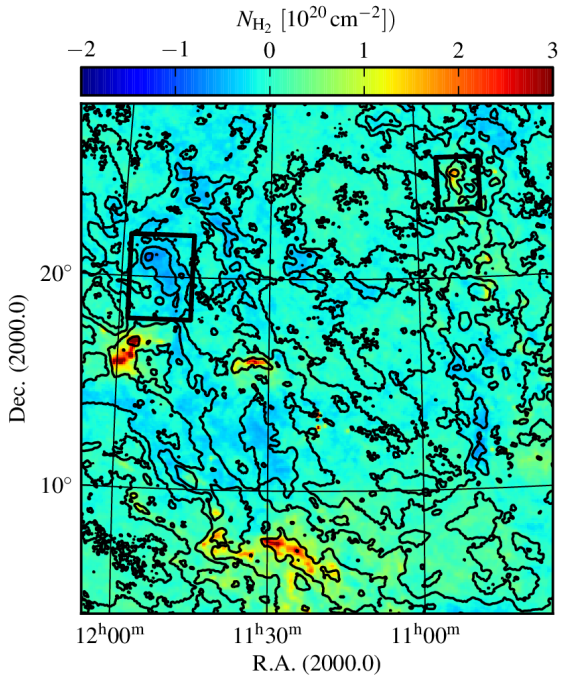

Fig. 3.5: Map of molecular hydrogen column density N_{H_2} with a $1-\sigma$ uncertainty of 0.2×10^{20} cm^{-2}. Negative values result from the derivation and are not physically meaningful. Black contours mark N_{HI} as in Fig. 3.1.

for the entire field (Table 3.2, first column).

A map of N_{H_2} is shown in Fig. 3.5; HI structures with local velocities are prominent, with N_{H_2} in the range $1-4 \times 10^{20}$ cm^{-2}. Negative H_2 column densities result from the derivation and are not physically meaningful. We do not clip these values in order to show the uncertainties of the H_2 map.

In Fig. 3.4 (right) the relation between T_D and N_{H_2} is shown. For $T_D \gtrsim 22$ K no significant amount of H_2 is observed, neither in local nor IVC gas.

The correlation parameters R_ν and ϵ_ν that are applied in Eq. (3.4) are statistically well constrained. In order to estimate an uncertainty for our N_{H_2} map, we use the scatter in the residuals from the HI-FIR correlation after subtracting the best fit. For 857 GHz this results in a 1σ scatter of 0.2×10^{20} cm^{-2} for N_{H_2}. In addition to this statistical error, systematic errors contribute, such as local changes in the grain emissivity, in metallicity, or in dust-to-gas ratio, all of which may mimic the presence of H_2.

The molecular gas we infer in the field is not observed in the large-scale CO survey on the northern high-latitude sky (Hartmann et al. 1998). Furthermore, the all-sky maps of CO emission extracted from the *Planck* foreground modelling also do not contain any CO in this area of the sky (Planck Collaboration XIII 2014).

3.4.3.2 Validation of the N_{H_2} map

The N_{H_2} map in Fig. 3.5 is derived directly from the 857 GHz intensity and the HI column density using Eq. (3.4). Together, HI and H_2 approximate the distribution of the total hydrogen column density N_H. The dust optical depths τ_{857} also trace N_H, in a manner completely independent from Eq. (3.4), since τ_{857} is obtained from modified black-body fits (Eq. 3.2) to the FIR spectra.

For the validation of our H_2 map, we compare the total hydrogen column density $N_H = N_{HI} + 2N_{H_2}$ to the dust optical depth τ_{857}. For this, negative N_{H_2} values are clipped. In Fig. 3.6 we plot N_H against τ_{857} for each pixel of the entire field. Above $N_H = 5 \times 10^{20}$ cm^{-2} we fit a linear function to the data, yielding the slope $\tau_{857}/N_H \simeq 5.1 \times 10^{-26}$ cm^{-2}. This agrees well with the value of $5.1 \times$

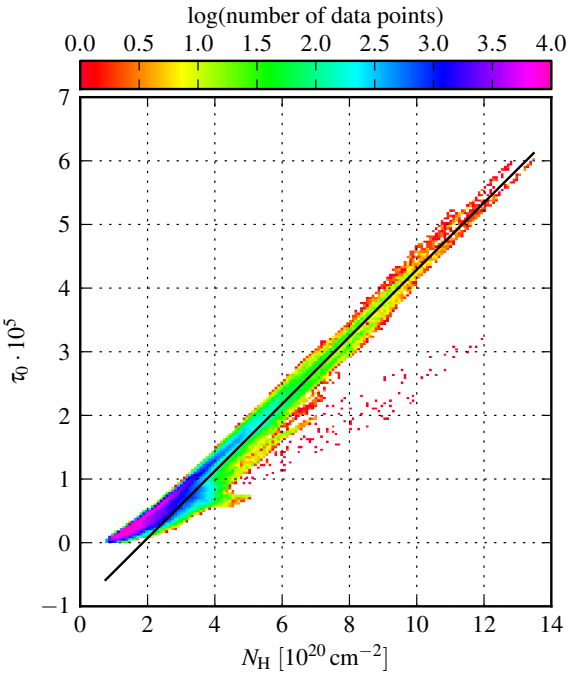

Fig. 3.6: Comparison between the estimated total hydrogen column densities N_H using Eq. (3.4) and the fitted dust optical depth τ_{857} from modified black-body fits (Eq. 3.2). For $N_H \geq 5 \times 10^{20}$ cm^{-2} a linear relation is fitted and shown by the black line.

10^{-26} cm^{-2} for 857 GHz given by Boulanger et al. (1996). Varying the fitting threshold in the range $4-6\times10^{20}$ cm^{-2} results in values of τ_{857}/N_H which range between $5.0-5.3\times10^{-26}$ cm^{-2}. Thus Eq. (3.4) gives a good approximation of the molecular hydrogen column densities from the FIR intensity and the HI distribution directly.

Figure 3.6 shows a significant enhancement of τ_{857} with respect to the linear fit below $N_H \simeq 2 \times 10^{20}$ cm^{-2}. This deviation is probably related to an increasing dust contribution from ionised hydrogen which is not considered here. In principle, a map of H^+ can be derived from the $N_H - \tau_{857}$ correlation by shifting the points above the linear fit towards higher N_H.

3.5 Analysis of individual clouds

In the following we focus on two IVCs distinguished by their different FIR properties, as is evident from the global residuals in Fig. 3.2 (right), where the locations of the clouds are given by the black rectangles. The FIR-dim IVC at the top-left of the field (IVC 1) belongs to the IV Spur, the FIR-bright cloud (IVC 2) to the IV Arch.

3.5.1 IVC 1

The cloud IVC 1 is located at (R.A., Dec.) = (11^h52^m, $20°30'$) and it is FIR dim. Désert et al. (1988) mention this region as a FIR-deficient IVC at -30 km s^{-1}, although the cloud structure cannot be resolved by their angular resolution of $\sim 40'$ in HI.

In Fig. 3.7 the HI-FIR correlations are shown for 857 GHz and 3000 GHz and for HI integrated between -100 km s^{-1} $\leq v_{LSR} \leq$ 100 km s^{-1}. For IVC 1 we fit Eq. (3.1) to the entire data range, since the correlation is linear throughout. The resulting dust emissivities $\epsilon_\nu^{IVC\,1}$ are compiled in Table 3.2 (third column). In the *Planck* frequency range the emissivities are lower than our estimated values over the

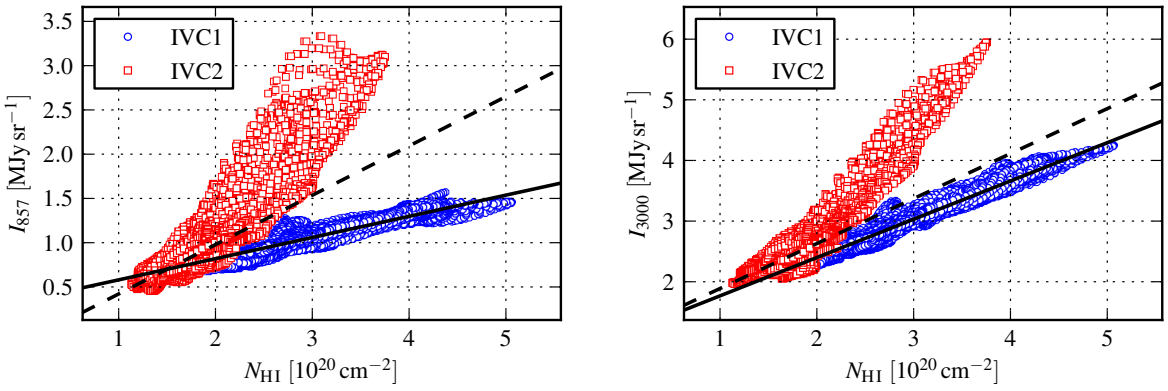

Fig. 3.7: HI-FIR correlations for IVC 1 and IVC 2 at 857 GHz (*left*) and 3000 GHz (*right*). The HI is integrated between $-100\,\mathrm{km\,s^{-1}} \leq v_{\rm LSR} \leq +100\,\mathrm{km\,s^{-1}}$. The black solid line is the linear fit applying Eq. (3.1) for IVC 1 and the dashed black line for IVC 2. For IVC 2 the fit is restricted to $N_{\rm HI} \leq 2.0 \times 10^{20}\,\mathrm{cm^{-2}}$, above which a FIR excess due to H_2 is evident. For IVC 2 the spread in $N_{\rm HI}$ for given I_ν is due to a second FIR maximum that is not associated with an HI peak (Fig. 3.12).

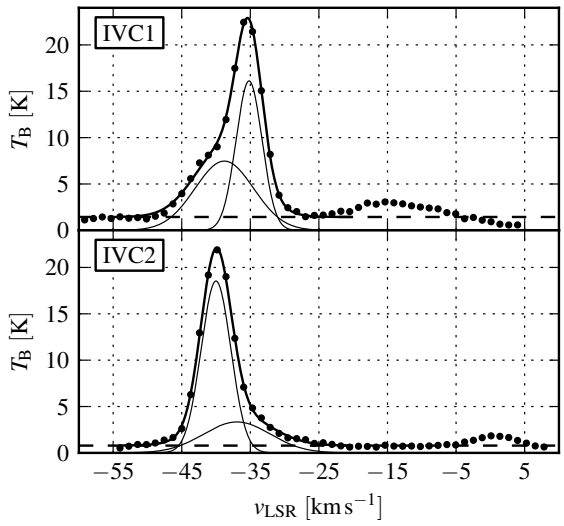

Fig. 3.8: HI spectra of IVC 1 (*top*) and IVC 2 (*bottom*) at their maximum brightness temperature. Both spectra are fitted by two Gaussians plus a constant offset.

entire field. There is no indication of FIR excess emission such as would indicate significant amounts of molecular hydrogen. In the CO survey performed by Hartmann et al. (1998), IVC 1 is not detected.

The HI spectrum at the peak brightness temperature is shown in Fig. 3.8 (top). It is a two-component spectral profile consisting of a bright line with FWHM $\simeq 4.5\,\mathrm{km\,s^{-1}}$ centred on $-35.2\,\mathrm{km\,s^{-1}}$ and a second fainter one at $-38.8\,\mathrm{km\,s^{-1}}$ with FWHM $\simeq 10.0\,\mathrm{km\,s^{-1}}$. About 50% of the HI is in the colder phase. In the spectrum there is not much HI at other radial velocities. A column density map of IVC 1 integrated over the spectral range between $-60\,\mathrm{km\,s^{-1}} \leq v_{\rm LSR} \leq -20\,\mathrm{km\,s^{-1}}$ is presented in Fig. 3.9. This shows a peak value of $N_{\rm HI} \simeq 3.9 \times 10^{20}\,\mathrm{cm^{-2}}$. The cloud consists of several cold clumps that are well connected in HI. Its morphology is curved and filamentary.

The dust spectrum of IVC 1 at its maximum $N_{\rm HI}$ is shown in Fig. 3.10 (top). The emission is well approximated by a modified black body with $\beta = 1.8$. The fitted dust parameters are given in Table 3.3.

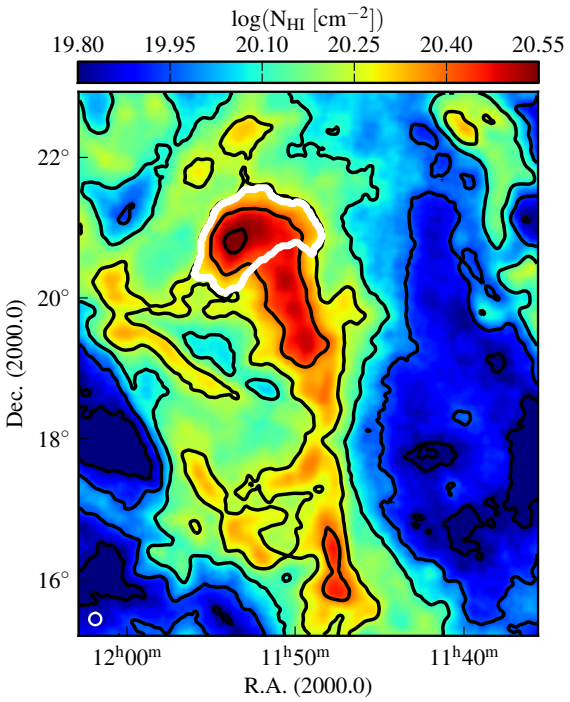

Fig. 3.9: HI column density map of IVC 1 integrated between $-60\,\mathrm{km\,s^{-1}} \leq v_{\mathrm{LSR}} \leq -20\,\mathrm{km\,s^{-1}}$. The black contours mark N_{HI} at the levels of the colour bar tick labels. The white contour encloses the core of the IVC which is analysed in further detail in Sect. 3.5.4. The white circle at the bottom left gives the angular resolution of EBHIS.

3.5.2 IVC 2

3.5.2.1 HI and FIR data

The cloud IVC 2 is located at the top right of the field at (R.A., Dec.) = ($10^{\mathrm{h}}52^{\mathrm{m}}$, 25°). The cloud is selected because of its bright FIR emission and its similarity to IVC 1 in HI.

In Fig. 3.7 the HI-FIR correlation plots are presented. The linear fits are performed below $N_{\mathrm{HI}} \leq 2.0 \times 10^{20}\,\mathrm{cm^{-2}}$ where a linear model is thought to be valid. This is the threshold we also apply for the entire field (Sect. 3.4.1). At the lowest N_{HI}, the cloud's FIR emission is equal to that of IVC1 (Fig. 3.7), although the fitted FIR emissivities of IVC 2 are notably larger (Table 3.2, fourth column). The emissivity increases even more when larger column densities are considered.

The HI spectrum at the highest brightness temperature (Fig. 3.8, bottom) resembles the spectrum of IVC 1. It is well approximated by two Gaussians with FWHM $\simeq 5.1\,\mathrm{km\,s^{-1}}$ centred on $-40.0\,\mathrm{km\,s^{-1}}$ and FWHM $\simeq 11.5\,\mathrm{km\,s^{-1}}$ at $-37.0\,\mathrm{km\,s^{-1}}$. In IVC 2 about 70% of the HI is in the colder phase. As with IVC 1, there is not much HI at different radial velocities in the spectrum. Figure 3.11 shows a column density map integrated between $-60\,\mathrm{km\,s^{-1}} \leq v_{\mathrm{LSR}} \leq -20\,\mathrm{km\,s^{-1}}$ with a maximum of $N_{\mathrm{HI}} \simeq 3.1 \times 10^{20}\,\mathrm{cm^{-2}}$, which is less than for IVC 1. Structures emerge from the central core in several directions showing other cold clumps.

The dust spectrum of IVC 2 at its maximum N_{HI} is shown in Fig. 3.10 (bottom). As for IVC 1, the emission is well described by a modified black body with $\beta = 1.8$. The fitted dust parameters are given in Table 3.3. The dust optical depth in IVC 2 is about four times larger, and the fitted grain temperatures are slightly lower, than in IVC 1.

The angular resolution of the FIR data is higher than in the HI (Table 3.1). Indeed IVC 2 shows more structure in the FIR than in HI: east of the central core a second maximum is evident in the FIR only (Fig. 3.12). In the HI-FIR correlation of IVC 2 (Fig. 3.7), this second FIR peak is causing the large spread in N_{HI} for given I_ν. This second FIR peak is fitted with $(\tau_{857}, T_{\mathrm{D}}) = ((5.4 \pm 0.1) \times 10^{-5},$

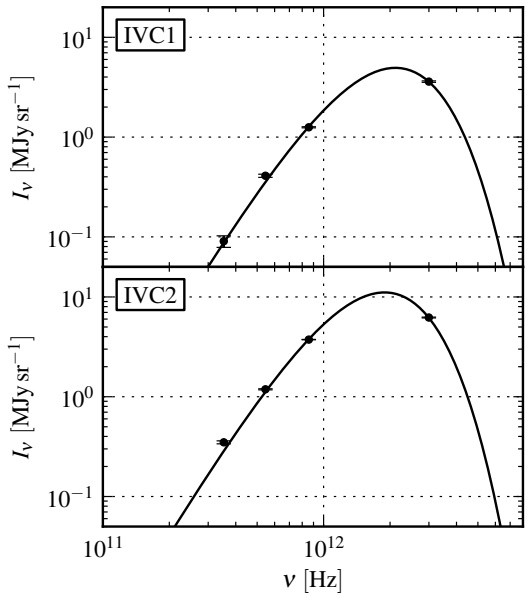

Fig. 3.10: FIR dust spectra and fitted modified black bodies with $\beta = 1.8$. The spectra are taken at the position of the largest $N_{\rm HI}$ for IVC 1 (*top*) and IVC 2 (*bottom*). The fitted dust parameters are $(\tau_{857}, T_{\rm D})_{\rm IVC\,1} = ((8.3 \pm 0.4) \times 10^{-6}, 21.2 \pm 0.2\,{\rm K})$ and $(\tau_{857}, T_{\rm D})_{\rm IVC\,2} = ((3.2 \pm 0.1) \times 10^{-5}, 19.1 \pm 0.2\,{\rm K})$.

17.7 ± 0.1 K), thus it has an even larger dust optical depth and lower dust temperature.

3.5.2.2 H_2 and CO data

Désert et al. (1990) report on pointed ^{12}CO observations of this particular cloud. The pointing positions are indicated in Fig. 3.12 by the black diamonds. They detect the central core in ^{12}CO(1→0) and the eastern FIR-peak in ^{12}CO(2→1). The CO emission is at $v_{\rm LSR} \simeq -40\,{\rm km\,s^{-1}}$ which is consistent with the radial velocity of the HI (Fig. 3.8, bottom). Désert et al. report on highly varying line intensities within two beams which indicates small-scale structure in the cloud. From CO they infer $N_{\rm H_2} = 10^{20} - 10^{21}\,{\rm cm^{-2}}$. Désert et al. conclude that IVC 2 is a molecular cloud at high radial velocity.

Our derived H_2 column densities (Sect. 3.4.3) for IVC 2 are in the range $1 - 2 \times 10^{20}\,{\rm cm^{-2}}$. Its largest molecular content is found at the eastern peak with $N_{\rm H_2} = 2.3 \times 10^{20}\,{\rm cm^{-2}}$. We estimate H_2 column densities from data with an angular resolution of 10.8′. The CO spectra of Désert et al. were obtained with a telescope beam of 60″ and 14″ which cannot be compared directly to our results since they probe different spatial scales. Désert et al. use a conversion factor of $X_{\rm CO} = 2.5{\times}10^{20}\,{\rm cm^{-2}}\,({\rm K\,km\,s^{-1}})^{-1}$ which is inherently a source of uncertainty for an individual cloud of sub-solar metallicity. Nevertheless, we can state that their estimates are compatible with what we find for IVC 2.

The molecular fraction $f_{\rm H_2}$ is calculated by

$$f_{\rm H_2} = \frac{2N_{\rm H_2}}{N_{\rm HI} + 2N_{\rm H_2}} = \frac{2N_{\rm H_2}}{N_{\rm H}}. \tag{3.5}$$

By summing up $N_{\rm HI}$ and $N_{\rm H_2}$ in each pixel of the cloud's core, the total molecular fraction obtained is $f_{\rm H_2}^{\rm IVC\,2} \simeq 0.4$.

With the estimated H_2 column densities we analyse the shielding conditions for H_2 and CO. Lee et al. (1996) calculate the corresponding shielding efficiencies. In their Table 10 they give the H_2 self-shielding efficiencies $\theta(N_{\rm H_2})$ for different H_2 column densities. For $N_{\rm H_2} \simeq 2 \times 10^{20}\,{\rm cm^{-2}}$ they find $\theta(N_{\rm H_2}) \simeq 7 \times 10^{-6}$. Thus the molecular hydrogen in IVC 2 is efficiently self-shielding.

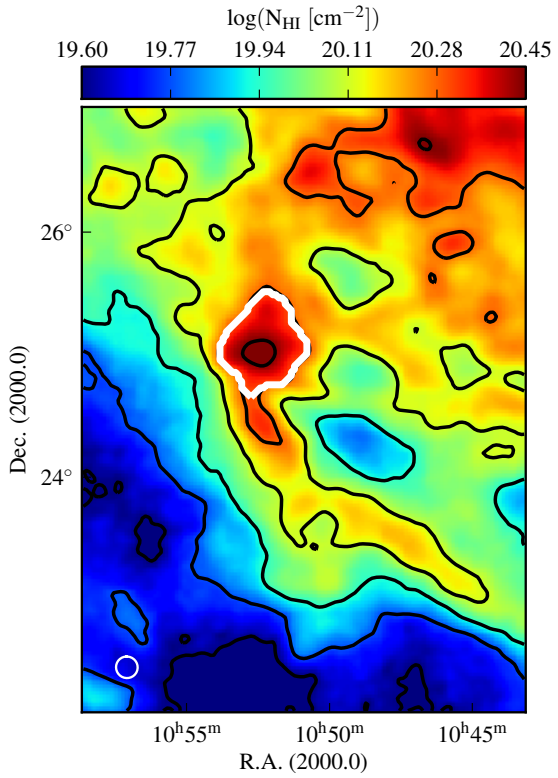

Fig. 3.11: HI column density map of IVC 2 integrated between $-60\,\mathrm{km\,s^{-1}} \leq v_{\mathrm{LSR}} \leq -20\,\mathrm{km\,s^{-1}}$. The black contours mark N_{HI} at the levels of the colour bar tick labels. The white contour encloses the core of the IVC which is analysed in further detail in Sect. 3.5.4. The white circle at the bottom left gives the angular resolution of EBHIS.

For CO formation one has to consider CO self-shielding, H_2, and dust shielding (Lee et al. 1996). Lee et al. estimate the shielding efficiencies for these three mechanisms (their Table 11). Taking the correspondence of $N_{\mathrm{H_2}}$ to N_{CO} from Pineda et al. (2010, their Fig. 14), which they derive for the Taurus molecular cloud, we assume that for IVC 2 $N_{\mathrm{CO}} \leq 10^{14}\,\mathrm{cm^{-2}}$. We adopt $N_{\mathrm{CO}} = 10^{14}\,\mathrm{cm^{-2}}$, $N_{\mathrm{H_2}} = 2 \times 10^{20}\,\mathrm{cm^{-2}}$, and $N_{\mathrm{H}} = 7.5 \times 10^{20}\,\mathrm{cm^{-2}}$, which gives $A_{\mathrm{v}} \simeq 0.4$ (Predehl & Schmitt 1995). The total shielding efficiency for IVC 2 concerning CO is the product of the three contributing shielding mechanisms: $\theta_1(\mathrm{CO})\theta_2(N_{\mathrm{H_2}})\theta_3(A_{\mathrm{v}}) \simeq 0.9 \times 0.7 \times 0.1 \simeq 0.1$. Thus, the CO molecules are well shielded by dust mostly and CO is expected to be found within IVC 2.

3.5.3 Metallicities and distances

In order to derive absolute quantities such as particle densities and cloud masses for the two IVCs, we need a distance estimate. The metallicity is of similar importance for the amount of dust and the formation of molecules.

The cloud IVC 1 is most likely part of the IV Spur and IVC 2 of the IV Arch. From absorption spectroscopy, near solar abundances are estimated for the IV Arch and slightly less in the IV Spur (Wakker 2001; Richter et al. 2001c; Savage & Sembach 1996). We note that these measurements yield precise values for specific lines of sight only. The two clouds could have different metallicities. However, we expect them to have a comparable metallicity because of their equal FIR brightness at the lowest N_{HI} (Fig. 3.7).

Since there is no accurate distance measurement for either IVC 1 or IVC 2, we constrain the distance by several different indicators. Stellar absorption lines restrict the distance to both IV Arch and Spur to the range 0.3 – 2.1 kpc (Wakker 2001). Similarly, Puspitarini & Lallement (2012) estimate distances in

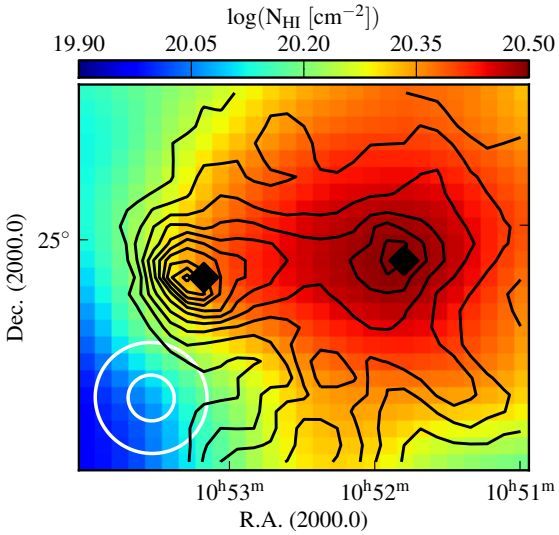

Fig. 3.12: HI column density map of IVC 2 overlayed with the unsmoothed 857 GHz data as black contours. A second FIR peak is located east of the HI core, but it is not evident in HI, implying that this structure is unresolved with our HI data. The pointing centres of the Désert et al. (1990) CO observations are given by the two black diamonds. Their corresponding beams are smaller than one pixel. The white circles indicate the angular resolution of EBHIS (larger) and *Planck* (smaller).

the range 95 − 157 pc to the gas with declinations $\delta \leq 10°$ at the bottom of our field. In addition they report on a negative velocity structure between $-40\,\mathrm{km\,s^{-1}} \leq v_{\mathrm{LSR}} \leq -20\,\mathrm{km\,s^{-1}}$ for which they detect no absorption. This IVC gas is at a minimal distance of 200 pc, which leads Puspitarini & Lallement to the conclusion that the IVCs are probably not associated with the local HI shells. A distance estimate for IVC 2 in the range 12 − 400 pc is given by Wesselius & Fejes (1973) based on calcium absorption lines.

To constrain the distance of both IVCs more accurately, we compare the ROSAT soft X-ray shadows (Snowden et al. 2000) to the shadow of the molecular IVC 135+54 for which Benjamin et al. (1996) establish a distance of 355±95 pc by interstellar absorption lines. Because of their high column densities ($N_{\mathrm{HI}} \geq 3 \times 10^{20}\,\mathrm{cm^{-2}}$), all three IVCs can be considered to be opaque for soft X-rays originating from beyond (Kerp 2003). Hence, the observed soft X-ray count rates towards the IVCs only trace the emission from the Galactic foreground plasma.

In the catalogue of soft X-ray shadows compiled by Snowden et al. (2000), IVC 1 is listed as cloud 273, IVC 2 as cloud 241, and our reference cloud IVC 135+54 as cloud 182. Assuming that for IVC 135+54 the soft X-ray count rate and its uncertainty fully correspond to the distance estimate of Benjamin et al. (1996), one can evaluate distances for IVC 1 and IVC 2 from their count rates. This yields $D_{\mathrm{IVC\,1}} = 420 \pm 190$ pc and $D_{\mathrm{IVC\,2}} = 510 \pm 140$ pc. Considering the uncertainties in the ROSAT count rates and the inaccuracies in transforming them into a distance, we adopt the distance estimate $D = 0.4$ kpc for both IVC 1 and IVC 2. This is compatible with all the other distance indicators we have.

3.5.4 Estimation of cloud parameters

To characterise the clouds more completely, we estimate the following parameters:

- An upper limit on the kinetic gas temperature T_{kin} is obtained from the HI line width Δv (Kalberla & Kerp 2009, their Eq. 4). In addition to Doppler broadening, turbulence and substructure also contribute to the spectral line width.

- The physical size d is estimated from the angular size and the distance D, assuming a circular cloud.

IVC	d [pc]	$T_{\rm kin}$ [K]	$n_{\rm HI}$ $\left[\mathrm{cm^{-3}}\right]$	$\frac{p_{\rm max}}{k_{\rm B}}$ $\left[\mathrm{K\,cm^{-3}}\right]$	$M_{\rm HI}$ [$\mathrm{M_\odot}$]	$M_{\rm D}$ [$\mathrm{M_\odot}$]	$\Sigma_{\rm HI}$ $\left[\mathrm{M_\odot\,pc^{-2}}\right]$	$\Sigma_{\rm D}$ $\left[\mathrm{M_\odot\,pc^{-2}}\right]$	$\tau_{857}^{\rm peak}$	$T_{\rm D}^{\rm peak}$ [K]
1	19	441	7	2880	620	2.1	2.1	0.0073	$(8.3 \pm 0.4) \times 10^{-6}$	21.2 ± 0.2
2	10	567	10	5890	140	1.2	1.9	0.0163	$(3.2 \pm 0.1) \times 10^{-5}$	19.1 ± 0.2

Table 3.3: Properties of the cores of IVC 1 and IVC 2 for a distance of $D = 0.4\,\mathrm{kpc}$. The columns give (from left to right) the linear diameter d, the upper limit of the gas temperature $T_{\rm kin}$ for the colder component, the HI volume density $n_{\rm HI}$, the maximum pressure $\frac{p_{\rm max}}{k_{\rm B}}$, the HI mass $M_{\rm HI}$, the dust mass $M_{\rm D}$, the HI surface mass density $\Sigma_{\rm HI}$, the dust surface mass density $\Sigma_{\rm D}$, the dust optical depth $\tau_{857}^{\rm peak}$, and dust temperature $T_{\rm D}^{\rm peak}$ at the peak HI column density.

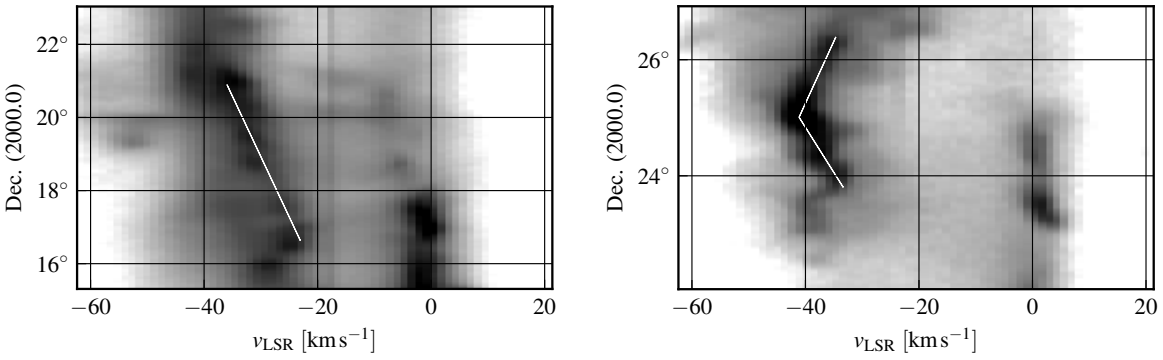

Fig. 3.13: Position-velocity (PV) diagrams of IVC 1 (*left*) integrated between $11^{\rm h}57^{\rm m} \geq$ R.A. $\geq 11^{\rm h}45^{\rm m}$ and IVC 2 (*right*) integrated between $10^{\rm h}54^{\rm m} \geq$ R.A. $\geq 10^{\rm h}48^{\rm m}$. The white lines indicate the orientation of the IVCs in PV space showing a velocity gradient which is interpreted as evidence for interactions of the clouds with the surrounding medium.

- The volume density $n_{\rm HI}$ is considered to be constant inside a spherically symmetric cloud of physical size d.
- The HI mass $M_{\rm HI}$ of a cloud is estimated by spatially integrating over $N_{\rm HI}$ given an estimate for the distance D.
- According to Hildebrand (1983), the dust mass $M_{\rm D}$ of a cloud is calculated from the observed FIR brightness by

$$M_{\rm D} = \frac{I_\nu \Omega D^2}{B_\nu(T_{\rm D})} \times \frac{\frac{4}{3} a \rho_{\rm D}}{Q_\nu} \simeq \frac{I_{857} \Omega D^2}{B_{857}(T_{\rm D})} \times 0.21\,\mathrm{g\,cm^{-2}} \tag{3.6}$$

  with the FIR intensity I_ν, the solid angle Ω of the cloud, the distance D, the grain radius a, the grain emissivity Q_ν, and the grain density $\rho_{\rm D}$. We estimate the dust mass for 857 GHz with the values for a, Q_ν, and $\rho_{\rm D}$ given by Hildebrand.

Many cloud parameters depend on the distance, for which we use $D = 0.4\,\mathrm{kpc}$ (Sect. 3.5.3). We calculate the physical quantities for the cores which are marked by the white contour in Figs. 3.9 and 3.11. We use a watershed algorithm (Beucher & Lantuéjoul 1979) to determine the extent of these cores.

The results for the parameters are compiled in Table 3.3. We note that for IVC 2 no molecular hydrogen is taken into account; H_2 adds to the total particle density and the total gas mass.

For the HI surface mass density, we obtain for the IVC cores $\Sigma_{\rm HI}^{\rm IVC\,1} \simeq 2.1\,\mathrm{M_\odot\,pc^{-2}}$ and $\Sigma_{\rm HI}^{\rm IVC\,2} \simeq 1.9\,\mathrm{M_\odot\,pc^{-2}}$. We calculate a corresponding dust surface mass density which results in $\Sigma_{\rm D}^{\rm IVC\,1} \simeq 0.0073$

$M_\odot\,pc^{-2}$ and $\Sigma_D^{IVC\,2} \simeq 0.0163\,M_\odot\,pc^{-2}$. The HI surface density is comparable, but in IVC 2 the dust surface density is more than twice as large.

Both IVC 1 and IVC 2 are not self-gravitating. Their Jeans masses, derived from the HI data, are larger than their gas masses by two orders of magnitude. This is still true when H_2 is considered. However, the gas temperature estimated from the HI serves only as an upper limit. Locally, the gas is certainly colder when we consider the CO within IVC 2, possibly even below 30 K (see e.g. Glover & Clark 2012). Nevertheless, we do not expect IVC 2 to form stars.

3.5.5 Interactions of IVCs with the ambient medium

Indications for dynamical interactions of IVC 1 and IVC 2 with their environment are inferred from position-velocity (PV) diagrams (Fig. 3.13) that show the velocity changes over the IVC filaments. The PV diagrams are integrated between $11^h57^m \geq$ R.A. $\geq 11^h45^m$ for IVC 1 and $10^h54^m \geq$ R.A. $\geq 10^h48^m$ for IVC 2. The white diagonal lines in the diagrams mark the location and orientation of the two IVCs in PV space, revealing a change of v_{LSR} over the IVCs and the filaments to which they are connected. These gradients are probably due to interactions of the clouds with their surroundings. The PV diagrams also reveal the clumpy structure along the IVC filaments.

The isothermal speed of sound in an ideal gas with the kinetic temperature of IVC 1 or IVC 2 is about 2.0 km s^{-1} for the colder components. Thus the observed radial LSR velocity gradient within the individual IVCs significantly exceeds the speed of sound in the cold neutral medium. If this gradient is physical and not the result of projection effects, it implies that the IVC cores are punching through the Galactic halo medium while material is being stripped off and decelerated. A supersonic deceleration would build up shocks that compress and fragment the clouds (e.g. McKee & Hollenbach 1980).

3.6 Discussion: a dynamical HI-H_2 transition

We observe two IVCs in close proximity to each other that show respectively a deficiency (IVC 1) and an excess (IVC 2) in FIR emission, despite their similarities in HI and in their environmental conditions:

- Both IVCs consist of distinct cold clumps marked by narrow spectral HI lines with FWHM $\simeq$ 5 km s^{-1}. Their HI profiles can be characterised by this cold component, plus a warmer component with FWHM $\simeq$ 11 km s^{-1}. About 50% of the HI emission of IVC 1 originates from the cold gas, whereas for IVC 2 70% is in the cold phase. It is remarkable that for IVC 1 we estimate $N_{HI} \simeq 3.9 \times 10^{20}\,cm^{-2}$, which is significantly larger than for IVC 2 with $N_{HI} \simeq 3.1 \times 10^{20}\,cm^{-2}$ (Sects. 3.5.1, 3.5.2).

- To constrain the distances to both IVCs, we compare the ROSAT soft X-ray shadows of the IVCs to the molecular IVC 135+54 for which there is a firm distance bracket. We conclude that IVC 1 and IVC 2 have a similar distance similar to IVC 135+54 of about $D = 0.4$ kpc (Sect. 3.5.3).

- Both IVCs show an equal HI surface mass density. However, the dust surface mass density of IVC 2 is more than twice as large as that of IVC 1 (Sect. 3.5.4).

- Both IVCs have radial velocities between -35 km s^{-1} and -40 km s^{-1}. They exhibit a velocity gradient of 10 km s^{-1} (Sect. 3.5.5).

- From the FIR excess emission we estimate molecular column densities for IVC 2 of $N_{H_2} = 1 - 2 \times 10^{20}\,cm^{-2}$ which gives a total molecular fraction of $f_{H_2}^{IVC\,2} \simeq 0.4$ (Sect. 3.4.3).

In order to reconcile the similarities in HI properties with the low FIR emission of IVC 1 and the excess emission of IVC 2 due to H_2, we propose that IVC 1 and IVC 2 represent different states in a phase transition from atomic to molecular clouds at the disk-halo interface. The descent of IVCs onto the Galactic disk is thought to compress the gas which increases the pressure locally, triggering the fast formation of H_2 (Odenwald & Rickard 1987; Désert et al. 1990; Weiß et al. 1999; Gillmon et al. 2006; Guillard et al. 2009).

3.6.1 The scenario of interacting IVCs

According to the Galactic fountain model, metal enriched disk material is ejected via supernovae into the disk–halo interface (Bregman 2004). This rising gas is warm and ionised as a result of the large energies involved in the expulsion.

After culmination, the ejected matter falls back onto the disk. The descent from the culmination point is accompanied by an increase in gas pressure due to ram pressure. Electrons and protons recombine and form the warm neutral medium (WNM). When the ram pressure becomes larger than the thermal pressure within the cloud, shocks are induced that propagate through the IVC. These shocks enhance the pressure locally by which the formation time of H_2 is decreased (Guillard et al. 2009). The shocks trigger cooling of the WNM into condensations of the cold neutral medium (CNM) where H_2 forms.

The ram pressure not only compresses the cloud, but also causes a deceleration. This has been modelled by Heitsch & Putman (2009). Eventually, the IVC may reach local velocities which make it indistinguishable from local clouds. Since there are only a few molecular IVCs (MIVCs) known (Magnani & Smith 2010), a certain fine tuning of the parameters seems necessary in order to create a MIVC that we can detect.

In the following we try to evaluate the scenario of ram pressure induced H_2 formation by looking at the pressures and the timescales involved in the cases of IVC 1 and IVC 2.

3.6.2 H_2 formation in compressed gas

Bergin et al. (2004) write the time evolution of the H_2 number density n_{H_2} as

$$\frac{\mathrm{d}n_{H_2}}{\mathrm{d}t} = R_{gr}(T) n_{H_2} n_H - [\zeta_{cr} + \zeta_{diss}(N_{H_2}, A_V)] n_{H_2} \tag{3.7}$$

with the temperature dependent grain formation rate $R_{gr}(T)$, the destruction rate by cosmic rays ζ_{cr}, and the photo-dissociation rate $\zeta_{diss}(N_{H_2}, A_V)$. The dissociation rate ζ_{diss} depends on the self-shielding of H_2 (Draine & Bertoldi 1996).

Equation (3.7) relates the formation time of H_2 to the particle density and hence the pressure. We refer to the late stages of the infall during which the IVC has accumulated particle densities $n_{HI} > 1\,\mathrm{cm}^{-3}$. Compressed gas is able to cool quickly (Sect. 3.6.3) which results in large particle densities.

In our picture ram pressure acts on the cloud because of its movement through the ISM. The ram pressure

$$p_{ram} = \rho \times v^2 \tag{3.8}$$

depends on the mass density ρ of the surrounding medium and the relative velocity v between cloud and surroundings. The cloud moves through the Galactic halo, for which we take the Milky Way model of Kalberla & Dedes (2008) to get estimates of the halo densities and pressures. We calculate the associated ram pressure for several velocities at the distances $0.5\,\mathrm{kpc} \leq D \leq 3\,\mathrm{kpc}$ in the line of sight towards IVC 2. In Fig. 3.14 we compare the ram pressure with the halo pressure. We note that we can observe only the radial velocity component. Any additional tangential velocity component is unknown.

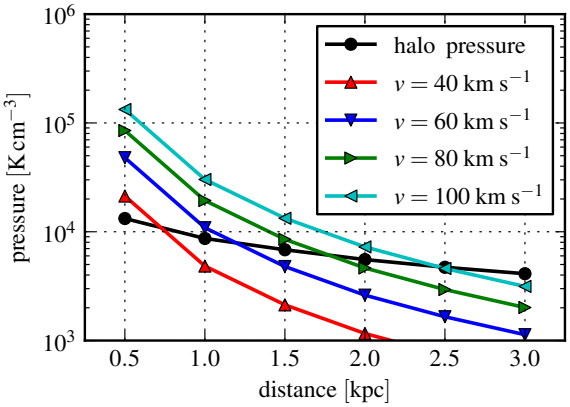

Fig. 3.14: Comparison of modelled halo pressure from Kalberla & Dedes (2008) to ram pressure at the given distance in the line of sight towards IVC 2. The ram pressure is calculated from Eq. (3.8) using the modelled halo density and the chosen cloud velocities 40, 60, 80, and 100 km s^{-1}.

At one point the ram pressure exceeds the halo pressure for all considered cloud velocities. The distance at which the ram pressure and the halo pressure are equal increases with cloud velocity. Thus, ram pressure interactions are expected to be important for all IVCs. For IVC 1 and IVC 2, which are at a distance of $D \simeq 0.4$ kpc (Sect. 3.5.3), the ram pressure is at least twice as large as the halo pressure. Hence, perturbations driven by ram pressure are not only possible, but likely. Indications for this are for example the morphology of the clouds (Sects. 3.5.1 and 3.5.2) and their velocity gradients (Sect. 3.5.5).

We emphasise the importance of magnetic fields for cloud compression and condensation. In the Galactic halo there are magnetic fields of a few μG which can be important for gas dynamics (Putman et al. 2012). Hartmann et al. (2001) show that clouds can form preferentially at kinks or bends in the magnetic field.

3.6.3 Timescales

From isobaric cooling models Guillard et al. (2009) find an inverse scaling between the H_2 formation timescale and the pressure which can be approximated by

$$t_{H_2}[\mathrm{yr}] \simeq 7 \times 10^5 f_{\mathrm{dust}} \left(\frac{2 \times 10^5\,[\mathrm{K\,cm^{-3}}]}{p_{\mathrm{th}}} \right)^{0.95} . \tag{3.9}$$

We note that the H_2 formation timescale in Eq. (3.9) is computed neglecting H_2 destruction in Eq. (3.7). Bergin et al. (2004) give full solutions to Eq. (3.7) with longer timescales by up to a factor of two. In our case $f_{\mathrm{dust}} = 1$ since the emissivity per H atom from IVC 2 is comparable to the mean value in the low velocity gas.

For a distance $D \simeq 0.4$ kpc the ram pressure in both IVC 1 and IVC 2 is $p_{\mathrm{ram}} \gtrsim 2 \times 10^4$ K cm^{-3}, resulting in a formation timescale of $t_{H_2} \lesssim 6$ Myr. In this time the clouds travel less than 0.25 kpc. Bergin et al. (2004) state that the actual formation timescale of H_2 is not the limiting factor in molecular cloud formation; it is merely a requirement of shielding of H_2 and CO which is governed by the accumulation of gas and dust and the formation of dense cores. Hence, t_{H_2} could be even smaller.

For the CNM, Kalberla & Kerp (2009) estimate a cooling time of $t_{\mathrm{cool}}(\mathrm{CNM}) \simeq 0.1$ Myr. This is significantly less than t_{H_2}, explaining why ISM clouds contain CNM without H_2. Above a sufficient particle density, compressed gas can cool faster and become denser.

To estimate the time an IVC has to form H_2, we need to compare the formation time with the free-fall time in the Galactic gravitational potential calculated by applying a simple linear, unaccelerated motion. Assuming an initial velocity of $v = 80$ km s^{-1}, the free-fall time from an altitude of 0.5 kpc in the halo

is about 6 Myr. Thus, the H_2 formation timescale is comparable or shorter than the descending time; H_2 may form before the IVC merge with gas in the Galactic plane.

It is not surprising that IVC 1 and IVC 2 are not different with respect to their estimated H_2 formation timescale, since t_{H_2} is inferred from the EBHIS data only, in which both clouds are very similar (Sect. 3.5). Hence, the observed differences in the FIR are a result of processes on angular scales which are unresolved with EBHIS.

3.6.4 Molecular gas in the field

For the molecular IVC we sketch a scenario of H_2 formation by the compression due to ram pressure reducing the H_2 formation timescale. However, two major questions remain: will IVC 1 become molecular in future? and how is the H_2 at $v_{LSR} = 0\,\mathrm{km\,s^{-1}}$ formed?

At present we consider the atomic IVC 1 to be in an intermediate state of molecular formation. Either it is already forming H_2 efficiently in small condensations within the cloud, or it will in the future.

In the PV diagrams of IVC 1 and IVC 2 (Fig. 3.13) both clouds are clearly connected to lower velocity gas. Furthermore, the observed velocity gradients along the IVC filaments may indicate a dynamical connection of IVC to lower velocity gas. It is tempting to speculate that some H_2 in the local gas represents the remnants of a past interaction between IVC gas and the Galactic disk. As IVC gas slows down, the ram pressure and the H_2 formation rate decrease. Once a sufficiently high amount of H_2 has been formed, self-shielding becomes important and maintains the large H_2 content.

The outlined dynamically-triggered formation of H_2 is not necessarily traceable by CO emission and might be considered as CO-dark gas (Wolfire et al. 2010; Planck Collaboration XIX 2011). In particular, a sufficiently high dust column density has to be built up in order to allow the formation of CO. Related to this is the X_{CO} factor which is known to be influenced by local conditions, especially by metallicity (Feldmann et al. 2012). Furthermore, CO has to be collisionally excited to become observable in emission. Bergin et al. (2004) point out that there could be a large reservoir of H_2 in the diffuse ISM which is not able to form CO detectable in emission.

3.7 Conclusion

We correlate HI emission to the brightness at various wavelengths in the FIR dust continuum using new data from the Effelsberg-Bonn HI Survey (EBHIS) and the *Planck* satellite complemented by IRIS data. We study in detail two IVCs that show many similarities in their HI properties, such as narrow spectral lines with FWHM $\simeq 5\,\mathrm{km\,s^{-1}}$ and HI column densities of $N_{HI} = 3 - 4 \times 10^{20}\,\mathrm{cm^{-2}}$. Despite their similarity in HI, their FIR emission exhibits large differences: one cloud is FIR bright while the other IVC is FIR faint.

From the quantitative correlation of HI and FIR emission, we calculate maps of molecular hydrogen column density revealing large amounts of H_2 in the field of interest for which no existing CO survey of the region has detected a CO counterpart. How much of this H_2 is actually CO-dark gas, we cannot tell since the CO survey data that is available today is not sensitive enough. We do, however, know that the molecular IVC contains CO. The HI emission traces only a part of the total gas distribution. Together with the inferred H_2 column densities, the relation between gas and dust is consistent.

Based on our findings we describe a scenario of a dynamical transition from atomic to molecular IVCs in the lower Galactic halo. During the descent of the IVCs through the Galactic halo, they are compressed as a result of external pressure and ram pressure. Once the ram pressure exceeds the thermal pressure, shocks are created which enhance the pressure locally and accumulate gas and dust. An increased pressure reduces the formation timescale of H_2 in condensations of the cold atomic medium.

The only physical distinctions between the two IVCs are the amount of dust within the clouds, measured by the dust surface mass density, and the amount of H_2. The molecular IVC has a factor of $2-3$ more dust within its central region than the atomic IVC, which is accompanied by a 50% higher total hydrogen column density. On the other hand, IVC 1 has more HI mass in total. Apparently, this mass is not distributed so as to allow efficient H_2 formation. According to the data presented in this paper, we expect that the atomic IVC will also turn molecular in a few Myrs.

Processes on spatial scales that are not resolved by our data govern the evolution of an IVC from an atomic to a molecular cloud. The $10.8'$ resolution of EBHIS corresponds to a spatial resolution of 1 pc at a distance of 0.4 kpc. However, the accumulation and condensation of smaller and denser clumps regulate the H_2 formation on sub-parsec scales. Radio-interferometric observations should reveal a different distribution of HI in the two IVCs on sub-parsec scales, for example compact cores in the molecular IVC.

Our approach appears to open a way to search for dark H_2 gas across the entire sky. Globally, this new search may reveal other clouds in transition from the atomic to the molecular gas phase. Compared to the low angular resolution of former large-scale HI single-dish surveys, the few detections of molecular IVCs so far may be due to the small-angular extent of the molecular cores.

Acknowledgements

We thank the anonymous referee for his useful comments and suggestions which helped to improve the manuscript considerably. The authors thank the Deutsche Forschungsgemeinschaft (DFG) for financial support under the research grant KE757/11-1. F. B. acknowledges support from the MISTIC ERC grant no. 267934. The work is based on observations with the 100 m telescope of the MPIfR (Max-Planck-Institut für Radioastronomie) at Effelsberg and the *Planck* satellite operated by the European Space Agency. The development of *Planck* has been supported by: ESA; CNES and CNRS/INSU-IN2P3-INP (France); ASI, CNR, and INAF (Italy); NASA and DoE (USA); STFC and UKSA (UK); CSIC, MICINN and JA (Spain); Tekes, AoF and CSC (Finland); DLR and MPG (Germany); CSA (Canada); DTU Space (Denmark); SER/SSO (Switzerland); RCN (Norway); SFI (Ireland); FCT/MCTES (Portugal); and PRACE (EU). T. R. is a member of the International Max Planck Research School (IMPRS) for Astronomy and Astrophysics at the Universities of Bonn and Cologne as well as of the Bonn-Cologne Graduate School of Physics and Astronomy (BCGS).

CHAPTER 4

High-resolution HI and CO observations of high-latitude intermediate-velocity clouds

This chapter is submitted as an article to the journal A&A with the title "High-resolution HI and CO observations of high-latitude intermediate-velocity clouds", T. Röhser, J. Kerp, N. Ben Bekhti, and B. Winkel. For consistency with the rest of the text, we made some minor adjustments to the submitted version.

Abstract

Intermediate-velocity clouds (IVCs) are HI halo clouds that are likely related to a Galactic fountain process. In-falling IVCs are natural candidates for the accretion of matter onto the Milky Way. We study the evolution of IVCs at the disk-halo interface, focussing on the transition from atomic to molecular IVCs. We compare an atomic IVC to a molecular IVC and characterise their structural differences in order to understand how molecular IVCs form high above the Galactic plane. With high-resolution HI observations of the Westerbork Synthesis Radio Telescope and ^{12}CO(1→0) and ^{13}CO(1→0) observations with the IRAM 30 m telescope, we analyse the small-scale structures within the two clouds. By correlating HI and FIR dust continuum emission from the *Planck* satellite, the distribution of molecular hydrogen (H_2) is estimated. We conduct a detailed comparison of the HI, FIR and CO data and study variations of the X_{CO} conversion factor. The structural properties of the two IVCs appear to determine their different chemical states. The atomic IVC shows no detectable CO emission and insignificant substructure in terms of HI column density, indicating that most of the atomic hydrogen is distributed smoothly. The molecular IVC exhibits a rich atomic and molecular structure. More HI is found in compact structures, increasing towards the eastern edge of the cloud where also most of the CO emission originates from. There is observational evidence that the molecular IVC is in a transient phase. The average X_{CO} factor is close to the canonical value of the Milky Way disk. We propose that the two IVCs represent different states in a gradual transition from atomic to molecular clouds in the Galactic fountain cycle. The molecular IVC is condensed allowing the formation of H_2 and CO in shielded regions all over the cloud. Ram pressure accumulates gas and may facilitate the formation of H_2. We have evidence that the atomic IVC will evolve also into a molecular IVC in a few Myr.

4.1 Introduction

In the evolution of a star-forming galaxy like the Milky Way, a cycle of matter is established by the expulsion from the disk and accretion from the halo (e.g. Ferrière 2001). One of the dominant mecha-

nisms is the Galactic fountain process which is caused by high-mass stars and their feedback onto the Galactic ISM (Shapiro & Field 1976; Bregman 1980): Stellar winds and supernovae expel gas and dust into the Galactic halo where a reservoir of metal-enriched material is sustained. The expelled gas cools down and condenses into clouds which are observable by their emission of HI 21 cm line emission. Eventually, these clouds fall back and refuel the Milky Way disk.

Usually, HI halo clouds are identified by their observed radial velocities which are incompatible with a simple model of Galactic rotation (e.g. Wakker 1991). Wakker (2001) uses a velocity range relative to the local-standard-of-rest (LSR) between $40\,\mathrm{km\,s^{-1}} \lesssim |v_{\mathrm{LSR}}| \lesssim 90\,\mathrm{km\,s^{-1}}$ to define intermediate-velocity clouds (IVCs). Most of the IVCs show metallicities close to solar, contain dust as seen by their far-infrared (FIR) continuum emission and have distances below 5 kpc (e.g. Wakker 2001). All these properties favour a connection of IVCs to Galactic fountains (Bregman 2004; Sancisi et al. 2008; Putman et al. 2012).

For the evolution of IVCs in the Galactic halo not only their atomic but also their molecular content is important. The most efficient formation mechanism of molecular hydrogen (H_2) is the formation on the surfaces of dust grains (Hollenbach & Salpeter 1971). Dust is present in IVCs as is evident from their FIR emission (e.g. Planck Collaboration XXIV 2011). As a likely product of a Galactic fountain, not only gas but also dust is expelled into the Galactic halo (Putman et al. 2012). Molecular hydrogen is observed in IVCs, either as a diffuse low column density component with $N_{\mathrm{H_2}} = 10^{14} - 10^{16}\,\mathrm{cm^{-2}}$ (Richter et al. 2003; Wakker 2006) or as molecular intermediate-velocity clouds (MIVCs) with significant molecular fractions such that ^{12}CO(1→0) emission is detectable (Magnani & Smith 2010).

It is important in which state the clouds impact the disk at the end of the fountain cycle. If the clouds are destroyed and get ionised, they cannot contribute to star formation for which cold gas is required (Putman et al. 2012). In-falling cold and dense clouds may integrate into the disk and feed star formation or even trigger the formation of molecular clouds and stars, for instance in the Gould Belt (Comeron & Torra 1992).

Röhser et al. (2014) propose a natural evolutionary sequence from pure atomic to molecular IVCs in the fountain cycle. During the infall of IVCs, ram pressure perturbs the clouds by their motion through the surrounding halo medium. Enhanced pressure leads to the faster formation of H_2 which is related to the compression and accumulation of the gas (Guillard et al. 2009; Hartmann et al. 2001). These effects are most important during the final stages of accretion of the clouds because the surrounding halo medium is densest.

Röhser et al. (2014) base their discussion on two prototypical IVCs at high Galactic latitudes that show an infalling motion. These IVCs appear as twins in HI single-dish data but are completely different in terms of the correlation with the FIR dust emission: One cloud is a linearly-correlating atomic IVC, the other is a FIR-excess MIVC.

Here, we present new high-resolution observations of these two clouds in HI and CO. The different chemical properties of the two clouds are expected to be imprinted in their spatial small-scale structure. We study the connection between the atomic and molecular gas. By correlating the HI emission to the FIR dust continuum, we estimate the distribution of H_2 within the clouds. Thus, variations of the conversion factor between CO and H_2, the X_{CO}-factor (Bolatto et al. 2013), are derived for the MIVC.

This paper is organised as follows. In Section 4.2 we present the data sets that are used in this study. In Section 4.3 we describe how we infer H_2 column densities. In Section 4.4 we present the characteristics of the two IVCs that are obtained from the new high-resolution data. In Section 4.5 we discuss our results and summarise in Section 4.6.

data	ν [GHz]	angular resolution	channel width $\left[\mathrm{km\,s^{-1}}\right]$	noise	Ref.
EBHIS	1.42	$10.8'$	1.29	$\lesssim 90\,\mathrm{mK}$	(1)
WSRT aIVC	1.42	$75.1'' \times 23.0''$	1.03	$1.3\,\mathrm{mJy\,(beam)^{-1}}$	(3)
WSRT mIVC	1.42	$49.1'' \times 17.9''$	1.03	$1.7\,\mathrm{mJy\,(beam)^{-1}}$	(3)
Planck τ_{353}	353	$5.27'$	–	–	(2)
IRAM FTS ^{12}CO(1→0)	115.27	$23.0''$	0.53	0.19 K	(3)
IRAM FTS ^{13}CO(1→0)	110.20	$24.1''$	0.53	0.09 K	(3)
IRAM VESPA ^{13}CO(1→0)	110.20	$24.1''$	0.13	0.14 K	(3)

References: (1) Winkel et al. (2016); (2) Planck Collaboration XI (2014); (3) This work.

Table 4.1: Characteristics of the different data sets used in this study. For IRAM and *Planck*, the data is gridded to maps with a Gaussian kernel, degrading the spatial resolution slightly. The angular resolution is that of the final gridded FITS maps.

4.2 Data

The characteristics and references for all data sets that are used in this study are compiled in Table 4.1. Henceforward, we refer to the atomic IVC as "aIVC" and to the molecular IVC as "mIVC". These are the clouds IVC 1 and IVC 2 from Röhser et al. (2014).

4.2.1 HI data

For our HI analyses, we use the new Effelsberg-Bonn HI Survey (EBHIS, Winkel et al. 2016; Kerp et al. 2011; Winkel et al. 2010) which is complemented by new high-resolution radio interferometric observations with the Westerbork-Synthesis Radio Telescope (WSRT). With the WSRT, the mIVC is observed with a single pointing and the aIVC with two pointings because of its larger angular extent. Each field of interest was observed for 12 hours to achieve both a good uv-coverage and sensitivity. The observations were conducted in June 2013. In the following a brief description of the data reduction and imaging is given. For more details, compare with Sect. 2.5.

The WSRT data is calibrated with the software package MIRIAD (Sault et al. 1995) and imaged with CASA (McMullin et al. 2007). Only a small fraction of the data has to be flagged due to contamination with radio frequency interference. Self-calibration is performed towards the brightest unresolved continuum sources within each field in order to improve the phase solutions. The continuum is subtracted for each pointing separately by fitting a low-order polynomial to the line-free channels. The data is iteratively cleaned using multiscale-clean in CASA by setting masks around the emission in order to avoid cleaning of the strong imaging artefacts. The cleaning is a crucial step because of the extended HI emission of both IVCs which covers the primary beam of the interferometer. We apply Briggs weighting with a robust parameter of 2 which is close to natural weighting in order to achieve the best sensitivity (Briggs et al. 1999). For the aIVC, the two pointings are imaged separately and combined into a mosaic image. The interferometric images are corrected for the primary beam. In the following this primary-beam-corrected data is used.

The calibrated and imaged interferometric data is supplemented by the EBHIS data to fill in the missing spacings. This is of great importance for nearby objects with extended HI emission that is not well recovered by the interferometer (e.g. Stanimirovic 2002). For the combination, we use the method of Faridani et al. (2014) which combines the science-ready data in the image domain. Because of residual negative emission in the cleaned maps, that is unphysical, we set all negative values to zero

prior to the combination. The properties of the final HI data cubes are given in Table 4.1.

For a proper analysis of the HI distribution of the two clouds, extensive mosaics would be required to cover the entire HI emission also with the interferometer. Our limited spatial coverage is a problem for the zero-spacing correction since the large beam of the single dish smears emission into the WSRT pointing. This introduces uncertainties in the analysis of the two clouds that are difficult to quantify because the small-scale structures of the surrounding HI gas is unknown.

4.2.2 CO data

With the IRAM 30 m telescope at the Pico Veleta (Spain) we mapped both IVCs in ^{12}CO(1→0) and ^{13}CO(1→0) emission applying on-the-fly (OTF) mode with position switching. We used the single-pixel receiver EMIR (Carter et al. 2012) in combination with the FTS spectrometer (Klein et al. 2012) in wide mode offering 8 GHz of total bandwidth at a spectral resolution of 195 kHz. The spectral band was chosen such that both the ^{13}CO(1→0) transition at 110.20 GHz and the ^{12}CO(1→0) transition at 115.27 GHz were observed simultaneously. In addition, the backend VESPA[1] was used for high spectral resolution spectroscopy with 50 kHz centred on the ^{13}CO(1→0) line. For more details, compare with Sect. 2.6.

The OTF stripes were positioned such that the data fulfils Nyquist sampling. The scanning direction was either along Right Ascension or Declination with an integration time of 1 s. Regularly, every 1-2 min an empty reference position near the scanned field is observed. About every 10 min the data is calibrated by observing the sky emission at the reference position and the counts from loads at ambient and cold temperatures. The average opacities were $\tau \simeq 0.2 - 0.3$ at 115 GHz. In total, 89 h of observing time was scheduled May 31 2014 – June 3 2014 and August 28 – September 04 2014. In the first session, lots of observation time was lost due to bad weather.

The mean elevation of the two clouds was about 60°. For the mIVC, we covered those regions which contain most of the FIR emission. Jorge L. Pineda kindly provided us with unpublished IRAM 30 m observations of the central core of the cloud. In total, the observations consist of 223481 individual spectra. For the aIVC, a field centred on the largest HI column densities was observed, in total 24946 spectra.

The data reduction is performed with GILDAS, the Grenoble Image and Line Data Analysis Software[2]. The OTF data is re-calibrated with the Multichannel Imaging and Calibration Software for Receiver Arrays (MIRA)[3] in order to improve on the standard automatic calibration scheme by applying time-weighted OFF measurements. With the Continuum and Line Analysis Single-dish Software (CLASS)[4], we extract 300 channels centred on the ^{12}CO(1→0) and ^{13}CO(1→0) and correct for the primary beam efficiency of the telescope.

With self-written python[5]-scripts, we fit a baseline of fifth order to the line-free channels of each spectrum and subtract the baseline polynomial from the entire spectrum. These spectra are gridded to FITS[6] datacubes with pixel size of 7″ using a Gaussian kernel of 1/3 of the telescope beam. Prior gridding, the additional data from Jorge L. Pineda data is spectrally smoothed and re-gridded in order to match the FTS data. The properties of the final CO data cubes are given in Table 4.1.

[1] http://www.iram.fr/IRAMFR/TA/backend/veleta/vespa/index.htm
[2] http://www.iram.fr/IRAMFR/GILDAS
[3] http://www.iram.fr/IRAMFR/GILDAS/doc/html/mira-html/mira.html
[4] http://www.iram.fr/IRAMFR/GILDAS/doc/html/class-html/class.html
[5] http://www.python.org/
[6] http://fits.gsfc.nasa.gov/

4.2.3 FIR data

In the FIR, we use the all-sky dust model from Planck Collaboration XI (2014) who fit modified black-bodies to the dust spectrum at 353, 545, 857, and 3000 GHz. In the dust model, the amplitude of the emission strength is given by the dust optical depth at 353 GHz τ_{353} to which we refer to in the following as τ. The dust model is at a spatial resolution of 5′, which is provided in HEALPix[7] format (Górski et al. 2005). For visualisation, we grid the HEALPix data to FITS maps by applying a Gaussian kernel which degrades the spatial resolution slightly (Table 4.1).

4.3 Methods

There is a linear correlation between the total hydrogen column density $N_{\rm H}$ and the FIR dust continuum emission I_ν at frequency ν (e.g. Boulanger et al. 1996). Equivalently, the dust emission strength can be expressed as the amplitude τ of a modified black-body (e.g. Planck Collaboration XI 2014). We use τ as the measure for the dust emission because it combines information from four different frequency bands reducing variations of the emissivity in individual bands.

We write the correlation as

$$\tau = R + \epsilon \times N_{\rm H} \simeq R + \epsilon \times (N_{\rm HI} + 2N_{\rm H_2}) \tag{4.1}$$

with a constant offset R and the dust emissivity ϵ. The ionised hydrogen column density is neglected here because of its low column density which is an order of magnitude smaller than $N_{\rm HI}$ (e.g. Lagache et al. 2000).

In order to model the observed FIR emission best, we adopt a two-component model consisting of a foreground and the IVC located beyond. These two components may have dust-to-gas ratios that are generally different. For the two IVCs of interest, the foreground HI column density is low and the foreground molecular fraction negligible. Thus, we write

$$\tau \simeq R + \epsilon^{\rm local} \times N_{\rm HI}^{\rm local} + \epsilon^{\rm IVC} \times (N_{\rm HI}^{\rm IVC} + 2N_{\rm H_2}^{\rm IVC}). \tag{4.2}$$

By the inversion of this relation, one obtains an expression for the non-linearly correlating gas component, which is molecular hydrogen, assuming a constant dust-to-gas ratio in both the local foreground and the IVC. Rearranging to the H_2 column density of the IVC, gives

$$N_{\rm H_2}^{\rm IVC} \simeq \frac{1}{2}\left(\frac{\tau - (R + \epsilon^{\rm local} \times N_{\rm HI}^{\rm local})}{\epsilon^{\rm IVC}} - N_{\rm HI}^{\rm IVC}\right). \tag{4.3}$$

The linear parameters R, $\epsilon^{\rm local}$, and $\epsilon^{\rm IVC}$ are estimated from fits to the linear part of the HI-τ correlation in which the influence of H_2 is negligible also in the IVC. For increasing HI column density, more atomic hydrogen turns molecular which leads to the FIR excess (e.g. Désert et al. 1988). The important limitation is the determination of the linear parameters in Eq. (4.2) in order to avoid systematic biases.

Instead of fitting the two-component linear function (Eq. 4.2) up to a fixed HI column density threshold, we iteratively remove data points from the HI-τ correlation that deviate too much from an initial fit. The deviation is calculated as the standard deviation of the residual emission. We start with the entire correlation data and subsequently exclude all points that deviate by more than 5σ from this initial estimate. For the new set of data points, Eq. 4.2 is fitted again, the deviation evaluated and data points

[7] http://healpix.sourceforge.net/

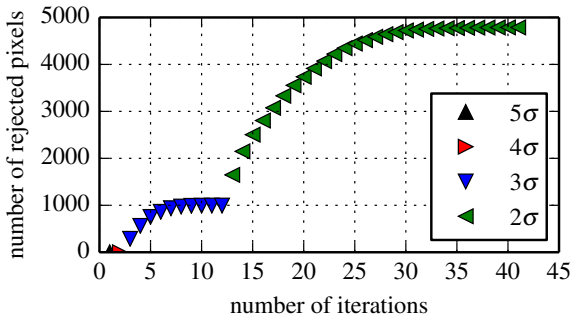

Fig. 4.1: Convergence of the iterative HI-τ fitting method as described in Sect. 4.3. The number of rejected data points for each iteration is shown cumulatively. The different colours and symbols indicate the different exclusion criteria.

excluded. This is continued in a loop until each remaining data point is consistent with the 5σ threshold. We repeat the loop with a 4σ, 3σ, and 2σ rejection criterion. Each loop is continued until all data points are consistent with the respective deviation criterion.

We devise a simple test of this iterative fitting procedure by adding a background cloud with non-linear HI-τ scaling to data of linear foreground emission with $N_{\mathrm{HI}}^{\mathrm{peak}} \simeq 5 \times 10^{20}\,\mathrm{cm}^{-2}$. As a background cloud, we take a 2D Gaussian with $N_{\mathrm{HI}} = 7 \times 10^{20}\,\mathrm{cm}^{-2}$ and white noise with 1% of the peak value. The non-linearity is introduced in the artificial background by switching the dust emissivity from $\epsilon^{\mathrm{IVC}} = 0.5 \times 10^{-26}\,\mathrm{cm}^2$ to $\epsilon^{\mathrm{IVC}} = 1.0 \times 10^{-26}\,\mathrm{cm}^2$ above $N_{\mathrm{HI}}^{\mathrm{IVC}} = 5 \times 10^{20}\,\mathrm{cm}^{-2}$. In addition, white noise is added to the FIR map with 1% of the peak value. The resulting map of τ is spatially smoothed slightly to smear out the artificial jump due to the switching of the dust emissivity. Consequently, the foreground and background cloud are also smoothed by the same amount.

The iterative linear two-component fit is applied in order to estimate the FIR emissivity at low N_{HI} yielding $\epsilon^{\mathrm{IVC}} = 0.515 \pm 0.001 \times 10^{-26}\,\mathrm{cm}^2$ which is close to the true value. The number of rejected data points per iteration and deviation criterion is shown cumulatively in Fig. 4.1. The different symbols and colours mark the different deviation criteria. Initially, a tighter deviation criterion omits most data points. After more iterations, the number of rejected data points decreases until all points are consistent. In this way the FIR-excess is iteratively removed and the bulk of the data points, that is the linearly correlating low HI column density part, dominates the fit. In this example, about one third of the data points is omitted. However, this method will still give emissivities that are slightly too large because of the smooth transition from the linear to the non-linear regime.

As a quantitative evaluation, a simple fit up to a chosen cut-off HI column density of $4 \times 10^{20}\,\mathrm{cm}^{-2}$ in either foreground or cloud gives the best value of $\epsilon^{\mathrm{IVC}} = 0.561 \pm 0.002 \times 10^{-26}\,\mathrm{cm}^2$. The iterative method performs better and, in addition, the best cut-off column density is not well constrained.

For the HI-τ correlation, we have different data sets with high and low spatial resolution (Table 4.1). Thus, one has to be careful to compare the data at the same spatial resolution. Due to the primary-beam correction of the interferometric data sets, the noise at the boundaries of the field of view is strongly enhanced. Thus, we blank the interferometric data below a primary-beam sensitivity level of 0.25 before we smooth the WSRT data to the angular resolution of the dust model from *Planck*. We choose this cut-off value because most HI emission is preserved. Then, the smoothed interferometric data is combined with EBHIS. For the remaining parts of the map, the interferometer does not give any additional information. Hence, outside the field-of-view of the WSRT, the limiting spatial resolution is EBHIS with $10.8'$. In this case the FIR data is smoothed to the angular resolution of EBHIS. Hence, we create HI and τ maps that comprise data at the resolution of the *Planck* dust model with $5.27'$ in the central region where the WSRT observations are sensitive and data at the EBHIS resolution of $10.8'$ surrounding the WSRT pointings.

4.4 Results

In this Section, we present the observational data of the atomic IVC (aIVC) and the molecular IVC (mIVC). For both clouds, the combined single-dish and interferometric HI data is presented first, followed by the CO data. Additional information about these two clouds is given in Röhser et al. (2014). All quantitative measures are derived from the primary-beam corrected interferometric HI maps that are corrected for the missing spacings.

4.4.1 Atomic IVC

The atomic IVC (aIVC) is located at (R.A., Dec.) = ($11^{\mathrm{h}}52^{\mathrm{m}}$, $20°30'$) with a radial velocity of $v_{\mathrm{LSR}} \simeq -35\,\mathrm{km\,s^{-1}}$. By position and velocity it can be associated with the Intermediate-Velocity (IV) Spur (Wakker 2004). The cloud has low FIR emission and is thought to be purely atomic on the basis of EBHIS and *Planck* (Röhser et al. 2014).

4.4.1.1 HI and FIR observations

The EBHIS only, WSRT only, combined single-dish and interferometric HI column density maps, and the *Planck* τ data are shown in Fig. 4.2. The column densities are calculated by summing over $-77.1\,\mathrm{km\,s^{-1}} \lesssim v_{\mathrm{LSR}} \lesssim -20.4\,\mathrm{km\,s^{-1}}$.

Both WSRT pointings disclose structures that are unresolved by the single dish. The peak column densities range up to $N_{\mathrm{HI}} \simeq 4.6 \times 10^{20}\,\mathrm{cm^{-2}}$ in the combined map. The column density contrast between the EBHIS and WSRT data is large: The peak column density in the primary-beam corrected WSRT data is $1.0 \times 10^{20}\,\mathrm{cm^{-2}}$, in the Effelsberg data $4.0 \times 10^{20}\,\mathrm{cm^{-2}}$. Similarly, about 16% of the total flux is recovered by the interferometer. Hence, most of the HI emission is not in the small-scale structure of the aIVC but smoothly distributed. These spatial scales are not probed by the WSRT data. In the combined HI data cube, the brightness temperatures range up to $T_{\mathrm{B}} \simeq 34\,\mathrm{K}$ with line widths as narrow as FWHM $\simeq 4\,\mathrm{km\,s^{-1}}$.

In the FIR, the aIVC is not as well defined as in the HI. However, the HI-τ correlation plot (Fig. 4.3, left) indicates that the same structures are traced. In the correlation plot, the black line is the IVC contribution to the linear two-component function (Eq. 4.2), which is fitted by the iterative method as described in Section 4.3. In Fig. 4.3, the LVC contribution to the total τ and the constant offset are subtracted, showing the IVC contribution only. About 15% of the data is rejected for the fit. The estimated linear parameters are listed in Table 4.2.

4.4.1.2 CO observations

At the location of the largest HI column densities, the aIVC is not detected in ^{12}CO(1→0) emission, even when the data is strongly spatially and spectrally smoothed. The 3σ detection limit in the smoothed data cube is ~0.02 K. Using the standard $X_{\mathrm{CO}} = 2 \times 10^{20}\,\mathrm{cm^{-2}}\,(\mathrm{K\,km\,s^{-1}})^{-1}$ (Bolatto et al. 2013), this corresponds to an upper limit of $N_{\mathrm{H_2}} \simeq 4.3 \times 10^{18}\,\mathrm{cm^{-2}}$. Hence, the aIVC is purely atomic with a possibly tiny fraction of H_2.

4.4.2 Molecular IVC

The molecular IVC (mIVC) is located at (R.A., Dec.) = ($10^{\mathrm{h}}52^{\mathrm{m}}$, $25°$) with a radial velocity of $v_{\mathrm{LSR}} \simeq -40\,\mathrm{km\,s^{-1}}$. By position and velocity, it is part of the IV Arch (Wakker 2004). As seen by EBHIS and *Planck*, the cloud shows bright FIR emission and a strong FIR excess which is indicative of H_2 (Röhser

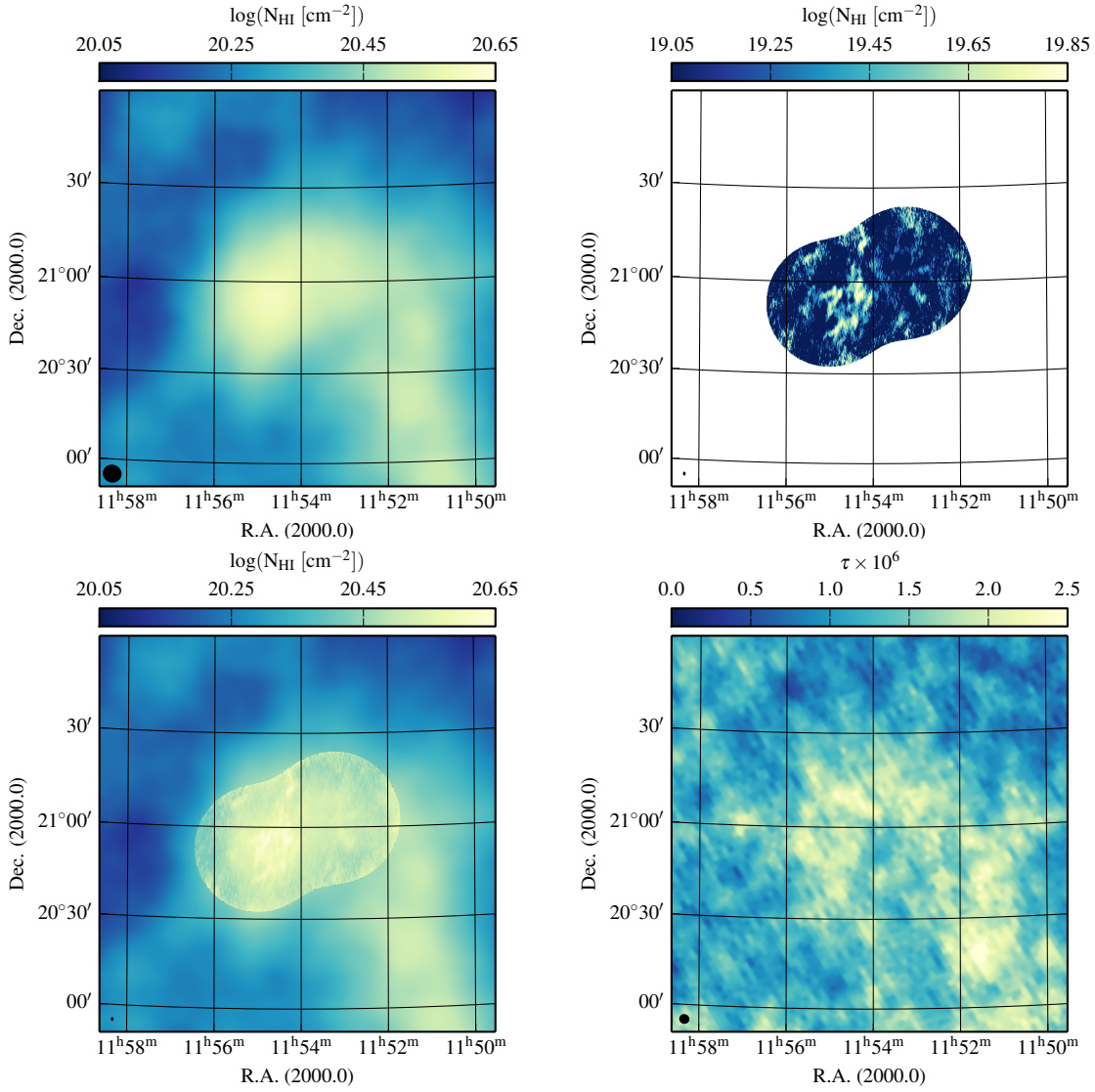

Fig. 4.2: HI column density maps of the aIVC for EBHIS only (*top-left*), WSRT only (*top-right*), and the combined single-dish and interferometric map (*bottom-left*). The column densities are calculated by summing over $-77.1\,\mathrm{km\,s^{-1}} \lesssim v_{\mathrm{LSR}} \lesssim -20.4\,\mathrm{km\,s^{-1}}$. At the bottom-right, the *Planck* τ data is shown. The colour-scaling is the same for the EBHIS-only and the combined map. The beam size of each map is given in the bottom-left corner.

et al. 2014). Pointed CO observations of Désert et al. (1990) detect the cloud and thus confirm its nature as a molecular cloud.

4.4.2.1 HI and FIR observations

The observed maps (EBHIS only, WSRT only, combined HI column density, *Planck* τ) are compiled in Figure 4.4. The column densities are calculated for channels with $-56.5\,\mathrm{km\,s^{-1}} \lesssim v_{\mathrm{LSR}} \lesssim -20.4\,\mathrm{km\,s^{-1}}$.

The peak HI column density in the combined map is $N_{\mathrm{HI}} \simeq 4.4 \times 10^{20}\,\mathrm{cm^{-2}}$. The peak column densities in EBHIS and WSRT are similar with $3.1 \times 10^{20}\,\mathrm{cm^{-2}}$ and $2.5 \times 10^{20}\,\mathrm{cm^{-2}}$. About 45% of the total flux is recovered by the interferometer. Hence, about half of the HI is located in the small-scale

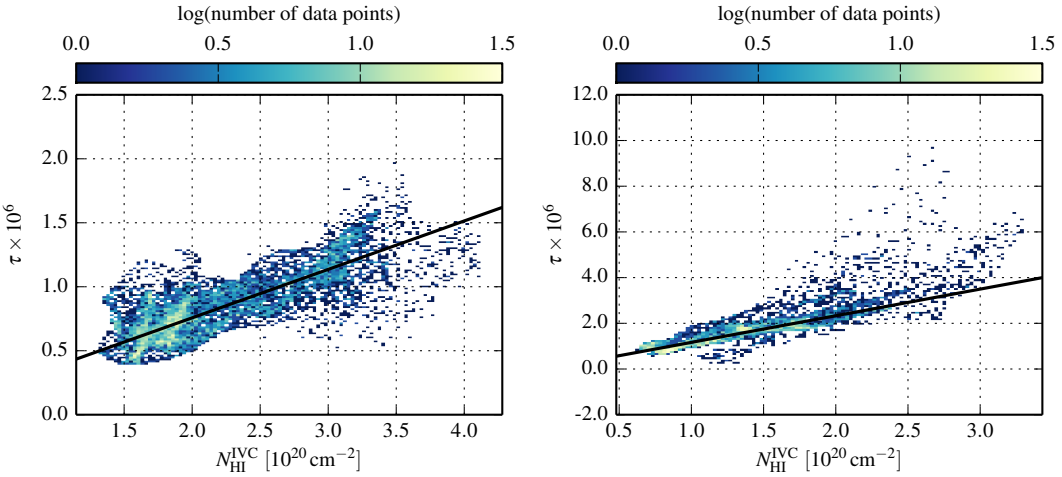

Fig. 4.3: HI-τ correlation plots for the aIVC (*left*) and mIVC (*right*). The LVC contribution to the total τ and the constant offset are subtracted, showing the IVC contribution only. The black lines mark the IVC component of the two-component linear model (Eq. 4.2) using the iterative fitting method (Section 4.3).

aIVC			mIVC		
$R\left[10^{-6}\right]$	$\epsilon^{\rm local}\left[10^{-26}\,{\rm cm}^2\right]$	$\epsilon^{\rm IVC}\left[10^{-26}\,{\rm cm}^2\right]$	$R\left[10^{-6}\right]$	$\epsilon^{\rm local}\left[10^{-26}\,{\rm cm}^2\right]$	$\epsilon^{\rm IVC}\left[10^{-26}\,{\rm cm}^2\right]$
0.13 ± 0.01	0.59 ± 0.01	0.38 ± 0.01	-0.95 ± 0.02	1.47 ± 0.03	1.17 ± 0.01

Table 4.2: Fitted linear parameters for the aIVC and mIVC. The values are derived by fitting the two-component model (Eq. 4.2) to the HI-τ correlation plots (Fig. 4.3) using the iterative method described in Sect. 4.3.

structure of the mIVC. In the combined HI data cube, the brightness temperatures range up to $T_{\rm B} \simeq 54$ K with line widths as narrow as FWHM $\simeq 3\,{\rm km\,s^{-1}}$.

In the high-resolution data, most HI is located at the eastern edge of the mIVC. However, in the combined map, most HI is located at the cloud centre towards the west. Thus, the HI appears to change its properties from being more clumpy to being more diffuse as seen from east to west.

The mIVC is prominent in the FIR with a double-peak structure that has been noted by Désert et al. (1990). From the combined HI map, however, it is evident that most of the HI is not found at the eastern edge, where the FIR maximum is, but at the western side of the WSRT pointing. This is an indication of FIR excess emission at the eastern side of the cloud.

The HI-τ correlation plot for the IVC component (Fig. 4.3, right) reveals strong FIR excess emission above IVC HI column densities of $N_{\rm HI}^{\rm IVC} \simeq 2 \times 10^{20}\,{\rm cm^{-2}}$. In Fig. 4.3, the black line marks the modelled τ of the IVC from the fitted linear two-component function (Eq. 4.2). The LVC contribution to the total τ and the constant offset are subtracted, showing the IVC contribution only. About 28% of the data points are rejected for the fit. The corresponding linear parameters are compiled in Table 4.2.

4.4.2.2 CO observations

As expected, the mIVC is detected in ^{12}CO(1→0) and ^{13}CO(1→0). The observed brightness temperatures range up to ∼7.3 K for ^{12}CO(1→0) and ∼1.5 K for ^{13}CO(1→0) with the FTS spectrometer.

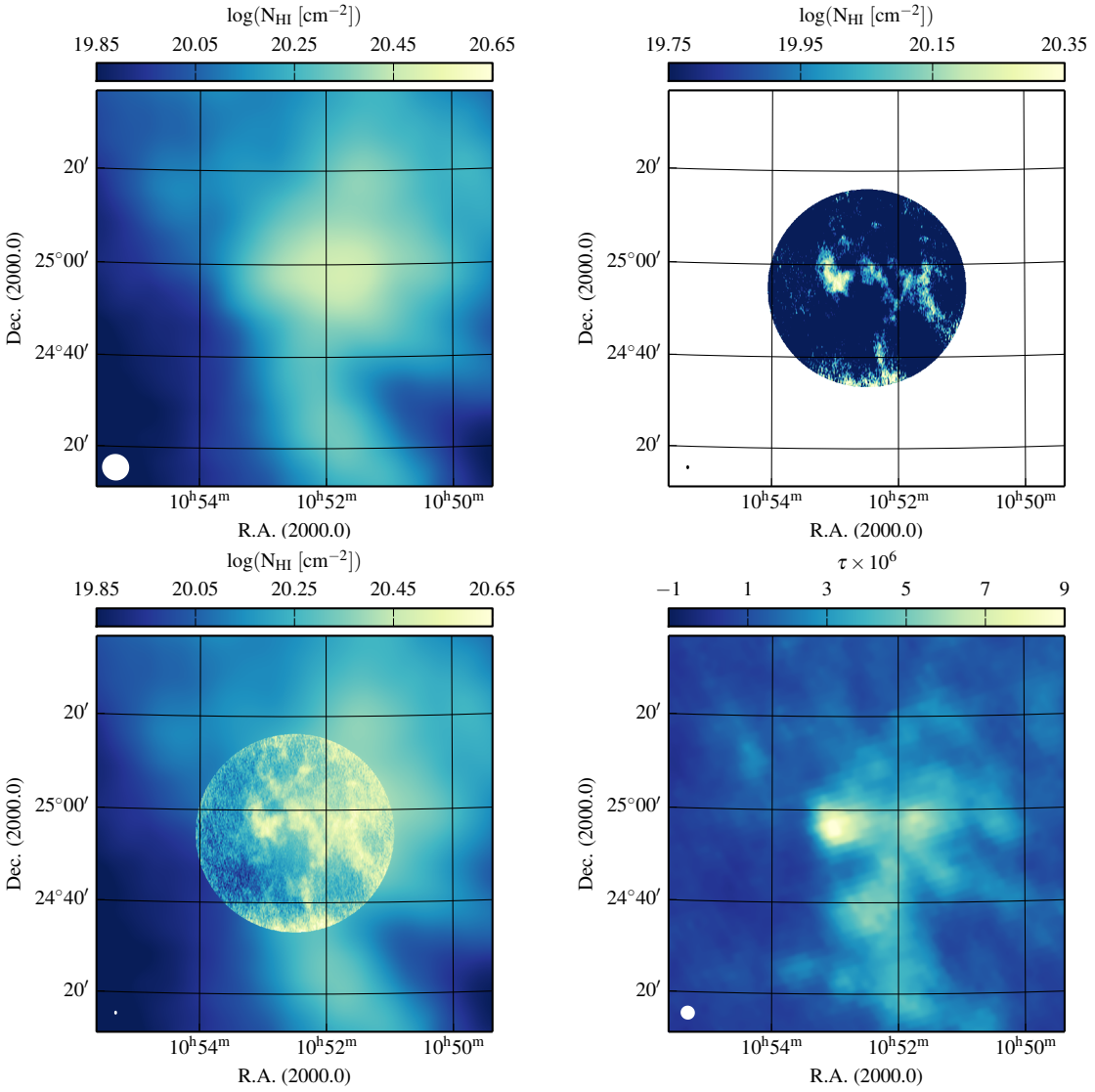

Fig. 4.4: HI column density maps of the mIVC for EBHIS only (*top-left*), WSRT only (*top-right*), and the combined single-dish and interferometric map (*bottom-left*). The column densities are calculated for channels with $-56.5\,\mathrm{km\,s^{-1}} \lesssim v_{\mathrm{LSR}} \lesssim -20.4\,\mathrm{km\,s^{-1}}$. At the bottom right, the *Planck* τ data is shown. The colour-scaling is the same for the EBHIS and the combined map. The beam size of each map is given in the bottom-left corner.

Moment maps of ^{12}CO(1→0) and ^{13}CO(1→0) integrated between $-45.8\,\mathrm{km\,s^{-1}} \lesssim v_{\mathrm{LSR}} \lesssim -33.1\,\mathrm{km\,s^{-1}}$ are shown in Fig. 4.5 overlayed with τ-contours from *Planck*. Note that the extent of the CO maps is smaller than the previously shown maps in Fig. 4.4.

In order to emphasise the CO emission that is spread over the mIVC, the data cubes are masked using a spatially and spectrally smoothed version of the data cube as a mask. The smoothed data is clipped at 5σ of its pixel-based noise map.

The CO distribution exhibits three different components (Fig. 4.5): Most of the ^{12}CO and ^{13}CO is found at the eastern edge where also the FIR peak is located. A second smaller ^{12}CO peak is detected near the second FIR peak to the west. In addition, multiple small CO clumps are spread across the entire mIVC, however, only detectable in ^{12}CO(1→0). Some clumps are observed close to the field

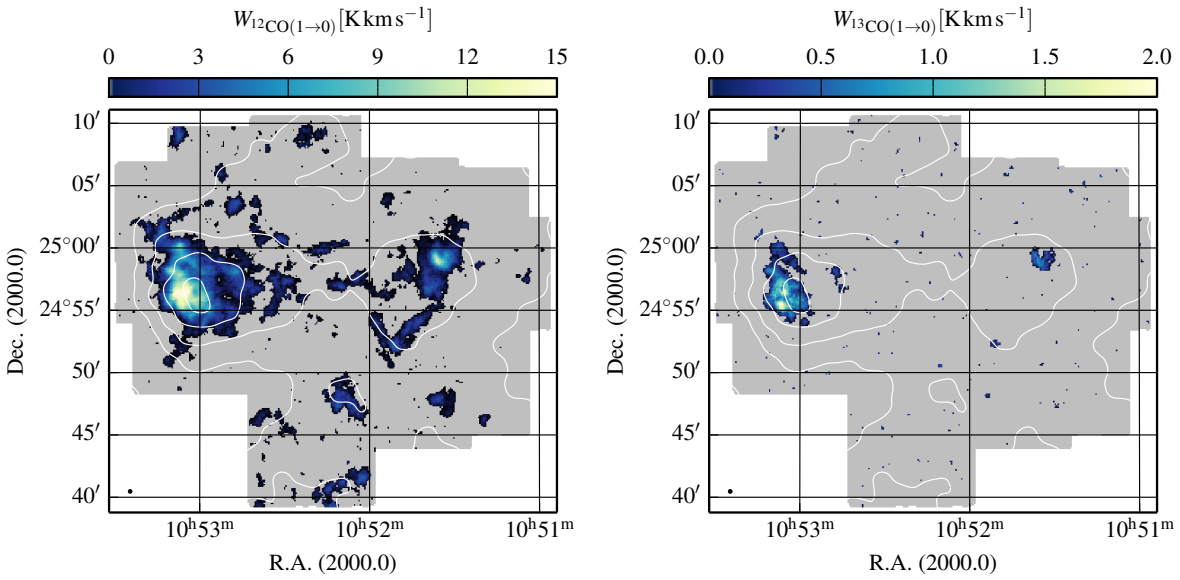

Fig. 4.5: Moment maps of the ^{12}CO(1→0) (*left*) and ^{13}CO(1→0) emission (*right*) of the mIVC integrated between $-45.8\,\mathrm{km\,s^{-1}} \lesssim v_{\mathrm{LSR}} \lesssim -33.1\,\mathrm{km\,s^{-1}}$. Before integration, the data cubes are masked using a spatially and spectrally smoothed version of the data cube as a mask. The contours mark the modelled τ from *Planck* from 1 to 9×10^{-6} in steps of 2×10^{-6}. The beam-sizes are plotted at the bottom left corner.

edges. Hence, the ^{12}CO is expected to be extended even beyond the measured fields. In ^{13}CO only the brightest ^{12}CO features are detected.

Generally, the ^{13}CO(1→0) lines are slightly broader with FTS than with VESPA. Hence, the ^{13}CO lines measured with FTS are likely narrower due to instrumental smearing.

The velocity structure of the ^{12}CO(1→0) emission is shown as a renzogram (e.g. Schiminovich et al. 1997) in Fig. 4.6. In the renzogram, for each channel of the masked data cube a contour at a fixed intensity is plotted. Here, we choose 0.5 K emphasising low-level emission. The colour of each contour corresponds to the radial velocity of the channel. Hence, a renzogram shows the structure of the emission as the shape of the contour and the velocity of the emission as the colour.

The renzogram reveals the complicated velocity structure of the mIVC. There is no coherent gradient across the mIVC. In some ^{12}CO clumps, the emission is shifted significantly even between neighbouring channels.

The bright CO peaks are spread over a large range of velocities. At the eastern edge, there is a CO structure between $-42\,\mathrm{km\,s^{-1}} \lesssim v_{\mathrm{LSR}} \lesssim -40\,\mathrm{km\,s^{-1}}$ that is elongated in north-south direction which is along the edge of the cloud towards a region of low N_{HI} at the eastern side of the cloud (Röhser et al. 2014). A second structure at lower absolute velocities is located on top that extends further to the west. These two components in the ^{12}CO emission have been identified already in the first observations of this cloud by Désert et al. (1990, their Fig. 1b).

Generally, there is a bimodal velocity structure within the mIVC. By summing up all the ^{12}CO(1→0) emission in each channel separately, the distribution of the emission shows two peaks, the larger one at $v_{\mathrm{LSR}} \simeq -38.8\,\mathrm{km\,s^{-1}}$ and the second smaller peak at $v_{\mathrm{LSR}} \simeq -41.5\,\mathrm{km\,s^{-1}}$ with a peak ratio of ∼0.6.

Many of the small molecular condensations show an elongation from bottom-left to top-right (Fig. 4.6). In addition, some molecular clumps appear to be located at similar separations to each other aligned on

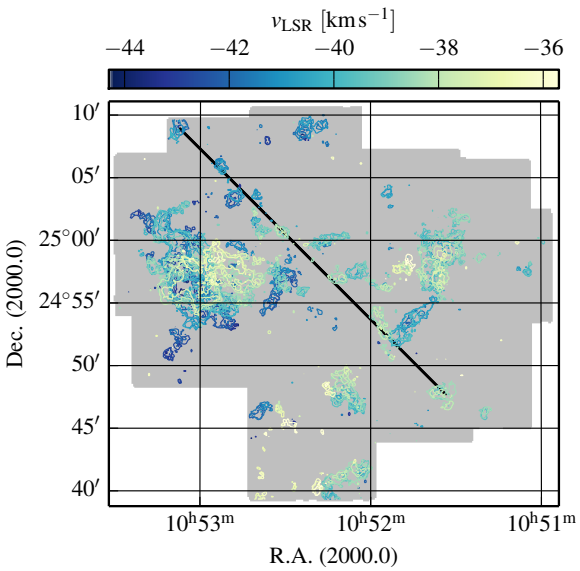

Fig. 4.6: Renzogram of ^{12}CO(1→0) emission of the mIVC. For each spectral channel of the masked data cube, a contour at an intensity value of 0.5 K is plotted. The colours of the contours encode the radial velocity of the channel. Along the black diagonal line, clumps of CO emission are arranged in an apparently regular spacing.

a straight line from the top-left to the bottom-right (the black line in Fig. 4.6). There is a typical angular separation of ∼6′ between these clumps, which corresponds to ∼0.7 pc for a distance of $D = 400$ pc (Röhser et al. 2014).

4.4.2.3 Deriving H_2 column densities

The FIR dust continuum emission traces the total hydrogen column density. As described in Section 4.3, the H_2 column densities depend on linear parameters of the HI-τ correlation by Eq. (4.3). In Table 4.2 we give the fitted linear parameters for the two IVCs which are used now to derive H_2 column densities. The resulting N_{H_2} distribution follows the FIR emission with a peak value of $N_{H_2} \simeq 2.8 \times 10^{20}$ cm^{-2}.

As a measure for the uncertainty of the derived N_{H_2}, we use the scatter of the residual FIR emission, e.g. the difference between the observed and modelled τ. This scatter reflects the intrinsic uncertainties of the HI-τ correlation. For all data points which are included in the fit, the scatter is $\Delta N_{H_2} \simeq 0.1 \times 10^{20}$ cm^{-2}.

4.4.2.4 The $X_{\rm CO}$-factor

We have independent measures of the ^{12}CO(1→0) emission and the spatial distribution of the H_2 within the mIVC. Now, we compare these quantities to infer the $X_{\rm CO}$ conversion factor and its variations across the cloud. For the comparison, the integrated ^{12}CO(1→0) emission $W_{^{12}{\rm CO}(1\rightarrow0)}$ is smoothed to the spatial resolution of the *Planck* τ data. This smoothed CO map is directly compared to the estimated H_2 column densities to derive

$$X_{\rm CO} = \frac{N_{H_2}}{W_{^{12}{\rm CO}(1\rightarrow0)}}. \tag{4.4}$$

Figure 4.7 shows the resulting $X_{\rm CO}$ distribution of the mIVC superimposed with the distribution of τ from *Planck* as contours. Due to the strong angular smoothing, we neglect all values for $X_{\rm CO}$ below $\tau = 4 \times 10^{-6}$. The values range between 0.6×10^{20} cm^{-2} (K km s^{-1})$^{-1}$ $\lesssim X_{\rm CO} \lesssim 20 \times 10^{20}$ cm^{-2} (K km s^{-1})$^{-1}$ spreading significantly around the canonical 2×10^{20} cm^{-2} (K km s^{-1})$^{-1}$ (Bolatto et al. 2013).

We derive a mean $X_{\rm CO}$ value by comparing the total N_{H_2} column density and the total ^{12}CO(1→0) flux over the mIVC. For the total fluxes, we use the masked ^{12}CO(1→0) map and all negative values in

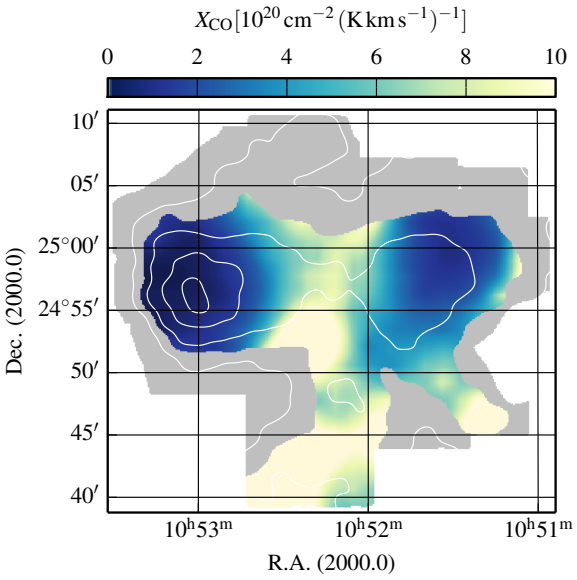

Fig. 4.7: Derived map of X_{CO} across the mIVC. The contours mark the modelled τ from *Planck* from 1 to 9×10^{-6} in steps of 2×10^{-6}. The X_{CO} map is clipped below $\tau = 4 \times 10^{-6}$. The values range between $0.6 \times 10^{20}\,cm^{-2}\,(K\,km\,s^{-1})^{-1} \lesssim X_{CO} \lesssim 20 \times 10^{20}\,cm^{-2}\,(K\,km\,s^{-1})^{-1}$.

the N_{H_2} map are blanked. This approach yields $\bar{X}_{CO} \simeq 2.3 \times 10^{20}\,cm^{-2}\,(K\,km\,s^{-1})^{-1}$ across the entire cloud. At the accuracy of this estimate, the inferred mean $\bar{X}_{CO}$ value over the entire mIVC is consistent with the canonical value of $X_{CO} \simeq 2 \times 10^{20}\,cm^{-2}\,(K\,km\,s^{-1})^{-1}$ for the Milky Way (Bolatto et al. 2013).

4.4.2.5 Excitation conditions of CO

We analyse the excitation conditions of CO by using the standard formulas as given by Pineda et al. (2008) that assume local thermal equilibrium (LTE). This allows us to estimate the excitation temperature T_{ex}, the optical depth $\tau_{^{13}CO}$, and the column density $N_{^{13}CO}$. ^{12}CO gets optically thick easily which does not allow a meaningful calculation of the same quantities for ^{12}CO.

The maps of T_{ex}, $\tau_{^{13}CO}$, $N_{^{13}CO}$, and $^{12}CO/^{13}CO$ are shown in Fig. 4.8. The excitation temperatures are $3.5\,K \lesssim T_{ex} \lesssim 10.5\,K$, significantly lower than the dust temperature from the modified modified blackbody fits with $T_d \gtrsim 18.8\,K$ (Planck Collaboration XI 2014). The derived optical depth are $\tau_{^{13}CO} \lesssim 0.3$ and the ^{13}CO column densities range up to $N_{^{13}CO} \lesssim 3.3 \times 10^{15}\,cm^{-2}$. The ratios $^{12}CO/^{13}CO$ are 4 – 20. Generally, these values are close to those of giant molecular clouds in the Milky Way (e.g. Pineda et al. 2008, 2010).

One particular feature at the eastern edge of the mIVC is unusually bright in ^{13}CO indicated by the largest optical depth and lowest intensity ratios. This may correspond to the largest CO column densities which are at the very edge of the CO distribution suggesting a very steep column density gradient.

4.4.2.6 Radiative transfer calculations

A detailed modelling of the radiative transfer within the mIVC is beyond the scope of this paper. In order to get an estimate on the kinetic temperature and density within the mIVC, we use the publicly available radiative transfer code RADEX (van der Tak et al. 2007) to approximate the observed and inferred parameters towards the brightest $^{13}CO(1\rightarrow0)$ emission. We use a grid of different input values for the kinetic temperature, the H_2 density, and the line width. The parameters that match the observed and inferred quantities best are $T_{kin} \simeq 52\,K$ and $n_{H_2} \simeq 440\,cm^{-3}$. The density is below that of the critical density of the line transition of $1 \times 10^3\,cm^{-3}$ (e.g. Snow & McCall 2006). Similarly, the inferred kinetic

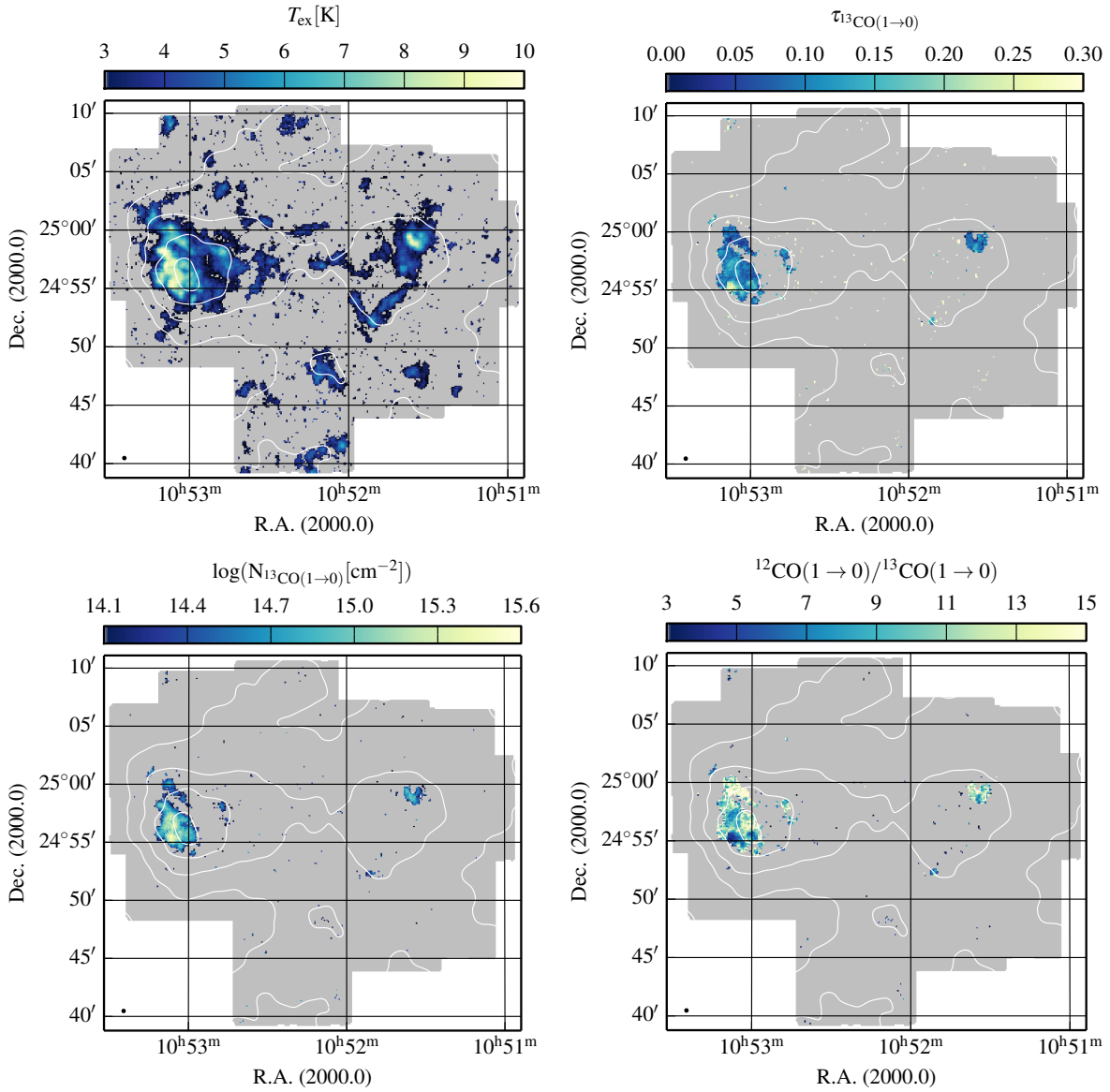

Fig. 4.8: Excitation conditions of CO within the mIVC. The plots show the excitation temperature T_{ex} (*top-left*), the optical depth $\tau_{^{13}CO}$ (*top-right*), the column density $N_{^{13}CO}$ (*bottom-left*), and the peak intensity ratios $^{12}CO/^{13}CO$ (*bottom-right*). The contours mark the modelled τ from *Planck* from 1 to 9×10^{-6} in steps of 2×10^{-6}. At the bottom left the beam size of the IRAM data is plotted.

temperature is much larger then the obtained excitation temperatures, indicating sub-thermal excitation conditions within the mIVC.

4.4.2.7 Comparing HI and CO

Here, we compare the distribution of HI and CO emission in the mIVC in more detail. For the comparison, the WSRT data is smoothed to a circular beam of 49.1″, the beam major axis, before the interferometric data is combined with the single dish data. The IRAM ^{12}CO data is smoothed to the same spatial resolution. In addition, the ^{12}CO data is re-gridded and smoothed in velocity to the spectral

resolution of the WSRT observations.

In order to illustrate the different HI and CO distribution across the mIVC, we plot in Fig. 4.9 a spatial slice through the integrated HI and ^{12}CO maps towards lower Right Ascension near the CO maximum at Dec. $\simeq 24^{\mathrm{d}}56^{\mathrm{m}}$. The fluxes are normalised to the maximum value in the slice. The integrated HI is given by the black dashed line, the integrated ^{12}CO(1→0) by the red solid line. The vertical lines indicate the positions of all HI emission peaks and the CO maximum. Figure 4.9 illustrates several things about the distribution of HI and CO:

- There is a significant spatial offset of ∼2′ between the HI and CO peaks at the eastern edge which corresponds to more than two beams of the smoothed data. The CO is located more towards the edge of the mIVC.
- The CO is embedded within the HI.
- Most of the HI is not located at the eastern edge where most of the CO is, but more to the west.
- Along the spatial slice, there is always a spatial offset between the HI maxima and corresponding CO peaks. Close to individual HI peaks a faint CO peak is found.

The spatial correspondence between HI and CO is indistinct, in general most CO peaks are off-set to nearby HI maxima. Under equilibrium conditions, it is thought that the spatial location of HI and CO peaks should coincide. When sufficient shielding is provided, the atomic hydrogen turns molecular in a sharp transition first, followed by the transition from ionised carbon to CO at larger densities (e.g. Snow & McCall 2006). Thus, there is a positionally tighter connection between H_2 and CO rather than between HI and CO.

4.4.3 The different structure of the atomic and molecular IVC

A quantitative measure of the structure of a cloud is the azimuthally averaged power spectral density (PSD). The PSD is calculated as the square of the modulus of the 2D Fourier transform of the integrated HI column density maps. By averaging the PSD in annuli around the centre, a radial profile is obtained.

In Fig. 4.10, we show the resulting PSDs for the combined single-dish and interferometric data of the aIVC and the mIVC. The black and red dashed lines are fits of power-laws to the PSD profiles up to the respective vertical dashed line at a spatial frequency of 1 (arcmin)$^{-1}$ for the aIVC and 0.5 (arcmin)$^{-1}$ for the mIVC. The fitted slopes are -3.02 ± 0.07 for the mIVC and -3.15 ± 0.03 for the aIVC indicating that the aIVC contains more power on smaller spatial frequencies (larger angular scales). These slopes are in good agreement with other studies (e.g. Burkhart et al. 2013; Roy 2015).

At the largest spatial scales (lowest spatial frequencies), both clouds are statistically identical, e.g. they have the same power at the same spatial scales. Towards smaller spatial scales (larger spatial frequencies), the PSDs decrease following a power-law down to the scale of ∼1 (arcmin)$^{-1}$. For larger spatial frequencies, there is an excess of power relative to the power-law in both PSDs. The excess is significantly stronger for the mIVC indicating more spatial substructure than in the aIVC.

The angular scale, at which the deviation of the fitted power law occurs, corresponds to a spatial scale of ∼0.1 pc for the distance of the clouds of ∼400 pc (Röhser et al. 2014).

Note that the total HI mass of the aIVC is larger than that of the mIVC at least by a factor of three (Röhser et al. 2014). There is more HI within the aIVC but it is not distributed such as to allow the formation of large amounts of molecular material. This again emphasises the different structural properties of the two clouds.

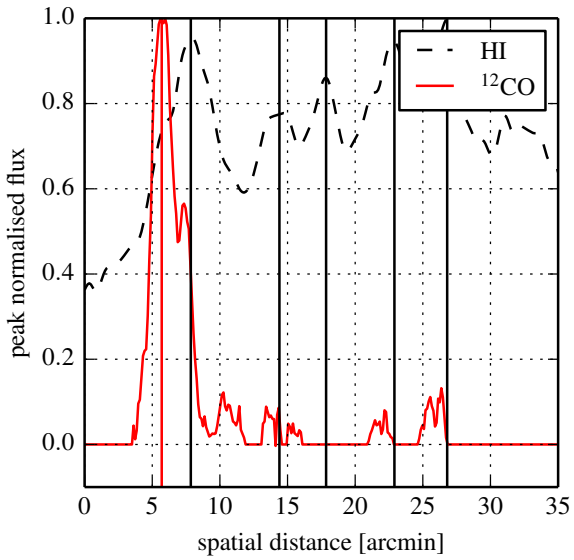

Fig. 4.9: Spatial cut through the integrated HI (black-dashed) and ^{12}CO(1→0) (red-solid) map. The integrated flux is normalised to the maximum flux along the cut. The cut is towards lower Right Ascension near the ^{12}CO peak at Dec. ≃ $24^{d}\,56^{m}$. The vertical black lines indicate the positions of local HI maxima, the vertical red line the location of the global CO peak.

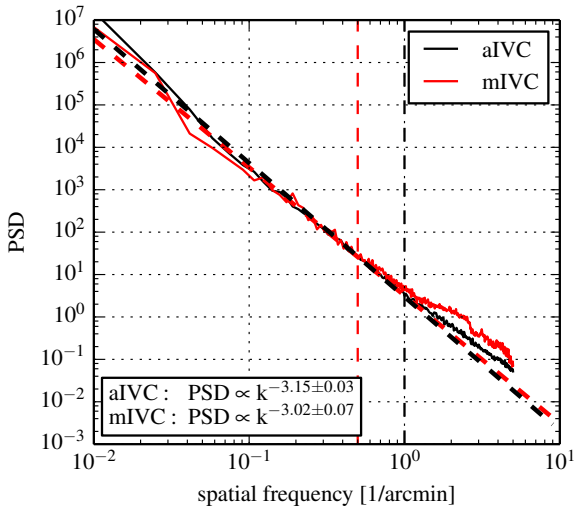

Fig. 4.10: Azimuthally averaged power spectral densities (PSDs) of the aIVC (black) and mIVC (red). The black and red dashed lines are fits of power laws to the PSDs up to a spatial frequency of 1 (arcmin)$^{-1}$ for the aIVC and 0.5 (arcmin)$^{-1}$ for the mIVC. At the bottom left the fitted power law exponents are given.

4.5 Discussion

The high-resolution HI and CO data reveal structural differences between the two IVCs that reflect the chemical state of the clouds. We briefly summarise the observational results from the high-resolution data, followed by the discussion.

4.5.1 The atomic IVC

The lack of ^{12}CO(1→0) emission in the atomic IVC (aIVC) (Section 4.4.1.2) suggests that the cloud is a pure atomic cloud with a negligible fraction of molecular gas, as is found by absorption spectroscopy studies towards many IVCs (e.g. Richter et al. 2003; Wakker 2006). From the spectrally and spatially smoothed ^{12}CO(1→0) data cube, we infer a 3σ detection limit of $N_{H_2} \simeq 4.3\times10^{18}$ cm^{-2} for the standard X_{CO}. Also the HI-FIR correlation does not reveal any considerable amounts of H_2 (Section 4.4.1.1).

The interferometer detects small-scale HI structure but its column density is low compared to the

single-dish measurements (Section 4.4.1.1). Most of the HI is distributed in a more diffuse way such that the interferometer does not detect it. However, there is cold HI with line widths as narrow as FWHM $\simeq 4\,\mathrm{km\,s^{-1}}$ in several clumps.

4.5.2 The molecular IVC

The extensive mapping of ^{12}CO(1→0) and ^{13}CO(1→0) reveals the rich molecular structure of the molecular IVC (mIVC): Most CO emission is found at the eastern edge of the cloud (Section 4.4.2.2). Furthermore, many smaller CO clumps are observed over the entire cloud and likely even beyond the mapped regions. Hence, the entire mIVC contains high-density regions throughout where H_2 and CO form, indicating a global condensation and compression.

In HI, high-column density peaks are resolved by the interferometer that are comparable to the column density seen by the single-dish (Section 4.4.2.1). The HI appears to change its properties across the mIVC from being more diffuse to being more clumpy, as viewed from west to east: In single-dish HI, the maximum is towards the west near the second lower FIR peak while in the interferometer the HI maximum is close to the eastern FIR peak (Section 4.4.2.1). This change of structure is represented similarly by the amount of CO, most of which is found at the eastern side of the cloud which is not where most of the HI is located. Hence, the molecular gas seems to condense from the atomic medium.

4.5.2.1 The X_{CO} factor

The quantitative comparison of H_2 column densities and ^{12}CO(1→0) emission results into conversion factors $0.6{\times}10^{20}\,\mathrm{cm^{-2}\,(K\,km\,s^{-1})^{-1}} \lesssim X_{\mathrm{CO}} \lesssim 20{\times}10^{20}\,\mathrm{cm^{-2}\,(K\,km\,s^{-1})^{-1}}$ (Section 4.4.2.4). Such variations of the conversion factor are expected since the canonical value of $X_{\mathrm{CO}} \simeq 2{\times}10^{20}\,\mathrm{cm^{-2}\,(K\,km\,s^{-1})^{-1}}$ emerges by averaging over different parts of the molecular clouds which either are overly CO-bright or not detected (Liszt et al. 2010; Liszt & Pety 2012; Bolatto et al. 2013).

We infer a mean conversion factor of $\bar{X}_{\mathrm{CO}} \simeq 2.3 \times 10^{20}\,\mathrm{cm^{-2}\,(K\,km\,s^{-1})^{-1}}$ over the entire mIVC. The lowest conversion factors are found at the locations of the CO peaks. Thus, CO-dark H_2 gas (Grenier et al. 2005; Wolfire et al. 2010; Planck Collaboration XIX 2011) is found mostly in regions of low CO abundances where X_{CO} is strongly enhanced. Generally, for a diffuse object like the mIVC, significant amounts of CO-dark gas are expected to be present that affect the inferred X_{CO} factors.

Studies of high-latitude MIVCs have in common that the authors attribute bright CO emission and large molecular abundances in general to dynamical phenomena in the Galactic halo (e.g. Herbstmeier et al. 1993, 1994; Moritz et al. 1998; Weiß et al. 1999; Lenz et al. 2015). However, according to Herbstmeier et al. (1994) for the Draco molecular cloud, the excitation conditions of CO, e.g. line ratios, are similar to other molecular clouds. They propose that either the CO abundances are unusual large or that CO is more efficiently excited.

4.5.2.2 Excitation conditions of CO

For the mIVC, we obtain similar values for the excitation temperature T_{ex}, optical depth for $\tau_{^{13}\mathrm{CO}(1\to0)}$, and ^{13}CO column density $N_{^{13}\mathrm{CO}}$ as, e.g., Pineda et al. (2008, 2010). For Perseus, Pineda et al. (2008) find that about 60% of the ^{12}CO(1→0) emission is sub-thermally excited corresponding to densities below $1 \times 10^3\,\mathrm{cm^{-3}}$ (e.g. Snow & McCall 2006). Sub-thermal excitation may be also very important for the mIVC since the RADEX grid calculations reproduce the observed peak ^{13}CO(1→0) emission best for $T_{\mathrm{kin}} \simeq 45\,\mathrm{K}$ and $n_{\mathrm{H_2}} \simeq 440\,\mathrm{cm^{-3}}$ (Section 4.4.2.6) which is significantly below the critical density of ^{12}CO(1→0).

According to Liszt et al. (2010), the specific brightness W_{CO}/N_{CO} is larger in warm and sub-thermally excited gas. Such environments correspond to kinetic temperatures that are much larger than the CO(1→0) excitation temperature which is in agreement with what we find. Generally, CO chemistry is more sensitive to the environmental conditions than H_2 is (e.g. Liszt & Pety 2012). For some of their lines-of-sight, Liszt & Pety (2012) describe strongly over-pressured molecular clumps which are likely transient.

4.5.2.3 Evidence for non-equilibrium conditions

There are observational indications that the formation of H_2 and CO in the mIVC does not occur in formation-dissociation equilibrium:

- There are spatial offsets between all the different data sets of observed emission, for the single-dish and interferometric HI, FIR and CO (Figs. 4.4,4.9). Also the spectral distribution of the HI and CO emission is different.
- The brightest CO emission is found at the edge of the integrated CO emission map, located eastwards of the nearby HI maximum close to the cloud's rim (Fig. 4.9). The ^{12}CO(1→0)/^{13}CO(1→0) ratios are lowest at one particular spot at the eastern side (Fig. 4.8) probably linked to the largest molecular abundances and column density contrasts.
- In general, the spectral and spatial properties of the mIVC are complicated. We observe several velocity components in both HI and CO and a rich clumpy structure (Figs. 4.4, 4.6). In ^{12}CO(1→0), there is a bimodal velocity distribution across the cloud but no coherent velocity gradient.
- The observed radial velocity of the mIVC is $\sim -40\,\mathrm{km\,s^{-1}}$ moving through a thin halo medium. This situation in itself may be unstable and subject to instabilities.
- There are several isolated CO clumps arranged like beads on a string with a characteristic distance (Fig. 4.6). The typical angular separation of $\sim 6'$ between these clumps corresponds to $\sim 0.7\,\mathrm{pc}$ for a distance of $\sim 400\,\mathrm{pc}$ (Röhser et al. 2014). If this arrangement is not just a coincidence, this regular spacing is evidence for the action of dynamical instabilities like Kevin-Helmholtz or Rayleigh-Taylor instabilities which occur when relative motions between fluids break up the interface region, creating structures at characteristic distances (e.g. Breitschwerdt et al. 2000; Berné et al. 2010).

A formation-dissociation equilibrium is justified only if all chemical timescales are shorter than the dynamical timescale of the system (Glover & Mac Low 2011). Röhser et al. (2014) estimate that the formation of H_2 in the mIVC should happen faster than $\sim 6\,\mathrm{Myr}$. However, the equilibrium formation timescale of H_2 is $10^9\,\mathrm{yr}/n\,[\mathrm{cm^{-3}}]$ (Hollenbach et al. 1971) which is $\sim 10^7$ yr for the typical density of the mIVC.

4.5.2.4 Is the mIVC able to form stars?

All known star-forming high-latitude clouds are not classified as IVCs (McGehee 2008). Thus, it would be surprising to find evidences of star formation in the mIVC. Within the innermost part of the mIVC that we measured with IRAM, the total combined HI and H_2 mass is about $M_H \simeq 37\,M_\odot$. This mass is low compared to other star-forming high-latitude clouds, like for instance MBM 12 with $\sim 500\,M_\odot$ (Pound et al. 1990), corrected for the revised distance from Luhman (2001), or MBM 20 with $\sim 50\,M_\odot$

(Liljestrom 1991) within the regions where ^{13}CO(1→0) is detected, correcting for the distance of Hearty et al. (2000). However, the mIVC is connected to more extended HI structures that contain significantly more mass (Röhser et al. 2014).

Using the virial parameter (Bertoldi & McKee 1992)

$$\alpha_{\rm vir} = \frac{M_{\rm vir}}{M} = \frac{5\sigma^2 R}{GM} \simeq 1.2 \left(\frac{\sigma_{\rm v}}{\rm km\,s^{-1}}\right)^2 \left(\frac{R}{\rm pc}\right) \left(\frac{M}{10^3\,{\rm M}_\odot}\right)^{-1}, \tag{4.5}$$

we estimate the importance of self-gravity for the individual clumps. For clumps with $\alpha_{\rm vir} >> 1$ gravity is unimportant, while for $\alpha_{\rm vir} \simeq 1$ the gravitational energy is comparable to the kinetic energy. We calculate the size of every clump by summing over the number of its individual pixels and converting it to the radius of a sphere with the same angular size. Using the estimated radius and gas mass for a typical line-width of CO of $\Delta v \simeq 1\,{\rm km\,s^{-1}}$, the typical virial parameters are $\alpha_{\rm vir} \simeq 106$ with a minimum value of ∼6. Hence, the combined atomic and molecular gas within the spatial regions of the CO clumps is unlikely to be gravitationally bound.

The result is similar when we consider the cloud globally. For the entire region covered with IRAM we get $\alpha_{\rm virial} \simeq 6$. Thus, also globally the cloud seems to be gravitationally unbound. The mIVC appears not to form stars which is expected because the densities and masses are not sufficiently large to form gravitationally bound structures. This is similar to the physical conditions within the Draco cloud in which gravity appears to be unimportant as well (McGehee 2008).

4.5.3 The formation of molecular clouds

Turbulence is thought to be important for the formation of molecular clouds and for subsequent star formation (Mac Low & Klessen 2004). Simulations of turbulent colliding flows of initially warm neutral medium (WNM) show the formation of non-linear density perturbations that lead to gaseous structures of cold neutral medium (CNM) due to dynamical and thermal instabilities (e.g. Audit & Hennebelle 2005; Heitsch et al. 2005; Glover & Mac Low 2007). The H_2 formation is rapid with timescales of ∼1 Myr or less.

The main limiting factor for H_2 formation is the time-dependent column density distribution which continuously re-exposes the molecular material to the radiation field (Heitsch et al. 2006). In their Fig. 7, Glover & Mac Low (2007) show that the chemical abundances are not in equilibrium indicating that molecular cores are likely transient features (Vázquez-Semadeni et al. 2005).

Audit & Hennebelle (2005) estimate the typical scale of expected CNM structures from the cooling length and the density contrast between WNM and CNM yielding CNM structures of ∼0.1 pc in size, which is confirmed by their simulations. Observationally, Arzoumanian et al. (2011) report an universal width of interstellar filaments of 0.10 ± 0.03 pc in molecular clouds over a wide range of column densities. They argue that this length scale may be set by the dissipation of large-scale turbulence down to the subsonic regime in the diffuse gas.

This particular length scale is similar to the spatial scale of the PSDs of both aIVC and mIVC for which both deviate statistically (Section 4.4.3). However, at the spatial scales probed by our HI data, there is no evidence for the dissipation of turbulent energy, which would cause a decrease of density structures and a corresponding drop in power of the PSD. Instead, there is an excess relative to the power-law. Hence, the identified structures appear to be related to the cooling and pressure equilibrium in the atomic medium.

High-latitude clouds and MIVCs may be thought of as flows of warm and cold gas through the surrounding halo medium. Thus, it is just a consequent step to assume that, given time, such objects

develop cold small-scale structures in which molecular hydrogen can form. The bimodal velocity distribution within the mIVC can be thought of as an imprint of flows of different gas components. The action of dynamical instabilities may be visible even from the distribution of the CO emission directly as a particular regular feature (Section 4.4.2.2).

The motion of halo clouds through the ambient medium creates ram pressure. In the mIVC, most of the small-scale structure and most H_2 and CO are found at the eastern side of the cloud where a sharp column density contrast at the cloud's rim is evident. We propose that the cloud moves in this direction and the largest molecular abundances are located at the leading front of the cloud. Hence, ram pressure appears to accumulate gas and facilitate the formation of small-scale structures and molecules. Note that the unknown tangential velocity of the cloud is likely substantial if the IVC originates from a Galactic fountain process (e.g. Melioli et al. 2008).

For typical densities of the WNM, Saury et al. (2014) find similarly that turbulent motions of the neutral gas alone do not cause the transition from WNM to CNM. Instead, an increase of the WNM density is required in the first place to trigger the rapid formation of CNM structures out of the WNM by turbulence. Thus for the aIVC and mIVC, ram pressure appears to be responsible for pressurising the WNM, pushing the gas to the thermally unstable regime from which the CNM is formed.

The general conditions are identical in both the aIVC and mIVC: The observed radial velocity is the same, there is cold gas with FWHM $\simeq 4\,\mathrm{km\,s^{-1}}$, the total HI mass is even larger for the aIVC and substructure has evolved. Thus, we give the same conclusion as Röhser et al. (2014) that the aIVC should evolve into a similar molecular IVC as the mIVC. This transition can occur rapidly, possibly within 1 Myr (Saury et al. 2014).

In simulations of the turbulent ISM, no particular triggering mechanism is required but gradually structures emerge. This is in contrast to possible interactions between IVCs and other halo clouds as the reason for the formation of molecules (Herbstmeier et al. 1993; Weiß et al. 1999; Lenz et al. 2015).

4.6 Summary

We present high-resolution HI and CO observations of two high-latitude intermediate-velocity clouds (IVCs). They are studied in the context of the transition from atomic to molecular clouds at the disk-halo interface. Our analysis elaborates on Röhser et al. (2014) who compared the two IVCs by using the most recent large-scale surveys in HI and the FIR, EBHIS and *Planck*.

New high-resolution data from the WSRT and the IRAM 30 m telescope clearly reveals differences between the gaseous structure of the clouds that Röhser et al. (2014) speculate on. The molecular IVC (mIVC) exhibits a pronounced substructure consisting of many clumps in HI and CO. The interferometer recovers ~45% of the total HI flux. The high column densities provide shielding, while the high densities accelerate the formation of molecules like H_2 and CO. Over those parts that are measured with IRAM, CO emission is detected indicating that the whole cloud is condensed to allow locally the formation of CO.

This is in contrast to the small-scale structures found in the atomic IVC (aIVC). The interferometric observations reveal also substructure. However, only ~16% of the single-dish flux is recovered by the interferometer, suggesting much less HI is located in clumps but more in a diffuse and smooth distribution. Consequently, no CO emission is detected near the largest HI column densities of the aIVC. Hence, the structural differences between the aIVC and mIVC reflect their different chemical states.

Using the dust optical depth from *Planck*, we infer the column densities of molecular hydrogen within the mIVC. The X_{CO} conversion factor varies significantly over the cloud with an average $\bar{X}_{\mathrm{CO}} \simeq 2.3 \times$

$10^{20}\,\mathrm{cm}^{-2}\,(\mathrm{K\,km\,s}^{-1})^{-1}$ close to the canonical value for the Milky Way. The lowest X_{CO} are found at the FIR peaks increasing outwards. Thus, most of the CO-dark H_2 gas is found in regions of low CO abundances.

The formation of molecular clouds is discussed in the context of simulations of colliding flows of neutral gas in the turbulent ISM (e.g. Audit & Hennebelle 2005; Heitsch et al. 2005; Glover & Mac Low 2007; Saury et al. 2014). These simulations show that quickly a pronounced substructure is established in which the H_2 formation is rapid within $1-2$ Myr. In this picture, the transition from atomic to molecular IVCs is a natural evolutionary step due to flows of different gaseous components. This reasoning is similar to Röhser et al. (2014) who consider the ram pressure due to the motion of the cloud as a driving agent for the accumulation and condensation of the halo cloud. For the mIVC, ram pressure appears to facilitate the formation of large amounts of molecular material at the hypothetical leading front of the cloud where most of the CO emission originates from.

A thorough study of similarities and differences between all high-latitude molecular and non-molecular IVCs would shed more light on a possible triggering mechanism and the requirements for the formation of such objects. It would give important insights into the Galactic fountain cycle, the fate of infalling material and into the evolution of the Milky Way as a whole.

Acknowledgements

The authors acknowledge valuable help of S. Faridani in the combination of single-dish and interferometric data, J. L. Pineda and P. Schilke for their help in preparing the observations. We are especially thankful to J. L. Pineda who provided additional unpublished data. The authors are grateful for the support by the IRAM staff during the observations and for the data reduction. The authors thank the Deutsche Forschungsgemeinschaft (DFG) for financial support under the research grant KE757/11-1. The work is based on observations with the 100 m telescope of the MPIfR (Max-Planck-Institut für Radioastronomie) at Effelsberg. The *Planck* satellite is operated by the European Space Agency. The development of *Planck* has been supported by: ESA; CNES and CNRS/INSU-IN2P3-INP (France); ASI, CNR, and INAF (Italy); NASA and DoE (USA); STFC and UKSA (UK); CSIC, MICINN and JA (Spain); Tekes, AoF and CSC (Finland); DLR and MPG (Germany); CSA (Canada); DTU Space (Denmark); SER/SSO (Switzerland); RCN (Norway); SFI (Ireland); FCT/MCTES (Portugal); and PRACE (EU). Some figures have been prepared with the Kapteyn package (Terlouw & Vogelaar 2015). T. R. is a member of the International Max Planck Research School (IMPRS) for Astronomy and Astrophysics at the Universities of Bonn and Cologne as well as of the Bonn-Cologne Graduate School of Physics and Astronomy (BCGS).

CHAPTER 5

A global view of the FIR properties of intermediate-velocity clouds

In this Chapter, we analyse the global FIR properties of intermediate-velocity clouds (IVCs) in light of the new all-sky HI and FIR data. We search for molecular and atomic IVCs over the entire sky. The study is restricted to Galactic latitudes of $|b| > 20^\circ$ because of two reasons: On the one hand the separation between halo and disk gets more and more unclear closer to the Galactic disk. On the other hand the number of individual clouds of gas and dust increases towards lower latitudes making it difficult to separate the dust emission into different components.

We subdivide our analysis between the northern and southern Galactic hemispheres allowing for different correlation parameters for the two hemispheres. Other studies (e.g. Désert et al. 1988; Reach et al. 1998) correlate the HI and FIR data in individual fields with sizes of a few degrees, studying variations on even smaller scales. On the southern hemisphere the Magellanic System (e.g. Nidever et al. 2010) causes potential complications in the analysis of the HI-FIR correlation because of the large amount of low-metallicity material also within the low-velocity cloud (LVC) and IVC regimes, requiring special treatment.

In Sect. 5.1 we present the data that is used here. Next, the search criteria for atomic and molecular IVCs as FIR-deficient and FIR-excess clouds are discussed in Sect. 5.2, where also a control or reference sample is defined with FIR emission that is compatible with the intrinsic scatter of the HI-τ correlation. Section 5.3 completes the discussion of the general methodology and how individual MIVC candidates are verified or falsified.

Then in Sect. 5.4, we begin with the global HI-FIR correlation on the northern Galactic hemisphere, including the search for the individual cloud types and their statistical analysis. Furthermore, the kinematical properties of the samples are analysed and put in the context of the Galactic fountain process. A very similar analysis of the southern Galactic hemisphere is conducted in Sect. 5.5. In Sect. 5.6 the different occurrences of the IVC sample clouds on the two hemispheres are discussed, followed by the estimation of various IVC properties in Sects. 5.7-5.9. We conclude in Sect. 5.10. Our main focus is on the identification of potential MIVCs and on the derivation of general properties of the MIVC candidates within the context of the Galactic fountain model.

5.1 Data sets

We calculate HI column density FITS maps of the combined GASS and EBHIS data (see Sects. 2.1 and 2.2 for details) in zenith-equal area projection (Calabretta & Greisen 2002) centred on the northern and southern Galactic pole. In this view, the Galactic north and south poles are located in the middle

surrounded by circles of constant Galactic latitudes. This projection allows a good visualisation of structures at high Galactic latitudes.

In order to get a uniform HI data set, we smooth the HI column density map from EBHIS to the angular resolution of GASS by the convolution with a Gaussian kernel. Note that due to the gridding of the GASS data, the effective angular resolution is degraded to FWHM $\simeq 16.2'$. EBHIS and GASS have an overlap at Declinations of $-5^\circ \leq \delta \leq 1^\circ$ (e.g. Winkel et al. 2016). In these regions the HI column densities from both surveys are averaged.

We separate the HI emission into different components by the radial velocity:

- Low-velocity clouds (LVCs): $-20\,\mathrm{km\,s^{-1}} \leq v_{\mathrm{LSR}} \leq +20\,\mathrm{km\,s^{-1}}$
- Negative intermediate-velocity clouds (IVCs$^-$): $-100\,\mathrm{km\,s^{-1}} \leq v_{\mathrm{LSR}} \leq -20\,\mathrm{km\,s^{-1}}$
- Positive intermediate-velocity clouds (IVCs$^+$): $+20\,\mathrm{km\,s^{-1}} \leq v_{\mathrm{LSR}} \leq +100\,\mathrm{km\,s^{-1}}$
- Total high-velocity clouds (HVCs): $100\,\mathrm{km\,s^{-1}} \leq |v_{\mathrm{LSR}}| \leq 450\,\mathrm{km\,s^{-1}}$.

Loosely, LVCs are thought to be part of the Galactic disk, while IVCs are located in the disk-halo interface region and HVCs within the Galactic halo. At high Galactic latitudes of $|b| \geq 20^\circ$, simple LSR velocity cuts are a valid assumption, since the observed radial velocities of the gas are the projection of the total velocity vectors onto the lines-of-sight, by which any rotational velocity component is decreased. This is why we do not apply, e.g., the deviation velocity (Wakker 1991), which accounts for the position-dependent rotational velocity of our Galaxy using a simple model of Galactic rotation.

We restrict the HI column densities to radial velocities of $|v_{\mathrm{LSR}}| \leq 100\,\mathrm{km\,s^{-1}}$, although there is significant HI emission also at larger absolute radial velocities. This HVC material is not considered in the HI-FIR correlation because to date there is no direct detection of FIR emission from HVCs (Wakker & Boulanger 1986; Peek et al. 2009; Planck Collaboration XXIV 2011; Williams et al. 2012) and the amount of H_2 within HVCs is thought to be low or negligible (Richter et al. 2001b) because of the low densities and metallicities. Nevertheless, there could be HVC-like HI gas with lower absolute radial velocities within the IVC regime. Such material would enter the HI-FIR correlation allowing in principle its identification (Peek et al. 2009).

For the dust emission, we use the all-sky dust model from Planck Collaboration XI (2014) who fit modified black-body spectra to the dust FIR spectrum at 353, 545, 857, and 3000 GHz. The intensity of the modelled emission is given by the dust optical depth at 353 GHz τ_{353}, to which we refer to as τ. The all-sky HEALPix map (Górski et al. 2005) of the estimated dust optical depths is smoothed to the angular resolution of GASS and gridded to the same FITS maps.

We use the dust optical depth as the measure for the dust emission because τ combines information from four different frequency bands in the FIR. Hence, variations of the emissivity in individual FIR bands are not expected to affect the optical depths significantly.

5.2 Search criteria

The global HI-τ correlation on either the northern or southern Galactic hemisphere is used as a reference dust-to-gas ratio of LVCs and IVCs. Relative to this average deviating objects are defined. The residual τ is converted fully into a corresponding H_2 column density of IVCs using the estimated linear parameters.

On global scales, the HI-τ correlation represents the superposition of very different gaseous structures with varying FIR emission properties, e.g., FIR-dim IVC gas or bright star-forming regions.

A two-component linear fit is applied to the HI-τ correlation data for either the northern and southern Galactic hemispheres, dividing the HI column densities into LVC gas with $-20\,\mathrm{km\,s^{-1}} \leq v_{\mathrm{LSR}} \leq$

$+20\,\mathrm{km\,s^{-1}}$ and total IVC gas with $20\,\mathrm{km\,s^{-1}} \leq |v_{\mathrm{LSR}}| \leq 100\,\mathrm{km\,s^{-1}}$. As an additional approximation, the IVCs$^{\pm}$ are given the same dust emissivity. The iterative fitting method is applied in linear space as described in Chapter 4 in addition to a fixed upper HI column density threshold of $N_{\mathrm{HI}} = 4 \times 10^{20}\,\mathrm{cm^{-2}}$ for the LVC and IVC HI column densities, respectively. The fitted parameters describe the linear part of the HI-τ correlation, which is dominated by atomic hydrogen. Objects with large amounts of H_2 deviate significantly from the mean HI-τ correlation and are excluded consequently from the fit. In addition, the point-source mask from Planck derived at 857 GHz (Planck Collaboration XXVI 2015) is applied.

From the derived linear parameters the corresponding H_2 column densities within IVCs are calculated across the northern or southern Galactic hemisphere as is introduced in Chapter 4:

$$N_{\mathrm{H_2}}^{\mathrm{IVC}} \simeq \frac{1}{2}\left(\frac{\tau - \left(R + \epsilon^{\mathrm{LVC}} \times N_{\mathrm{HI}}^{\mathrm{LVC}}\right)}{\epsilon^{\mathrm{IVC}}} - N_{\mathrm{HI}}^{\mathrm{IVC}}\right). \tag{5.1}$$

Such an H_2 map reflects the residual FIR emission of the fit (e.g. compare with Fig. 2 of Chapter 3), revealing individual objects either as FIR dim or bright structures relative to the surroundings, corresponding to negative or positive $N_{\mathrm{H_2}}$, respectively. Negative H_2 column densities are unphysical and due to an over-prediction of the FIR emission by the model. We use these negative column densities as a measure of FIR deficiency.

This approach assigns the entire deviation from the linear HI-τ correlation into H_2 column densities of IVCs. In regions with FIR excess emission in the LVC gas, this is not valid since the dust emissivities in IVCs are generally smaller than for the LVCs (Table 5.1 or e.g. Planck Collaboration XXIV 2011). Thus, the derived H_2 column densities are over-estimated. A separation of FIR excess emission cannot easily be done.

In order to identify the different types of IVCs, we define search criteria for molecular IVCs (MIVCs), atomic IVCs (AIVCs), and the control sample or normal IVCs (NIVCs) in the next three subsections. These criteria are applied to the entire northern or southern Galactic hemisphere.

5.2.1 Molecular IVCs

A candidate for a molecular IVC (MIVC) is characterised observationally by the spatial coincidence of four different measures:

1. Only when a sufficient amount of gas is piled up, the densities and the shielding get large enough to allow the existence of large amounts of H_2. Various studies find different thresholds for the HI-H_2 transition ranging from $N_{\mathrm{HI}} = 1 - 5 \times 10^{20}\,\mathrm{cm^{-2}}$ (e.g. Savage et al. 1977; Reach et al. 1994; Lagache et al. 1998; Gillmon et al. 2006; Gillmon & Shull 2006; Planck Collaboration XXIV 2011; Röhser et al. 2014; Lenz et al. 2015). In order to find as many plausible objects as possible, we take the weakest criterion of $N_{\mathrm{HI}}^{\mathrm{IVC}} = 1 \times 10^{20}\,\mathrm{cm^{-2}}$. Such a threshold depends also on the angular resolution of the data.

2. The significance of the globally derived H_2 column densities is given by the intrinsic scatter of the HI-τ correlation assuming that no systematic bias exists. For all pixels that have a total HI column density $N_{\mathrm{HI}} < 1 \times 10^{20}\,\mathrm{cm^{-2}}$ within $-100\,\mathrm{km\,s^{-1}} \leq v_{\mathrm{LSR}} \leq +100\,\mathrm{km\,s^{-1}}$, we calculate the median and standard deviation of the derived H_2 column densities. Below $N_{\mathrm{HI}} = 1 \times 10^{20}\,\mathrm{cm^{-2}}$, empirically, no significant amounts of H_2 are expected (e.g. Planck Collaboration XXIV 2011). On the northern Galactic hemisphere we estimate a median of $\tilde{N}_{\mathrm{H_2}} \simeq 0.05 \times 10^{20}\,\mathrm{cm^{-2}}$ and a standard deviation of $\sigma(N_{\mathrm{H_2}}) \simeq 0.20 \times 10^{20}\,\mathrm{cm^{-2}}$, for the southern hemisphere $\tilde{N}_{\mathrm{H_2}} \simeq 0.13 \times 10^{20}\,\mathrm{cm^{-2}}$ and $\sigma(N_{\mathrm{H_2}}) \simeq 0.15 \times 10^{20}\,\mathrm{cm^{-2}}$. These values show that any systematic offset in the derived

H_2 column densities is smaller than the intrinsic scatter of the HI-τ correlation. Note that these statistics are of the same order as the accuracy of the HI column densities from EBHIS and GASS (Winkel et al. 2016). As a 3σ criterion combined with the positive offset as $\tilde{N}_{H_2} + 3\sigma(N_{H_2})$, a potential MIVC requires $N_{H_2} > 0.65 \times 10^{20}\,\mathrm{cm}^{-2}$ for the northern and $N_{H_2} > 0.58 \times 10^{20}\,\mathrm{cm}^{-2}$ for the southern Galactic hemisphere to be statistically significant.

3. If the LVC HI column density N_{HI}^{LVC} is large, the associated FIR emission is also bright, rendering any FIR-counterpart of a potential MIVC along these lines-of-sight difficult or impossible to be detectable. To reduce the number of MIVC candidates with such blending, we require all candidates to have $N_{HI}^{LVC} < 2N_{HI}^{IVC}$. This criterion can be relaxed in the initial selection if an accurate modelling of the total FIR emission afterwards is possible nonetheless.

4. Molecules form in dense and cold environments (e.g. Herbst & van Dishoeck 2009). An upper limit of the gas temperature is given by the HI line width. We require MIVCs to have spectral Gaussian components with amplitudes of more than 10 K and line widths of FWHM $< 5\,\mathrm{km\,s^{-1}}$. The central line velocities have to be within $20\,\mathrm{km\,s^{-1}} \leq |v_{LSR}| \leq 100\,\mathrm{km\,s^{-1}}$ in order to be classified as IVCs in the first place. The information on the line widths is not drawn from the HI spectra directly, but a Gaussian decomposition of the HI data cubes is used, which is explained later in more detail. HI lines with these requirements are found, e.g., in the MIVC that is studied in Chapters 3 and 4. A line width of FWHM $< 5\,\mathrm{km\,s^{-1}}$ corresponds to a kinetic temperature of $T_{kin} < 550$ K, which is in the regime of the thermally stable cold atomic medium (e.g. Kalberla & Kerp 2009). This gas is found mostly within the Galactic disk, for which Haud & Kalberla (2007) estimate a mean width of FWHM $= 3.9 \pm 0.6\,\mathrm{km\,s^{-1}}$. Hence, our line-width criterion selects most of the line components that are associated with the cold atomic medium, which may be related to molecules. Larger HI line widths are much more common (Haud 2008).

In conjunction these four criteria identify potential MIVCs, which are examined individually in order to sort out the most promising objects. The number of candidates can be increased by the relaxation of any of the four criteria. In the first place our goal is to find as many reasonable MIVC candidates as possible, which are analysed in more detail.

Small angular offsets are allowed between the maps of the different measures (N_{HI}, N_{H_2}, FWHM) by applying maximum filters[1] with the size of the angular resolution of GASS. This results into more candidates as compared with a direct pixel matching. Reasons for offsets in the different sets may be, e.g., FIR contamination from unrelated LVC emission or spatial displacements due to non-equilibrium processes (e.g. compare with Chapter 4). Furthermore, the narrowest and brightest HI lines may not originate from the peaks in HI column density.

A potential candidate needs to be spatially extended, otherwise it cannot be evaluated reasonably. We do not consider candidates that cover a solid angle of less than about half a GASS beam.

We use the Gaussian decomposition of EBHIS and GASS as performed by D. Lenz and L. Flöer (private communication). In their algorithm simultaneous fits of a varying number of Gaussian components are compared for each individual spectrum. Based on the Akaike information criterion (Akaike 1974), they pick the best matching solution, penalising models with more parameters. The upper limit for the number of Gaussian components for each spectrum is set to 15 in order to avoid overfitting. Physically motivated priors for the amplitudes and line widths of the components are applied: the amplitudes have to be positive and larger than the noise, the line width have to reflect physically reasonable gas temperatures. The decomposition provides HEALPix tables of the Gaussian parameters amplitude, line velocity,

[1] A maximum filter searches the spatial neighbourhood of each individual pixel and determines its value by the maximum within a box of given width and height.

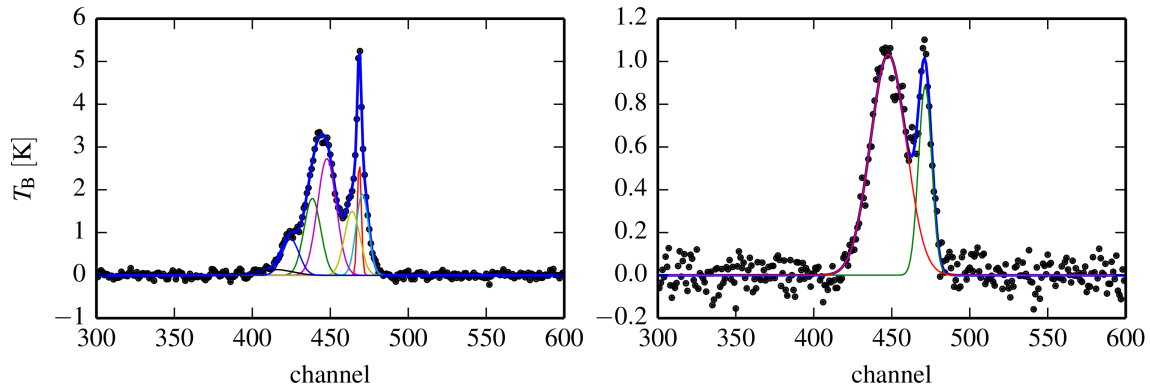

Fig. 5.1: Exemplary Gaussian decompositions along two randomly chosen lines-of-sight. The data (the black dots) is well modelled by the total spectrum (the blue solid line). All individual Gaussian components are plotted in different colours.

and line widths. From these components FITS maps are gridded in north- and south-polar projection containing the narrowest and brightest components in the IVC velocity intervals.

In Fig. 5.1 we show two randomly chosen lines-of-sight and the corresponding Gaussian decomposition. The spectra are plotted as black dots while the total modelled spectra are the blue curves. All other colours show individual Gaussian components that are fitted. The spectra are reasonably fitted, especially narrow and bright components are well modelled.

An important point of criticism in the study of HI halo clouds is the simple distinction between LVCs, IVCs, and HVCs by the application of some hard velocity cuts. The radial velocity is just a convenient way to distinguish between the different categories from the observations directly. However, in our approach here, the additional criterion imposed by certain Gaussian components allows to physically differentiate between different types of halo clouds. HVCs contain mostly warm HI gas (e.g. Putman et al. 2012) and are thus excluded to a large extent as candidates. The selection by radial velocity removes the dominant LVC HI emission revealing kinematically peculiar objects that deviate significantly from the bulk of the Galactic HI gas.

5.2.2 Atomic IVCs

A large negative H_2 column density together with bright and narrow HI lines are indicative of FIR-deficient or atomic IVCs (AIVCs). As we show in Chapter 3 for two clouds explicitly, on angular scales probed by EBHIS and GASS, AIVCs appear to be very similar to MIVCs in terms of their HI properties like HI column densities, HI morphologies, HI line profiles, and HI velocity structure. Hence, we search for AIVC candidates in the same way as for MIVCs. Only criterion no. 2 is changed accordingly to $\tilde{N}_{H_2} - 3\sigma N_{H_2}$, requiring $N_{H_2} < -0.55 \times 10^{20}\,\mathrm{cm}^{-2}$ for the northern and $N_{H_2} < -0.32 \times 10^{20}\,\mathrm{cm}^{-2}$ for the southern hemisphere.

5.2.3 Normal IVCs

We define a reference sample similar to the AIVCs and MIVCs but with a different criterion on H_2 column densities: The normal IVCs (NIVCs) have $-0.55 \times 10^{20}\,\mathrm{cm}^{-2} \leq N_{H_2} \leq 0.65 \times 10^{20}\,\mathrm{cm}^{-2}$, which is compatible with the intrinsic scatter of the HI-τ correlation.

5.3 Verification of molecular IVC candidates

The search criteria (Sect. 5.2) define spatially distinct and extended regions. Since a large number of individual candidates is identified, we require methods that verify or falsify the candidates. Since our focus is in on the MIVC candidates, we do not apply similar treatments for the other two samples.

5.3.1 Automated ranking

In order to evaluate the robustness of each MIVC candidate, we use an automated procedure ranking the candidates according to their evidence. We apply the same two-component linear fit as before to estimate the dust emissivities and resulting H_2 column densities more accurately in a small region with $2^\circ \times 2^\circ$ around the centre coordinate of each candidate. In this small field the candidate itself and gaseous structures around are incorporated to assess the linear part of the local HI-τ correlation.

As a measure of the significance S of the estimated IVC emissivity ϵ^{IVC}, we calculate the quantity

$$S = \frac{\epsilon^{\mathrm{IVC}}}{\sigma\left(\epsilon^{\mathrm{IVC}}\right)} \times \sqrt{N} \tag{5.2}$$

with the number of data points N of the individual candidate and the fitting error on the emissivity $\sigma(\epsilon^{\mathrm{IVC}})$. The weighting with the square root of the number of pixels of the candidate emphasises larger coherent regions that fulfil the search criteria. The significances S establish a ranking, allowing to reject candidates altogether and to pick out the most interesting ones.

This is one way to rank the inferred candidates, by which some specific objects receive more significance. One could apply other ranking schemes, like the maximum inferred H_2 column density of the candidate divided by its error. In this ranking scheme, however, candidates with obvious bright LVC emission would be picked preferably, which are difficult to evaluate.

5.3.2 Inspection of data cubes

A thorough inspection of each candidate is mandatory, which comprises the following steps:

1. For each candidate, that is not proven to be a MIVC, we grid an HI data cube with a size of $5^\circ \times 5^\circ$ centred on the location of the candidate to fully encompass it.

2. The HI spectra are separated into LVCs and IVCs by minima in the median or standard deviation of each spectral channel (e.g. Planck Collaboration XXIV 2011; Lenz et al. 2015). The median and standard deviation spectra are calculated in a small field of 10×10 pixels centred at the candidate cloud. In this way the MIVC candidate dominates the separation procedure and not the ambient gas. When the median spectrum is not allowing a unique separation between LVC and IVC gas, the minimum in the standard deviation spectrum is used to separate the emission. Using these velocity intervals, we compute HI column density maps for the LVC and IVC gas.

3. With these LVC and IVC HI column density maps the two-component fit to the HI-τ correlation data is re-computed. The same fitting procedure is applied as for the largest scales (Sect. 5.2). The fit parameters are used to compute H_2 column densities for the candidate.

4. The peak HI spectrum of the MIVC candidate is fitted by a multi-Gaussian model (in most cases with two components) in order to quantify the amount of warm and cold gas within the cloud.

north			south		
R $\left[10^{-6}\right]$	ϵ^{LVC} $\left[10^{-26}\,\mathrm{cm}^2\right]$	ϵ^{IVC} $\left[10^{-26}\,\mathrm{cm}^2\right]$	R $\left[10^{-6}\right]$	ϵ^{LVC} $\left[10^{-26}\,\mathrm{cm}^2\right]$	ϵ^{IVC} $\left[10^{-26}\,\mathrm{cm}^2\right]$
0.068	0.754	0.451	−0.148	0.723	0.637

Table 5.1: Fitted global linear parameters for the northern and southern Galactic hemispheres at latitudes of $|b| > 20°$. Details of the fitting procedure are given in the text. The statistical errors on the parameters are of the order of $\sim 10^{-4}$ in the given units.

5. The Spearman rank coefficients (see next subsection) are calculated between the LVC/IVC HI column densities and the total dust optical depths.

A confirmation of a MIVC candidate is the detection of ^{12}CO(1→0) line emission at the radial velocities of its atomic gas. However, such CO data is not available for most candidates. The only all-sky map of ^{12}CO(1→0) from the Planck Collaboration (Planck Collaboration XIII 2014) does not offer spectral information, but only the integrated ^{12}CO(1→0) emission. Dedicated CO observations would be required that target the candidates individually.

5.3.3 Spearman's rank correlation coefficient

A measurable positive relation between the HI column density of the IVC and the total dust optical depth is used as additional statistical evidence for the significance of the MIVC candidate. For this we apply the Spearman rank correlation coefficient ρ_{xy} (Spearman 1904, 1906). As a non-parametric measure, ρ_{xy} quantifies the statistical dependency between two variables x and y assuming a monotonic function. In our application to MIVC candidates, the correlation is not expected to be linear due to the FIR excess but a monotonic increasing function with HI column density. The data series x_i and y_i are sorted independently in increasing order assigning ranks according to their position. From these ranks the standard Pearson correlation coefficient is computed.

With ρ_{xy} we quantify if there is any relation between the LVC or IVC HI column density and the total dust optical depth and which of the LVCs or IVCs is related more significantly to τ. The rank coefficient is calculated only for the data points that are designated as the candidate cloud.

ρ_{xy} does not decide if a candidate is a MIVC or not. It is most useful for MIVC candidates with strong LVC emission because in these cases it may be difficult to relate FIR emission to the IVC at all.

5.4 The HI-FIR correlation on the northern Galactic hemisphere

The HI-τ correlation plot for the northern Galactic hemisphere for Galactic latitudes $b > 20°$ is shown in Fig. 5.2. The HI column densities are integrated between $-100\,\mathrm{km\,s^{-1}} \leq v_{\mathrm{LSR}} \leq +100\,\mathrm{km\,s^{-1}}$ separated into LVCs and IVCs. The linear parameters for the two-component linear fit are given in Table 5.1.

The fitted two-component model is plotted as the black points, which are thinned out by choosing randomly 10000 different data points of the model. The bulk of the HI-τ correlation is linear at the low HI column density end with a large intrinsic scatter as is indicated by the broad distribution for given N_{HI}. Near $\log\left(N_{\mathrm{HI}}^{\mathrm{TOT}}\left[\mathrm{cm}^{-2}\right]\right) \simeq 20.4$ the correlation steepens towards larger τ suggesting the presence of considerable amounts of H_2. There are lines-of-sight with up to $N_{\mathrm{HI}}^{\mathrm{TOT}} \simeq 2 \times 10^{21}\,\mathrm{cm}^{-2}$, which most likely are located at lower latitudes and contain significant amounts of molecular gas.

From the fitted linear parameters (Table 5.1), we estimate the distribution of H_2 within IVCs for $b > 20°$ attributing the entire deviation between the observed and modelled FIR emission to an H_2

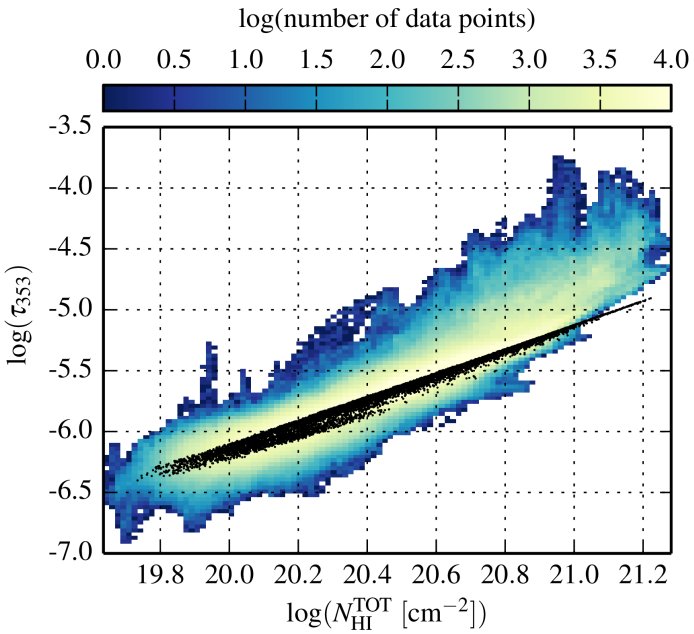

Fig. 5.2: HI-τ correlation plot for the northern Galactic hemisphere with $b > 20°$. The HI column density is the combined LVC and IVC emission between $-100\,\mathrm{km\,s^{-1}} \leq v_{\mathrm{LSR}} \leq +100\,\mathrm{km\,s^{-1}}$. The black dots show the two-component linear model consisting of LVC and IVC contributions. From this model, 10000 data points are chosen randomly and plotted.

column density of IVCs. The resulting map of $N_{\mathrm{H_2}}$ is shown in Fig. 5.3 with the H_2 column density distribution in colours. All blueish colours indicate positive $N_{\mathrm{H_2}}$ while all reddish give negative $N_{\mathrm{H_2}}$, indicating an over- or under-prediction of the FIR emission. The light- and dark-grey contours denote the total integrated (negative and positive) IVC HI gas at $N_{\mathrm{HI}}^{\mathrm{IVC}} = 0.75 \times 10^{20}\,\mathrm{cm^{-2}}$ and $1.5 \times 10^{20}\,\mathrm{cm^{-2}}$, respectively, tracing the location of IVC complexes. The red contours give the location of the inferred MIVC$^-$ candidates as described in Sect. 5.4.1. Other known high-latitude molecular clouds that are likely LVCs are marked by the green diamonds (Reach et al. 1998, their Table 3), additional FIR-excess clouds identified by Reach et al. (1998, their Table 4) as the green squares. The green circles show the position of confirmed ^{12}CO(1→0) emission towards IVCs as summarised by Magnani & Smith (2010).

In light of the new HI and FIR data, it is evident that previous studies of the HI-FIR correlation (e.g. Reach et al. 1998) do not account for the full inventory of high-latitude FIR excess clouds. In the H_2 map (Fig. 5.3), there are lots of small objects with significant H_2 column densities that are not identified by Reach et al. (1998). In our analysis, only a few of their objects are not found here as FIR excess clouds, most likely due to the different frequency coverage of the FIR data and the different angular resolution of the data. Note that the map of $N_{\mathrm{H_2}}$ presented in Fig. 5.3 is quantitatively not valid for the LVCs because the H_2 column densities are calculated for the IVCs, which have smaller dust emissivities (Table 5.1). Hence, the inferred H_2 column densities of LVCs are likely smaller.

One the one hand there are small and rather isolated excess objects that are often associated with larger complexes of excess emission. On the other hand there are large regions of strong excess emission, e.g. towards $l = 0°$ or $l = 120°$.

On the northern hemisphere, there is lots of IVC gas (compare with Fig. 3a from Wakker 2004) that appears to be generally FIR deficient, as indicated by $N_{\mathrm{H_2}} < 0$. The fitted IVC dust emissivity is smaller than for the LVCs (Table 5.1). This is expected because the metallicity of IVCs is often sub-solar indicating also less dust (e.g. Wakker 2001) and because the distances are up to ~5 kpc (e.g. Albert & Danly 2004). This reduces the heating of dust by UV radiation emitted by high-mass stars within the Galactic disk (e.g. Wolfire et al. 1995a). There are only a few exceptions of IVCs that are FIR bright and contain molecular gas potentially, which are the MIVC candidates (the red contours in Fig. 5.3).

There are regions of strong FIR deficiency with few IVC gas, e.g. near $(l, b) = (270°, 45°)$, $(l, b) = (250°, 40°)$, and $(l, b) = (340°, 60°)$, which are associated with gas in the LVC regime. On the one hand this is expected because the fitted HI-τ correlation is a mean over the entire sky, which naturally results in to the over-prediction of FIR emission. On the other hand the differentiation between different cloud populations (LVC, IVCs, HVCs) by the observed radial velocity is just a convenient way to categorise the HI emission but its physically not always well motivated, especially for lower absolute velocities. There may be IVC or HVC gas at LVC velocities and vice versa.

5.4.1 Search for northern molecular IVCs

We formulated criteria (Sect. 5.2) that are thought to reflect the requirements for the existence of a MIVC. These criteria are met in spatially distinct regions, which are marked in Fig. 5.3 as red contours superimposed onto the northern H_2 distribution. Now, these candidates are automatically ranked and analysed as described in Sect. 5.3. The best ten MIVC$^-$ candidates and the single MIVC$^+$ candidate are compiled in Table 5.2. The resulting complete list (Table A.1 in the appendix) contains 161 northern MIVC$^-$ and one MIVC$^+$ candidates.

All previously known MIVCs that are associated with ^{12}CO(1→0) emission (Magnani & Smith 2010) are recovered as top-ranked candidates, except for one object. The identified MIVCs are Draco, IVC 135, IVC 210, G 288.4+53.2, and G 283.9+54.9. This is an excellent confirmation of our search strategy and shows that these objects are well-defined. The missing MIVC (G 295.0+57.1) is not identified because the HI emission is not well separated at $v_{\rm LSR} = -20\,{\rm km\,s^{-1}}$, but the MIVC extends to lower absolute velocities. Otherwise, the cloud would have been found also. Note that Draco, IVC 135, and IVC 210 are not identified as a single large object but are split up into several individual candidates.

There is only one MIVC candidate on the northern hemisphere for positive radial velocities, which is located towards bright LVC emission. It is not evaluated because within $2° \times 2°$ $N_{\rm HI}^{\rm LVC} > 4 \times 10^{20}\,{\rm cm^{-2}}$. Thus, this candidate is potentially the result of FIR excess emission from LVCs.

Because of large LVC HI and FIR excess emission, we discard some candidates towards the Outer Arm and the Polaris Flare (e.g. Dame et al. 2001). These regions are marked by the black shapes in Fig. 5.3 towards $(l, b) = (125°, 25°)$ and $(150°, 35°)$. The MIVC candidates that are located within these regions are listed in Table 5.2 but are filtered out in the subsequent statistical analysis (Sect. 5.4.4).

Since the number of candidates is so large, we do not check each candidate in detail. Instead, we look at the top-ranked 20 candidates for closer inspection. For the analysis, the different steps are conducted as described in Sect. 5.3. We compile five plots for each candidate: 1) the median and standard-deviation spectrum that is used to separate the LVC and IVC gas, 2) the multi-component Gaussian fit to the peak HI spectrum, 3) the map of the smoothed τ with the IVC HI column densities as black contours, a black cross at the location of the candidate, and the inferred H_2 column densities as red contours, 4) the total HI-τ correlation plot, and 5) the IVC contribution to the HI-τ correlation, which is the residual τ after subtracting the LVC contribution and the constant offset. In the HI-τ plots, the pixels of the MIVC candidate are marked as red points.

We first discuss general properties and peculiarities of the individual northern candidates. The derived cloud properties are presented in the upper part of Table 5.3 on page 94. The best northern MIVC$^-$ candidate no. 3$^-$ is shown in more detail here, other candidates in Sect. A.1 in the appendix.

General properties of northern MIVC$^-$ candidates The northern MIVC$^-$ candidates have median Galactic coordinates of $(\tilde{l}, \tilde{b}) \simeq (216°, 41°)$, indicating that the candidates are identified towards the outer Galaxy at high latitudes, well above the latitude limit of $b > 20°$. For many of the northern MIVC$^-$ candidates, separation velocities of $-20\,{\rm km\,s^{-1}} \lesssim v_{\rm LSR}^{\rm sep} \lesssim -15\,{\rm km\,s^{-1}}$ are required, which reflects the

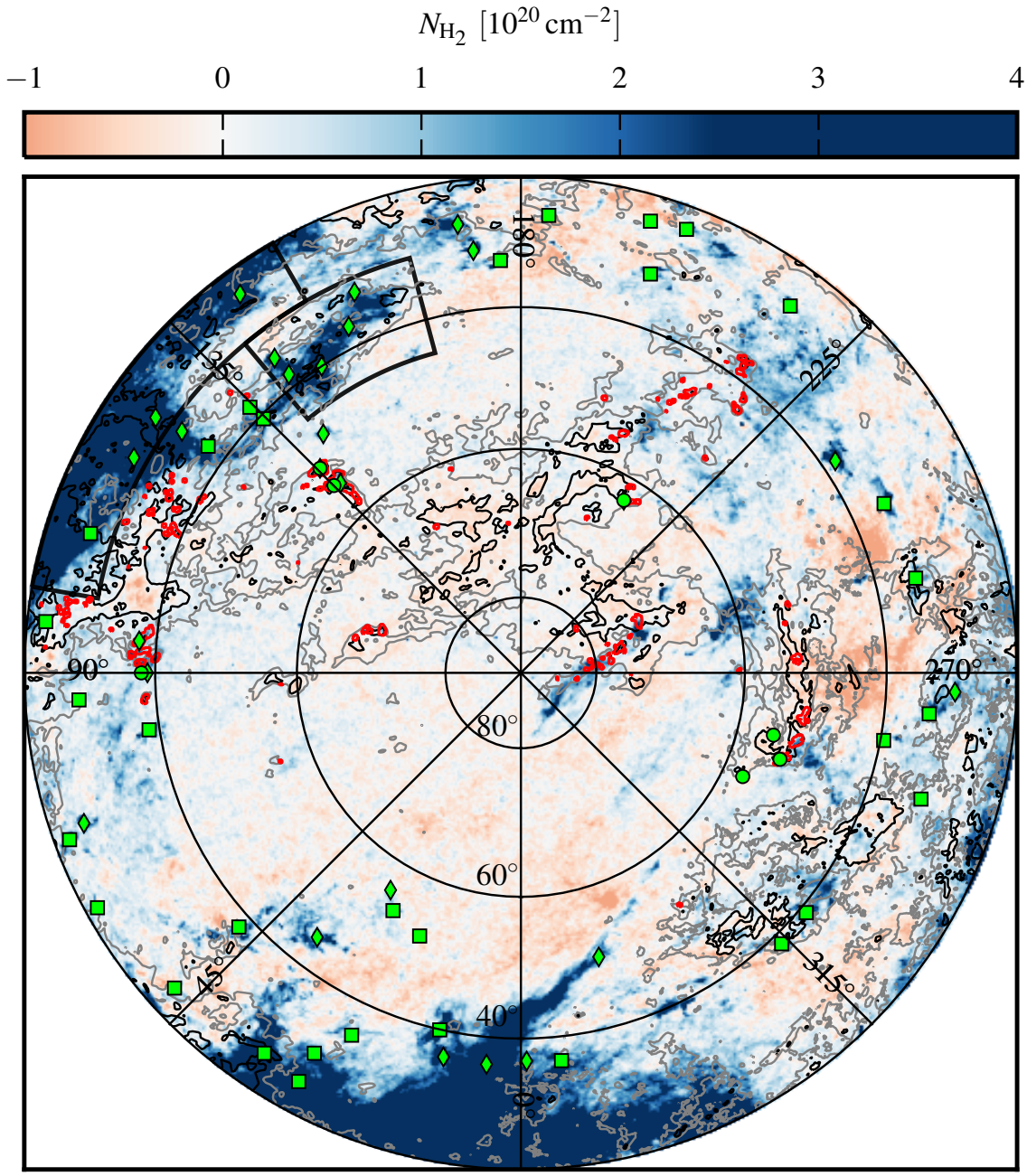

Fig. 5.3: Distribution of inferred H_2 column densities and MIVC$^-$ candidates for the northern Galactic hemisphere at $b > 20°$. The map is plotted in zenith-equal area projection centred on the northern Galactic pole with Galactic coordinates. Blueish and reddish colours indicate positive and negative N_{H_2}. The light- and dark-grey contours denote the total integrated (negative and positive) IVC HI gas at $N_{HI}^{IVC} = 0.75 \times 10^{20}$ cm^{-2} and 1.5×10^{20} cm^{-2} respectively tracing the location of IVC complexes. The red contours give the location of the inferred MIVC$^-$ candidates (Sect. 5.4.1). The green circles mark the location of confirmed MIVCs as listed in Magnani & Smith (2010). The green diamonds indicate known high-latitude molecular clouds from FIR excess emission, the green squares give the positions of unidentified FIR excess sources as listed in Reach et al. (1998, their Tables 3 and 4). The two regions framed in black show bright LVC HI and FIR excess emission. MIVC candidates within these regions are omitted in the statistical analysis (Sect. 5.4.4).

no.	l [deg]	b [deg]	ϵ^{IVC} $\left[10^{-26}\,\mathrm{cm}^2\right]$	$N_{\mathrm{H_2}}^{\mathrm{peak}}$ $\left[10^{20}\,\mathrm{cm}^{-2}\right]$	S	MIVC designation
$v_{\mathrm{LSR}} < -20\,\mathrm{km\,s}^{-1}$						
1^-	135.23	51.36	1.40 ± 0.01	0.26 ± 0.06	4370	IVC 135
2^-	136.01	54.59	1.70 ± 0.02	0.29 ± 0.09	4320	IVC 135
3^-	278.73	51.45	0.81 ± 0.01	0.72 ± 0.09	3040	
4^-	95.49	38.15	1.90 ± 0.03	0.98 ± 0.05	2290	Draco
5^-	211.41	63.11	1.05 ± 0.01	0.95 ± 0.08	2070	IVC 210
6^-	106.97	70.69	1.07 ± 0.01	0.37 ± 0.09	1500	
7^-	216.46	37.20	1.08 ± 0.01	0.66 ± 0.09	1370	
8^-	215.06	37.23	1.04 ± 0.01	0.32 ± 0.10	1350	
9^-	288.39	53.04	0.91 ± 0.02	1.35 ± 0.15	1330	G 288.4+53.2
10^-	85.99	38.37	0.75 ± 0.01	0.35 ± 0.10	1310	
$v_{\mathrm{LSR}} > +20\,\mathrm{km\,s}^{-1}$						
1^+	259.71	35.02	0.00 ± 0.00	0.00 ± 0.00	0	

Table 5.2: Locations of MIVC$^{\pm}$ candidates on the northern Galactic hemisphere. The columns give the cloud number, the Galactic longitude l and latitude b, the fitted IVC dust emissivity ϵ^{IVC} and its error, the peak H_2 column density $N_{\mathrm{H_2}}^{\mathrm{peak}}$ and its error, the significance S as defined in Eq. (5.2), and the MIVC designation if it is a known cloud. The entire list of 162 candidates is given in Table A.1 in the appendix. The candidate 1^+ is not evaluated because $N_{\mathrm{HI}}^{\mathrm{LVC}} > 4 \times 10^{20}\,\mathrm{cm}^{-2}$ within $2^\circ \times 2^\circ$ of the candidate.

blending of spectral lines of LVCs and IVCs. The peak HI column densities $N_{\mathrm{HI}}^{\mathrm{peak}}$ are similar within a factor of two with a median of $\tilde{N}_{\mathrm{HI}}^{\mathrm{peak}} \simeq 2.5 \times 10^{20}\,\mathrm{cm}^{-2}$.

All clouds consist of atomic two-phase media comprising warm and cold components. Sometimes, there is a significant velocity offset between the two components. There is some evidence that the cold components have larger absolute radial velocities than the warm components, which is in agreement with Haud (2008). The line widths of the warm components are compatible with the warm neutral medium (e.g. Kalberla & Kerp 2009). The MIVC candidates were selected to have $\mathrm{FWHM}^{\mathrm{cold}} < 5\,\mathrm{km\,s}^{-1}$ from a Gaussian decomposition, which is confirmed by the manual fitting. It is noteworthy, that the highest-ranked MIVC$^-$ candidates have median line widths $\tilde{\mathrm{FWHM}}^{\mathrm{cold}} \simeq 4.0 \pm 0.5\,\mathrm{km\,s}^{-1}$, narrower than the initial selection criterion. This suggests that HI line width criterion may capture the underlying physical requirements for cold atomic and molecular gas.

The central velocities of the cold line components derived from the Gaussian decomposition were also used as a selection criterion by the requirement $-100\,\mathrm{km\,s}^{-1} \leq v_0^{\mathrm{gauss}} \leq -20\,\mathrm{km\,s}^{-1}$. The median velocity is $\tilde{v}_0^{\mathrm{cold}} = -30.2 \pm 0.3\,\mathrm{km\,s}^{-1}$, which does not appear to be biased by the cut in radial velocity.

All MIVC$^-$ candidates that are classified as "likely" being a MIVC have cold gas fractions of $f^{\mathrm{cold}} > 50\%$. On average, about on quarter of all data points is rejected during the iterative HI-τ fitting, suggesting fairly simple environments with not too large HI column densities and FIR excess.

The fitted offsets R vary significantly, indicating different surroundings of the objects. Also the estimated dust emissivities ϵ^{LVC} and ϵ^{IVC} show a large spread. The median values are consistent with Planck Collaboration XXIV (2011). The inferred peak H_2 column densities are statistically significant with a median of $\tilde{N}_{\mathrm{H_2}} \simeq 1.2 \pm 0.2 \times 10^{20}\,\mathrm{cm}^{-2}$. This is about half of the peak IVC HI column densities suggesting large molecular fractions. The Spearman rank coefficients $\rho^{\mathrm{LVC}-\tau}$ and $\rho^{\mathrm{IVC}-\tau}$ indicate for most candidates that the IVCs are more related to the IVC HI column densities. This suggests that many of the northern MIVC$^-$ candidates dominate the total FIR emission along their lines-of-sight.

The inspection of the HI spectra and distribution shows that the candidates are not isolated. Both

no.	l [deg]	b [deg]	$v_{\rm LSR}^{\rm sep}$ [km s^{-1}]	$N_{\rm HI}^{\rm peak}$ [10^{20} cm^{-2}]	$v_0^{\rm warm}$ [km s^{-1}]	FWHM$^{\rm warm}$ [km s^{-1}]	$v_0^{\rm cold}$ [km s^{-1}]	FWHM$^{\rm cold}$ [km s^{-1}]	$f^{\rm cold}$	$f^{\rm rej}$	R [10^{-6}]	$\epsilon^{\rm LVC}$ [10^{-26} cm^2]	$\epsilon^{\rm IVC}$ [10^{-26} cm^2]	$N_{\rm H_2}^{\rm peak}$ [10^{20} cm^{-2}]	$\rho^{\rm LVC-\tau}$	$\rho^{\rm IVC-\tau}$	comment
northern Galactic hemisphere																	
3$^-$	278.73	51.45	-17.9	3.6	-27.7 ± 1.0	15.4 ± 0.9	-30.9 ± 0.1	4.4 ± 0.1	58%	43%	0.72 ± 0.01	0.252 ± 0.003	0.445 ± 0.002	1.9 ± 0.1	0.19	0.69	likely
6$^-$	106.97	70.69	-20.5	2.1	-30.0 ± 1.7	17.3 ± 3.0	-29.4 ± 0.1	3.7 ± 0.1	60%	28%	0.013 ± 0.005	0.561 ± 0.008	0.597 ± 0.004	1.1 ± 0.1	0.37	0.87	likely
7$^-$	216.46	37.20	-16.6	2.5	-26.6 ± 0.5	14.0 ± 0.7	-24.7 ± 0.5	3.3 ± 0.7	9%	23%	0.52 ± 0.01	0.882 ± 0.004	0.249 ± 0.006	3.2 ± 0.5	0.49	0.97	possibly
8$^-$	215.06	37.23	-16.6	2.5	-22.5 ± 1.8	22.2 ± 2.8	-20.0 ± 0.5	3.1 ± 0.6	10%	18%	-0.14 ± 0.01	1.06 ± 0.01	0.448 ± 0.007	1.6 ± 0.4	0.75	0.89	possibly
10$^-$	86.99	38.37	-29.5	2.3	-43.5 ± 0.6	5.8 ± 1.2	-43.2 ± 0.2	3.5 ± 0.6	51%	35%	0.210 ± 0.003	0.840 ± 0.002	0.372 ± 0.008	0.9 ± 0.2	0.56	0.83	possibly
12$^-$	203.15	55.01	-15.4	3.0	-42.2 ± 1.2	18.5 ± 1.3	-49.2 ± 0.3	4.6 ± 0.4	25%	23%	-0.192 ± 0.004	1.340 ± 0.003	0.510 ± 0.003	0.6 ± 0.1	0.41	0.82	possibly
13$^-$	112.15	38.58	-23.1	2.4	-28.5 ± 5.5	14.3 ± 5.7	-35.2 ± 0.2	3.6 ± 0.2	71%	30%	-0.183 ± 0.004	0.957 ± 0.004	0.580 ± 0.003	0.8 ± 0.1	0.59	0.82	likely
16$^-$	219.23	43.65	-16.6	2.3	-30.4 ± 0.8	15.4 ± 1.4	-29.5 ± 0.4	4.9 ± 0.6	26%	19%	-0.20 ± 0.01	1.069 ± 0.005	0.492 ± 0.007	0.8 ± 0.3	−0.16	0.39	possibly
17$^-$	101.91	67.43	-15.4	2.6	-28.8 ± 0.9	10.0 ± 1.9	-28.5 ± 0.2	4.2 ± 0.4	54%	22%	0.37 ± 0.01	-0.001 ± 0.011	0.531 ± 0.003	0.6 ± 0.1	0.14	0.72	likely
18$^-$	216.05	39.09	-17.9	2.3	-28.8 ± 2.9	20.2 ± 3.9	-31.2 ± 0.4	4.2 ± 0.6	27%	26%	0.52 ± 0.01	0.922 ± 0.004	0.025 ± 0.005	24 ± 5	0.75	0.51	unclear
19$^-$	215.89	38.13	-15.4	2.4	-26.8 ± 0.5	13.9 ± 0.6	-24.5 ± 0.5	3.1 ± 0.7	8%	23%	0.48 ± 0.01	0.916 ± 0.004	0.131 ± 0.006	6.9 ± 1.1	0.43	0.95	unclear
20$^-$	266.77	52.80	-20.5	3.0	-27.7 ± 1.2	15.0 ± 1.1	-30.9 ± 0.2	4.2 ± 0.3	36%	29%	0.34 ± 0.01	0.477 ± 0.002	0.511 ± 0.002	1.3 ± 0.2	0.66	0.73	possibly
median quantities																	
	215.48	41.37	-17.3	2.5	-28.7 ± 1.1	15.2 ± 1.4	-30.2 ± 0.3	4.0 ± 0.5	32%	25%	0.28 ± 0.01	0.899 ± 0.004	0.470 ± 0.005	1.2 ± 0.2	0.46	0.82	
southern Galactic hemisphere																	
1$^-$	125.21	-20.75	-41.1	3.6	-53.4 ± 2.0	22.9 ± 2.0	-59.2 ± 0.1	5.3 ± 0.1	60%	>72%[a]	1.15 ± 0.02	0.297 ± 0.005	1.125 ± 0.006	0.8 ± 0.1	0.19	0.67	unclear
2$^-$	137.96	-20.37	-42.4	2.1	-51.8 ± 2.2	18.3 ± 2.2	-56.3 ± 0.2	5.0 ± 0.3	50%	>67%[a]	0.45 ± 0.02	0.507 ± 0.006	1.446 ± 0.008	0.3 ± 0.1	0.36	0.81	unclear
6$^-$	126.64	-27.76	-37.3	1.3	-48.7 ± 4.0	17.7 ± 4.0	-52.5 ± 0.5	5.2 ± 0.7	38%	80%	0.64 ± 0.04	0.489 ± 0.010	0.795 ± 0.007	0.5 ± 0.1	0.57	0.38	unclear
mean quantities																	
	129.94	-22.96	-40.3	2.3	-51.3 ± 2.7	19.6 ± 2.7	-56.0 ± 0.3	5.2 ± 0.4	49%	73%	0.75 ± 0.03	0.431 ± 0.007	1.122 ± 0.007	0.5 ± 0.1	0.37	0.62	
1$^+$	257.73	-21.18	20.7	2.5	26.6 ± 0.2	9.6 ± 0.2	–	–	–	36%	-0.92 ± 0.02	1.598 ± 0.008	0.471 ± 0.005	0.8 ± 0.6	0.92	0.87	unlikely
2$^+$	234.52	-32.90	16.8	1.4	18.3 ± 2.8	17.9 ± 3.0	22.1 ± 0.1	3.4 ± 0.2	53%	31%	0.316 ± 0.004	0.588 ± 0.003	1.244 ± 0.005	0.4 ± 0.1	0.40	0.77	possibly
4$^+$	240.19	-20.89	15.6	3.2	15.7 ± 2.6	21.5 ± 2.2	22.0 ± 0.1	4.2 ± 0.1	43%	48%	0.929 ± 0.005	0.458 ± 0.003	0.866 ± 0.003	0.4 ± 0.1	−0.11	0.88	possibly
mean quantities																	
	244.15	-24.99	17.7	2.4	20.2 ± 1.9	16.3 ± 1.8	22.1 ± 0.1	3.8 ± 0.2	48%	38%	0.11 ± 0.01	0.881 ± 0.005	0.860 ± 0.004	0.5 ± 0.3	0.40	0.84	

Table 5.3: Derived properties of top-ranked unknown MIVC$^{\pm}$ candidates. The Table is divided into the northern and southern Galactic hemispheres. The columns list from left to right the candidate number from the ranked order (Tables 5.2 and A.1 for the northern, Table 5.4 for the southern Galactic hemisphere), Galactic longitude l, Galactic latitude b, separating velocity $v_{\rm LSR}^{\rm sep}$ between LVC and IVC regime, peak IVC HI column density $N_{\rm HI}^{\rm peak}$, central velocity $v_0^{\rm warm}$ and width FWHM$^{\rm warm}$ of the warm gas component, central velocity $v_0^{\rm cold}$ and width FWHM$^{\rm cold}$ of the cold gas component, cold gas fraction $f^{\rm cold} = N_{\rm HI}^{\rm cold}/(N_{\rm HI}^{\rm cold} + N_{\rm HI}^{\rm warm})$, fraction of rejected data points $f^{\rm rej}$ during iterative HI-τ fitting, the fitted offset R and dust emissivities for LVCs $\epsilon^{\rm LVC}$ and IVCs $\epsilon^{\rm IVC}$ of the HI-τ correlation, the inferred peak H_2 column density $N_{\rm H_2}^{\rm peak}$, Spearman's rank coefficient $\rho^{\rm LVC-\tau}$ for $N_{\rm HI}^{\rm LVC}$-τ, Spearman's rank coefficient $\rho^{\rm IVC-\tau}$ for $N_{\rm HI}^{\rm IVC}$-τ, and a comment about the validity of the candidate. In the row after all candidates of a given type (north/south, MIVC$^{\pm}$), the median or mean quantities are given. For the northern hemisphere we use the median since there are many candidates.
[a]The fitting threshold is increased to 5×10^{20} cm^{-2}, otherwise most of the data would be omitted for the fit. That is why $f^{\rm rej}$ is larger than the given value.

in spectral and spatial dimensions the objects connect to other LVC or IVC gas. Sometimes, the surrounding IVC emission is clumpy or filamentary. The candidates that are classified as being "possibly" MIVCs or as being "unclear" often show bright HI lines within the LVC regime or generally complicated spectra with multiple velocity components. This leads to a difficult modelling of the dust optical depth, since these other velocity components may be associated with comparable or even larger amounts of gas and dust as the candidate cloud.

Candidate no. 3^- Candidate no. 3^- has a larger significance than some of the known MIVCs. Its velocity separation and other plots are shown in Fig. 5.4. In the spectra, the LVC and IVC HI gas connect continuously. The candidate dominates the HI emission along its lines-of-sight. The HI-τ plots show FIR excess emission of the cloud relative to the field. Some LVC gas within the field exhibits even larger FIR excess.

The IVC is associated with FIR excess emission and the inferred H_2 distribution follows the HI column densities of the IVC. The spectra show a large fraction of cold gas within the cloud. Summarising, candidate no. 3^- is likely a MIVC.

5.4.2 Search for northern atomic IVCs

In the same manner as MIVCs are identified, FIR-deficient IVCs or atomic IVCs (AIVCs) can be found. The search criteria (Sect. 5.2.2) are chosen to select cold HI gas together with the most negative H_2 column densities that correspond to the most FIR-deficient IVCs on the sky. Inferred negative H_2 column densities result from an over-prediction of the dust optical depth relative to the environment. The AIVCs are compared with the MIVC candidates because both samples may represent clouds at different stages in the Galactic fountain cycle (Röhser et al. 2014).

Similarly as for the MIVCs (Fig. 5.3), we plot the locations of the identified AIVCs in Fig. 5.5. The red contours show the locations of the AIVC^- candidates and the dark-violet coloured contours show the AIVC^+ candidates. There are 86 AIVC^- and 8 AIVC^+ candidates.

Sometimes, there are MIVC and AIVC candidates nearby projected on the sky or within the same IVC structure. For instance close to the Draco cloud at $(l, b) \simeq (90°, 40°)$ there is an AIVC at $(l, b) \simeq (100°, 37°)$. Also in the extended IVC structure near $(l, b) \simeq (270°, 53°)$, there are many small AIVCs that are close to the three Magnani & Smith (2010) MIVCs, which are located at the tip of the IVC structure as defined by the velocity thresholds here.

In Sect. 5.4.4 the two samples of MIVCs and AIVCs are compared with a control sample, that is defined in the next Section.

5.4.3 Search for northern normal IVCs

In order to compare the statistical properties of the global population of MIVC and AIVC candidates, we define a control sample (Sect. 5.2.3). These normal IVCs (NIVCs) contain cold HI gas and have inferred H_2 column densities that are compatible with the intrinsic scatter of the global HI-τ correlation.

Similarly as for the MIVCs (Fig. 5.3) and AIVCs (Fig. 5.5), we plot the spatial locations of the NIVCs in Fig. 5.6. The red and dark-violet coloured contours show the locations of the NIVC^- and NIVC^+ candidates. For the NIVCs^- there are 288 candidates and for the NIVCs^+ 22.

The NIVCs are spread over large fractions of the northern IVC structures, showing that lots of the IVC gas contains cold gas. Often, the candidates surround MIVC or AIVC candidates.

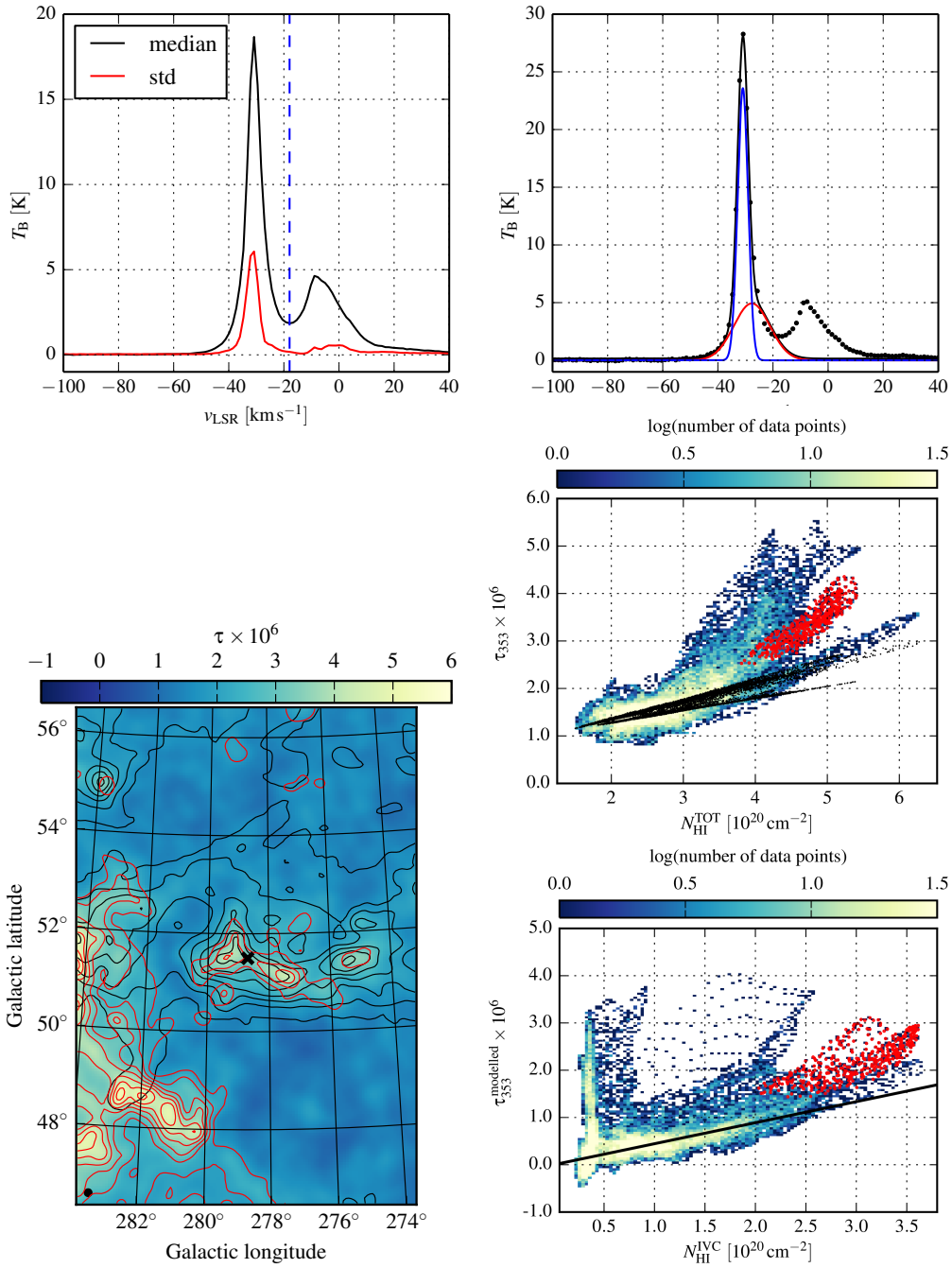

Fig. 5.4: Plots for MIVC$^-$ candidate no. 3$^-$. The top-left plot shows the velocity separation with the median and standard-deviation spectrum in black and red. The separating velocity is given by the vertical dashed blue line. In the top-right, the two-component Gaussian fit to the peak HI spectrum is presented with the data as black dots and the total Gaussian fit as the black line. The narrow and wide Gaussian components are plotted as the blue and red curves. In the bottom-left, the τ-map is plotted overlayed with the IVC HI column densities in black and the inferred H_2 column densities in red. Both the HI and H_2 contours start at 0.5×10^{20} cm^{-2} increasing in steps of 0.5×10^{20} cm^{-2}. The position of the candidate is shown by the black cross. The middle-right plot shows the HI-τ plot for the total N_{HI} and total τ. In the bottom-right plot the modelled IVC contribution to τ is given after subtracting the LVC contribution and the constant offset from the total τ. In both HI-τ plots, the red points mark the data points of the MIVC candidate while the black line or black points indicate the modelled HI-τ relation.

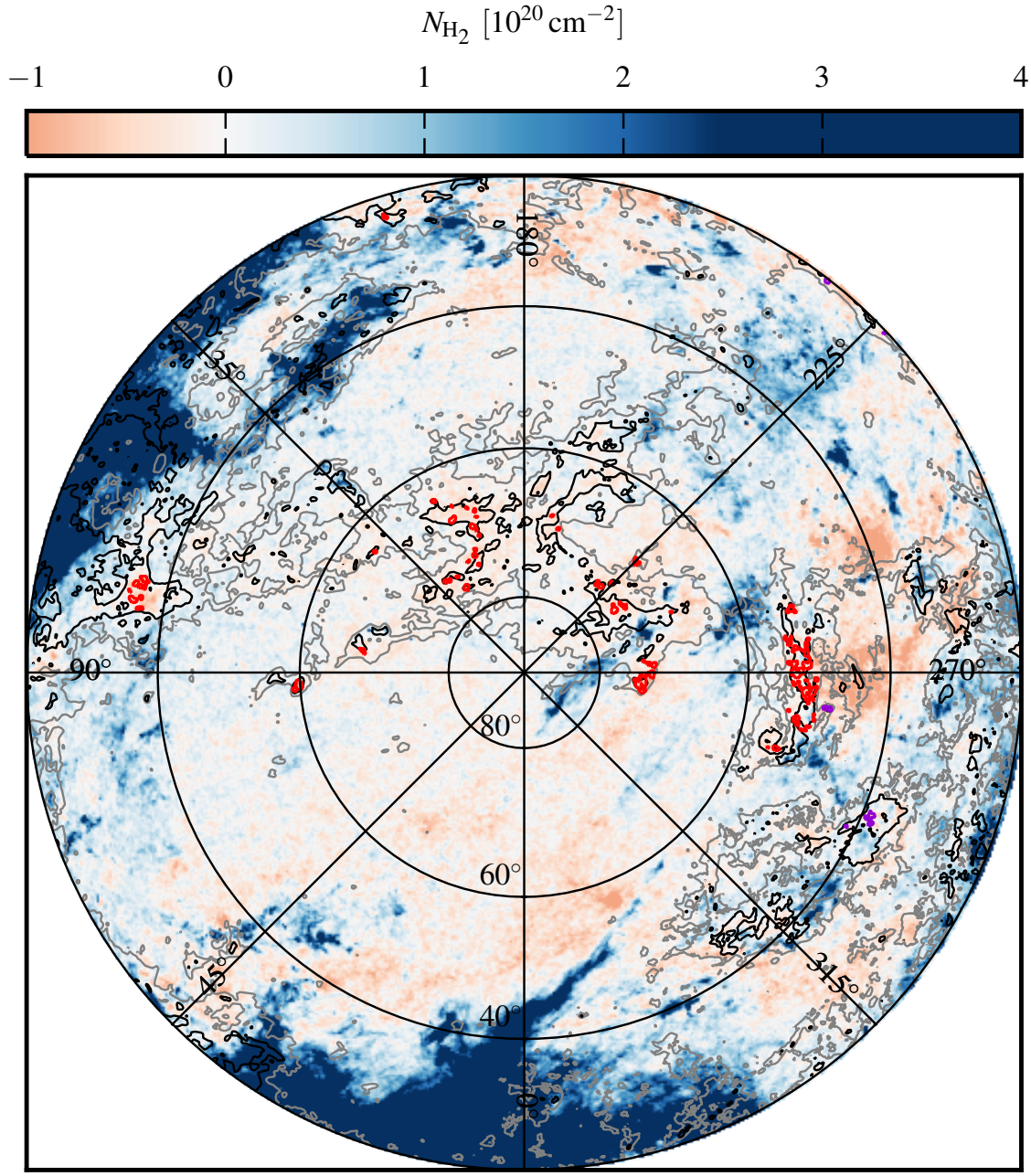

Fig. 5.5: Distribution of northern AIVC$^{\pm}$ candidates at $b > 20°$ on top of the inferred H_2 column densities. The map is plotted in zenith-equal area projection centred on the northern Galactic pole with Galactic coordinates. All blueish colours indicate positive N_{H_2}, all reddish negative N_{H_2}. The light- and dark-grey contours denote the total integrated (negative and positive) IVC HI gas at $N_{HI}^{IVC} = 0.75 \times 10^{20}$ cm^{-2} and 1.5×10^{20} cm^{-2} respectively tracing the location of IVC complexes. The red contours give the locations of the inferred AIVC^{-} candidates from the criteria as described in Sect. 5.2.2. The dark-violet contours show the AIVC^{+} candidates.

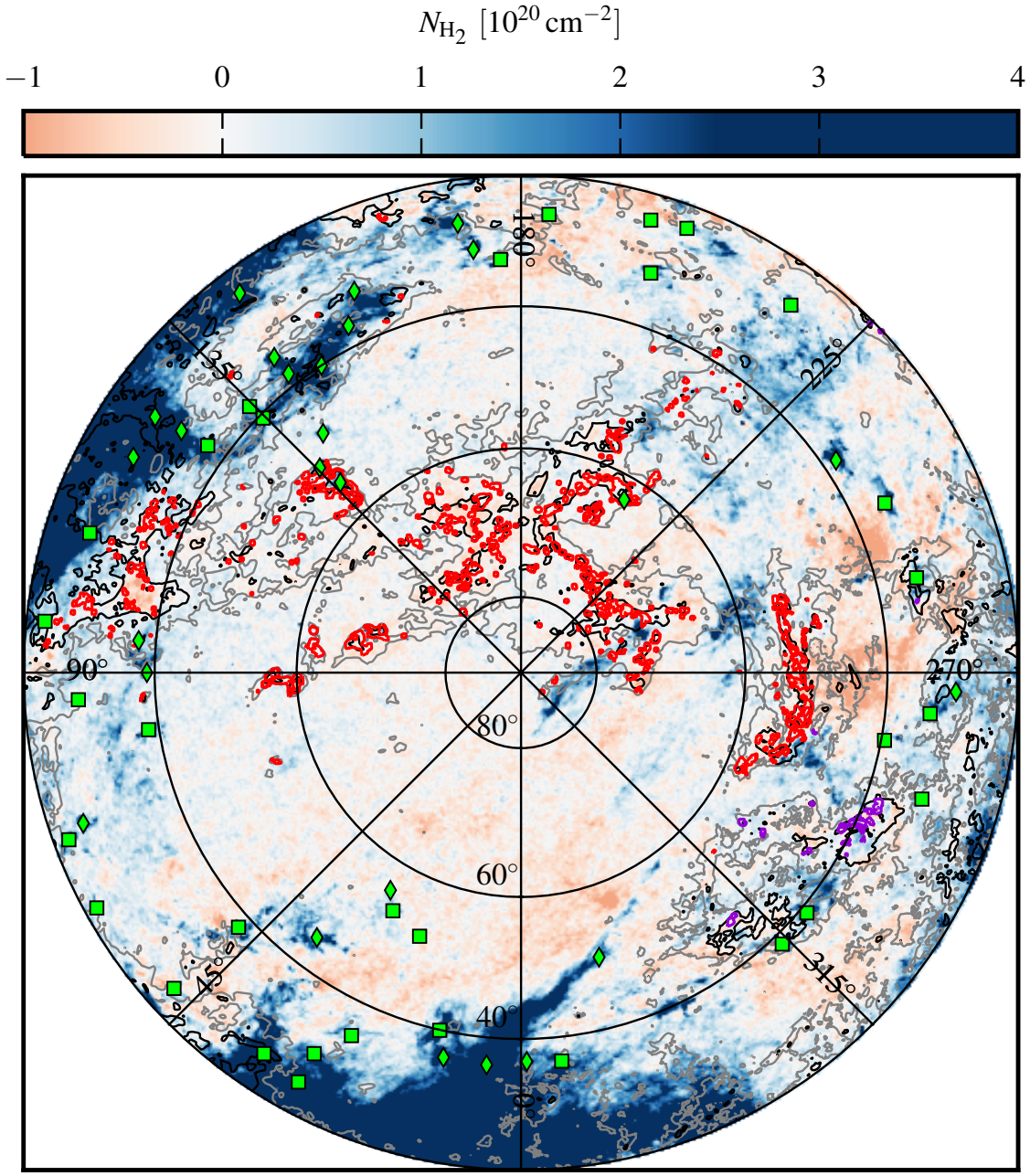

Fig. 5.6: Distribution of northern NIVC$^{\pm}$ candidates at $b > 20°$ on top of the inferred H_2 column densities. The map is plotted in zenith-equal area projection centred on the northern Galactic pole with Galactic coordinates. All blueish colours indicate positive N_{H_2}, all reddish negative N_{H_2}. The light- and dark-grey contours denote the total integrated (negative and positive) IVC HI gas at $N_{HI}^{IVC} = 0.75 \times 10^{20}$ cm^{-2} and 1.5×10^{20} cm^{-2} respectively tracing the location of IVC complexes. The red contours give the location of the inferred NIVC^{-} candidates from the criteria as described in Sect. 5.2.2. The dark-violet contours shows the NIVC^{+} candidates. The green diamonds indicate known high-latitude molecular clouds from FIR excess emission, the green squares give the positions of unidentified FIR excess sources as listed in Reach et al. (1998, their Tables 3 and 4).

5.4.4 Statistical properties of northern samples

In the statistical analysis of the MIVC, AIVC, and NIVC samples, we distinguish between negative and positive radial velocities. The large discrepancy in the number of candidates is discussed in more detail in Sect. 5.6. For the northern hemisphere only the IVC$^-$ candidates are analysed here, since these provide the largest samples. The same plots for the IVC$^+$ samples are shown for completeness in Sect. A.2 in the appendix with only one MIVC$^+$ candidate.

We are interested in properties that distinguish the different IVC samples in histograms and correlation plots between observables. These observables all have the angular resolution of the GASS data. In order to quantify how similar or different the IVC populations are, we apply Kolmogorov-Smirnov tests. Note that some MIVC candidates are not used in the statistical analysis because these are located towards bright LVC gas and dust emission (compare with Fig. 5.3).

5.4.4.1 Histograms

In Fig. 5.7 we plot histograms of the observables of the AIVC$^-$, MIVC$^-$, and NIVC$^-$ samples. The black, red, and blue histograms are for the AIVCs$^-$, MIVCs$^-$, and NIVCs$^-$ respectively. The histograms are normalised such that the sum of all bins is unity. The data points are the observables at the pixel locations of the different sample objects. In the following we discuss the histograms (Fig. 5.7) from left to right and top to bottom.

LVC HI column density $N_{\rm HI}^{\rm LVC}$: The LVC column densities are typically $N_{\rm HI}^{\rm LVC} \lesssim 3 \times 10^{20}\,{\rm cm}^{-2}$ for all three samples. In a few lines-of-sight towards MIVC$^-$ candidates, there is up to $N_{\rm HI}^{\rm LVC} \simeq 6 \times 10^{20}\,{\rm cm}^{-2}$. Towards many AIVCs$^-$ there is significant LVC column density, which is surprising since the LVCs are expected to compensate for the low FIR emission of the AIVCs$^-$ reducing the FIR deficiency along these lines-of-sight. There are some MIVCs$^-$ and NIVCs$^-$ with no significant LVC column density of $N_{\rm HI}^{\rm LVC} \lesssim 0.5 \times 10^{20}\,{\rm cm}^{-2}$.

IVC HI column density $N_{\rm HI}^{\rm IVC^-}$: The HI column densities peak between $N_{\rm HI}^{\rm IVC^-} \simeq 1 - 2 \times 10^{20}\,{\rm cm}^{-2}$ for all three samples. In comparison, the AIVCs$^-$ have the largest HI column densities with a significant excess at $N_{\rm HI}^{\rm IVC^-} \gtrsim 2.5 \times 10^{20}\,{\rm cm}^{-2}$.

Total HVC HI column density $N_{\rm HI}^{\rm HVC}$: Towards none of the three samples there is significant HI column density in HVCs. However, there are a few MIVCs$^-$ towards which also HVC HI emission is observed. Hence, the suggestions of interactions of HVCs with IVCs (e.g. Herbstmeier et al. 1993, 1994; Moritz et al. 1998; Weiß et al. 1999; Lenz et al. 2015) cannot be considered as an universal requirement for the formation of MIVCs.

Dust optical depth τ: As expected the MIVC$^-$ sample shows the largest dust optical depth, which are linked to the FIR excess emission and molecular hydrogen. Their distribution shows a long tail towards large τ. The AIVCs$^-$ tend to have larger τ than the NIVCs$^-$. This is likely related to the large HI column densities of the AIVCs$^-$, which are consequently associated with more dust as compared with the NIVCs$^-$.

Dust temperature $T_{\rm d}$: Of all samples, the MIVCs$^-$ typically have the smallest dust temperatures with $T_{\rm d} \simeq 19.5\,{\rm K}$ and $\sim$21 K. This is found similarly in other studies of high-latitude molecular clouds and FIR-excess emission (e.g. Reach et al. 1998; Planck Collaboration XXIV 2011; Reach et al. 2015).

The low dust temperatures rule out enhanced dust heating as the cause for the bright FIR emission. The AIVCs$^-$ peak also near the second peak of the MIVCs$^-$ at $T_\mathrm{d} \simeq 21$ K. For the AIVCs$^-$ there is another peak at ∼22.5 K extending to the largest dust temperatures. The dust temperatures towards the NIVCs$^-$ follow a broad distribution with $T_\mathrm{d} \simeq 20.5 - 23$ K.

Dust exponent β: The exponent β describes the modification of the pure FIR black-body dust spectrum with frequency, incorporating the influence of dust grain physics onto the FIR emission. The dust exponents of the MIVCs$^-$ and the NIVCs$^-$ peak at $\beta \simeq 1.5$ and are similarly distributed. The MIVCs$^-$ have a broader distribution towards smaller and larger β. The AIVCs$^-$ generally have slightly larger exponents with $\beta \simeq 1.6$. The largest β are found in AIVCs$^-$ with up to $\beta \simeq 2.4$.

Inferred H_2 column density N_{H_2}: By design, the H_2 column densities give the cleanest separation between the three samples. The MIVCs$^-$ show the largest H_2 column densities up to $N_{H_2} \simeq 10 \times 10^{20}\,\mathrm{cm}^{-2}$, which are found in the Draco cloud (e.g. Mebold et al. 1985). For MIVCs$^-$, the most common H_2 column densities are $N_{H_2} \lesssim 1 \times 10^{20}\,\mathrm{cm}^{-2}$. The AIVCs$^-$ are selected to have significant negative H_2 column densities, meaning FIR deficiency relative to the environment. The NIVCs$^-$ are found in between.

Integrated ^{12}CO(1→0) emission: All three samples are generally not associated with CO emission as measured by the Planck satellite (Planck Collaboration XIII 2014). Only towards a few MIVCs$^-$ there is CO emission detected by Planck with $W_\mathrm{CO} \gtrsim 1\,\mathrm{K\,km\,s}^{-1}$. The lack of CO detections also towards known MIVCs$^-$ is either related to a lack of sensitivity or to the extraction procedure of the CO emission.

Total dust reddening: The total dust reddening inferred by Green et al. (2015) is largest towards the MIVCs$^-$, as expected, because these objects contain the most dust of the three samples. However, the magnitude of the reddening is low with typically less than 0.05 mag. The reddening towards the AIVCs$^-$ and NIVCs$^-$ is very similar, which is in contrast to the dust optical depth τ, which showed some notable differences. This may indicate that the reddening, at least towards the AIVCs$^-$ and NIVCs$^-$, is given mainly by the dust in the foreground of the candidates and not by their intrinsic dust content.

Galactic longitude l: There is no clear distribution of the samples with Galactic longitude. There are several peaks at various longitudes, which are sometimes similar for the different samples. IVC 135 dominates the MIVC$^-$ sample towards $l = 135°$, similar Draco at $l = 90°$, and IVC 210 at $l = 210°$. These objects are fairly large and extended compared with other candidates. Most AIVCs$^-$ are found towards $l = 275°$, which is the high-latitude tail of the IVC structure that contains the three Magnani & Smith (2010) CO clouds. The NIVCs$^-$ are more uniformly distributed. There is a lack of candidates in all samples towards the Galactic centre for longitudes of $l \simeq 300° - 60°$.

Galactic latitude b: Similar to the Galactic longitudes, the distribution of Galactic latitudes of the samples is dominated for the MIVCs$^-$ by the known large objects with the majority of candidates at $b \lesssim 60°$. The AIVCs$^-$ and the NIVCs$^-$ tend to be located at higher latitudes of $30° \gtrsim b \gtrsim 50°$.

Amplitudes of Gaussian components $T_\mathrm{B}^\mathrm{gauss}$: The MIVCs$^-$ have the largest amplitudes of the fitted Gaussian components of the HI data. The AIVCs$^-$ and NIVCs$^-$ are similar, while the AIVCs$^-$ tend to have the smallest amplitudes.

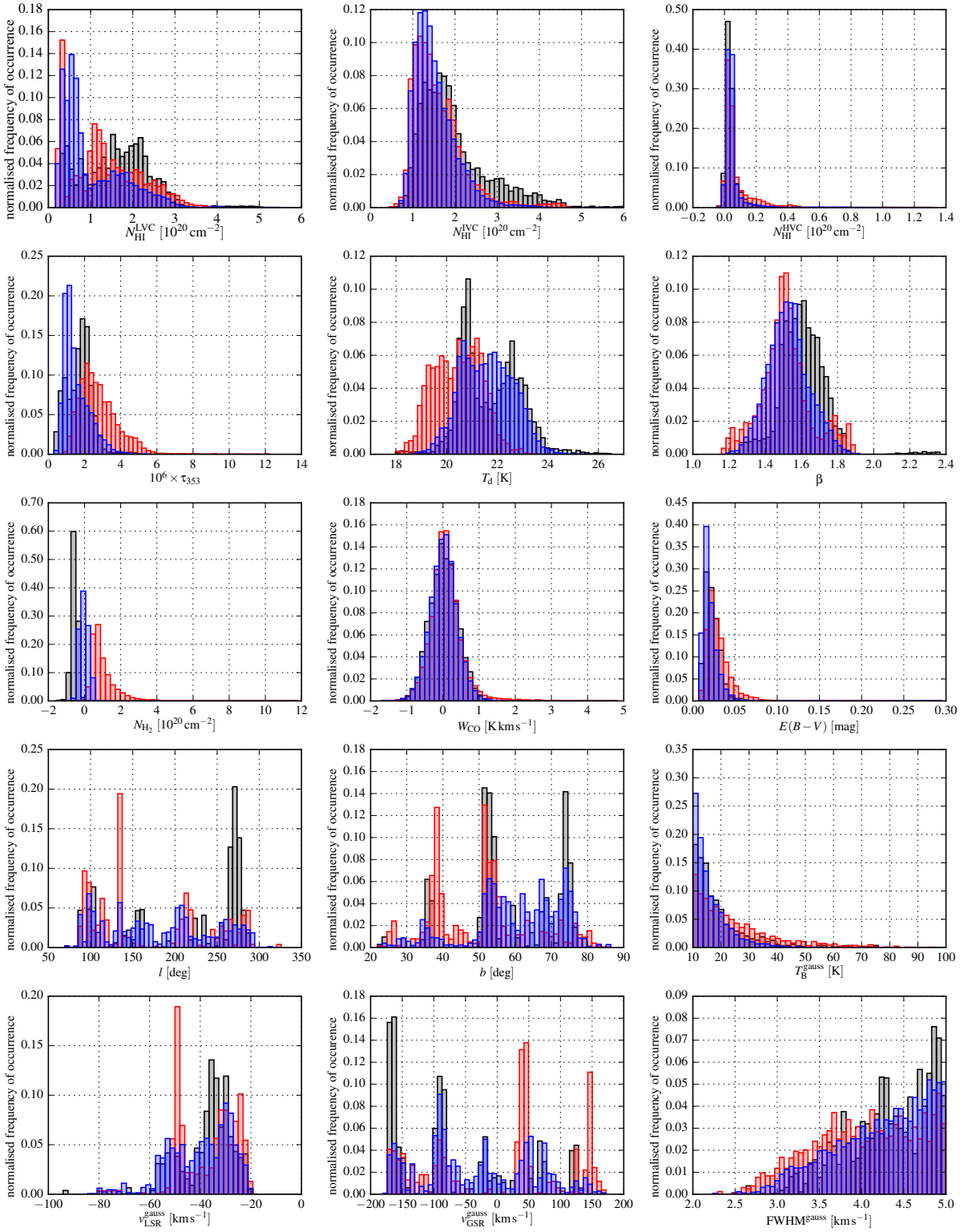

Fig. 5.7: Statistical properties of northern AIVC$^-$, MIVC$^-$, and NIVC$^-$ candidates. The black, red, and blue histograms show the AIVC$^-$, MIVCs$^-$, and NIVCs$^-$ candidates.

Central velocity of Gaussian components v^{gauss} in LSR and GSR: Most of the MIVCs$^-$ are found with $v_{\mathrm{LSR}}^{\mathrm{gauss}} \gtrsim -50\,\mathrm{km\,s^{-1}}$ with the peak near $v_{\mathrm{LSR}}^{\mathrm{gauss}} \simeq -50\,\mathrm{km\,s^{-1}}$. Furthermore, the MIVCs$^-$ connect to the LVC regime, as do Draco or the Magnani & Smith (2010) objects. All of the samples have $v_{\mathrm{LSR}}^{\mathrm{gauss}} > -60\,\mathrm{km\,s^{-1}}$. Moreover, the AIVCs$^-$ and NIVCs$^-$ peak between $-40\,\mathrm{km\,s^{-1}}$ and $-30\,\mathrm{km\,s^{-1}}$. In the Galactic standard of rest (GSR), the entire velocity range between $-180\,\mathrm{km\,s^{-1}}$ and $+180\,\mathrm{km\,s^{-1}}$ is filled showing an asymmetry between AIVCs$^-$ and MIVCs$^-$: The AIVCs$^-$ are found more with negative GSR velocities, the MIVCs with positive GSR velocities. The NIVCs$^-$ are spread more uniformly.

Width of Gaussian components FWHM$^{\mathrm{gauss}}$: The MIVCs$^-$ contain the narrowest HI lines, followed by the NIVCs$^-$. The AIVCs$^-$ have the largest HI line widths typically. Note that the Gaussian components are selected to have FWHM $< 5\,\mathrm{km\,s^{-1}}$, up to which the distributions extend. This illustrates that there are more and more IVCs with broader HI lines.

5.4.4.2 Kolmogorov-Smirnov tests

In order to quantify if the distributions of observables are drawn from the same parent distribution (the null hypothesis), we apply the two-sided Kolmogorov-Smirnov (KS) test (Kolmogorov 1933; Smirnov 1936) for pairs of the AIVC$^-$, MIVC$^-$, or NIVC$^-$ samples. The two-sided KS test is a widely used non-parametric test to compare two continuous distribution with each other. The KS-statistic is the maximum distance between the two cumulative distribution functions. The KS-statistic can be converted into the probability (the p-value) that the samples are drawn from the same parent distribution. Large KS-statistics or small p-values mean that the distributions are not drawn from the same parent distribution. Otherwise, for small KS-statistics and large p-values, this hypothesis cannot be rejected. Hence, the KS test allows to decide if two distributions do not have the same parent distribution.

The KS tests are applied to the sample data of AIVCs$^-$-MIVCs$^-$, AIVCs$^-$-NIVCs$^-$, and MIVCs$^-$-NIVCs$^-$. The calculated p-values are all less than 2×10^{-5} for all combinations of samples. This result implies that all distributions are statistically different. For the integrated CO emission W_{CO} from Planck Collaboration XIII (2014), the AIVCs$^-$ and NIVCs$^-$ have the largest p-value of 2×10^{-5}. These low p-values are likely related to the large number of sample points.

5.4.4.3 Correlations

In the following we look for correlations between observed quantities. These may be related to physical or observational reasons. The correlation plots are shown in Figs. 5.8 and 5.9.

Molecular hydrogen column density $N_{\mathrm{H_2}}$ and IVC HI column density $N_{\mathrm{HI}}^{\mathrm{IVC^-}}$: For the AIVC$^-$ sample there is a weak trend that the H_2 column densities get more negative for increasing $N_{\mathrm{HI}}^{\mathrm{IVC^-}}$. For the NIVCs$^-$, the data just scatters around zero for all HI column densities. For the MIVC$^-$ candidates, $N_{\mathrm{H_2}}$ increases with $N_{\mathrm{HI}}^{\mathrm{IVC^-}}$. The different branches are related to different MIVC$^-$ candidates.

Molecular hydrogen column density $N_{\mathrm{H_2}}$ and HVC HI column density $N_{\mathrm{HI}}^{\mathrm{HVC}}$: For the majority of candidates there is only a negligible amount of HVC HI column density with less than $N_{\mathrm{HI}}^{\mathrm{HVC}} \lesssim 0.2 \times 10^{20}\,\mathrm{cm^{-2}}$. Only for some MIVCs$^-$ and NIVCs$^-$ there is notable HVC HI. For a few MIVC$^-$ candidates, there is some sort of correlation meaning that the larger $N_{\mathrm{HI}}^{\mathrm{HVC}}$, the more molecules appear to be present. A physical interaction of HVCs with IVCs has been proposed as a formation scenario of MIVCs, e.g. for the Draco cloud (Herbstmeier et al. 1993) or IVC 135 (Weiß et al. 1999; Lenz et al.

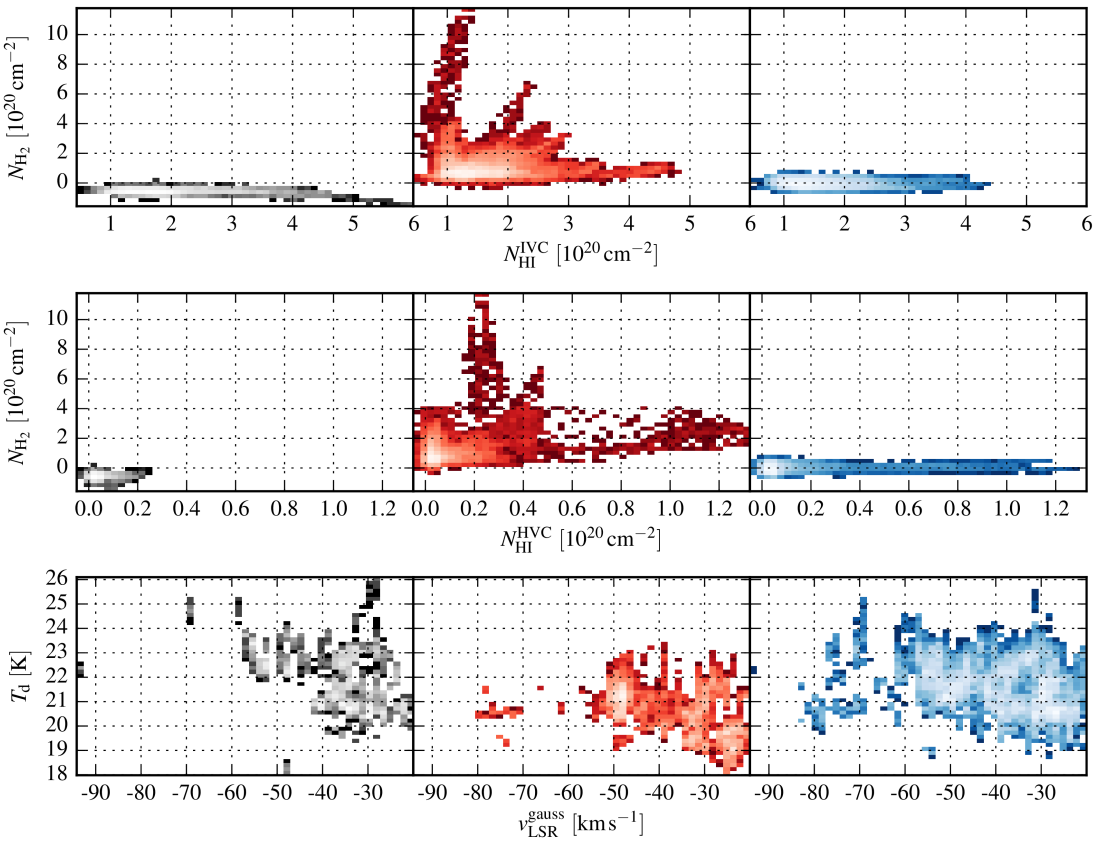

Fig. 5.8: Correlation properties of northern AIVCs$^-$, MIVCs$^-$, and NIVCs$^-$. The left, middle, and right plots show the correlation for the AIVCs$^-$, MIVCs$^-$, and NIVCs$^-$ respectively.

2015). For these particular objects there may indeed be a physical interaction between IVCs and HVCs. This is not true for the entire ensemble of MIVC$^-$ and NIVC$^-$ candidates.

Dust temperature T_d and central velocities v_{LSR}^{gauss} of Gauss components: For all three samples the dust temperatures from the modified black-body fits (Planck Collaboration XI 2014) decrease for lower absolute radial LSR velocities.

Total dust reddening $E(B-V)$ and LVC HI column density N_{HI}^{LVC}: For all three samples there is a slight positive correlation between the amount of LVC HI column density N_{HI}^{LVC} and the amount of total dust reddening $E(B-V)$ from Green et al. (2015) in these lines-of-sight. Presumably, LVC gas is located in front of the IVCs containing dust and causing a reddening signal. However, the amounts of reddening are slightly different for the different samples: For the AIVCs$^-$ the reddening is generally below 0.05 mag, while towards the MIVCs$^-$ there is somewhat larger reddening from the LVC material. The largest reddening magnitudes appear to be un-associated with the LVC gas.

Total dust reddening $E(B-V)$ and IVC HI column density $N_{HI}^{IVC^-}$: The correlation between N_{HI}^{LVC} and the total dust reddening $E(B-V)$ is more pronounced than that for $N_{HI}^{IVC^-}$. Hence, the IVC material does not cause the same amount of reddening as the LVC dust. Still, towards some MIVC$^-$ candidates

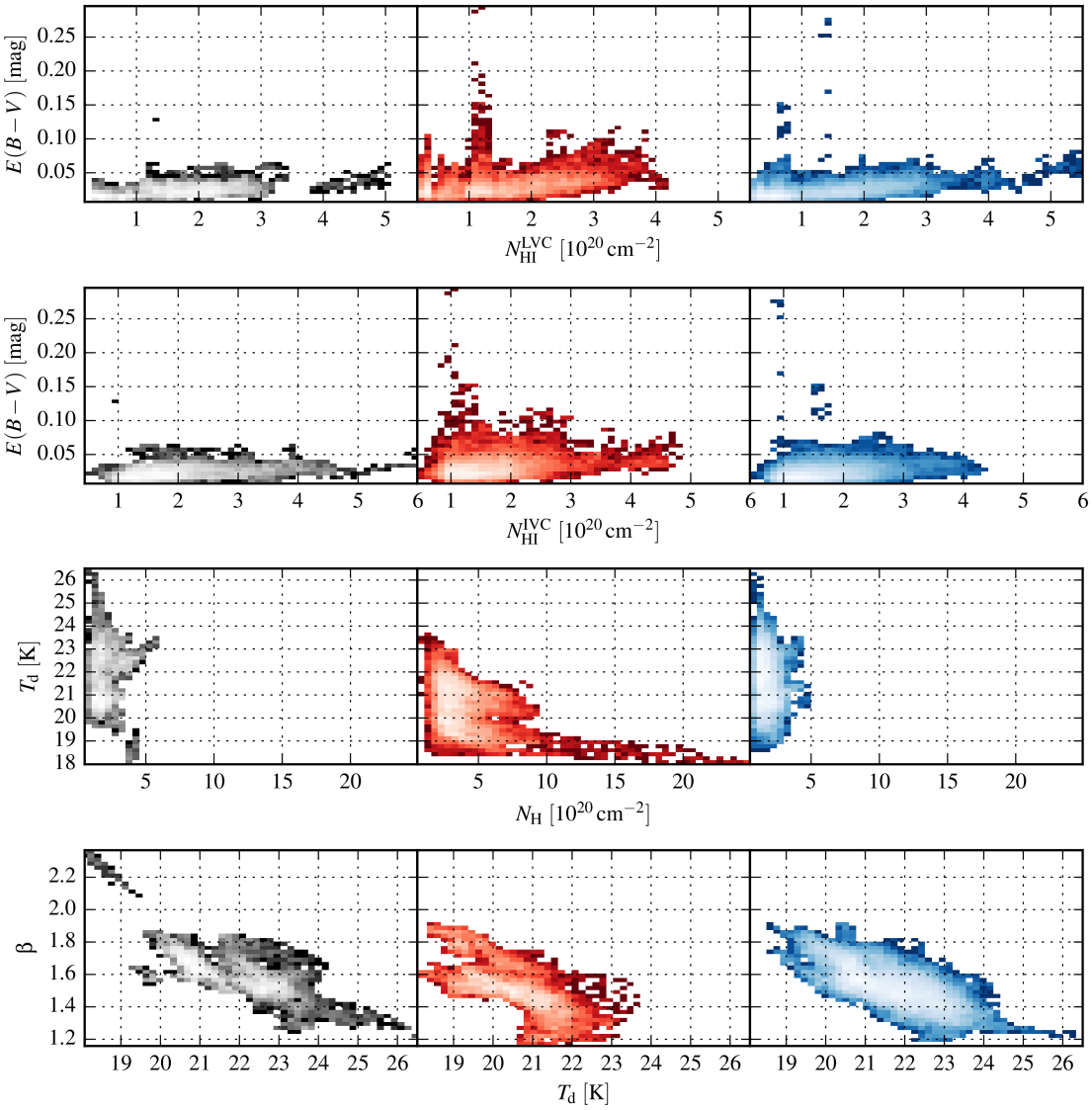

Fig. 5.9: Correlation properties of northern AIVCs$^-$, MIVCs$^-$, and NIVCs$^-$. The left, middle, and right plots show the correlation for the AIVCs$^-$, MIVCs$^-$, and NIVCs$^-$ respectively.

the reddening is somewhat correlated to the HI column densities. For the AIVCs$^-$ and NIVCs$^-$ there is no apparent correlation. If at all, there may be a very weak positive correlation.

Dust temperature $T_{\rm d}$ and total hydrogen column density $N_{\rm H}$: Only for the MIVC$^-$ candidates the dust temperatures decrease with increasing total hydrogen column density. For the other two samples, the two quantities appear to be uncorrelated. This could imply that for $N_{\rm H} \lesssim 5 \times 10^{20}\,{\rm cm}^{-2}$ the dust is not able to cool significantly with respect to the environment of the cloud.

Dust emissivity exponent β and dust temperature $T_{\rm d}$: The generally observed anti-correlation between $T_{\rm d}$ and β (e.g. Planck Collaboration XI 2014) is recovered for all three samples. There are two distinct distributions of objects at low $T_{\rm d}$ with either $\beta \simeq 1.6$ or $\beta \simeq 1.8$, which is best seen

for the MIVCs. These two categories are spatially distinct: The larger $\beta \simeq 1.8$ is found only around $(l, b) \simeq (280°, 55°)$ while $\beta \simeq 1.6$ is typical for the general population of candidates. This may reflect different dust properties within the structure near $(l, b) \simeq (280°, 55°)$.

5.4.5 Dust reddening

In the diffuse ISM, distances to individual gas clouds are difficult to estimate, like for IVCs (e.g. Putman et al. 2012). One approach is to use the reddening of stellar light by dust grains along the line-of-sight towards stars with known distance. This technique is increasingly more successful due to the large number of measured stellar colours and stellar distances in our Galaxy. One of the most recent works on the interstellar reddening by dust grains is by Green et al. (2015), who use about 800 million stars in their analysis. For each of these stars they probabilistically infer the distance and reddening. Green et al. estimate the reddening within individual distance bins. In this way they perform a 3D tomography of dusty structures in our Galaxy, constraining how much dust is located within some distance interval. The dust is related to gaseous structures, allowing to gain information about the 3D gas distribution as well. We use their data set to search for reddening signals towards the IVC$^-$ samples with the aim to constrain the distances to these objects. Green et al. (2015) give uncertainties of up to ∼50% on the estimated distances. Their reddening measurements are consistent with other methods within ∼0.05 mag.

We compute maps of dust reddening for distance bins of 100, 200, 316, 398, 501, 794, 1000, 1995, 5012, and 10,000 pc as given by Green et al. (2015). Differences between two consecutive distance bins give the dust reddening between these bins. The resulting difference maps are evaluated for the AIVCs$^-$, MIVCs$^-$, and NIVCs$^-$ as the black, red, and blue histograms in Fig. 5.10. Note that the y-axes have a logarithmic scale. When all the different reddening signals from all distance bins are summed up, the total reddening is obtained, which was shown in Fig. 5.7 already.

Several conclusions are drawn from these plots:

- The total reddening signal is contained within ∼2 kpc.
- There is some finite reddening signal in all distance intervals up to ∼794 pc with an occurrence of more than 10^{-2}.
- The largest reddening is found in individual distance intervals towards the MIVC$^-$ candidates.
- In the lowest distance bin of 100 – 200 pc, all three samples are very similar. This reddening is expected to be associated with the foreground since the IVC candidate clouds are thought to be located at larger distances of up to 2 kpc.
- Within 200 – 316 pc, the MIVCs$^-$ show significantly larger reddening as compared with the other two samples, which is associated with the Draco cloud.
- For distances larger than ∼316 pc, the AIVCs$^-$ show less reddening than the MIVCs$^-$ or NIVCs$^-$.

The reddening signals within the distance bins 501 – 794, 794 – 1000, and 1000 – 1995 pc with $b \lesssim 40°$ are apparently associated with gas and dust in the thick disk and lower halo of the Milky Way, not necessarily to the candidates themselves. This is evident from the smooth distribution of the reddening, which is extended over much larger scales than the individual candidates.

In the distance bin 398 – 501 pc, there are reddening signals towards some of the known MIVCs. Most prominent is Draco contributing the largest reddening, but also towards IVC 135 and IVC 210 there is a signal. The MIVCs around $l \simeq 280°$ do not show any reddening in this distance interval. For 301 – 398 pc there is reddening towards most of the known MIVCs increasing even more for 200 – 301 pc. In this

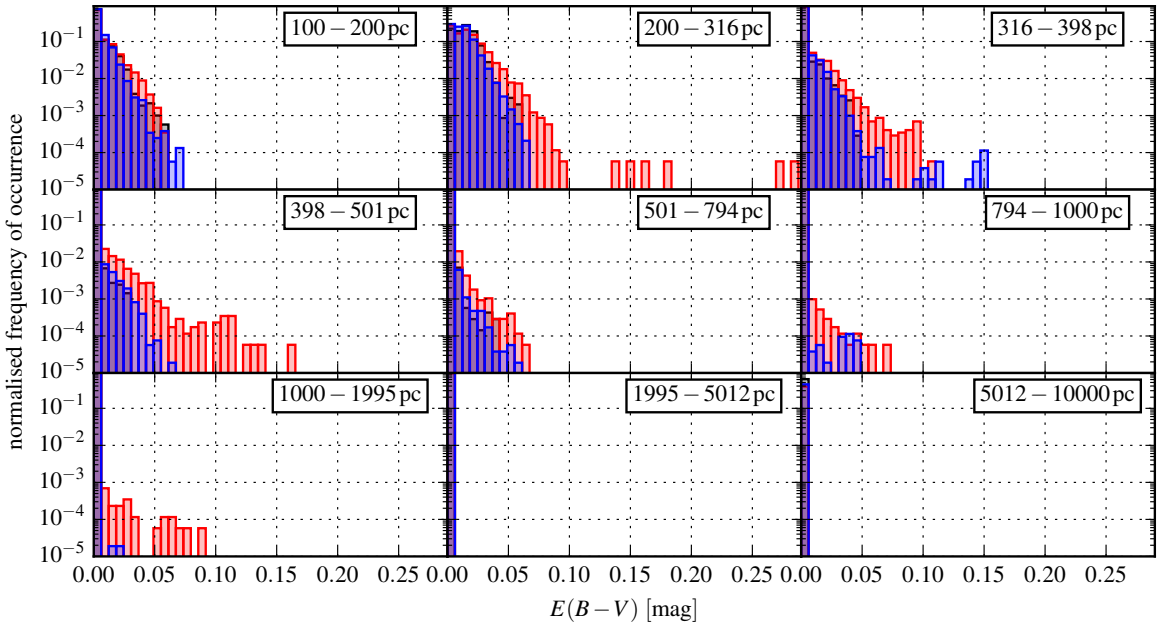

Fig. 5.10: Reddening signal as inferred by Green et al. (2015) towards AIVC$^-$, MIVC$^-$, and NIVC$^-$ samples for different distance bins. In each plot, at the top-right we plot the distance interval in which the reddening signal is contained. The histograms for each distance bin is normalised to unity. The AIVCs$^-$ are plotted in black, the MIVCs$^-$ in red, and the NIVCs$^-$ in blue.

bin, also the known MIVCs around $l \simeq 280°$ show a strong signal. Hence, the dust reddening towards the known MIVC candidates suggest upper distances of ∼300 pc for the Magnani & Smith (2010) CO clouds near $l \simeq 280°$, and ∼500 pc for Draco, IVC 135, and IVC 210. These distances are compatible with published limits (Gladders et al. 1998; Benjamin et al. 1996; Röhser et al. 2014).

The derived dust reddening maps of Green et al. (2015) suggest that all three samples of MIVCs$^-$, AIVCs$^-$, and NIVCs$^-$ are found within a distance of ∼500 pc. The question is if this can be really true for all clouds of the samples. For the MIVCs$^-$ there are clear reddening peaks located at the cloud's locations, especially for the known MIVCs. However, AIVCs$^-$ contain significantly less dust than MIVCs$^-$. If an AIVC$^-$ is located at larger distances, the reddening signal would decrease accordingly. The inferred reddening for all samples within 200 pc is very similar. We interpret this as a similar amount of reddening due to foreground objects, not by the clouds themselves. The remaining reddening signals of AIVCs$^-$ for larger distances like 398 – 501 pc and 501 – 794 pc is likely also completely related to an AIVC candidate at $b \simeq 40°$, which may be dominated by foreground dust. This would imply that the AIVCs$^-$ are generally too far away to cause a measurable reddening signal, since we know that they contain dust from their associated weak FIR emission. This may argue for a larger distance of the AIVCs$^-$ as compared with the other samples. Note that the maximum reliable distances of the reddening as given by Green et al. (2015, their Fig. 8) is well above 2 kpc for most lines-of-sight at high Galactic latitudes. Hence, the lack of detections of dust is likely not related to a lack of stars.

5.4.6 Kinematical properties of northern samples

Next, we analyse the kinematical properties of the Gaussian components of the IVC$^\pm$ samples. The GSR radial velocities are compared with a model of Galactic rotation, which is explained in the following.

5.4.6.1 Rotational model

The rotation curve of our Galaxy is converted into the corresponding radial velocity we would observe at given coordinates l and b. The rotational velocity of the Sun is fixed to $\theta_0 = 220\,\mathrm{km\,s^{-1}}$ and its Galactocentric distance to $R_0 = 8.5\,\mathrm{kpc}$ (Brand & Blitz 1993). The parametrisation of the rotation curve $\theta(R)$ is taken from Brand & Blitz (1993, their Eq. 6) applying their fitted parameters. The rotational velocities at Galactocentric distance R, Galactic longitude l, and Galactic latitude b are transformed to the observable LSR velocity using Eq. 1 of Brand & Blitz (1993).

In this way the observed rotation curve is calculated for different Galactocentric radii. For a more intuitive measure for the solar neighbourhood, instead, we compute the observed rotation curve depending on the heliocentric distance d. The heliocentric distance d is converted to the Galactocentric radius R for l and b using Eq. 2 from Brand & Blitz (1993):

$$R = \sqrt{d^2 \cos^2 b + R_0^2 - 2R_0 d \cos l \cos b}. \tag{5.3}$$

As the result, the observed rotation curve is obtained depending on Galactic longitude l, latitude b, and heliocentric distance d.

For a more realistic kinematical model of the IVC sky, we include additional velocity components of the HI halo as inferred by Marasco & Fraternali (2011). They model the 3D HI distribution of the Milky Way in comparison to the LAB survey (Kalberla et al. 2005). Marasco & Fraternali (2011) estimate a vertical scale height of the extra-planar gas of $z = 1.6^{+0.6}_{-0.4}\,\mathrm{kpc}$ with a rotational vertical lagging of $-15 \pm 4\,\mathrm{km\,s^{-1}\,kpc^{-1}}$, i.e. the rotational velocity decreases away from the disk. Furthermore, they find evidence for a global vertical motion with $v_z = -20^{+5}_{-7}\,\mathrm{km\,s^{-1}}$ and a global radial infall towards the Galactic centre with $v_r = -30^{+7}_{-5}\,\mathrm{km\,s^{-1}}$.

These vertical and radial velocity components are projected onto the lines-of-sight for l and b by applying Eq. 3 of Marasco & Fraternali (2011):

$$v_{\mathrm{LSR}}(l, b, R) = v_r \left(\frac{R^2 + d^2 - R_0^2 - z^2}{2Rd} \right) + v_z \sin b + \left(\frac{\theta(R, z)\, R_0}{R} - \theta_0 \right) \times \sin l \cos b. \tag{5.4}$$

Without the solar rotational velocity θ_0, the corresponding GSR velocities $v_{\mathrm{GSR}}(l, b, R)$ are obtained. For the projection of the radial velocity component, one has to assume some height above or below the disk, for which we take $z = 1.6\,\mathrm{kpc}$ as estimated by Marasco & Fraternali (2011). The vertical lagging of $-15 \pm 4\,\mathrm{km\,s^{-1}\,kpc^{-1}}$ is included in the rotational velocity $\theta(R, z)$. Note that z is not considered in the heliocentric distance d. Hence, d quantifies the heliocentric distance within the 2D plane of the Milky Way disk.

5.4.6.2 Results

The distributions of $v_{\mathrm{GSR}}^{\mathrm{gauss}}$ with Galactic longitude l are shown for the IVC$^{\pm}$ samples in Fig. 5.11. The top and bottom rows are for the IVC^{-} and IVC^{+} samples. In the left, middle, and right column the AIVCs$^{\pm}$, MIVCs$^{\pm}$, and NIVCs$^{\pm}$ are plotted in black, red, and blue. On top of the data, we plot the rotational model as described in Sect. 5.4.6.1 including a radial, vertical, and lagging velocity component. The velocity curves are plotted for Galactic latitudes of $b = 20°$ (solid), $b = 50°$ (dashed), and $b = 80°$ (dotted). The different line colours indicate different heliocentric distances. The size and colour of the data points encode the latitude coordinate b of the candidates, being large and bright for low latitudes or small and dark for high latitudes.

The kinematics of the IVCs$^{\pm}$ appear to be reproduced by the rotational model, suggesting that the

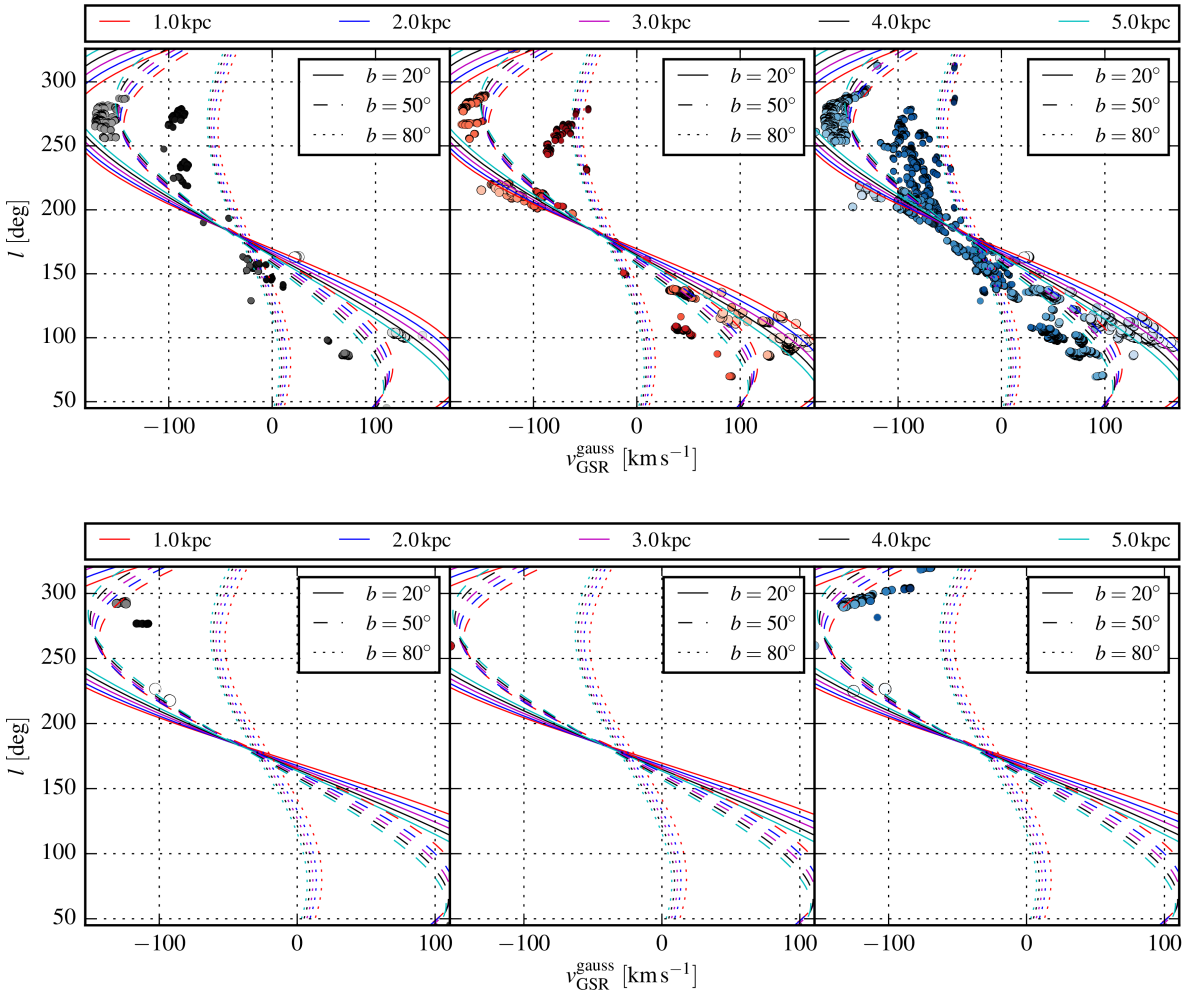

Fig. 5.11: Radial GSR velocities of northern IVC$^{\pm}$ samples compared with Galactic longitudes l. The top row is for the IVC^{-} and the bottom row for the IVC^{+} samples. The left column is for the AIVCs$^{\pm}$ in black, the middle column for the MIVCs$^{\pm}$ in red, and the right column for the NIVCs$^{\pm}$ in blue. The velocities of the individual candidates are given by the $v_{\mathrm{GSR}}^{\mathrm{gauss}}$ from the Gaussian decomposition of the HI survey data. The size and colour of each point encode the latitude coordinate b of the candidates, being large and bright for low latitudes or small and dark for high latitudes. The different lines show the modelled rotation velocities including a radial, vertical, and lagging velocity component (see Sect. 5.4.6.1 for details). A vertical height $z = 1.6$ kpc is assumed, for which the velocities are modelled at some heliocentric distances d and latitudes b as given in the legends. The solid, dashed, and dotted lines are for $b = 20°$, $b = 50°$, and $b = 80°$. The red, blue, magenta, black, and cyan lines are for heliocentric distances within the Galactic plane of $d = 1$ kpc, 2 kpc, 3 kpc, 4 kpc, and 5 kpc.

samples contain velocity contributions from Galactic rotation. Furthermore, the velocity components inferred by Marasco & Fraternali (2011) appear to describe the IVC$^{\pm}$ candidates well and not only the large-scale extra-planar HI gas in general. Because of the low number of IVC^{+} candidates, the results are not as conclusive as for the IVC^{-} samples. Large heliocentric distances within the Galactic plane of 5 kpc or more are not required to model the kinematics of the IVC$^{\pm}$ samples, which would be incompatible with the distances constraints of IVCs in general (Albert & Danly (2004), also Sect. 5.4.5).

5.4.7 Models of Galactic fountains

The Galactic fountain is studied in many simulations that analyse the kinematics and distributions of ejected clouds in the Galactic halo. Melioli et al. (2008) simulate a Galactic fountain with 100 supernovae of type II that go off at the solar radius at $R_0 = 8.5$ kpc.

Melioli et al. find that the ejecta rise vertically and, due to the differential rotation of the Galactic disc and a slowly rotating halo, the ejecta experience drag and stretch along the orbit forming a large low-density tail of material over several kilo-parsecs (Melioli et al. 2008, their Fig. 3). The simulated fountain lifts a mass of $\sim 2.5 \times 10^5$ M$_\odot$ into the Galactic halo. At the launch of the fountain, the ejected material tends to move outwards towards larger Galactiocentric radii because of angular momentum conservation. After approximately 50 Myr the lifted material reaches its maximum height of $|z| \simeq 2$ kpc. From that point on most of the material reverts its radial motion going back towards lower Galactocentric radii because of loss of angular momentum, which is transferred to the resting halo material. After 150 Myr about half of the ejected material has moved down to scale heights of $|z| \lesssim 800$ pc. The ejected material returns within a radial distance of $\Delta R \simeq 0.5$ kpc from the launching radius. There is no significant radial mixing of material.

The ejected material condenses into cool clouds due to the action of thermal instabilities once the ascending gas has inverted its direction of motion back towards the disk again. The newly formed and infalling clouds show negative vertical velocities between $v_z = -50\,\mathrm{km\,s^{-1}}$ and $-100\,\mathrm{km\,s^{-1}}$. Most of the fountain gas condenses into clouds without being chemically altered or mixed with the halo.

For fountains that are launched at lower Galactocentric radii, e.g. $R \simeq 4.5$ kpc, Melioli et al. (2008) find that these fountains are trapped easily within the disk due to the large densities and vertical pressures within the inner Galaxy.

5.4.7.1 Orbits of fountain ejecta

In order to get a better understanding of how the orbital motions of Galactic fountain ejecta look like, we use an unpublished code by P. Kalberla. In this code the Milky Way mass model of Kalberla & Dedes (2008) is used to calculate for given input parameters the ballistic trajectory of clouds due to gravity and some simple treatments of gas physics.

The input parameters are the 3D spatial location (x, y, z) of the ejection point and the 3D velocity components (v_x, v_y, v_z) of the ejected material in addition to Galactic rotation. The drag is parametrised by the HI column density of the ejecta and the drag coefficient.

The ejection point should be located above the Galactic disk, otherwise the material may get stuck within the disk. A real fountain will likely ionise and free its surroundings by radiation, stellar winds, and supernovae, which is not taken into account. Hydrodynamical simulations show that initially spherical objects are elongated and flattened as they move through a thin halo medium (e.g. Heitsch & Putman 2009). This corresponds to a drag coefficient of ~ 1.

We show a model with the ejection point 0.5 kpc above the Sun and 0.5 kpc ahead in the direction of Galactic rotation towards $l = 90°$. The initial velocity in addition to the rotational motion is set to $(v_x, v_y, v_z) = (0, 0, +100\,\mathrm{km\,s^{-1}})$ moving straight up. The HI column density of the cloud is chosen to be $1 \times 10^{20}\,\mathrm{cm^{-2}}$ with a drag coefficient of unity.

In Fig. 5.12, l, b, v_{LSR}, and the spatial lagging d_{lag} behind a pure rotation are plotted for the fountain model. In all of the Figures the position of the moving Sun is plotted as the black circle. The orbital parameters are chosen to be $R_0 = 8.5$ kpc and $v_0 = 220\,\mathrm{km\,s^{-1}}$ (Brand & Blitz 1993). The orbit is calculated until the ejected object has hit the Galactic disk at $b = 0°$. The coloured points show the position of the ejected cloud as time progresses, colour-coding the time-evolution of a particular quantity

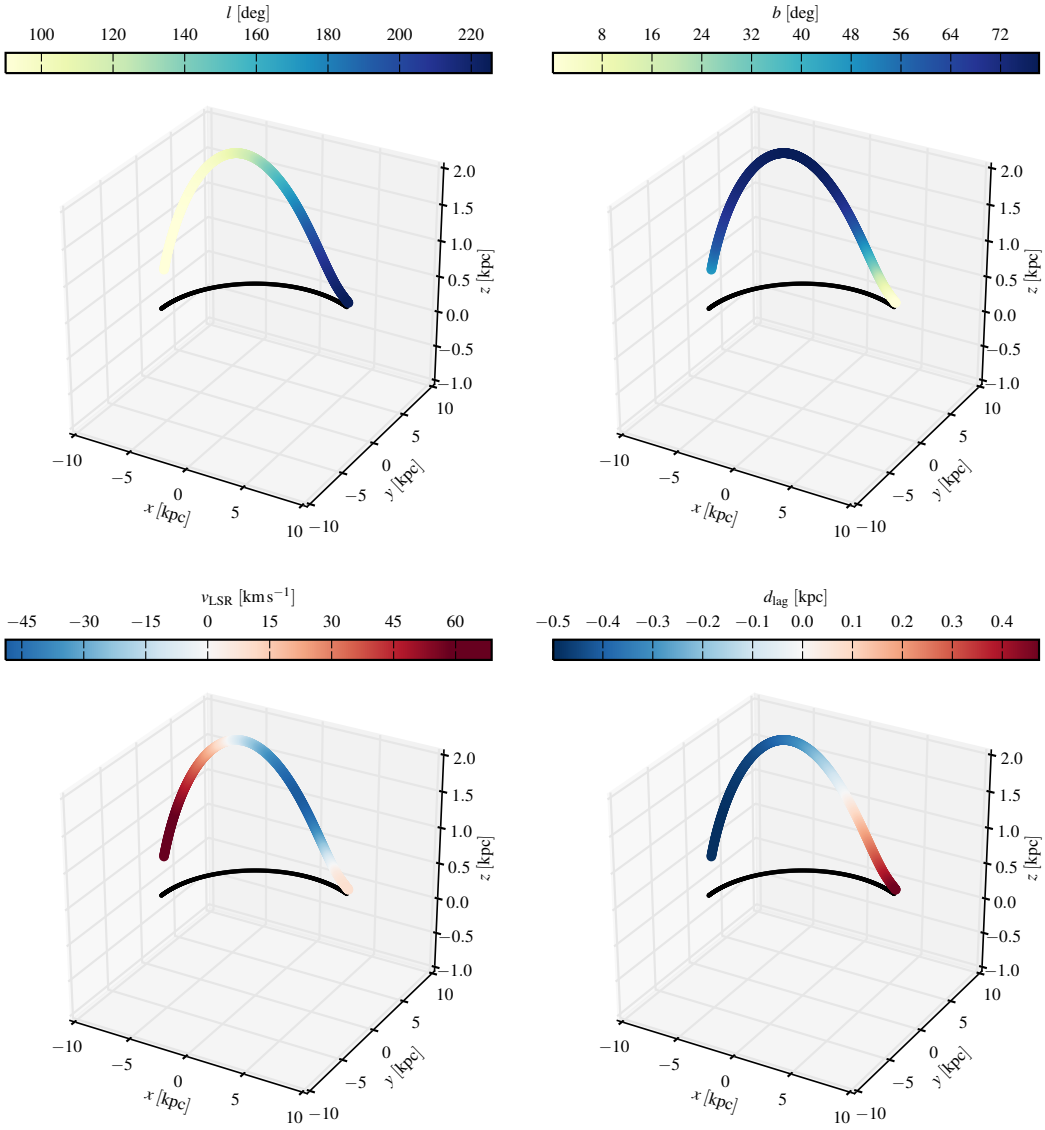

Fig. 5.12: Observable Galactic longitude l (*top-left*), latitude b (*top-right*), LSR velocity $v_{\rm LSR}$ (*bottom-left*), and spatial displacement $d_{\rm lag}$ (*bottom-right*) of an ejected cloud (see text for details). The orbits are computed using an unpublished code by P. Kalberla. The Sun moves around the Galactic centre, plotted as the black circle. The fountain is launched at $z = 0.5$ kpc and 0.5 kpc ahead of the orbit towards $l = 90°$.

along the fountain orbit.

The longitude coordinate increases with time, suggesting a lagging of the ejecta behind the rotation of the Sun. The latitudes decrease continuously until the cloud hits the disk at $b = 0°$. Initially, the ejecta move away from the Sun towards high Galactic latitudes, which is indicated by the positive radial velocities $v_{\rm LSR}$. Near the peak of the orbit, the observable radial velocity is vanishing and turns negative further along the orbit. Towards the end of the cycle the radial velocities are again close to 0 km s^{-1} due to projection effects. The most negative velocity is $\sim$−50 km s^{-1}, which is not reproducing the maximum negative radial velocity of the northern IVC sky.

If an ejected fountain object is not fully ionised during launch such that HI emission is observable, this material is mixed up in HI observations with the disk gas around $v_{\rm LSR} \simeq 0\,{\rm km\,s^{-1}}$. This does not allow to distinguish from HI emission alone between normal disk gas that is rotating within the disk and fountain clouds that are near the peak of the fountain orbit. However, the FIR emission of this gas may be different than for the normal disk material.

In the bottom-right part of Fig. 5.12, we show the lagging of the ejected material relative to the pure disk rotation of the Sun. The lagging is calculated by determining the difference in orbital phase of the ejecta and the orbital phase of the Sun within the *xy*-plane of the disk. This phase difference is converted into an approximate spatial distance at the Galactocentric radius of the Sun. Initially, the ejected cloud is ahead of the orbit because of the displacement in the direction of rotation. Eventually, the rotation catches up leading to a maximal lag of ∼0.5 kpc. The lagging is likely explained by 1) the increase in Galactocentric distance of the ejecta and 2) the drag exerted onto the clouds by the halo. Over the orbit, the pure rotational velocity decreases by ∼6%.

The maximum height of the ejecta is $z \simeq 1.8\,{\rm kpc}$, which is reached after ∼30 Myr. After another ∼30 Myr, the ejecta are again at a scale height of $z \simeq 0.5\,{\rm kpc}$. Towards the end of the fountain cycle, the ejecta are observed at large Galactic longitudes of $l \simeq 180 - 235°$. Note that the fountain is launched at $z = 0.5\,{\rm kpc}$, which is chosen because of computational reasons. A real fountain is launched around $z \simeq 0\,{\rm pc}$ and is accelerated within some time, increasing the duration of the fountain cycle.

Summarising, the spatial and temporal properties of the ballistic orbits of the fountain ejecta are comparable to the properties of the simulated hydrodynamical fountain by Melioli et al. (2008).

5.4.7.2 Possible origins of the northern IVC sky

Assuming that a large fraction of the northern IVC sky originates from a Galactic fountain process, the simulations of Melioli et al. (2008) and the calculations of ballistic orbits suggest that strong star formation activity near the solar radius should have happened ∼100 Myr ago. Between $l \simeq 90 - 270°$ we observe infalling IVC gas, most of which is nearby with less than 2 kpc distance. This material shows evidence for a global vertical and radial (towards the Galactic centre) infall motion in addition to a signature of Galactic rotation (Marasco & Fraternali (2011), Sect. 5.4.6).

The star formation activity that may have driven the fountain should have occurred ahead in the rotational direction of the disk because of the stretching and lagging of the ejected material behind the purely rotating orbit. We estimate a lagging ∼1 kpc for a fountain duration of ∼60 Myr. This suggests a launching towards $l \simeq 45 - 135°$ for which the material has time to lag behind the disk rotation such that fountain material could be observed also towards the Outer Galaxy and trailing the Sun's orbit. Thus, the disk rotation sets boundary conditions on any Galactic fountain that is thought to be related to the northern IVC sky as we observe it.

In this scenario a star formation event like in the simulations of Melioli et al. (2008) is imagined that launches over a time scale of 30 Myr material into the halo with a total mass compatible with the northern IVC sky. Smaller individual events could also continuously eject material into the halo (e.g. de Avillez 2000). In combination this could also lead to a coherent and continuous infall of IVCs on the northern sky. Spiral density waves would, however, may cause naturally episodic star formation activity (e.g. Elmegreen 2011).

5.4.7.3 Observational evidence for past star formation activity

There are numerous studies of local star formation activity that is still observable today, either directly or by its remnants. A major limitation in finding evidence for past high-mass star formation is that

high-mass stars have a short lifetime and stellar remnants die out quickly, e.g. within some 10^5 yr (e.g. Blondin et al. 1998), as compared with the total fountain time scale of tens of Myr. High-mass star formation is needed for the occurrence of supernovae of type II. In the solar neighbourhood, the Gould Belt contains most of the local star formation activity with an age of less than 60 Myr (for a recent review Bobylev 2014). The spatial dimensions of the Gould Belt are $350 \times 250 \times 50$ pc with an inclination of $\sim 20^\circ$ with respect to the Galactic disk (Bobylev 2014). Above, we estimate the spatial distance the fountain ejecta lag behind the pure Galactic rotation. This lagging is of the order of 1 kpc. If star formation in the Gould Belt is the origin of the IVC sky, this would lead to a clustering or over-abundance of IVCs in the longitude range $l \simeq 180 - 270^\circ$ in the trailing direction of Galactic rotation. Such asymmetry is not observed. Hence, more distant star formation activity is more plausible that happened even longer ago.

De la Fuente Marcos & De la Fuente Marcos (2008) study the number and age distribution of young stellar clusters with ages of up to 100 Myr within a distance of 2.5 kpc from the Sun considering different bins of Galactic longitude. Young stellar clusters can be thought of as a tracer for past star formation activity because these star clusters have been formed in specific star formation events and these clusters are not dispersed and incorporated into the population of field stars of the Galaxy yet.

In their Fig. 4, De la Fuente Marcos & De la Fuente Marcos (2008) show the resulting age distribution of young clusters. For $l = 90 - 180^\circ$ there are two peaks of cluster abundance at ages of 60 Myr and 20 Myr. The peak at 60 Myr is only seen at these longitudes. Towards $l = 45 - 90^\circ$ they report a peak in the abundance with ages of 90–100 Myr in addition to a peak at 20 Myr.

These relative over-abundances could indicate episodes of more intense star formation. Their positions and ages would match the requirements discussed above in order to reproduce the northern IVC^- sky as it is observed today. This could have happened also at the solar radius in the Sagittarius or Perseus spiral arms (compare with Fig. 1 of Vallée 2008).

If the IVC^+ candidates are also part of a Galactic fountain, they should originate from star formation nearby that has ejected the material within the last $\sim$50 Myr, since the IVCs^+ apparently move away from us, perhaps upwards into the halo, being in an initial stage of the fountain. Towards $l = 180 - 270^\circ$ the distribution of young clusters shows peaks at 20 Myr (De la Fuente Marcos & De la Fuente Marcos 2008). Qualitatively, this could match the origin of the IVCs^+ if these are observable in HI in the stage of ejection during the fountain cycle and not fully ionised.

The general question remains if it is possible or even sensible to pinpoint a particular star formation event that is responsible for the IVC distribution around our Galaxy. It may be a continuous process and the feedback of even small star formation sites may contribute to the ejection of mass. However, also such small star formation events have to fulfil the boundary conditions set by the rotation of the disk.

5.5 The HI-FIR correlation on the southern Galactic hemisphere

Now, we turn to the southern Galactic hemisphere and perform the same analysis as for the northern. The HI-τ correlation plot for $b < -20^\circ$ is shown in Fig. 5.13, the corresponding linear parameters are given in Table 5.1 on page 89. The same fitting method is applied as for the northern hemisphere (Sect. 5.2). However, there is one difference in the fitting method related to the Magellanic System.

On the southern hemisphere, there is the Magellanic System consisting of the Large and Small Magellanic Clouds, the Magellanic Stream, and the Leading Arm (e.g. Nidever et al. 2010). All these structures cover a large fraction of the southern HI sky. We expect an influence of the Magellanic System on the HI-τ correlation. The Magellanic Stream and the Leading Arm are so-far undetected in FIR emission (e.g. Planck Collaboration XXIV 2011; Brüns et al. 2005). The Magellanic Stream stretches

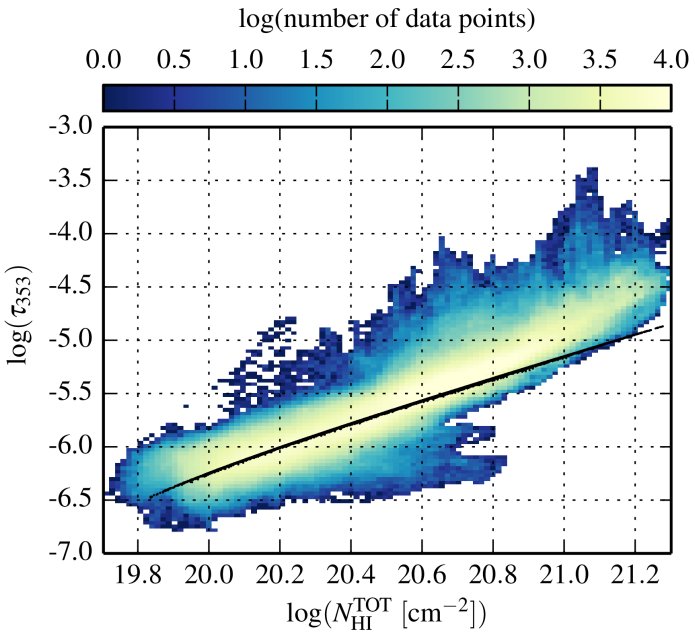

Fig. 5.13: HI-τ correlation plot for the southern Galactic hemisphere for $b < -20°$ latitudes. The HI column density is the combined LVC and IVC emission between $-100\,\mathrm{km\,s^{-1}} \leq v_{\mathrm{LSR}} \leq +100\,\mathrm{km\,s^{-1}}$. The black dots show the two-component linear model consisting of LVC and IVC contributions. From this model, 10000 data points are chosen randomly and plotted.

over the entire LVC and IVC velocity ranges and beyond (e.g. Nidever et al. 2010, their Fig. 8). The Magellanic System enters the correlation as pixels with large HI column density but low or vanishing dust optical depth. Thus, these structures should be excluded from the fit to the HI-τ correlation.

We apply the method of Planck Collaboration XVII (2014) who use the 3D HI model of the Milky Way from Kalberla & Dedes (2008) to separate the HI data cube into Milky Way and Magellanic System. All HI emission with a particular radial velocity is attributed to the Magellanic System if the modelled Milky Way HI emission is below $T_{\mathrm{B}}^{\mathrm{model}} = 60\,\mathrm{mK}$. These pixels are blanked for the HI column densities of the different velocity intervals. The threshold of 60 mK corresponds to a deviation velocity of about $45\,\mathrm{km\,s^{-1}}$ (Planck Collaboration XVII 2014). In the following plots the Magellanic System is included. Only for the fitting the masked data is used.

The blanking of the Magellanic System alters the fitted linear parameters of the HI-τ correlation notably but not significantly: The offset and the IVC emissivity are increased by less than 10% while the LVC emissivity is almost the same. This reflects the robustness of the iterative fitting method: Although the Magellanic System covers a large fraction of the sky with significant HI column densities, it is mostly rejected from the fit and its influence on the fitted parameters is small.

Despite the masking of the Magellanic System, still a negative offset in the global correlation is inferred (Table 5.1). This is in contrast to the northern hemisphere for which a positive offset is found. The implications of this negative offset in the HI-τ correlation is discussed at the end of this Section.

The HI-τ correlation is following a linear prescription at the low HI column density end that widens both towards larger and lower τ near $\log\left(N_{\mathrm{HI}}^{\mathrm{TOT}}\left[\mathrm{cm^{-2}}\right]\right) \simeq 20.4$ (Fig. 5.13). This suggests 1) the presence of considerable amounts of H_2 above this total HI column density and 2) the peculiarity of the Magellanic System that introduces HI gas with low τ. There is a large intrinsic scatter in the correlation indicated by the broad distribution for given N_{HI}.

Despite the low τ due to the Magellanic System, the global HI-τ correlation resembles that for the northern sky. Although, the two-component model does not produce such a large scatter of modelled data values as for the northern hemisphere. This indicates the dominance of the LVC gas on the southern hemisphere, or the low amount of IVC gas.

From the fitted linear parameters (Table 5.1), we estimate the distribution of H_2 within IVCs for $b < -20°$. The unmasked HI column densities including the Magellanic System are used. We decide for this since the masked material may falsely be associated with the Magellanic System. The resulting H_2 map is shown in Fig. 5.14, all blueish colours indicate positive N_{H_2}, all reddish negative N_{H_2}, i.e. FIR deficiency. The light- and dark-grey contours denote the total integrated (negative and positive) IVC HI gas at $N_{HI}^{IVC} = 0.75 \times 10^{20}\,cm^{-2}$ and $1.5 \times 10^{20}\,cm^{-2}$ respectively tracing the location of IVC complexes. The red and dark-violet contours show the locations of the inferred $MIVC^-$ and $MIVC^+$ candidates (Sect. 5.5.1). Known high-latitude molecular clouds and additional FIR-excess clouds identified by Reach et al. (1998) are shown by the green diamonds and squares (Reach et al. 1998, their Tables 3 and 4). On the southern hemisphere, no MIVC is known to date.

As for the northern hemisphere, the new HI and FIR data point out that previous studies of the HI-FIR correlation do not account for the full inventory of high-latitude FIR-excess clouds. In the H_2 map (Fig. 5.14) there are lots of small objects with significant H_2 column densities that are not identified by Reach et al. (1998). Again, there are some objects that are not identified in our analysis.

There are small and rather isolated excess objects that are often associated with larger complexes of excess emission. There are large regions of strong excess emission related to large amounts of gas and dust, e.g. towards $l \simeq 180°$. This excess emission is likely related to nearby star-formation activity in the Taurus and Orion molecular clouds (e.g. Dame et al. 2001). Again, note that the H_2 column densities are calculated applying the IVC dust emissivity. This is not correct for LVC gas and its molecular content, in which we are not interested here.

In contrast to the northern hemisphere, there is not much IVC gas on the southern hemisphere (Wakker 2004; Putman et al. 2012). In addition, most of the IVC material is located at $b > -40°$ closer in projection to the disk. The IVC features towards the southern pole are generally FIR deficient as indicated by the inferred negative H_2 column densities. This FIR deficient material is likely part of the Magellanic Stream, for which no FIR emission has been detected. Hence, both the southern IVC and HVC sky may be strongly influenced by the Magellanic System (compare also with Fig. 8 of Nidever et al. 2010). Most of the IVC gas can be assigned to negative H_2 column densities, but also LVC gas is associated with negative H_2 column densities, e.g. towards $(l, b) = (330°, -35°)$.

The negative offset in the southern HI-τ correlation The inferred negative offset of the HI-τ correlation (Table 5.1) is non-physical because there is no negative intensity. A negative offset indicates that the fit to the HI-τ correlation is too steep. Since this issue does not arise for the northern hemisphere, this in itself may be an interesting observation suggesting some differences between the two Galactic hemispheres because for both the same fitting procedure is applied. The presence of the Magellanic System is not accounting for the negative offset.

In the following we argue that this difference between the hemispheres may be related to the fact that the Sun is located 20.5 ± 3.5 pc above the Galactic plane (Humphreys & Larsen 1995). Towards the southern pole the lines-of-sight pass longer through the innermost parts of the Galactic disk. In his Table 3, Kalberla (2003) estimates a vertical scale height of 75 pc for the molecular component, 150 pc for the cold neutral medium, 400 pc for the warm neutral medium, and 950 pc for the diffuse ionised medium. Hence, the offset position of the Sun is equivalent to ~25% of the vertical scale height of the molecular gas and ~10% of the cold neutral medium.

Hence, one would expect to observe more cold and dense gas towards the southern Galactic hemisphere than for the northern. There should be more molecular gas, which is, however, not observable directly but inferable by the HI-FIR correlation. Indeed, on the southern hemisphere the amount of LVC HI emission at $b < -20°$ is larger by ~23% than on the northern hemisphere. The total Hα maps from

Finkbeiner (2003) show ∼27% more Hα emission on the southern hemisphere.

It is plausible that the amount of ionised and molecular hydrogen is enhanced especially for the mid-plane of the Milky Way as compared with other Galactic latitudes. The vertical distribution of stellar light is approximated by an exponential profile with a vertical scale height of ∼250 pc (e.g. Kent et al. 1991). Hence, at low latitudes the stellar density is highest and accordingly the ionising radiation. Furthermore, there is a correlation between mid-plane pressure and the amount of molecular gas in the disks of galaxies (Wong & Blitz 2002; Mac Low & Glover 2012). In the innermost plane, the atomic hydrogen may be more effectively converted into molecular hydrogen because of the large pressures.

Concluding, the negative offset in the HI-τ correlation on the southern Galactic hemisphere may be related to larger amounts of ionised and molecular hydrogen towards the southern as compared with the northern pole. This material is likely present within the fitting threshold of $N_{\mathrm{HI}} = 4 \times 10^{20}\,\mathrm{cm}^{-2}$ and may cause the negative offset in the southern HI-τ correlation by introducing FIR excess already at lower HI column densities, steepening the fit.

5.5.1 Search for southern molecular IVCs

By applying the search criteria for MIVCs (Sect. 5.2), we identify spatially distinct regions on the southern hemisphere that fulfil these requirements. In Fig. 5.14 (compare also with Figs. 2 and 5 of Planck Collaboration XVII (2014)) the red and dark-violet contours superimposed onto the southern H_2 distribution show the MIVC$^-$ and MIVC$^+$ candidates. The resulting list of ranked candidates is compiled in Table 5.4 containing a total number of 24 MIVC$^-$ and 20 MIVC$^+$ candidates. The ranking is done as described in Sect. 5.3.

In Table 5.4 the southern MIVC$^\pm$ candidates are listed with the most significant at the top. One can immediately tell that the southern IVC sky is different from the northern: On the northern hemisphere the most prominent MIVCs (Draco, IVC 135, IVC 210) are located at high Galactic latitudes of $b > +40°$. On the southern hemisphere such objects appear not to be existent. There, all the MIVC candidates are located at lower absolute Galactic latitudes of $b > -40°$, many at the lower latitude boundary near $b = -20°$. The amount of IVC gas and FIR excess emission is generally lower towards the southern pole (compare with Figs. 5.3 and 5.14). Note that on the southern Galactic hemisphere no MIVC has been found so far.

In the examination of the top-ranked southern MIVC$^\pm$ candidates, the same methods are applied as for the northern (Sect. 5.4.1).

General properties of southern MIVC$^\pm$ candidates The individual candidates are examined and their properties are derived and listed in the lower part of Table 5.3 on page 94. The southern MIVC$^-$ candidates have mean Galactic coordinates of $(\bar{l}, \bar{b}) \simeq (130°, -23°)$, indicating that the candidates are identified towards the rotational direction of our Galaxy close to the latitude limit of $b = -20°$. The southern MIVC$^+$ candidates have mean Galactic coordinates of $(\bar{l}, \bar{b}) \simeq (244°, -25°)$, which is roughly opposite to the Galactic rotation and similarly close to the latitude limit. The mean separation velocity for the MIVC$^-$ sample is $v_{\mathrm{LSR}}^{\mathrm{sep}} \simeq -40\,\mathrm{km\,s}^{-1}$, which is considerably different from the velocity cut of the IVCs at $v_{\mathrm{LSR}} = -20\,\mathrm{km\,s}^{-1}$. The MIVCs$^+$ have $v_{\mathrm{LSR}}^{\mathrm{sep}} \simeq +18\,\mathrm{km\,s}^{-1}$, which is in conflict with the IVC definition at $v_{\mathrm{LSR}} = +20\,\mathrm{km\,s}^{-1}$ indicating blending of LVC and IVC spectra. The mean peak HI column densities for both MIVC$^\pm$ samples are $\bar{N}_{\mathrm{HI}}^{\mathrm{peak}} = 2.3 - 2.4 \times 10^{20}\,\mathrm{cm}^{-2}$.

Except for MIVC candidate no. 1$^+$, all examined clouds consist of atomic two-phase media comprising warm and cold components. For most of the MIVC$^\pm$ candidates, there is a significant velocity offset between the two components. Similar as for the northern MIVC$^\pm$ candidates, there is evidence that the cold components have larger absolute radial velocities than the warm components. The estimated line

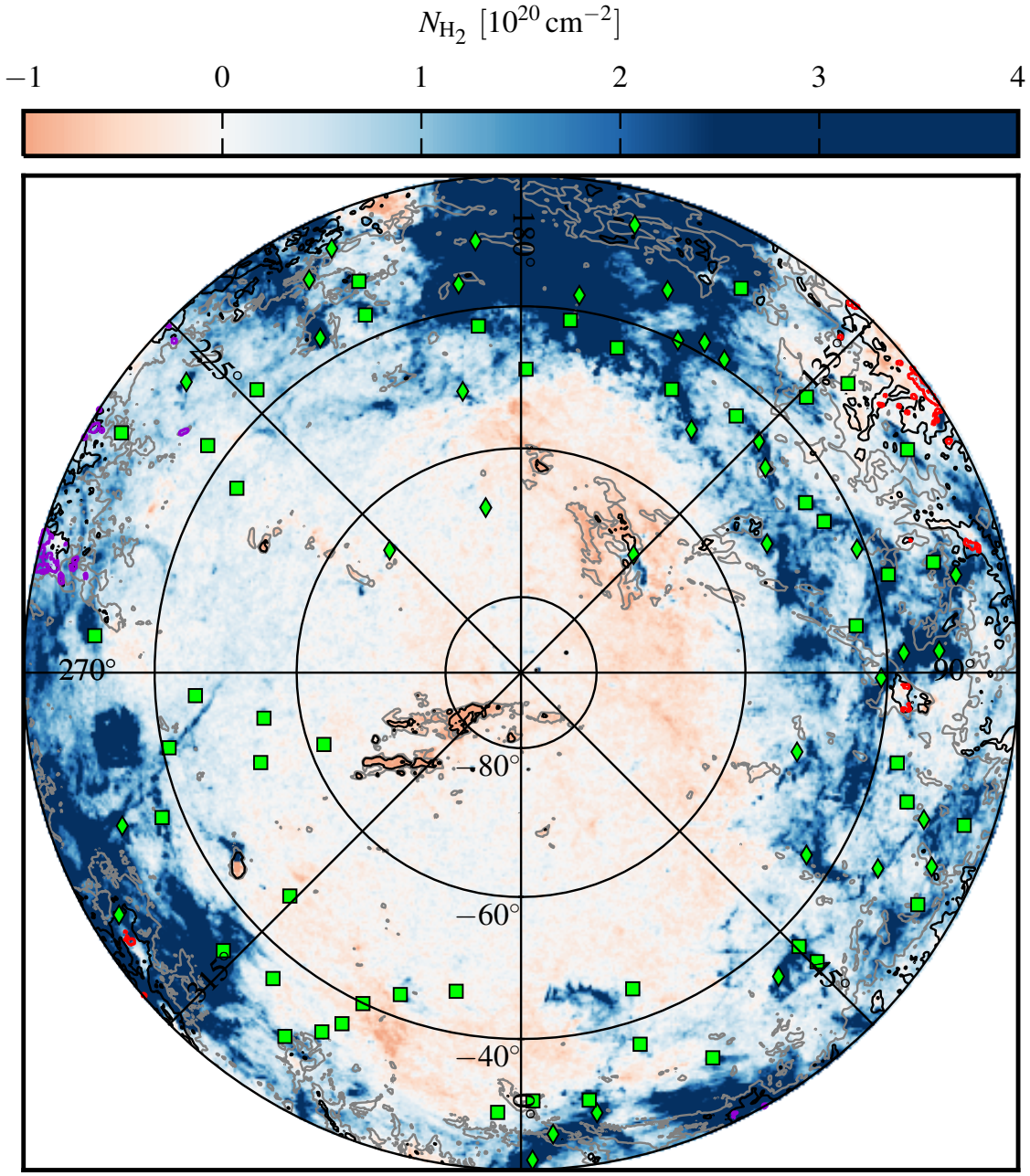

Fig. 5.14: Distribution of southern MIVC$^{\pm}$ candidates at $b < -20°$ on top of the inferred H_2 column densities. The map is plotted in zenith-equal area projection centred on the southern Galactic pole with Galactic coordinates. All blueish colours indicate positive N_{H_2}, all reddish negative N_{H_2}. The light- and dark-grey contours denote the total integrated (negative and positive) IVC HI gas at $N_{HI}^{IVC} = 0.75 \times 10^{20}$ cm^{-2} and 1.5×10^{20} cm^{-2} respectively tracing the location of IVC complexes. The red and dark-violet contours give the location of the inferred MIVC^{-} and MIVC^{+} candidates. The green diamonds indicate known high-latitude molecular clouds from FIR excess emission, the green squares give the positions of unidentified FIR excess sources as listed in Reach et al. (1998, their Tables 3 and 4).

no.	l [deg]	b [deg]	ϵ^{IVC} $\left[10^{-26}\,\mathrm{cm}^2\right]$	$N_{\mathrm{H_2}}^{\mathrm{peak}}$ $\left[10^{20}\,\mathrm{cm}^{-2}\right]$	S
			$v_{\mathrm{LSR}} < -20\,\mathrm{km\,s}^{-1}$		
1	125.21	−20.75	1.30 ± 0.01	0.47 ± 0.07	5420
2	137.96	−20.37	1.14 ± 0.02	0.28 ± 0.10	750
3	127.81	−20.32	1.19 ± 0.01	0.33 ± 0.08	670
4	129.29	−21.4	0.76 ± 0.01	1.29 ± 0.13	550
5	125.08	−22.83	0.91 ± 0.02	0.94 ± 0.10	490
6	126.64	−27.76	0.65 ± 0.01	0.61 ± 0.17	390
7	136.41	−25.49	1.13 ± 0.02	0.78 ± 0.10	380
8	127.26	−26.36	0.97 ± 0.02	0.22 ± 0.10	300
9	125.19	−25.6	0.92 ± 0.03	0.68 ± 0.10	240
10	118.39	−21.82	1.76 ± 0.08	0.95 ± 0.06	230
11	122.09	−20.87	0.79 ± 0.04	10.76 ± 0.22	220
12	108.73	−33.44	0.69 ± 0.01	0.54 ± 0.10	190
13	121.26	−21.83	1.46 ± 0.07	6.99 ± 0.29	180
14	121.91	−21.61	0.78 ± 0.03	10.93 ± 0.27	170
15	123.97	−25.1	0.44 ± 0.03	1.27 ± 0.22	120
16	121.18	−22.47	1.12 ± 0.07	8.90 ± 0.36	100
17	84.52	−36.64	0.25 ± 0.02	2.61 ± 0.18	80
18	85.25	−36.75	0.13 ± 0.02	4.78 ± 0.28	20
19	105.71	−24.56	0.00 ± 0.00	0.00 ± 0.00	0
20	303.25	−23.86	0.00 ± 0.00	0.00 ± 0.00	0
21	304.48	−23.68	0.00 ± 0.00	0.00 ± 0.00	0
22	310.58	−20.15	0.00 ± 0.00	0.00 ± 0.00	0
23	87.93	−37.26	−0.01 ± 0.02	30.01 ± 12.57	0
24	84.47	−37.52	−2.20 ± 0.30	0.10 ± 0.02	−40
			$v_{\mathrm{LSR}} > +20\,\mathrm{km\,s}^{-1}$		
1	257.73	−21.18	1.00 ± 0.01	0.45 ± 0.15	1460
2	234.52	−32.9	2.10 ± 0.02	0.13 ± 0.04	1420
3	258.16	−21.41	1.13 ± 0.01	0.34 ± 0.10	740
4	240.19	−20.89	0.66 ± 0.02	0.54 ± 0.17	710
5	238.08	−20.05	0.97 ± 0.01	0.25 ± 0.09	550
6	240.01	−22.14	0.71 ± 0.01	0.51 ± 0.14	400
7	254.18	−20.45	0.53 ± 0.05	1.51 ± 0.54	310
8	226.31	−22.8	0.95 ± 0.03	0.43 ± 0.12	300
9	256.91	−22.38	0.38 ± 0.04	2.49 ± 0.88	300
10	255.83	−25.96	0.49 ± 0.03	1.25 ± 0.42	160
11	257.52	−28.09	0.33 ± 0.02	1.26 ± 0.17	160
12	241.68	−20.24	0.47 ± 0.03	2.01 ± 0.35	130
13	225.51	−20.54	0.90 ± 0.05	0.75 ± 0.24	100
14	256.79	−25.93	0.13 ± 0.02	3.36 ± 1.43	70
15	254.28	−23.85	0.25 ± 0.01	1.77 ± 0.41	70
16	255.96	−20.47	0.04 ± 0.02	9.95 ± 3.81	40
17	29.3	−20.06	0.00 ± 0.00	0.00 ± 0.00	0
18	25.84	−21.25	0.00 ± 0.00	0.00 ± 0.00	0
19	25.52	−20.78	0.00 ± 0.00	0.00 ± 0.00	0
20	258.5	−24.45	−0.32 ± 0.02	1.04 ± 0.36	−230

Table 5.4: Locations of MIVC$^{\pm}$ candidates on the southern Galactic hemisphere. The columns give the cloud number, the Galactic longitude l and latitude b, the fitted IVC dust emissivity ϵ^{IVC} and its error, the peak H_2 column density $N_{\mathrm{H_2}}^{\mathrm{peak}}$ and its error, and the significance S as defined in Eq. (5.2).

widths are typical for the cold and warm neutral medium. The highest-ranked MIVC$^-$ candidates have a mean line widths of $\bar{\mathrm{FWHM}}^{\mathrm{cold}} \simeq 5.2 \pm 0.4\,\mathrm{km\,s^{-1}}$ close to the selection FWHM $< 5\,\mathrm{km\,s^{-1}}$, while the MIVC$^+$ candidates have narrower lines of $\bar{\mathrm{FWHM}} \simeq 3.8 \pm 0.2\,\mathrm{km\,s^{-1}}$. Hence, for the MIVC$^+$ candidates the criterion on line width is no issue, while even the top-ranked MIVC$^-$ candidates contain barely such cold gas. The mean line velocities are $\bar{v}_0^{\mathrm{cold}} = -56.0 \pm 0.3\,\mathrm{km\,s^{-1}}$ and $\bar{v}_0^{\mathrm{cold}} = +22.1 \pm 0.1\,\mathrm{km\,s^{-1}}$ respectively, the latter of which may be biased by the velocity cut at $v_{\mathrm{LSR}} = +20\,\mathrm{km\,s^{-1}}$.

The cold gas fractions are $f^{\mathrm{cold}} > 40\%$. For the MIVCs$^-$, most of the data is rejected for the local HI-τ correlation surrounding the candidates indicating large amounts of LVC gas and dust. Also for the MIVC$^+$ candidates the fraction is on average larger than for the northern MIVC$^-$ candidates. This indicates larger amounts of gas and dust towards the southern MIVC$^\pm$ candidates.

Because of the larger amounts of gas and dust, the fitting of the local HI-τ correlation results into more scattered offsets R, dust emissivities ϵ^{LVC}, and ϵ^{IVC}. Some IVC emissivities are larger by a factor of three as compared with the northern hemisphere. This, again, suggests bright HI and FIR emission of the surroundings complicating and biasing the fits. The inferred peak H_2 column densities are statistically not as significant as for the northern hemisphere with means of $\bar{N}_{\mathrm{H_2}} = 0.5 \pm 0.1 \times 10^{20}\,\mathrm{cm^{-2}}$ and $0.5 \pm 0.3 \times 10^{20}\,\mathrm{cm^{-2}}$, respectively. The Spearman rank coefficients $\rho^{\mathrm{LVC}-\tau}$ and $\rho^{\mathrm{IVC}-\tau}$ indicate for most of the considered candidates that the IVCs are more related to the total dust optical depths than the LVCs.

The inspection of the data cubes reveals that the southern MIVC$^\pm$ candidates are not isolated and often located close to significant LVC emission. Both in spectral and spatial dimensions the objects connect to other LVC or IVC gas. Sometimes, the additional IVC emission is clumpy or filamentary. None of the southern MIVC$^\pm$ candidates are characterised as being likely MIVCs because of the difficulties with the LVC gas and dust emission. Some of the highest ranked southern MIVC$^\pm$ candidates are connected to larger IVC structures that stretch even closer towards the disk. This may suggest that at least some of the candidates are more likely associated with the Milky Way disk rather than to the halo.

Here, the respective top-ranked MIVC$^-$ and MIVC$^+$ candidate is discussed in more detail, while two additional MIVC$^\pm$ candidates each are shown in the appendix (Sect. A.3).

Candidate no. 1$^-$ The MIVC candidate no. 1$^-$ is located towards significant LVC HI emission with at least $N_{\mathrm{HI}}^{\mathrm{LVC}} \simeq 4 \times 10^{20}\,\mathrm{cm^{-2}}$. The MIVC candidate is coherently connected in projection to the emission of the Andromeda galaxy (Fig. 5.15). For the two-component fit to the HI-τ correlation, we increase the upper HI column density threshold to $N_{\mathrm{HI}} = 5 \times 10^{20}\,\mathrm{cm^{-2}}$, otherwise the fit would not work because almost all LVC HI column densities are larger than the usual threshold.

There is an association of the FIR emission to the IVC and the H_2 column densities follow the HI of the IVC. The resulting linear parameters of the HI-τ correlation are peculiar because the dust emissivity is significantly larger for the IVCs than for the LVCs. In the HI-τ correlations the cloud is located above the general correlation. However, there is significant LVC emission in this region in addition to the Andromeda galaxy influencing the fit. Even for the increased upper HI fitting-threshold, a large number of data points is rejected in the fit. Summarising, candidate no. 1$^-$ is unclear.

There are a few other candidates close to candidate no. 1$^-$. We do not investigate those because these candidates are spatially less extended and their analysis would suffer from the same problems as for candidate no. 1$^-$, namely the large LVC HI column densities. These other candidates could potentially be other MIVCs, although they are difficult to identify from the HI-τ correlation.

Candidate no. 1$^+$ The plots for MIVC candidate no. 1$^+$ are shown in Fig. 5.16. The candidate pixels do not match the HI IVC distribution very well. The candidate is located at the end of a larger filament that stretches towards the disk into the LVC regime. The spectral line of the HI emission is fitted quite

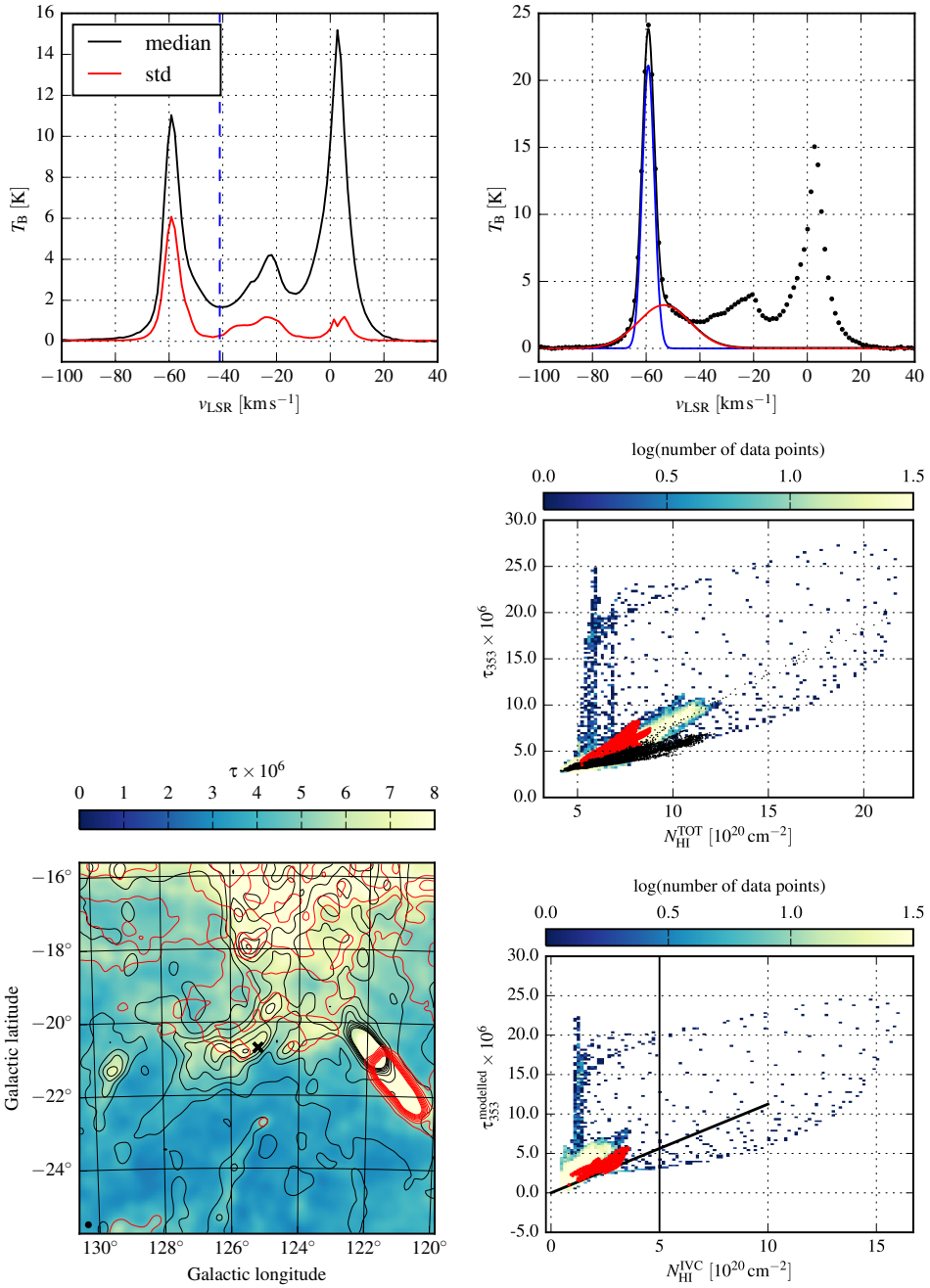

Fig. 5.15: Plots for MIVC candidate no. 1^-. The top-left plot shows the velocity separation with the median and standard-deviation spectrum in black and red. The separating velocity is given by the vertical dashed blue line. In the top-right, the two-component Gaussian fit to the peak HI spectrum is presented with the data as black dots and the total Gaussian fit as the black line. The narrow and wide Gaussian components are plotted as the blue and red curves. In the bottom-left, the τ-map is plotted overlayed with the IVC HI column densities in black and the inferred H_2 column densities in red. Both the HI and H_2 contours start at 0.5×10^{20} cm^{-2} increasing in steps of 0.5×10^{20} cm^{-2}. The position of the candidate is shown by the black cross. The middle-right plot shows the HI-τ plot for the total N_{HI} and total τ. In the bottom-right plot the modelled IVC contribution to τ is given after subtracting the LVC contribution and the constant offset from the total τ. In both HI-τ plots, the red points mark the data points of the MIVC candidate while the black line or black points indicate the modelled HI-τ relation.

well with a single Gaussian with $v_0 = 26.6 \pm 0.2\,\mathrm{km\,s^{-1}}$ and FWHM $= 9.6 \pm 0.2\,\mathrm{km\,s^{-1}}$.

The candidate is associated with FIR emission, however, the H_2 column densities do not follow the HI column densities of the IVC well. This is true also for other candidates within the field. In the HI-τ correlations the cloud is located on the general correlation or slightly above but there is no FIR excess that steepens for larger HI column densities. There is significant LVC emission in this region. Because of the lack of cold gas, candidate no. 1^+ is likely not a MIVC.

5.5.2 Search for southern atomic IVCs

By applying the respective criteria (Sect. 5.2.2), we search for the most FIR-deficient IVCs or AIVCs on the southern Galactic hemisphere. In general most of the southern IVC$^\pm$ gas is associated with negative H_2 column densities, similar as for the northern hemisphere.

The locations of the identified southern AIVCs are plotted in Fig. 5.17. The red coloured contours show the location of the AIVC$^-$ candidates. There there are 23 AIVC$^-$ candidates but none for the AIVCs$^+$. Some AIVCs$^-$ are located at high Galactic latitudes of $b \simeq -60°$.

As for the northern hemisphere not all negative H_2 column densities or FIR-deficient regions are associated with AIVC$^\pm$ candidates. Towards the southern pole there is material of the Magellanic Stream that is strongly FIR deficient. However, this material does not contain cold gas. The negative features around $(l, b) \simeq (340°, -35°)$ are likely associated with the LVC gas.

5.5.3 Search for southern normal IVCs

In order to compare the statistical properties of the global population of MIVC and AIVC candidates, we define a control sample, or normal IVCs (NIVCs). These objects show narrow HI lines but are consistent with the intrinsic scatter of the HI-τ correlation (Sect. 5.2.3).

We plot the spatial locations of the inferred NIVCs$^\pm$ in Fig. 5.18. The red and dark-violet coloured contours mark the NIVCs$^-$ and NIVCs$^+$. There are 31 NIVC$^-$ candidates and 5 NIVC$^+$ candidates. The NIVCs$^\pm$ are found close to other MIVC$^\pm$ and AIVC$^\pm$ candidates, almost all at $b > -40°$.

5.5.4 Statistical properties of southern samples

In complete analogy to the northern Galactic hemisphere, the statistical properties of the MIVC$^\pm$, AIVC$^\pm$, and NIVC$^\pm$ candidates are discussed. We present the IVC$^-$ candidates here, the plots for the IVCs$^+$ are shown in the appendix (Sect. A.4) without any AIVC$^+$ candidate. Generally, the total number of objects is small compared with the northern hemisphere and one should be cautious in the interpretation of the results.

5.5.4.1 Histograms

In Fig. 5.19 we compare the observables of the three IVC$^-$ samples with each other. The black, red, and blue histograms are for the AIVC$^-$, MIVC$^-$, and NIVC$^-$ candidates. The histograms are normalised such that the sum of all bins for each cloud type is unity. The observables are discussed in the order from top to bottom and from left to right.

LVC HI column density $N_{\mathrm{HI}}^{\mathrm{LVC}}$: Generally, there are substantial amounts of LVC HI column density towards the three samples. Except for the AIVCs$^-$, one typically finds $N_{\mathrm{HI}}^{\mathrm{LVC}} \gtrsim 3 \times 10^{20}\,\mathrm{cm^{-2}}$. For the MIVCs$^-$ the distribution extends towards the largest column densities. There are some AIVCs$^-$ with

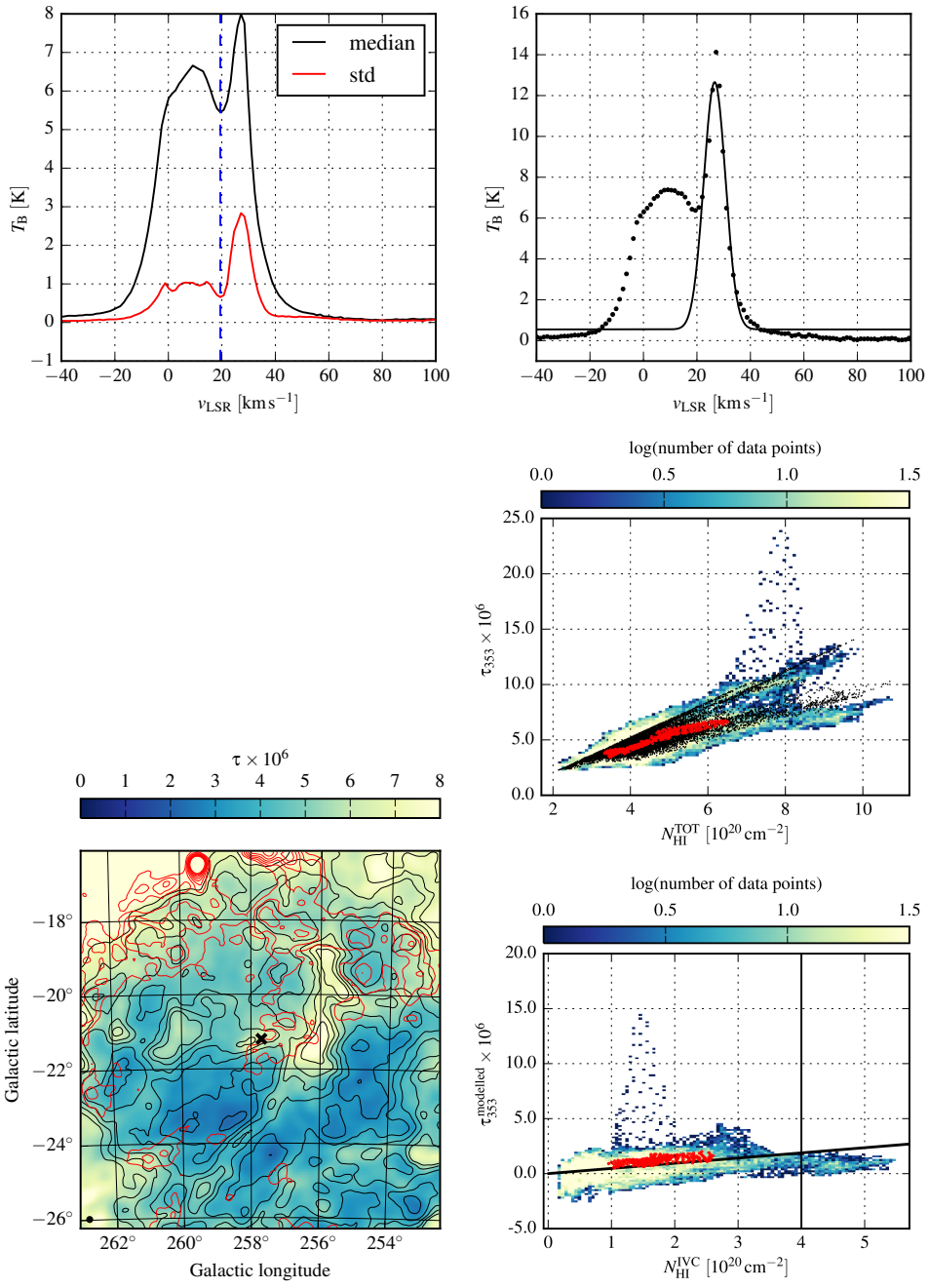

Fig. 5.16: Plots for MIVC candidate no. 1$^+$, same as in Fig. 5.15.

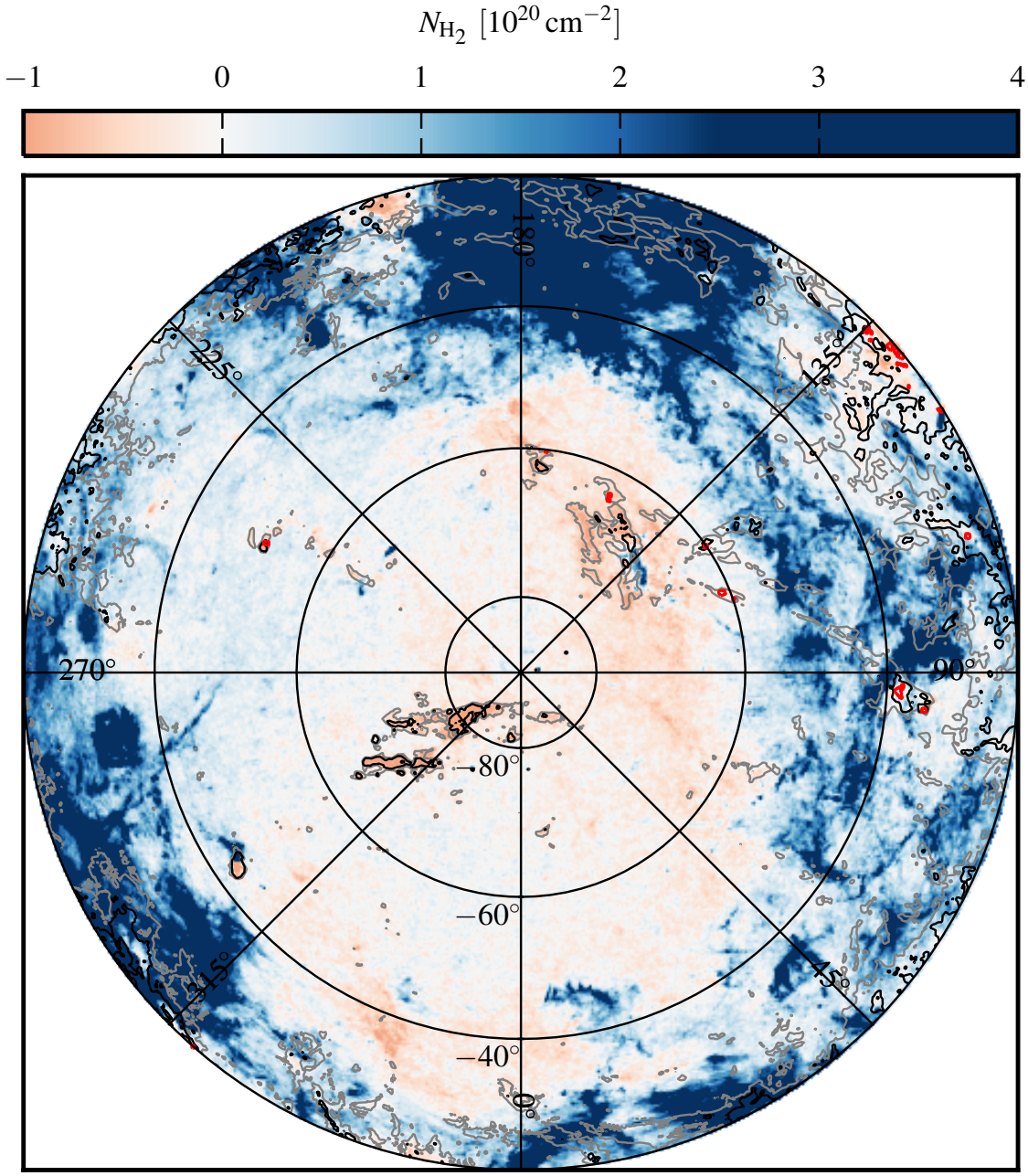

Fig. 5.17: Distribution of southern AIVC$^{\pm}$ candidates at $b < -20°$ on top of the inferred H_2 column densities. The map is plotted in zenith-equal area projection centred on the southern Galactic pole with Galactic coordinates. All blueish colours indicate positive N_{H_2}, all reddish negative N_{H_2}. The light- and dark-grey contours denote the total integrated (negative and positive) IVC HI gas at $N_{HI}^{IVC} = 0.75 \times 10^{20}$ cm^{-2} and 1.5×10^{20} cm^{-2} respectively tracing the location of IVC complexes. The red contours give the location of the inferred AIVC^{-} candidates from the procedure as described in Sect. 5.2.2. There is no AIVC^{+} candidate.

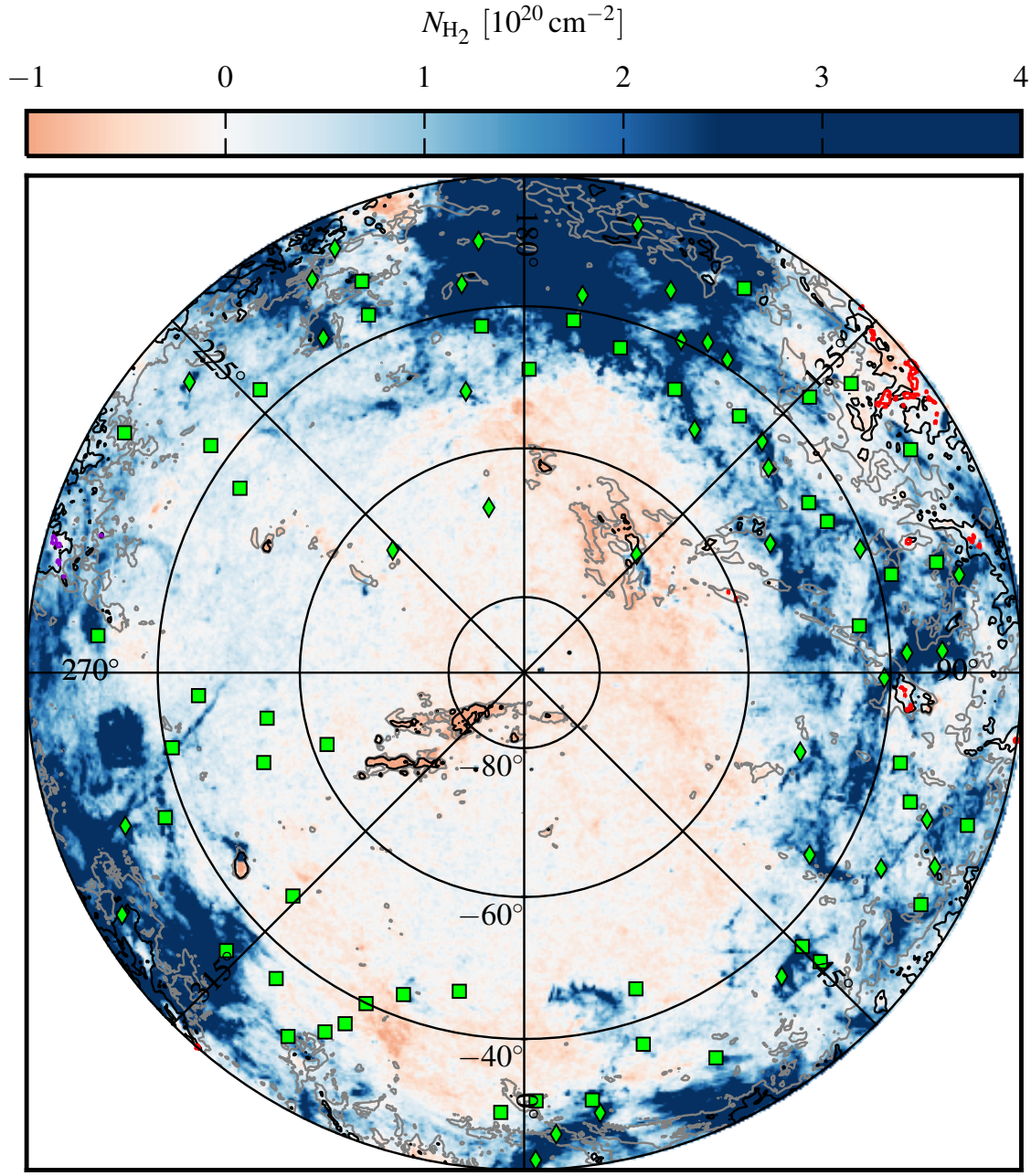

Fig. 5.18: Distribution of southern NIVC$^{\pm}$ candidates at $b < -20°$ on top of the inferred H_2 column densities. The map is plotted in zenith-equal area projection centred on the southern Galactic pole with Galactic coordinates. All blueish colours indicate positive N_{H_2}, all reddish negative N_{H_2}. The light- and dark-grey contours denote the total integrated (negative and positive) IVC HI gas at $N_{HI}^{IVC} = 0.75 \times 10^{20}$ cm^{-2} and 1.5×10^{20} cm^{-2} respectively tracing the location of IVC complexes. The red contours give the location of the inferred NIVC^{-} candidates from the procedure as described in Sect. 5.2.2. The dark-violet contours show the candidates of the NIVC^{+} sample. The green diamonds indicate known high-latitude molecular clouds from FIR excess emission, the green squares give the positions of unidentified FIR excess sources as listed in Reach et al. (1998, their Tables 3 and 4).

$N_{\rm HI}^{\rm LVC} \leq 2.5 \times 10^{20}\,{\rm cm}^{-2}$, which is the lowest foreground for the respective samples. These objects are located at the highest latitudes.

IVC HI column density $N_{\rm HI}^{\rm IVC^-}$: The IVC$^-$ HI column density is comparable for all three samples peaking between $N_{\rm HI}^{\rm IVC^-} \simeq 2-3 \times 10^{20}\,{\rm cm}^{-2}$. The MIVC$^-$ candidates show the largest and the AIVC$^-$ candidates the lowest HI column densities, which is opposite to the northern samples.

HVC HI column density $N_{\rm HI}^{\rm HVC}$: None of the three samples is associated with HI emission of HVCs. There are, however, a few pixels of MIVC$^-$ candidates that have $N_{\rm HI}^{\rm HVC} \simeq 10 \times 10^{20}\,{\rm cm}^{-2}$ or more. These candidates are related to the Andromeda Galaxy.

Total dust optical depth τ: As expected, the MIVC$^-$ sample shows the largest τ. The distribution exhibits a long tail that is related to the Andromeda Galaxy. In terms of dust optical depth, there are very FIR dim AIVCs$^-$ and some with similar τ as the NIVCs$^-$.

Dust temperature $T_{\rm d}$: The MIVCs$^-$ contain the lowest dust temperatures with most typical dust temperatures of $T_{\rm d} \lesssim 20\,{\rm K}$. Both the AIVCs$^-$ and the NIVCs$^-$ peak around $T_{\rm d} \simeq 20.5\,{\rm K}$. In some AIVCs$^-$ the dust temperatures are largest.

Dust exponent β: The distributions are fairly similar for all three samples spreading over a range of $\beta \simeq 1.4-1.7$. Some MIVC$^-$ candidates show the largest β while some AIVC$^-$ candidates are associated with the lowest.

Inferred H_2 column density $N_{\rm H_2}$: As expected, the MIVCs$^-$ have the largest H_2 column densities peaking near $N_{\rm H_2} \simeq 1 \times 10^{20}\,{\rm cm}^{-2}$. The AIVCs$^-$ have significant negative H_2 column densities while the NIVCs$^-$ are in between. The largest H_2 column densities are associated with the Andromeda Galaxy.

Integrated ^{12}CO(1→0) emission: All three samples are not associated with CO emission as measured inferred by Planck Collaboration XIII (2014). Only towards a few pixels of MIVCs$^-$, there is CO emission detected indicated by the tail towards positive values. These values are associated mostly to the Andromeda Galaxy.

Total dust reddening: The total dust reddening, as inferred by Green et al. (2015), is largest towards the MIVCs$^-$, however, not as significant as for the northern hemisphere. All three samples peak near $E(B-V) \simeq 0.05\,{\rm mag}$ with typical values of $E(B-V) \lesssim 0.1\,{\rm mag}$. As for the dust optical depth, there is a population of AIVCs$^-$ with very low dust reddenings. Generally, the reddening is larger for the southern hemisphere as compared with the northern: South, the peaks are at $\sim$0.05 mag, north at $\sim 0.02-0.025\,{\rm mag}$ (compare with Fig. 5.7). The candidates with vanishing reddening are located in a region where no data of dust reddening is available.

Galactic longitudes l: Most of all candidates are found towards $l \simeq 125°$. This is the region close to the Andromeda Galaxy.

Galactic latitudes b: Most of the MIVCs$^-$ and NIVCs$^-$ are found at $b > -30°$ while many AIVCs$^-$ are identified at $b < -35°$.

Amplitudes of Gaussian components $T_{\rm B}^{\rm gauss}$: The MIVCs$^-$ tend to have the largest amplitudes of the Gaussian components. Otherwise the AIVCs$^-$ and NIVCs$^-$ are very similar.

Central velocity of Gaussian components $v_0^{\rm gauss}$: In the LSR, most of the samples are clearly distinct from the LVC velocity regime. Only the AIVCs$^-$ have a large peak near $-20\,{\rm km\,s^{-1}}$. Some MIVC$^-$ candidates show the largest absolute radial velocities with $v_{\rm LSR} \simeq -70\,{\rm km\,s^{-1}}$. A second peak of the MIVCs$^-$ is found around $v_{\rm LSR} \simeq -30\,{\rm km\,s^{-1}}$, where also AIVCs$^-$ and NIVCs$^-$ are identified. The AIVCs$^-$ are more numerous at lower absolute velocities, while the NIVCs$^-$ have most typically $v_{\rm LSR} \simeq -55\,{\rm km\,s^{-1}}$. In the GSR velocity frame there are objects with $-200\,{\rm km\,s^{-1}} \leq v_{\rm GSR}^{\rm gauss} \leq +200\,{\rm km\,s^{-1}}$ showing a strong bimodality: Most of the sample objects are observed to have $v_{\rm GSR}^{\rm gauss} \simeq 100-150\,{\rm km\,s^{-1}}$ towards the rotational direction of the Galaxy.

FWHM of Gaussian components FWHM$^{\rm gauss}$**:** The three samples have similar line widths. The most narrow lines are found in some AIVCs$^-$, which is contrary to the northern hemisphere. Note that the Gaussian components are selected to have FWHM $< 5\,{\rm km\,s^{-1}}$.

5.5.4.2 Kolmogorov-Smirnov tests

For a statistical comparison of the observables, we perform Kolomogorov-Smirnov (KS) tests (compare with Sect. 5.4.4.2). The KS tests are calculated for pairs of the sample data. The resulting p-values are less than 1×10^{-6} for most of the observables. There are a few cases, however, where the same parent distribution cannot be rejected. For the following distributions the KS test is inconclusive:

- $N_{\rm HI}^{\rm HVC}$: The AIVCs$^-$ and NIVCs$^-$ have a p-value of 0.06.
- $W_{\rm CO}$: The AIVCs$^-$ and NIVCs$^-$ have a p-value of 0.06, the NIVCs$^-$ and MIVCs$^-$ 1×10^{-4}.
- FWHM$^{\rm gauss}$: The NIVCs$^-$ and MIVCs$^-$ have a p-value of 0.56.

5.5.4.3 Correlations

In the following, we look for correlations of observed quantities towards the different IVC$^-$ samples (Figs. 5.20 and 5.21). For the IVC$^+$ samples, the plots are put in the appendix (Sect. A.4).

IVC HI column density $N_{\rm HI}^{\rm IVC}$ and molecular hydrogen column density $N_{\rm H_2}$: For all samples, there is good correlation between the quantities. Only for the MIVC$^-$ and AIVC$^-$ candidates at the largest IVC HI column densities, that are associated with Andromeda, the H_2 column densities increase. For Andromeda such a positive correlation is not surprising since it just reflects the normal HI-τ correlation in its ISM. Note that the positive H_2 column densities for some AIVCs$^-$ are due to the application of maximum filters allowing small angular displacements between the different maps (Sect. 5.2).

HVC HI column density $N_{\rm HI}^{\rm HVC}$ and molecular hydrogen column density $N_{\rm H_2}$: For the MIVC$^-$ candidates, very weakly also for the AIVCs$^-$, there is the trend that larger HVC HI column densities are associated with larger H_2 column densities. Those pixels are all associated with the Andromeda Galaxy. For Andromeda such a positive correlation is again not surprising since it just reflects the normal HI-τ correlation in the ISM of Andromeda. For the other candidates there is no apparent correlation.

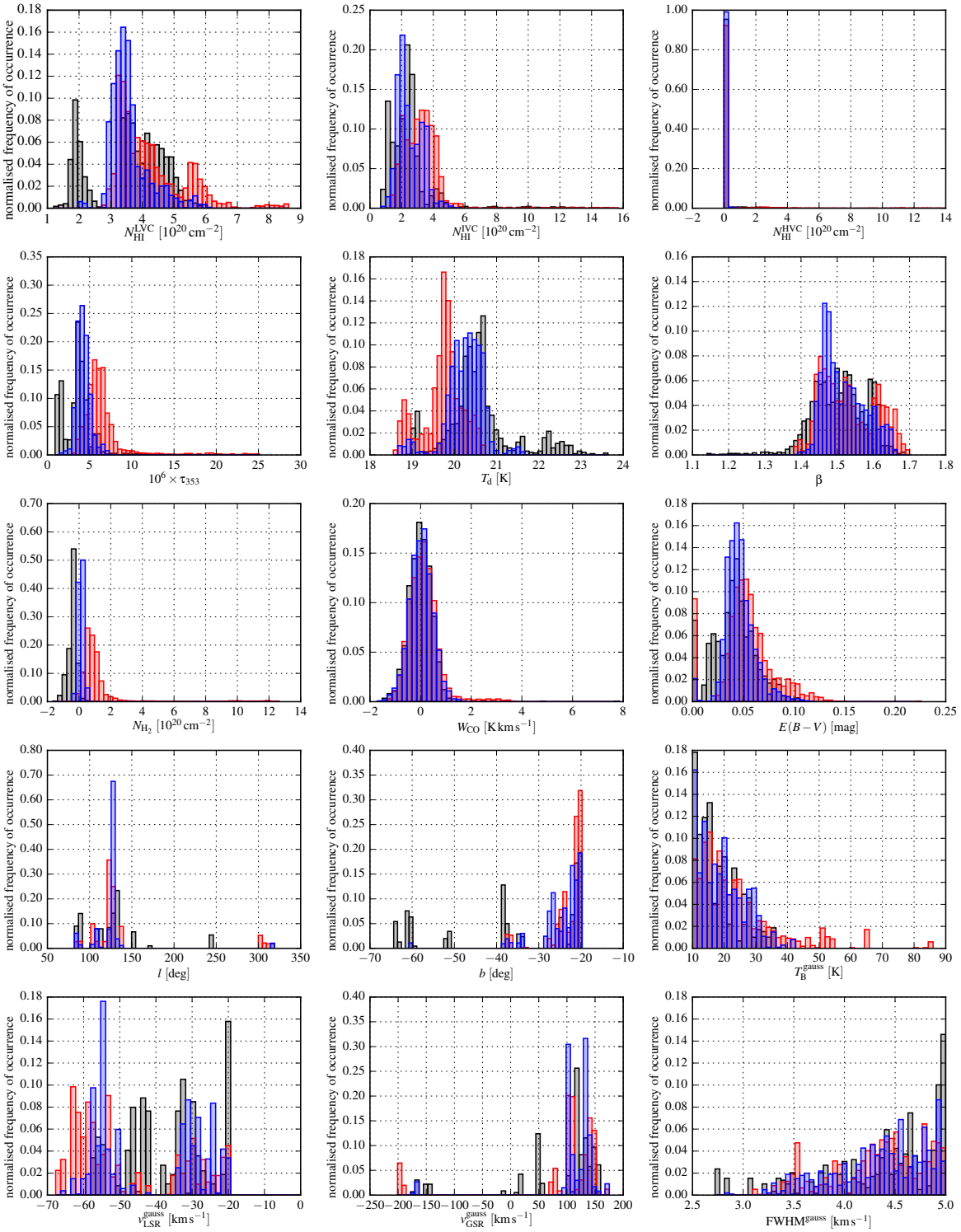

Fig. 5.19: Statistical properties of southern AIVC$^-$, MIVC$^-$, and NIVC$^-$ candidates. The black, red, and blue histograms show the AIVC$^-$, MIVC$^-$, and NIVC$^-$ candidates.

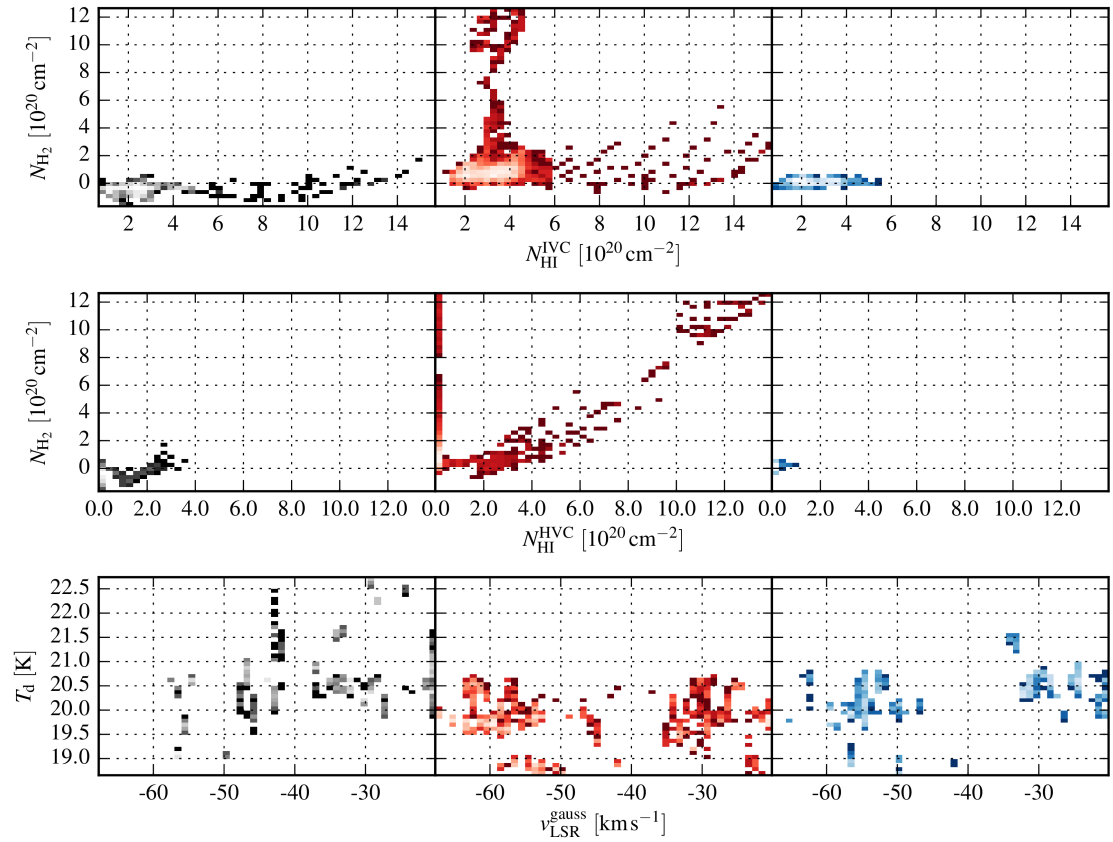

Fig. 5.20: Correlation properties of southern AIVC$^-$, MIVC$^-$, and NIVC$^-$ candidates. The left plots (black) show the AIVCs$^-$, the middle plots (red) the MIVCs$^-$, and the right plots (blue) the NIVCs$^-$.

Central velocities v_{LSR}^{gauss} of Gauss components and dust temperature T_d: For none of the three samples, there is a clear trend. For the AIVC$^-$ candidates, the dust temperatures may slightly increase for lower absolute velocities.

LVC HI column density N_{HI}^{LVC} and total dust reddening $E(B-V)$: For all three samples there is a correlation between the amount of LVC HI column density N_{HI}^{LVC} and the total dust reddening in these lines-of-sight. The amount of reddening is slightly larger for the MIVC$^-$ candidates.

IVC HI column density $N_{HI}^{IVC^-}$ and total dust reddening $E(B-V)$: The correlation between N_{HI}^{IVC} and the total dust reddening $E(B-V)$ is similarly valid as for the LVC gas. This may argue that the IVC gas may be LVC gas in fact. Furthermore, the largest IVC HI column densities are close to Andromeda.

Total hydrogen column density N_H and dust temperature T_d: For the AIVC$^-$ and MIVC$^-$ candidates, the dust temperatures decrease with increasing total hydrogen column density. These data points are again showing the properties of the Andromeda Galaxy, but also for some other MIVC$^-$ candidates.

Dust temperature T_d and dust emissivity exponent β: The anti-correlation between T_d and β (e.g. Planck Collaboration XXIV 2011) is confirmed for all three samples. The most pronounced anti-

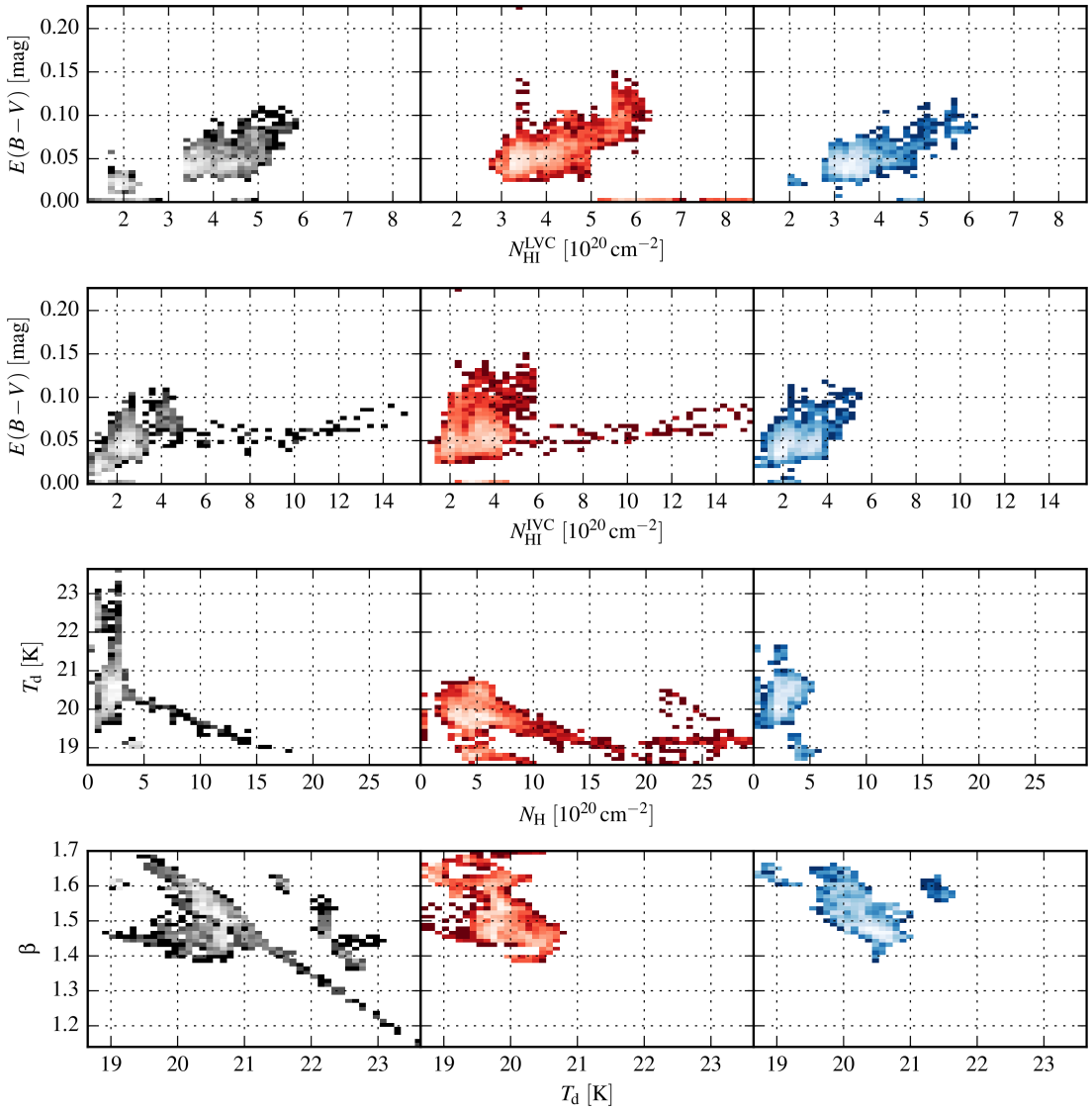

Fig. 5.21: Correlation properties of southern AIVC$^-$, MIVC$^-$, and NIVC$^-$ candidates. The left plots (black) show the AIVCs$^-$, the middle plots (red) the MIVCs$^-$, and the right plots (blue) the NIVCs$^-$.

correlation is evident for the AIVCs$^-$. However, the smallest values of $\beta \simeq 1.2$ are associated with one bright point-source.

5.5.5 Dust reddening

Like for the northern hemisphere (Sect. 5.4.5), we plot the dust reddening signal within distance bins (Fig. 5.22) as estimated by Green et al. (2015). The MIVCs$^-$ are plotted in red, the AIVCs$^-$ in black, and the NIVCs$^-$ in blue. In each plot in this Figure the amount of reddening towards the respective samples is shown for a particular distance interval.

Several conclusions can be drawn from these plots:

- There is significant reddening in all distance intervals up to ~5 kpc.

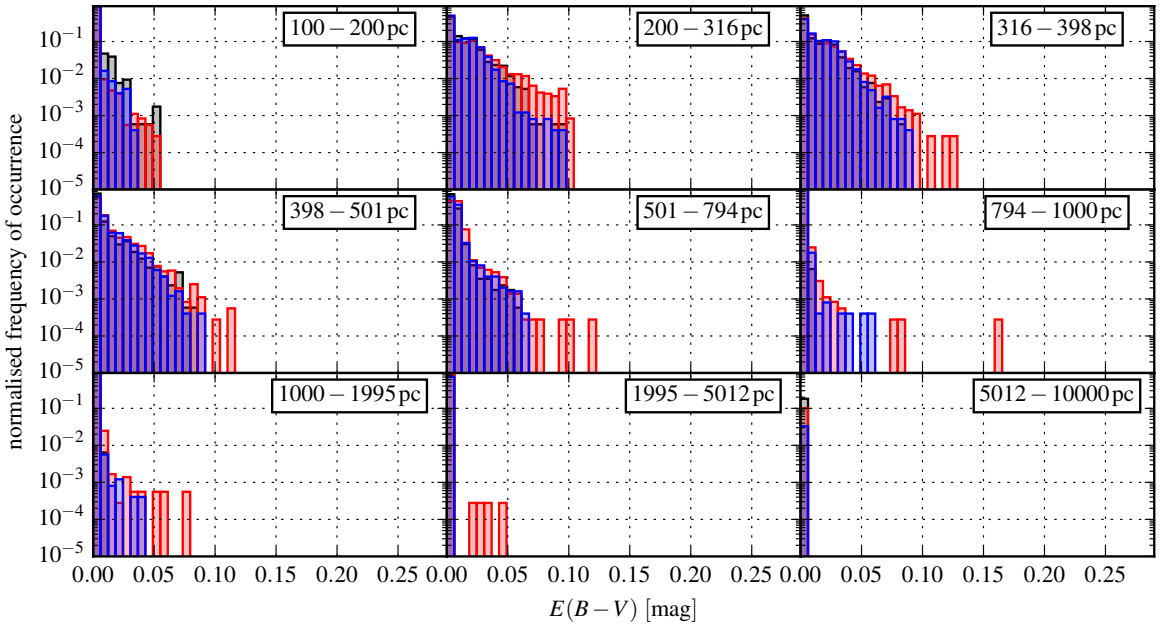

Fig. 5.22: Reddening signal from Green et al. (2015) of AIVC$^-$, MIVC$^-$, and NIVC$^-$ samples for different distance bins. In each plot, at the top-right we plot the distance interval in which the reddening signal is contained. The AIVCs$^-$ are plotted as black histograms, the MIVCs$^-$ in red, and the NIVCs$^-$ in blue.

- Towards the MIVC$^-$ candidates there is the largest reddening in the individual distance intervals.
- In most distance bins the bulk of data points for all samples shows a larger reddening than on the northern hemisphere (Fig. 5.10).

Many of the sample candidates are located at latitudes $b \lesssim -30°$, where, like for the northern hemisphere, there is a widespread underlying reddening distribution. This reddening signal is likely associated with the thick Galactic disk and not necessarily to the candidates themselves. This suggests that many of the IVC candidates are difficult to evaluate because of the confusion with disk material. Furthermore, we cannot rule out the possibility that some of these candidates are in fact normal disk objects.

5.5.6 Kinematical properties of southern samples

Here, we analyse the kinematical properties of the Gaussian components of the IVC$^\pm$ samples. The observed radial velocities are compared with the model of Galactic rotation that is also used for the northern hemisphere (Sect. 5.4.6). Note that on the southern hemisphere there is no AIVC$^+$ candidate. The corresponding plots do not contain any data but only the rotational model.

It appears that all IVC samples for both negative and positive velocities match the expectations from the rotational model (Fig. 5.23). The velocities can be reproduced by the rotational model. This is especially true for those candidates at lower absolute latitudes, which are most of the MIVC$^\pm$ and NIVC$^\pm$ candidates. The high-latitude AIVCs$^-$ appear to be slightly off the expected rotation for their actual latitudes of $b \simeq -60°$. This may suggest that these objects are kinematically anomalous and potentially belong to the Magellanic System.

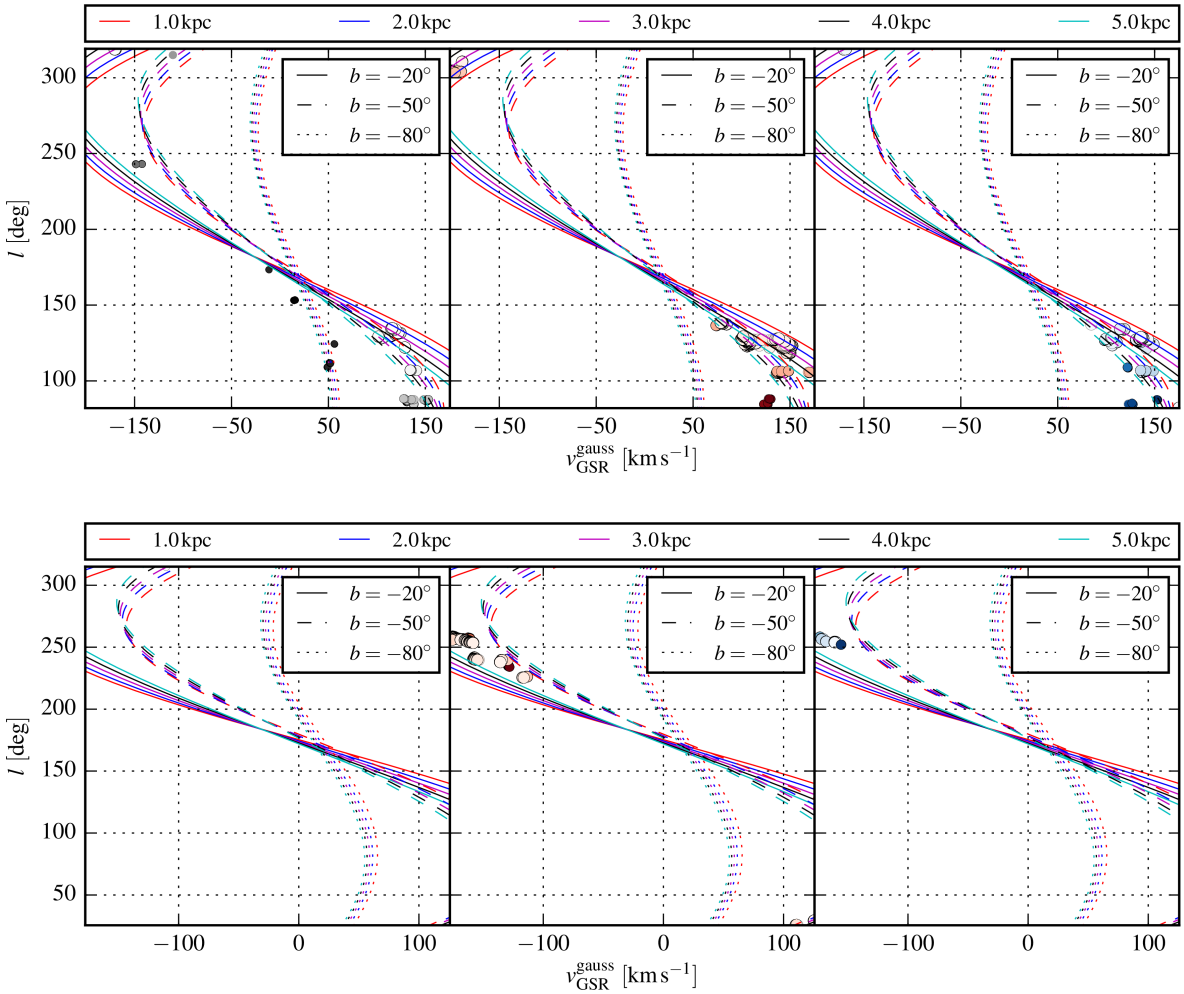

Fig. 5.23: Radial GSR velocities of southern IVC$^{\pm}$ samples compared with Galactic longitudes l. The top row is for the IVC^{-} and the bottom row for the IVC^{+} samples. The left column is for the AIVCs$^{\pm}$ in black, the middle column for the MIVCs$^{\pm}$ in red, and the right column for the NIVCs$^{\pm}$ in blue. The velocities of the individual candidates are given by the $v_{\mathrm{GSR}}^{\mathrm{gauss}}$ from the Gaussian decomposition of the HI survey data. The size and colour of each point encode the latitude coordinate b of the candidates, being large and bright for low absolute latitudes or small and dark for high absolute latitudes. The different lines show the modelled rotation velocities (see Sect. 5.4.6.1 for details). A vertical height $z = -1.6$ kpc is assumed, for which the velocities are modelled at some heliocentric distances d and latitudes b as given in the legends. The solid, dashed, and dotted lines are for $b = -20°$, $b = -50°$, and $b = -80°$. The red, blue, magenta, black, and cyan lines are for heliocentric distances within the Galactic plane of $d = 1$ kpc, 2 kpc, 3 kpc, 4 kpc, and 5 kpc. Note that there is no AIVC^{+} candidate (*bottom-left*).

5.6 Occurrences of IVC candidates

The distribution of IVC gas on the northern and southern Galactic hemispheres is generally different, which results in different numbers and evidence of the inferred MIVC$^{\pm}$ candidates. As an overview, we list the number of identified candidates for the two Galactic hemispheres in Table 5.5. Under the assumption that IVCs are related a Galactic fountain process, it is a priori unexpected to find a significant distinction between the northern and southern Galactic hemisphere. The lack of IVC gas on the southern

	northern Galactic hemisphere		southern Galactic hemisphere	
	$v_{\rm LSR} < -20\,{\rm km\,s^{-1}}$	$v_{\rm LSR} > +20\,{\rm km\,s^{-1}}$	$v_{\rm LSR} < -20\,{\rm km\,s^{-1}}$	$v_{\rm LSR} > +20\,{\rm km\,s^{-1}}$
# AIVCs	86	8	23	0
# MIVCs	161	1	24	20
# NIVCs	288	22	31	5

Table 5.5: Numbers of inferred IVC$^{\pm}$ candidates for both Galactic hemispheres as described in Sects. 5.4 and 5.5.

hemisphere, except for the Magellanic Stream, is an interesting observation. This has been known for a long time (e.g. Wakker 2004) but no good explanation is put forward.

On the southern hemisphere there is roughly a similar number of candidates identified for the three IVC$^-$ samples. This is in contrast to the northern hemisphere, for which there are about two times more MIVC$^-$ than AIVC$^-$ candidates and about three times more NIVC$^-$ than AIVC$^-$ candidates.

There is a lack of detections of all IVC$^+$ types in general. The only northern MIVC$^+$ candidate may be related to bright LVC emission. Because of the low number of candidates for positive velocities, any statistical analysis of the IVC$^+$ samples is not conclusive. The corresponding Figures are shown in the appendix (Sects. A.2 and A.4).

The differences between the northern IVC$^{\pm}$ samples may be related to two main reasons: 1) For $b > 20°$ there is about three times more HI column density in IVCs$^-$ than in IVCs$^+$, for $b > 40°$ the difference increases to a factor of five. 2) The median ratios $N_{\rm HI}^{\rm IVC^-}/N_{\rm HI}^{\rm LVC}$ are about four times larger than for $N_{\rm HI}^{\rm IVC^+}/N_{\rm HI}^{\rm LVC}$. Together, the larger amounts of northern IVC$^-$ gas and the larger fraction of LVC gas towards IVC$^+$ HI emission may account for the lower number of identified northern AIVC$^+$ and NIVC$^+$ candidates.

However, this is not true for the MIVCs$^+$, for which no good candidate is identified. Assuming a similar occurrence ratio as for the AIVCs$^{\pm}$ and NIVCs$^{\pm}$, one would expect at least 10 MIVC$^+$ candidates. The lack of northern MIVC$^+$ objects may hint towards a physical reason for the existence of MIVCs in general that may be linked to the LSR velocity and the kinematics of the clouds within the Galactic fountain cycle (Röhser et al. 2014).

At $b < -20°$ differences in total IVC$^{\pm}$ HI column density are of the order of 1–3%. Hence, for the southern Galactic hemisphere such an observational reason is unlikely accounting for the low number of AIVC$^+$ and NIVC$^+$ candidates.

5.7 Angular distances of IVC samples to borders of IVC complexes

All known and confirmed MIVCs, e.g., those that are associated with CO emission, are located at the edges of larger IVC complexes: Draco, IVC 135, IVC 210, and the Magnani & Smith (2010) clouds (the red circles in Fig. 5.3). Here, we look in general at the angular distances between the inferred IVC$^{\pm}$ samples and the borders of IVC complexes quantifying if this is a general property of MIVCs.

The IVC complex border is defined by a threshold HI column density. Because this threshold is not well defined, we take three different HI column density thresholds at $N_{\rm HI}^{\rm IVC^{\pm}} = 0.3 \times 10^{20}\,{\rm cm^{-2}}$, $0.5 \times 10^{20}\,{\rm cm^{-2}}$, and $1.0 \times 10^{20}\,{\rm cm^{-2}}$ and compare the results. If the column density drops below these values, we consider this as the edge of a larger IVC complex.

In a region of $20° \times 20°$ around each candidate, we look for the closest pixel that falls below the chosen IVC$^{\pm}$ HI column density threshold. Accordingly, we compute the angular distance between the particular candidate and the IVC complex border. A larger HI column density threshold of an IVC complex is found likely closer to the candidate cloud. The resulting median distances are compiled

$N_{\rm HI}^{\rm IVC^{\pm}}$ threshold	sample	$v_{\rm LSR} < -20\,{\rm km\,s^{-1}}$		$v_{\rm LSR} > +20\,{\rm km\,s^{-1}}$	
		north	south	north	south
$1 \times 10^{20}\,{\rm cm^{-2}}$	AIVCs	0.62	1.18	*0.25*	–
	MIVCs	*0.38*	*1.12*	0.52	0.52
	NIVCs	0.46	1.18	0.27	*0.43*
$0.5 \times 10^{20}\,{\rm cm^{-2}}$	AIVCs	1.82	*3.58*	1.02	–
	MIVCs	*1.75*	5.06	1.09	1.57
	NIVCs	2.18	4.70	*0.73*	*1.30*
$0.3 \times 10^{20}\,{\rm cm^{-2}}$	AIVCs	3.98	*6.72*	1.60	–
	MIVCs	*3.25*	8.59	1.81	3.88
	NIVCs	5.25	7.22	*1.51*	*2.34*

Table 5.6: Median angular distances of IVC$^{\pm}$ samples to borders of IVC complexes measured in degree. We apply three definitions of IVC complex borders as determined by HI column density thresholds. For a particular threshold value the smallest distance of the three samples (AIVCs$^{\pm}$, MIVCs$^{\pm}$, NIVCs$^{\pm}$) on either hemisphere is printed in italic.

in Table 5.6. In this Table, for a particular threshold value the smallest distance of the three samples (AIVCs$^{\pm}$, MIVCs$^{\pm}$, NIVCs$^{\pm}$) on either hemisphere is printed in italic.

It appears that on the northern hemisphere MIVCs^{-} tend to be located closer to the border of larger IVC structures as compared with NIVCs^{-} and AIVCs^{-}. This trend is not evident for the other samples. Since the northern IVC^{-} sky contains the only known MIVCs^{-}, this may hint towards the importance of dynamical interactions at the borders of larger IVC structures that could be responsible for the existence of MIVCs (Chapters 3 and 4).

5.8 Angular displacements between HI and FIR data

For the MIVC IVC 210 we show that there are angular offsets between the HI and FIR peaks of the cloud for both low and high spatial resolution data (Chapters 3 and 4). These offsets may be interpreted as the indication for non-equilibrium processes. In equilibrium the peaks should roughly coincide spatially. In the case of IVC 210 the shift of the FIR peak eastwards of the HI peak is related to the presence of large amounts of molecular gas in the eastern part of the cloud.

Such a shift between the data sets may be evident for other MIVC candidates as well. Hence, we analyse the MIVC$^{\pm}$ candidates and look for their brightest HI and FIR emission and compute the angular offset between these two peaks. For the AIVC and NIVC candidates this is not sensible because these candidates often are not tracing the structure of the underlying emission but are located around other LVC or IVC structures. Hence, the peaks of AIVCs and NIVCs in HI and FIR may not be the global maxima of the candidates.

For the northern MIVC^{-} sample, which is the largest, the median offset between the HI and FIR peaks is ~9.4 arcmin, which is non-zero and non-negligible. However, this offset is still less than one beam of the GASS HI data. This angular displacement could potentially indicate substructure and spatial offsets between the gas and dust. One should be cautious in the interpretation of this offset since the FIR emission value traces the entire FIR emission along the line-of-sight. Only for objects that dominate the lines-of-sight the offset is likely intrinsic to the candidate.

5.9 Physical properties of molecular IVC candidates

The formation of molecules is intimately related to the existence of dense sub-structures within larger clouds (e.g. Glover & Mac Low 2007). Supersonic turbulence is thought to be one of the main drivers for the creation of dense substructure from a diffuse medium (e.g. Audit & Hennebelle 2005; Glover & Mac Low 2007). This transition from the warm neutral medium (WNM) to the cold neutral medium (CNM) can be related to the pressure of the gas (Guillard et al. 2009). As the final part of this Chapter, we estimate physical properties of the inferred MIVC$^{\pm}$ candidates.

In Sect. 5.9.1 we briefly describe how physical properties are inferred. A discussion is given in Sect. 5.9.2 on the distances to the global IVC population. In Sect. 5.9.3 the resulting physical properties and in Sect. 5.9.4 the masses of the IVC ensembles are discussed.

We estimate the physical properties only for the MIVCs$^{\pm}$ on both Galactic hemispheres and not for the AIVCs or the NIVCs. This is because only for the MIVC$^{\pm}$ candidates the identified pixels trace or match the morphology of the underlying HI distribution in most cases justifying the application of spherical symmetry for the derivation of the parameters.

5.9.1 Derivation

The pressure p of an HI gas is calculated from the observables HI particle density $n_{\rm HI}$ and kinetic gas temperature $T_{\rm kin}$ by

$$\frac{p}{k_{\rm B}} = n_{\rm HI} T_{\rm kin} \tag{5.5}$$

in units of the Boltzmann constant $k_{\rm B}$.

Assuming spherical symmetry, the HI particle density of an individual candidate is inferred from its peak HI column density and its spatial extent d by

$$n = \frac{N_{\rm HI}}{d}. \tag{5.6}$$

The candidate clouds are likely located within the disk-halo interface of our Galaxy, embedded in a thin and diffuse HI layer. This layer contributes to the HI column density of the candidate cloud also. In order to subtract this additional contribution, we take the median HI column density within a circle with a radius of 5° around the candidate and subtract this background column density from the peak HI column density of the candidate before the density is estimated. In this way for most candidates an approximate correction of the surrounding HI column density is obtained. Note that the total particle density of the MIVCs is significantly larger due to the existence of H_2, potentially by a factor of two.

The spatial extent of each candidate is estimated by assuming spherical symmetry. Each candidate is defined by a number of connected pixels. This angular extent, given by the number of pixels with some angular size, is converted into the angular diameter α of a sphere. The actual spatial size d of a candidate depends on the distance D to the cloud by $d = \alpha D$. However, the distance is generally unknown for most candidates (Sect. 5.9.2).

The kinetic temperature of the HI gas is obtained from the Gaussian components. However, the observed and modelled line widths are only upper limits to the kinetic gas temperature. In addition to the thermal motion of the gas particles, that cause the Doppler-broadened line shape, an additional source to the line broadening is unresolved velocity structure. From the observed FWHM, the upper

limit to the kinetic gas temperature is obtained with the mass of a hydrogen atom m_H by

$$T_\mathrm{kin} \leq \frac{m_\mathrm{H}}{8\,k_\mathrm{B}\,\ln 2} \times (\mathrm{FWHM})^2 \simeq 21.8\,\mathrm{K} \times \left(\frac{\mathrm{FWHM}}{[\mathrm{km\,s^{-1}}]}\right)^2 . \tag{5.7}$$

The HI mass M_HI of a candidate cloud is the integral of the HI column densities over the angular extent of the object. This integral is written as a sum over the object's pixels:

$$M_\mathrm{HI} = m_\mathrm{H} D^2 \tan\phi^2 \sum_i N^i_\mathrm{HI} \tag{5.8}$$

where ϕ is the angular size of an individual pixel of the map for quadratic pixels.

Equivalently, the total hydrogen mass M_H of a candidate cloud is the sum of the HI mass M_HI and the mass in molecular hydrogen:

$$M_\mathrm{H} = M_\mathrm{HI} + M_{\mathrm{H}_2} = M_\mathrm{HI} + 2m_\mathrm{H} D^2 \tan\phi^2 \sum_i N^i_{\mathrm{H}_2}. \tag{5.9}$$

The additional factor of two is because a hydrogen molecule consists of two hydrogen atoms.

The molecular fraction f_mol of a candidate MIVC is given by

$$f_\mathrm{mol} = \frac{2N_{\mathrm{H}_2}}{N_\mathrm{HI} + 2N_{\mathrm{H}_2}} = \frac{M_{\mathrm{H}_2}}{M_\mathrm{HI} + M_{\mathrm{H}_2}}. \tag{5.10}$$

All these quantities are derived directly from the candidate and the data maps without any manual input for individual candidates. For MIVC IVC 210, we have estimated parameters in Chapter 3 from the EBHIS data. After the correction for differences in data and methodologies, the derived pressure is about 37% larger in a detailed analysis as compared with the result from the general approach. This apparently large discrepancy is completely compatible with the different estimates for the kinetic temperatures. Thus, the automatic estimation of the cloud properties like sizes, particle densities, and pressures are reasonable and compatible with a detailed analysis.

5.9.2 Distances to the IVC population

For the MIVCs Draco and IVC 135, there are good distance constraints of $D = 300 - 400$ pc (Gladders et al. (1998); Benjamin et al. (1996), see also Sect. 5.4.5). However, such precise estimates are not available for the IVC population as a whole. There are several possibilities how to assign distances to all IVCs: 1) One distance is assumed to all IVCs. 2) One assumes that IVCs are related to a Galactic fountain process, which suggests some distribution of vertical scale heights of the IVC gas, from which distances are derived. 3) The distance limits for individual lines of sight are expanded for larger IVC complexes.

All these methods are simplifying and problematic in their own ways. One distance to all IVCs is likely the worst assumption, since at lower latitudes IVCs may be located further away. The available distance brackets for lines-of-sight towards IVCs are often not very accurate, ranging from ~0.2 kpc up to ~4 kpc (e.g. Albert & Danly 2004). These estimates are only valid for individual lines-of-sight and it is difficult to extend them to the entire IVC sky.

Hence, we decide for the assumption of a single height z over the Galactic disk for the entire IVC population assuming different heights. Besides its drawbacks, this approach reflects the characteristics of a Galactic fountain process. We infer the quantities for a scale height of $z = 0.5$ kpc. For a given

scale height z, the corresponding distance D is calculated from the Galactic latitude b by $D = z/\sin|b|$. For a larger scale height of $z = 1.0$ kpc, the estimated HI densities and pressures decrease by a factor of two, the HI masses increase by a factor of four, respectively (Sect. 5.9.1).

5.9.3 Results for molecular IVC candidates

For the three MIVC samples (northern MIVCs$^-$, southern MIVCs$^\pm$), the resulting median properties of the entire populations are listed in Table 5.7. Histograms of the derived physical sizes d, HI particle densities $n_{\rm HI}$, and pressures $p/k_{\rm B}$ are shown for the northern MIVCs$^-$ in Fig. 5.24 for $z = 0.5$ kpc. Note that $n_{\rm HI}$ and $p/k_{\rm B}$ are derived from the HI data alone without any H_2. The total hydrogen particle densities are larger than the given HI particle densities. Before we discuss the physical parameters of the samples, we remark that the presented values may be uncertain for some candidates due to the automated approach. In addition, the distances D calculated from $z = 0.5$ kpc for the respective latitudes b may be doubtful.

The main findings are:

- The MIVC candidates are small with median angular diameters of less than ∼35′, corresponding to spatial diameters of $d \simeq 6 - 13$ pc. Hence, in previous studies using the LAB HI data (Kalberla et al. 2005), most of these objects would be unresolved and likely undetectable. This would result into a fainter FIR-excess because the excess emission is averaged with the linearly correlating gas and dust.

- The upper limits on the median kinetic temperatures are for all samples similarly $T_{\rm kin} \lesssim 400$ K. This temperature is typical for the CNM in the Milky Way (e.g. Kalberla & Kerp 2009). Note that we apply a criterion on the line width to be smaller than FWHM$< 5\,{\rm km\,s^{-1}}$, corresponding to a kinetic temperature of $T_{\rm kin} \lesssim 545$ K. This criterion is not in conflict with the bulk of candidates.

- The inferred HI particle densities of $n_{\rm HI} \simeq 3-7\,{\rm cm^{-3}}$ are comparable to the typical CNM densities (e.g. Kalberla & Kerp 2009).

- The resulting median pressure is accordingly $p/k_{\rm B} \simeq 1000 - 3000\,{\rm K\,cm^{-3}}$, which is typically less than the equilibrium thermal pressure in the ISM of $\sim 3000\,{\rm K\,cm^{-3}}$ (e.g. Wolfire et al. 2003).

- The molecular fractions are $f_{\rm mol} \simeq 0.4 - 0.6$. Hence, the total hydrogen particle densities and pressures increase by a factor of ∼2.

There is evidence that some fraction of the MIVC candidates are over-pressured since their estimated pressures from their combined atomic and molecular content is above the equilibrium thermal pressure. Furthermore, the thermal equilibrium pressure decreases for larger scale heights, however only weakly for $z \lesssim 1$ kpc (Wolfire et al. 1995b, their Fig. 2).

Still, the total pressure within the ISM is much larger than the thermal pressure with contributions from turbulence, magnetic fields, and cosmic rays (e.g. Cox 2005). This is puzzling because the cold gas could not be in any thermal equilibrium state but is quenched continuously. The solution to this issue is likely related to the scale-dependency of the turbulent pressure (Wolfire et al. 2003): Turbulent motions within the ISM govern the temporal and spatial structure of the gas (e.g. Audit & Hennebelle 2005; Glover & Mac Low 2007). However, turbulence is scale-dependent as is the turbulent energy. Thus, the neutral gas in both the cold and warm phases can be in a thermal equilibrium on spatial scales of less than ∼0.3 pc and less than ∼215 pc respectively (Wolfire et al. 2003). Only the outer layers of a gas cloud should be in an equilibrium situation, the inner regions do not necessarily have to be. Otherwise clouds as a whole would contract or expand to accommodate to the surrounding pressure.

	d [pc]	$T_{\rm kin}$ [K]	$n_{\rm HI}$ $\left[\rm cm^{-3}\right]$	$p/k_{\rm B}$ $\left[\rm K\,cm^{-3}\right]$	$f_{\rm mol}$	$M_{\rm HI}$ [$\rm M_\odot$]	$M_{\rm H}$ [$\rm M_\odot$]
northern MIVCs$^-$	6.2	412	4.7	1766	0.51	33	67
southern MIVCs$^-$	10.2	440	7.2	2920	0.37	165	300
southern MIVCs$^+$	13.3	388	3.2	980	0.57	170	400

Table 5.7: Median values of estimated spatial extents d, kinetic temperatures $T_{\rm kin}$, densities $n_{\rm HI}$, pressures p, molecular fractions $f_{\rm mol}$, HI masses $M_{\rm HI}$, and total hydrogen masses $M_{\rm H}$ of northern and southern MIVC$^\pm$ samples. A scale height of $z = 0.5$ kpc is assumed, from which the distances to the candidates are calculated for their latitudes b.

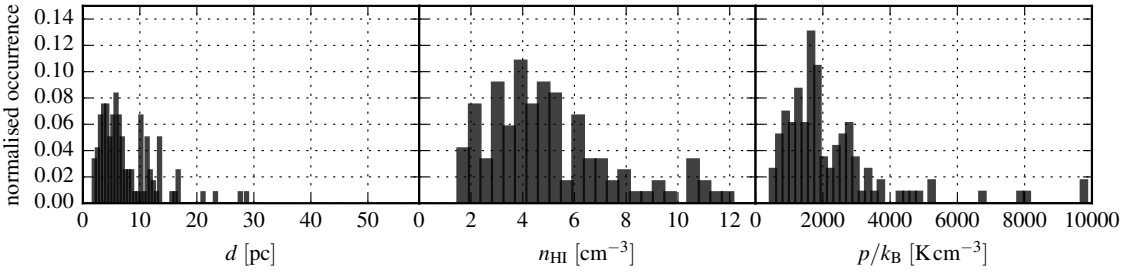

Fig. 5.24: Spatial sizes d, HI particle densities $n_{\rm HI}$, and pressures $p/k_{\rm B}$ of northern MIVC$^-$ ensemble. Each histogram is normalised to unity. The properties are derived assuming a vertical scale height of $z = 0.5$ kpc.

Note that for larger scale heights z the median HI densities would decrease accordingly. In order to be obtain plausible CNM HI densities, the assumed scale height of $z = 0.5$ kpc appears to be sensible. For $z = 1.0$ kpc or even $z = 1.6$ kpc (Marasco & Fraternali 2011), the derived densities would decrease by factors of ∼2 and ∼3, respectively, which would be very low for the CNM.

5.9.4 Mass estimates

In order to put the amount of molecular hydrogen contained in the northern and southern MIVC$^\pm$ and NIVC$^\pm$ samples in context of the accretion of matter onto the Milky Way, we estimate their total inferred H_2 mass. For this, we consider $N_{\rm H_2} > 0$ and $z = 0.5$ kpc.

The derived ensemble HI, H_2, and total hydrogen masses of the northern and southern AIVC$^\pm$, MIVC$^\pm$, and NIVC$^\pm$ samples are listed in Table 5.8. For the MIVCs, the molecular masses are significant or even dominating. The mass of the NIVCs is determined mostly by the atomic component with a small molecular fraction only. The AIVC candidates have comparably small HI masses.

When we assume average scale heights of $z = 0.5$ kpc to the entire IVC$^\pm$ gas of the Milky Way above $|b| > 20°$, the total HI mass of all this IVC$^\pm$ gas is $M_{\rm HI}^{\rm IVC} \simeq 3.1 \times 10^6\,\rm M_\odot$. For the northern Galactic hemisphere only, the total IVC$^\pm$ HI mass $\sim 1.7 \times 10^6\,\rm M_\odot$.

The total inferred molecular mass in IVCs on both Galactic hemispheres amounts to $\sim 1 - 2\%$ of the total HI mass of IVCs. Hence, the total amount of potential molecular material within IVCs, as inferred by the HI-FIR correlation, is small compared with the total amount of HI within the IVC population. This is in consensus with the low number of confirmed MIVCs and the low H_2 column densities in many IVCs (Richter et al. 2003; Wakker 2006).

The estimate of the total H_2 masses can be converted into an accretion rate of molecular IVC gas when some infall velocity is assumed. Marasco & Fraternali (2011) infer a vertical motion of the IVC Milky

	$M_{\rm HI}$ [$M_\odot$]	$M_{\rm H_2}$ [$M_\odot$]	$M_{\rm H}$ [$M_\odot$]	$M_{\rm HI}$ [$M_\odot$]	$M_{\rm H_2}$ [$M_\odot$]	$M_{\rm H}$ [$M_\odot$]	$M_{\rm HI}$ [$M_\odot$]	$M_{\rm H_2}$ [$M_\odot$]	$M_{\rm H}$ [$M_\odot$]
	MIVC$^-$ samples			NIVC$^-$ samples			AIVC$^-$ samples		
north	10 600	14 100	24 700	23 300	3000	26 300	4300	0	4300
south	15 400	11 600	27 000	7400	800	8200	4300	0	4300
	MIVC$^+$ samples			NIVC$^+$ samples			AIVC$^+$ samples		
north	70	25	95	2300	300	2600	590	0	590
south	10 200	11 800	22 000	680	170	850	0	0	0

Table 5.8: Ensemble masses of IVC$^\pm$ samples on northern and southern Galactic hemispheres. A vertical scale height of $z = 0.5$ kpc is assumed towards all samples. Only positive H_2 column densities are considered.

Way halo and IVC gas of $v_z = -20^{+5}_{-7}\,\mathrm{km\,s^{-1}}$. Using Eq. 1 from Putman et al. (2012), the accretion rate of the northern infalling molecular IVC gas in MIVC$^-$ and NIVC$^-$ candidates is $\dot{M} \simeq 5 \times 10^{-4}\,M_\odot\,\mathrm{yr^{-1}}$ for $z = 0.5$ kpc.

In order to estimate an upper bound for the accretion rate resulting from the infalling IVC$^-$ gas, we consider both the molecular content of the MIVC$^-$ and NIVC$^-$ samples and the total HI mass of the northern and southern IVC$^-$ sky of $\sim 8 \times 10^6\,M_\odot$ at $z = 1.0$ kpc. For an accretion velocity of $v_{\rm in} \simeq -50\,\mathrm{km\,s^{-1}}$, which is the sum of the vertical and radial inflow velocities inferred by Marasco & Fraternali (2011), this results into $\dot{M} \simeq 0.08\,M_\odot\,\mathrm{yr^{-1}}$, which is dominated completely by the HI mass. This maximum accretion rate is similar to the estimated rate for the HVCs of $0.08\,M_\odot\,\mathrm{yr^{-1}}$ (Putman et al. 2012). However, this rate is significantly less than the $\sim 1\,M_\odot\,\mathrm{yr^{-1}}$ that is required for sustaining star formation in the Milky Way (Putman et al. 2012).

We stress that the estimates of the total HI and H_2 masses in IVCs and the corresponding accretion rates depend highly on uncertain quantities and simplifications. The derived distances for the assumed z-heights may be different, since there are certainly IVCs in different stages of the fountain orbits (compare with Sect. 5.4.7.1). The separation of the HI emission into LVCs and IVCs by applying a simple LSR criterion is not strict over the sky. This leads to contamination with LVC gas, also IVCs may be found in the LVC regime.

The low amount of molecular gas in IVCs in general and the resulting low accretion rates of cold (molecular) gas may be explained by several arguments.

Sources of accretion Putman et al. (2012) distinguish between three major classes of fuelling sources of galaxy disks: 1) accretion from the halo by HVCs or cosmic filaments, 2) gas at the disk-halo interface, some of which related to galactic fountains, and 3) stellar ejecta and gas transport within the disk itself. Hence, it is not required that the entire accretion rate of the Milky Way is accounted for by IVCs. Especially the intra-disk sources are not well understood and the amount of fuelling is unclear. Hence, the total amount of cold (molecular) gas in IVCs may be a small contribution to the global accretion rate of matter onto our Galaxy. Nevertheless, the accreted material is thought to be metal-poor and cold in order to feed star formation.

Improper modelling of the HI-τ correlation We follow a simplistic approach by using a single two-component linear model to infer the distribution of molecular hydrogen in IVCs. A single HI-τ correlation for the entire northern or southern Galactic hemisphere may be too simplifying because locally there are variations that have to be modelled more precisely. One could argue that we do not detect all the molecular hydrogen in IVCs. However, we recover all confirmed MIVCs, which are located at

different locations on the sky. This shows that our approach captures some essential conditions.

In the estimate of the global H_2 mass, we also include the molecular hydrogen within the NIVC sample, which statistically is compatible with scatter in the HI-τ correlation. By applying a better modelling, for example by allowing spatial and spectral variations, one may be able to find a larger significance for NIVC candidates moving them to the class of MIVC candidates. Vice versa one would find that some MIVC candidates are likely not real. However, this should not change the total amount of inferred molecular hydrogen too much because it still requires FIR excess emission relative to the surroundings. We do not find a systematic bias in the global HI-τ correlation.

The biggest challenge may be the influence of the FIR emission of the LVC gas onto the modelling of the IVC dust emission. This comes in two different aspects. First, in our analysis here we do not look for molecular gas in IVCs that are located towards too much LVC gas and dust. Second, when LVC and IVC HI emission overlap on the celestial sphere, contributions from either one can affect the conclusions of the other. Although, this usually leads to the assignment of FIR emission from LVCs to the IVCs increasing the inferred amount of H_2 in IVCs.

Furthermore, one needs to separate the HI gas in LVC and IVC gas in the first place. This is often not easily done, especially when there are multiple HI emission components. In these cases simple velocity cuts do not provide a good separation. Other possibilities are to decompose the spectra by a Gaussian decomposition and using individual components to build up the respective classes of halo clouds. Or one could resign the artificial differentiation into distinct components but use all channels individually to model the total FIR emission in a generalised linear model (Lenz et al. 2016).

Selection effects IVCs and HVCs are defined and selected by their observed radial velocity. This has several drawbacks since the observed radial velocities depend on the motion of the targets relative to the Sun, as we show explicitly by the observables of ballistic orbits (Sect. 5.4.7.1). Furthermore, we select IVCs only at $|b| > 20°$. Thus, the observable IVC sky with $|b| > 20°$ and $20\,\mathrm{km\,s^{-1}} \leq |v_{\mathrm{LSR}}| \leq 100\,\mathrm{km\,s^{-1}}$ certainly represents only some fraction of the entire Galactic IVC population. For example, no MIVC candidate has been found towards the Galactic centre. This is most likely a selection effect because there star-formation happens also that should cause outflows into the halo.

The Galactic fountain scenario pictures a disk-wide ejection of material by stellar feedback all over the Galactic disk. As a typical large fountain, we take the model of Melioli et al. (2008). This fountain ejects a mass of $2.5 \times 10^5\,\mathrm{M_\odot}$ to scale heights of up to 2 kpc. The downward motion is $-100\,\mathrm{km\,s^{-1}}$ at most. Melioli et al. (2008) model a single large fountain event, which ejects material in a certain part of the Galaxy. Hence, these simulations naturally suggest that in our local Galactic neighbourhood only some specific fountain processes are evident.

We investigate how a plane-parallel slab of fountain material at $z = 2\,\mathrm{kpc}$ with $v_z = -100\,\mathrm{km\,s^{-1}}$ would be observed when it is placed all over the Milky Way disk. This consideration is similar to Schwarz & de Boer (2004). We look at the dependency of the observable Galactic latitude b and projected vertical velocity v_z^{proj} on the heliocentric distance x (Fig. 5.25). For simplicity the heliocentric distance is taken to be 1D along the Galactic disk. The Galactic latitude b (black) and the absolute projected vertical velocity v_z^{proj} (blue) decrease for increasing heliocentric distance x. The vertical and horizontal lines mark the limits of our global search for MIVCs of $|b| > 20°$ and $20\,\mathrm{km\,s^{-1}} \leq |v_{\mathrm{LSR}}| \leq 100\,\mathrm{km\,s^{-1}}$.

From simple geometry it can be shown analytically that at a heliocentric distance of $x \simeq 5.5\,\mathrm{kpc}$ the fountain ejecta would be observable at $b \simeq 20°$ with a projected vertical velocity of $v_z^{\mathrm{proj}} \simeq -34\,\mathrm{km\,s^{-1}}$. At a heliocentric distance of $x \simeq 9.8\,\mathrm{kpc}$, $v_z^{\mathrm{proj}} \simeq -20\,\mathrm{km\,s^{-1}}$ and $b \simeq 12°$. The corresponding observable parameter spaces in Fig. 5.25 are coloured in black and blue. Hence, for the chosen setting, the main limiting factor in the observations of vertically infalling fountain material all over the Milky Way is given

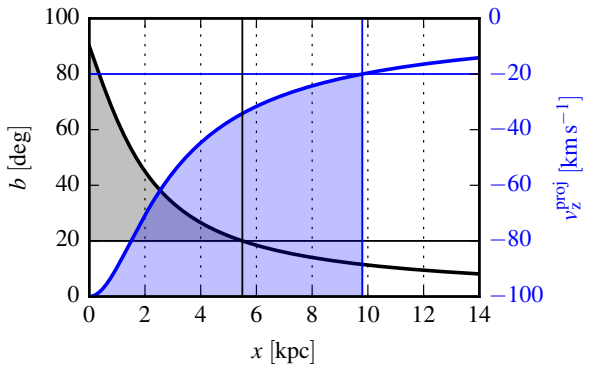

Fig. 5.25: Dependency of observable Galactic latitude b (black) and projected vertical velocity $v_z^{\rm proj}$ (blue) on heliocentric distance x for a plane-parallel slab of fountain objects at vertical scale height z = 2 kpc with a downward motion of $v_z = -100\,\mathrm{km\,s^{-1}}$. The 1D heliocentric distance x is measured within the plane of the disk. The vertical and horizontal lines mark the limits of our search for MIVCs of $|b| > 20°$ and $20\,\mathrm{km\,s^{-1}} \leq |v_{\rm LSR}| \leq 100\,\mathrm{km\,s^{-1}}$. The coloured areas mark the observable parameter spaces.

by the decreasing Galactic latitude. This reflects the low heights of the fountain objects as compared with the large extent of the Milky Way disk.

Note that we assume a fountain layer at $z = 2$ kpc. The known MIVCs are located all at lower heights of $z \lesssim 0.5$ kpc. For this configuration the situation is even worse and these objects can only be observed for $x \lesssim 1.4$ kpc.

Thus, in our study here we approximately trace a cylindrical volume in our Galaxy with 5.5 kpc radius and 2×2 kpc thickness, two times the z-height of the plane-parallel slab. The whole volume in which fountain ejecta are expected is approximately given by the largest radius of high-mass star formation in our Galaxy, which is about 16 kpc (Reid et al. 2009). Thus, we trace ∼12% of the volume of interest in the Milky Way.

If we assume that the local neighbourhood is typical for our Galaxy, we can extrapolate from the amount of H_2 within the local IVC population to the entire Galaxy. This gives an upper value for the global H_2 mass in IVCs of $\sim 3 - 4 \times 10^5\,M_\odot$ for $z = 1.0$ kpc. With $v_{\rm in} = -50\,\mathrm{km\,s^{-1}}$, the resulting accretion rate of molecular H_2 from IVCs$^-$ is $\sim 0.02\,M_\odot\,\mathrm{yr^{-1}}$. Similarly, the extrapolated upper total HI and H_2 accretion rate is $\sim 0.67\,M_\odot\,\mathrm{yr^{-1}}$. This is a significant fraction of the present star-formation rate of our Galaxy.

5.10 Conclusions

In this Chapter, we addressed the global IVC population and studied its FIR properties and molecular content. The HI-τ correlation is analysed on global scales of our Galaxy for latitudes of $|b| > 20°$. The HI emission is separated into LVCs, IVCs, and HVCs by applying LSR thresholds of $20\,\mathrm{km\,s^{-1}} \leq |v_{\rm LSR}| \leq 100\,\mathrm{km\,s^{-1}}$ for the selection of IVCs. We formulate search criteria to identify molecular IVCs (MIVCs), atomic IVCs (AIVCs), and normal IVCs (NIVCs). MIVCs show significantly more FIR emission than expected from the HI-τ correlation while AIVCs show significantly less. NIVCs are compatible with the intrinsic scatter of the correlation.

The study of the global HI-τ correlation is performed separately for the northern and southern Galactic hemispheres because the southern IVC sky may be influenced by the Magellanic System, which could cause unexpected differences in the HI-τ correlation or IVC populations. From the global correlations a wealth of small objects is revealed that show significant deviations from the global mean correlation. Many of these objects have not been identified in previous studies (Désert et al. 1988; Reach et al. 1998). This underlines the large amount of information gained by the new HI and FIR all-sky survey data. We focus here on the particular class of MIVCs, but many of the individual objects, that appear peculiar in terms of the mean gas-and-dust correlation, would deserve their own consideration and analysis. Especially a dedicated study of FIR deficient objects would be interesting, since these objects may be

related to a low metal content. In this way the combination of HI and FIR data allows to disentangle physically distinct gas components in the ISM.

There are clear differences between the IVC populations on the two Galactic hemispheres (north and south) and between the two radial velocity regimes ($-100\,\mathrm{km\,s^{-1}} \leq v_{\mathrm{LSR}} \leq -20\,\mathrm{km\,s^{-1}}$ and $+20\,\mathrm{km\,s^{-1}} \leq v_{\mathrm{LSR}} \leq +100\,\mathrm{km\,s^{-1}}$, compare with Table 5.5 on page 131). There are much more candidates on the northern hemisphere simply because of the higher abundance of IVC gas as compared with the southern hemisphere. There are less candidates for positive LSR velocities. While the low number of northern AIVC$^+$ and NIVC$^+$ candidates appears to be compatible with the different amounts of total IVC gas, the lack of MIVC$^+$ candidates is perhaps related to different physical processes of infall versus outflow.

In total we identify 206 MIVC$^\pm$ candidates including the known MIVCs (see Magnani & Smith 2010), except for one. The one missing MIVC is not found because it is located in between the LVC and IVC regimes outside the chosen velocity bracket. Among the large number of MIVC candidates, there are a few objects that like are true MIVCs, especially on the northern hemisphere.

This large sample of different IVC classes allows to study properties in a statistical approach. We find that MIVC candidates in general are not related to HVC HI emission except for very few cases, for which this connection has been explicitly proposed (e.g. Herbstmeier et al. 1993, 1994; Moritz et al. 1998; Weiß et al. 1999; Lenz et al. 2015). The dust temperatures are lowest in MIVCs excluding enhanced dust heating as the source of the FIR excess emission in these objects (e.g. Reach et al. 1998). Except for the brightest known MIVCs, there is no associated CO emission as inferred by Planck Collaboration XIII (2014). There are some longitude regimes in which no IVC candidate is identified, mostly due to a lack of IVC gas. MIVCs tend to be located at lower latitudes showing the narrowest and brightest HI line profiles as compared with the other samples.

For most candidates, the latitudes, LSR velocities, HI column densities, and HI line widths are distinct from the selection criteria. Hence, apparently our initial selection criteria do not bias the samples severely. There is also no problem with the differentiation between IVCs and HVCs at $|v_{\mathrm{LSR}}| = 100\,\mathrm{km\,s^{-1}}$, mostly because HVCs do not contain much cold gas.

There is an imprint of Galactic rotation in the kinematics of the IVC samples (e.g. Schwarz & de Boer 2004; Marasco & Fraternali 2011). A model of Galactic rotation complemented by the vertical, radial, and lagging velocity components obtained by Marasco & Fraternali (2011) is apparently able to reproduce the observed radial velocities of the IVC populations. This suggests that the IVC samples originate from the Galactic disk.

For the known MIVCs, an upper distance limit of $D \simeq 500\,\mathrm{pc}$ is estimated from the dust reddening maps of Green et al. (2015). This limit is compatible with the available distance information (Gladders et al. 1998; Benjamin et al. 1996; Röhser et al. 2014).

We study the kinematical evolution of Galactic fountain ejecta by calculating their ballistic orbits. The observables of a fountain orbit are highly time-dependent, especially the observable LSR velocity by which the IVCs are defined. The ejecta tend to lag behind the pure rotating Galactic orbit. These considerations constrain the potential origin of the northern IVC sky. It should have originated nearby within ∼1 kpc and ahead of the Galactic rotation towards $l \simeq 90°$. Compatible with these requirements, there is evidence for enhanced past star-formation activity from over-abundances of nearby young stellar clusters with ages of 60 Myr and 100 Myr (De la Fuente Marcos & De la Fuente Marcos 2008).

The southern Galactic hemisphere is different from the northern in several aspects. There is the Magellanic System, which enters as metal-poor and FIR-deficient gas in the HI-τ correlation. We infer a negative offset in the correlation that may be related to the position of the Sun $20.5 \pm 3.5\,\mathrm{pc}$ above the Galactic mid-plane (Humphreys & Larsen 1995). Accordingly, towards the southern Galactic hemisphere, the lines-of-sight pass through the innermost mid-plane where likely more ionised and molecular

gas is expected than compared with larger heights. This additional molecular gas at lower total hydrogen column densities may bias the fit.

On the southern hemisphere there are no similar IVC structures as on the northern. A considerable fraction of the observed IVC gas may be associated with the Magellanic System and not to our Galaxy. This is puzzling, also in light of the considerations of potential origins of the northern IVC sky. A breakout into the halo by stellar feedback is expected to occur more or less symmetrically north and south of the plane, unless the star-formation sites were located significantly above the plane, offset to the north.

The southern sample candidates are found mostly at latitudes between $-40°$ and $-20°$ where also the LVC emission is bright, which complicates the confirmation of any MIVC candidate. In fact, some MIVC candidates appear to be associated with extensions of lower-latitude disk structures. Additional evidence for a larger foreground at lower latitudes is provided by the larger dust reddening as compared with the northern hemisphere.

MIVC candidates appear to be over-pressured and located towards the borders of IVC complexes where stronger interactions with the surrounding environment are expected. For the global MIVC candidate population there are small shifts between the HI and FIR peaks similar as for the MIVC IVC 210 (Chapters 3 and 4).

On both hemispheres, but mainly on the northern simply because of the large number of IVCs, the physical and kinematical properties of the IVC samples match the expectations of a Galactic fountain process. The global study of molecular gas in IVCs gives more evidence for the picture of a dynamically driven natural evolution from atomic to molecular IVCs (Chapters 3 and 4). The importance of collisions with HVC gas is unlikely to be a general driver in this transition.

The estimated H_2 mass in the global IVC population is negligible and results into a very low gas accretion rate, also when the HI mass is added. This may be related to fundamental limitations in the observations of Galactic fountain material. First, the selection of IVCs by a radial velocity is problematic, not only because of the projection of the 3D velocity along the orbit but also because of the separation between LVC and IVC gas. Second, from the location of the Sun only ~10% of the entire population of fountain ejecta may be accessible when criteria of $|b| > 20°$ and $20\,\mathrm{km\,s^{-1}} \leq |v_{\mathrm{LSR}}| \leq 100\,\mathrm{km\,s^{-1}}$ are chosen. Extrapolating from the local Galactic environment to the entire Milky Way, the mass in IVCs and the corresponding accretion rates of cold (molecular) gas are significantly larger. Thus, the global census of fountain material, which is in part observable as IVCs in the local Galactic vicinity, may be an important contribution to the accretion of matter onto the Milky Way and the sustaining of its star-formation activity.

CHAPTER 6

Summary and outlook

The evolution of galaxies over cosmic time is a complex interplay between internal and external processes that shape the structure and properties of galaxies. In conjunction, the merging of galaxies, the accretion of metal-poor material from the intergalactic medium, and the ejection of metal-enriched gas into the galactic halos lead to the appearances of galaxies as we observe them in the Universe. The re-distribution and circulation of matter within and around galaxies ultimately causes the formation of new stars that power and sustain this cycle of matter.

Besides more and more sophisticated numerical models, multi-frequency observations of the multi-phase interstellar and intergalactic medium are essential for a thorough and deeper understanding of the processes that govern the evolution of galaxies. The Milky Way plays a central role in this endeavour. Because of our location within the Milky Way, there are inherent difficulties in the interpretation of Galactic observations. Nevertheless, we are able to gain a glimpse on the full variety and complexity of the dynamical, thermal, and chemical processes that are at work from the smallest to the largest scales, from cores of molecular clouds to the entire Galaxy.

In this thesis we present an observational study of the connection between the Galactic disk and halo. Out- and in-flowing gas clouds are identified as intermediate-velocity clouds (IVCs), which are thought be the result of the stellar feedback processes in our Galaxy that drive a Galactic fountain. Our main focus is on the molecular content of IVCs because molecules are an indicator of cold and dense gas, which is of major importance for the accretion of matter onto our Galaxy and the sustaining of its star-formation activity.

We examine two different aspects of the IVC sky. On the one hand a detailed study of two individual clouds is conducted, an atomic and molecular IVC, which are prototypical objects. On the other hand the first global analysis of the molecular content of the IVC population of our Galaxy is performed.

6.1 Results from the detailed study of atomic and molecular IVCs

In Chapters 3 and 4 an atomic IVC (AIVC) and a molecular IVC (MIVC) are analysed in large detail. While in Chapter 3 only single-dish HI data is used, we present in Chapter 4 dedicated high-resolution HI and CO observations of the two clouds.

The single-dish HI data discloses very similar gaseous properties of the two clouds like gas morphologies, HI column densities, and spectral lines (Chapter 3). Only by the combination of HI and FIR data the different physical nature of the two clouds is evident. The HI-FIR correlation of the AIVC is modelled well by a single linear function, whereas the MIVC shows significant FIR excess emission for HI column densities of $N_{\rm HI} \gtrsim 2 \times 10^{20}\,{\rm cm}^{-2}$.

The MIVC exhibits significantly more dust emission than expected from the observed HI content and the surrounding gas-to-dust correlation. This FIR excess emission is converted into a corresponding amount of molecular hydrogen. Fits of modified black-body spectra to four different FIR frequencies show that the MIVC is associated with significantly colder dust than the AIVC. Generally, the dust temperatures are anti-correlated to the hydrogen column densities. This suggests that the enhanced emission of FIR excess clouds is not related to enhanced heating of the dust that would cause brighter FIR emission also. Instead the FIR excess is related to the presence of molecular hydrogen, as is confirmed for many FIR excess objects. For the MIVC a molecular fraction of $f_{\mathrm{H_2}} \simeq 0.4$ is inferred.

Despite the different amount of dust within the AIVC and MIVC relative to the observed HI, the AIVC exhibits less cold gas than the MIVC. This is the only indication from the HI data alone that the clouds may be physically different. While the AIVC contains more HI than the MIVC, it appears not to be spatially distributed such that the efficient formation of large amounts of molecules is possible yet.

Both IVCs are associated with large-scale IVC features that show continuous velocity gradients of $\sim 10\,\mathrm{km\,s^{-1}}$. These gradients may be signs of interactions between the clouds and the surrounding medium.

The similarities and differences of the AIVC and MIVC lead us to the suggestion of a dynamically driven transformation of purely atomic IVCs into molecular IVCs as a natural evolutionary step within the Galactic fountain cycle. Within this picture the two clouds are at different states in the transition from purely atomic to molecular clouds. The motion of the clouds onto the disk is thought to be key in this transformation since it is connected to ram pressure and an increasing halo pressure towards lower Galactic latitudes.

We connect the ambient halo pressure to the ram pressure of the clouds. The ram pressure is determined by the halo density and the relative velocity of the clouds to their environment. At the assumed distance of the clouds, the ram pressure is at least twice as large as the halo pressure. This pressure difference causes pressure forces that disturb the objects. These density fluctuations are thought to enhance the pressure within the clouds locally, by which the cooling of the warm neutral medium (WNM) into cold neutral medium (CNM) is triggered. In the cool and dense gas the formation time of H_2 is greatly decreased and shielding of the molecules is provided.

The H_2 formation timescale should be $t_{\mathrm{H_2}} \lesssim 6\,\mathrm{Myr}$, which is similar or less than the time until the IVCs will hit the Galactic disk. These considerations lead to identical results for the AIVC and MIVC suggesting that the AIVC will evolve into a MIVC in a few Myr. This conclusion emphasises that the physical processes and chemistry within the two clouds are acting on angular and spatial scales unresolved by the HI single-dish data. The angular resolution of EBHIS corresponds to a spatial resolution of $\sim 1\,\mathrm{pc}$ within the clouds, indicating that the condensation of gas and the subsequent formation of molecules happens on smaller scales.

This is the motivation for additional high-resolution HI and CO observations of the two clouds with the goal to resolve the structures that should be associated with the different gaseous properties (Chapter 4). While the AIVC is not detected in ^{12}CO(1→0) emission setting an upper limit of $N_{\mathrm{H_2}} \simeq 0.02 \times 10^{20}\,\mathrm{cm^{-2}}$, a rich molecular substructure is disclosed within the MIVC. For the AIVC, the high-resolution HI data recovers about 16% of the total HI flux from the single-dish data, indicating that there is some small-scale HI substructure. However, most of the HI emission is not associated with the small-scale structure but with a smooth HI distribution that is not measured by the radio interferometer, lacking high-column density cores. This is in contrast to the MIVC for which about half of the emission is recovered in the high-resolution data suggesting a much more pronounced small-scale structure. The significance of the HI substructure appears to be reflecting the lack or richness of molecular hydrogen within the clouds.

The power spectral densities show that both the AIVC and MIVC are statistically similar on large

scales. However, the MIVC has significantly more structure on small scales below $\sim 1'$. For the estimated distance of 400 pc, these angular scales correspond to spatial scales of less than ~ 1 pc.

The distribution of ^{12}CO(1→0) emission within the MIVC is characterised by three different components. 1) Most of the CO emission originates from the eastern edge of the cloud where also the brightest FIR peak is located. 2) A second smaller CO peak is detected near the second FIR peak of the cloud where the largest amounts of HI are found. 3) All over the MIVC small blobs of CO emission are observed. The velocity structure of the CO emission is complex showing a bimodal velocity distribution with the peaks shifted by $\sim 2.7\,\mathrm{km\,s^{-1}}$.

The different locations of the HI, FIR, and CO peaks within the MIVC suggest that the cloud contains regions with different chemical properties. From west to east, the cloud apparently turns clumpier and contains more and more molecular hydrogen.

By estimating the H_2 distribution within the MIVC from the HI-FIR correlation, we can compare these inferred amounts of molecular hydrogen to the CO emission, allowing to measure the variations of the X_{CO} factor across the cloud. There is a large spread between $0.6 \times 10^{20}\,\mathrm{K\,km\,s^{-1}} \lesssim X_{\mathrm{CO}} \lesssim 20 \times 10^{20}\,\mathrm{K\,km\,s^{-1}}$ with a mean if $\bar{X}_{\mathrm{CO}} \simeq 2.3 \times 10^{20}\,\mathrm{K\,km\,s^{-1}}$, close to the Galactic average.

A large column density contrast is inferred at the eastern edge of the CO distribution towards the rim of the MIVC. Radiative transfer calculations constrain the kinetic temperature to $T_{\mathrm{kin}} \simeq 52\,\mathrm{K}$ and the H_2 volume density to $n_{\mathrm{H_2}} \simeq 440\,\mathrm{cm^{-3}}$, which indicates sub-thermal excitation conditions of ^{12}CO. Even the most high-mass HI and CO clumps within the MIVC appear to be gravitationally unbound. Hence, within the cloud no star formation is expected to occur.

A detailed comparison of the HI and CO data reveals spatial offsets, especially at the eastern edge of the cloud. The CO peak is shifted eastwards closer to the cloud's boundary than the HI peak. This is interpreted as the leading front of the cloud since there ram pressure should cause the strongest perturbations of the cloud. There is evidence for non-equilibrium chemistry within the MIVCs hinting towards the dynamical nature of the transition from atomic to molecular gas driven by gas dynamics.

In the literature, the importance of the dynamics of this transition is illustrated by numerical simulations of turbulent colliding flows of atomic gas. Due to dynamical and thermal instabilities, non-linear density perturbations of CNM form in which the H_2 formation time is rapid with ~ 1 Myr or less. The simulations give a typical spatial scale of ~ 0.1 pc for the molecular CNM structures. This scale is coincident with the spatial scale at which the two clouds differ in the power spectral densities.

We propose the analogy that infalling IVCs constitute flows of WNM and CNM that develop small-scale structure and molecular hydrogen when there is a sufficient relative velocity between the clouds and the halo medium and a sufficiently large halo density, which exerts forces onto the clouds. In the high-resolution HI and CO spectra of the MIVC, the different velocity components indicate flows of atomic and molecular material with respect to each other.

In fact, the simulations show that turbulence alone cannot cause the transition from WNM to CNM unless the WNM density is enhanced by some triggering mechanism. This could be for instance a ram pressure interaction as it is indicated for the MIVC. Once a critical WNM density is reached and the WNM gets thermally unstable, CNM forms from the WNM. Subsequently, in these CNM structures rapid H_2 occurs. This triggering mechanism may be a gradual and slow process. Since the AIVC has a larger HI mass but a less pronounced substructure, it is justified to assume that the AIVC will turn into a molecular IVC eventually, possibly within a few Myr. Its disturbed morphology indicates ongoing interaction processes anyhow.

These studies suggest that a dynamically driven transformation of purely atomic IVCs into molecular IVCs is a natural evolutionary step within the Galactic fountain cycle. During the final phase of the fountain, the ejecta, which are thought to be observable in part as IVCs, move closer to the Galactic disk where the halo density and pressure increase. The interactions with the surrounding halo medium

condense and compress the clouds at the leading front, which may be an essential part in order to trigger the transition from thermally stable WNM into thermally unstable WNM, which cools down to CNM eventually. Once a critical condensation of the infalling IVC is reached, CNM evolves in which the formation of H_2 occurs rapidly. For different stages in this transition the substructure is more or less pronounced. Hence, the detailed structural properties of the individual IVCs appear to be linked to the stage of the chemical transition.

6.2 Results from the global study of IVCs

The study of the global FIR properties of IVCs, the inference of molecular hydrogen, and the search for MIVCs as conducted in this work is the first of its kind specifically focussing on the population of MIVCs. This analysis benefits greatly from the new all-sky survey data in HI and FIR.

The HI-τ correlation is performed resulting in numerous small clouds that deviate from the global average of the Galactic gas-to-dust ratio. Many of these objects are not recognised in earlier studies of the HI-FIR correlation. The global correlation allows the inference of the global H_2 distribution within some approximations and simplifications. The correlation is restricted to high Galactic latitudes $|b| > 20°$, separately for the northern and southern Galactic hemispheres.

We define search criteria for MIVCs by requirements on HI and H_2 column densities and HI line profiles, that should reflect cold and dense gas. The application of these criteria recovers all the known MIVCs except for one. The missing one is not identified because of the strict velocity threshold at $v_{\mathrm{LSR}} = -20\,\mathrm{km\,s^{-1}}$ to differentiate between the LVC and IVC gas. Furthermore, the classes of atomic and normal IVCs (AIVCs and NIVCs) are defined with different criteria on the deviation from the mean HI-τ correlation.

The main results of the global search are the compilations of MIVC candidates for both hemispheres. In total 206 MIVC candidates are inferred including the already known MIVCs. The detailed analysis of the most promising candidates results in four objects that are considered to be likely MIVCs, to which associated CO emission is expected. The other candidates are less clear but could still be actual MIVCs.

The northern and southern IVC populations exhibit clear differences both in terms of number and distribution. There are significantly more candidates of all three classes on the northern hemisphere as compared to the southern. The clear lack of MIVC candidates with positive LSR velocities on the northern sky, however, appears to be related to fundamental physical reasons potentially connected to the mechanisms of outflow versus inflow.

This large sample of different IVC classes allows to study properties in a statistical approach. We find that MIVC candidates in general are not related to HVC HI emission except for very few cases, for which this connection has been explicitly proposed. The dust temperatures are lowest in MIVCs excluding an enhanced dust heating as the source of the FIR excess emission in these objects. Except for the brightest northern known MIVCs, there is no CO emission associated with the candidates as measured by the *Planck* satellite. There are some longitude regimes in which no IVC candidate is identified, mostly due to a lack of IVC gas. MIVCs tend to be located at lower latitudes as compared to AIVCs and NIVCs and contain the narrowest and sharpest HI line profiles.

There is an imprint of Galactic rotation in the kinematics of the IVC samples. Additional vertical, radial, and lagging velocity components appear to match the observed kinematics better.

The observables of a fountain orbit are highly time-dependent, especially the LSR velocity by which the IVCs are defined. The ejecta tend to lag behind the pure rotating Galactic orbit. These considerations constrain the potential origin of the northern IVC sky. It should have originated nearby within $\sim$1 kpc and ahead of the Galactic rotation towards $l \simeq 90°$. Compatible with these requirements, there is

evidence for enhanced past star-formation activity from over-abundances of nearby young stellar clusters with ages of 60 Myr and 100 Myr.

For the southern hemisphere, the negative offset in the HI-τ correlation is potentially attributed to the 20.5 ± 3.5 pc offset of the Sun above the Galactic mid-plane. This spatial displacement may lead to different amounts of ionised and molecular gas that apparently bias the HI-τ correlation slightly.

In general, on the southern hemisphere there are no similar IVC structures as on the northern. This is unexpected, since a breakout into the halo by stellar feedback is expected to occur more or less symmetrically north and south of the plane, unless the star-formation sites were located significantly above the plane. The southern candidates are found mostly at latitudes between $-40°$ and $-20°$ where also the LVC emission is large, which complicates the confirmation of any MIVC candidate. In fact, some MIVC candidates appear to be associated with extensions of lower-latitude disk structures.

The physical and kinematical properties of the IVC samples match the expectations of a Galactic fountain process. MIVC candidates appear to be over-pressured and located towards IVC complex borders where stronger interactions with the surrounding environment are expected. For the global MIVC candidate population there are small shifts between the HI and FIR peaks. Hence, the global study of molecular gas in IVCs gives more evidence for the picture of a dynamically driven natural evolution from atomic to molecular IVCs.

The estimated H_2 mass in the global IVC population is negligible and results into a very low gas accretion rate, also when the HI mass is added. This may be related to fundamental limitations in the observations of Galactic fountain material. First, the selection of IVCs by a radial velocity is problematic. Second, from the location of the Sun only $\sim$10% of the entire population of fountain ejecta may be accessible when criteria of $|b| > 20°$ and $20\,\mathrm{km\,s^{-1}} \leq |v_{\mathrm{LSR}}| \leq 100\,\mathrm{km\,s^{-1}}$ are chosen. When we extrapolate from the local Galactic environment to the entire Milky Way, the mass in IVCs and the corresponding accretion rates of cold (molecular) gas are significantly larger. Thus, the global census of fountain material, which is in part observable as IVCs in the local Galactic vicinity, may be an important contribution to the accretion of matter onto the Milky Way and the sustaining of its star-formation activity.

6.3 Outlook

This work presents a new step in the understanding of the physical properties of the global IVC population and their importance for the evolution of our Galaxy. The combination of HI, FIR, and CO data is essential for a comprehensive picture of the IVC sky. The use of large-scale survey data and dedicated high-resolution observations of individual objects allows to probe different aspects. This combination of multi-wavelength and multi-resolution observations are key in future studies of the IVC sky.

The natural next step in this work is to conduct CO observations to confirm or disprove the MIVC candidates. Ideally this should happen as part of a blind survey of the ^{12}CO($1\rightarrow0$) emission at high Galactic latitudes using small telescopes. An angular resolution of a few arcminutes would be useful matching approximately the resolution of the *Planck* FIR data. Such a survey should cover the entire polar caps with $|b| > 20°$ that are not mapped in CO emission yet. One could initially target the MIVC candidates and extend the survey more and more to reach a full coverage of Galactic CO emission eventually.

In itself such a CO survey would be beneficial for a whole range of other questions regarding molecular clouds and star formation in our Galaxy. Since one measures the kinematic properties of the CO gas, the molecular gas within the IVC sky would be a by-product. The high-latitude LVC molecular gas would be covered also. As compared to the Galactic disk, the total amount of molecular gas at high

latitudes is low. However, these objects are nonetheless interesting in themselves since they present a different kind of molecular clouds above or below the Galactic plane where the environmental conditions are different and not well studied.

Targeted high-resolution CO observations with, e.g., the IRAM 30 m telescope would be more suited as follow-up observations for detected CO emission from individual molecular clouds. Because of the high spatial resolution coverages of larger regions in a blind survey are very time-consuming. High-resolution observations would allow the detailed study of the formation of molecular gas.

High-resolution CO observations are ideally complemented by interferometric HI observations to get a complete picture of the gaseous properties of the atomic and molecular IVCs. This may allow to trace the formation sequence of these objects during the Galactic fountain cycle by observational data.

The results show also the limitations of our approach for the analysis of the complete population of IVCs in the Milky Way. In terms of data the new HI and FIR surveys will set the standard for the coming decades. In terms of methodology there are improvements possible, for example in the modelling of the FIR emission. This requires also the overcoming of the simplified velocity criteria that are used to classify HI clouds within the Galactic disk and halo. The radial velocity is only a proxy for the distance in the Milky Way which works quite well within the rotating thin disk but fails for higher latitudes. Instead more physically motivated definitions of LVCs, IVCs, and HVCs are required that are connected to the gaseous properties and the metallicity content of the objects. Without a better classification of these different classes, any study will suffer from the issue that gas is associated falsely to one or the other classes.

A dedicated study of FIR deficient objects would be interesting also, since these objects may be related to a low metal content. In this way the combination of HI and FIR data allows to disentangle physically distinct gas components in the ISM.

The fundamental uncertainty in all studies of IVCs is the unknown distance to the objects. There are different approaches in the determination of distances. The 3D tomography of the Milky Way has come a long way. However, still the distances to IVCs are not well constrained. The few available distance brackets from absorption measurements of stellar spectra give the best constraints for some of the large IVC and HVC complexes, although these estimates are only valid for individual lines-of-sight. Maybe in the near future the *Gaia* satellite (e.g. Jordan 2008, and references therein) is able to provide better constraints.

All this work will help to gain more insight into the amount and distribution of molecular gas in the Milky Way halo and to put this material in the context of galaxy evolution. The accretion of matter happens at the disk-halo interface in which the IVCs are located. Hence, objects at the disk-halo interface, despite the naive classification of LVCs, IVCs or HVCs, are key in the accretion process and deserve further studies.

APPENDIX A

Appendix

A.1 Northern molecular IVC candidates

Table A.1: Locations of MIVC$^{\pm}$ candidates on the northern Galactic hemisphere. The columns give the cloud number, the Galactic longitude l and latitude b, the fitted IVC dust emissivity ϵ^{IVC} and its error, the peak H_2 column density $N_{\mathrm{H_2}}^{\mathrm{peak}}$ and its error, the significance S as defined in Eq. (5.2) on page 88, and the MIVC designation if it is a known cloud.

no.	l [deg]	b [deg]	ϵ^{IVC} $\left[10^{-26}\,\mathrm{cm}^2\right]$	$N_{\mathrm{H_2}}^{\mathrm{peak}}$ $\left[10^{20}\,\mathrm{cm}^{-2}\right]$	S	MIVC designation
			$v_{\mathrm{LSR}} < -20\,\mathrm{km\,s}^{-1}$			
1	135.23	51.36	1.40 ± 0.01	0.26 ± 0.06	4370	IVC 135
2	136.01	54.59	1.70 ± 0.02	0.29 ± 0.09	4320	IVC 135
3	278.73	51.45	0.81 ± 0.01	0.72 ± 0.09	3040	
4	95.49	38.15	1.90 ± 0.03	0.98 ± 0.05	2290	Draco
5	211.41	63.11	1.05 ± 0.01	0.95 ± 0.08	2070	IVC 210
6	106.97	70.69	1.07 ± 0.01	0.37 ± 0.09	1500	
7	216.46	37.20	1.08 ± 0.01	0.66 ± 0.09	1370	
8	215.06	37.23	1.04 ± 0.01	0.32 ± 0.10	1350	
9	288.39	53.04	0.91 ± 0.02	1.35 ± 0.15	1330	G 288.4+53.2
10	85.99	38.37	0.75 ± 0.01	0.35 ± 0.10	1310	
11	105.46	68.73	0.85 ± 0.01	1.91 ± 0.08	1230	
12	203.15	55.01	0.58 ± 0.01	0.37 ± 0.12	1210	
13	112.15	38.58	0.70 ± 0.01	0.51 ± 0.11	1180	
14	136.79	57.76	0.81 ± 0.01	0.37 ± 0.11	1010	IVC 135
15	91.36	37.83	1.97 ± 0.04	1.79 ± 0.08	920	Draco
16	219.23	43.65	0.77 ± 0.02	0.71 ± 0.16	860	
17	101.91	67.43	0.93 ± 0.01	0.42 ± 0.09	840	
18	216.05	39.09	1.15 ± 0.02	0.31 ± 0.09	810	
19	215.89	38.13	1.13 ± 0.02	0.29 ± 0.10	790	
20	266.77	52.80	0.97 ± 0.02	0.53 ± 0.17	760	
21	89.79	38.66	2.44 ± 0.05	1.66 ± 0.06	760	Draco
22	211.11	45.48	0.93 ± 0.02	0.48 ± 0.11	740	
23	279.56	50.82	0.68 ± 0.01	0.70 ± 0.15	720	
24	99.59	29.27	0.49 ± 0.01	0.56 ± 0.17	670	
25	214.33	62.35	0.88 ± 0.01	0.38 ± 0.08	660	
26	256.21	76.58	0.73 ± 0.02	0.44 ± 0.13	650	
27	325.69	52.10	1.25 ± 0.02	0.26 ± 0.06	650	
28	283.97	51.71	0.58 ± 0.02	1.28 ± 0.32	640	
29	115.32	37.71	0.58 ± 0.01	0.41 ± 0.15	630	
30	105.67	29.48	0.67 ± 0.01	0.68 ± 0.13	610	
31	132.47	53.32	1.02 ± 0.02	0.27 ± 0.07	590	IVC 135
32	143.77	40.03	1.82 ± 0.05	3.64 ± 0.11	590	
33	110.87	31.49	0.89 ± 0.02	0.58 ± 0.10	570	

34	100.64	24.55	0.57 ± 0.01	5.16 ± 0.14	560	
35	132.38	26.64	2.04 ± 0.03	0.36 ± 0.06	520	
36	202.00	56.24	0.61 ± 0.01	0.38 ± 0.09	520	
37	102.94	24.41	1.01 ± 0.03	3.85 ± 0.16	510	
38	95.92	26.30	0.47 ± 0.01	0.92 ± 0.19	510	
39	106.62	25.94	0.68 ± 0.03	1.75 ± 0.41	500	
40	93.30	38.13	0.94 ± 0.04	1.31 ± 0.11	480	Draco
41	283.90	54.93	0.45 ± 0.01	1.01 ± 0.14	480	G 283.9+54.9
42	210.79	46.45	1.32 ± 0.02	0.23 ± 0.08	460	
43	98.00	24.76	0.61 ± 0.01	0.61 ± 0.20	460	
44	210.74	61.02	0.75 ± 0.02	0.55 ± 0.10	450	IVC 210
45	97.51	25.18	0.55 ± 0.01	0.74 ± 0.28	440	
46	162.98	34.90	0.89 ± 0.01	0.39 ± 0.09	420	
47	147.55	38.19	2.03 ± 0.12	2.04 ± 0.26	410	
48	231.35	80.67	0.60 ± 0.01	0.40 ± 0.08	400	
49	153.54	32.82	0.96 ± 0.03	0.51 ± 0.14	400	
50	96.47	25.64	0.50 ± 0.01	1.14 ± 0.20	390	
51	210.02	46.73	1.30 ± 0.02	0.25 ± 0.06	390	IVC 210
52	99.22	25.73	0.46 ± 0.01	0.65 ± 0.21	380	
53	151.73	40.85	1.40 ± 0.03	0.91 ± 0.09	380	
54	219.09	41.97	0.63 ± 0.02	0.53 ± 0.16	370	
55	146.33	36.07	2.33 ± 0.06	0.92 ± 0.08	360	
56	133.89	34.41	1.00 ± 0.02	0.26 ± 0.08	350	
57	92.32	40.03	1.41 ± 0.07	0.82 ± 0.13	350	Draco
58	209.29	47.81	1.46 ± 0.03	0.18 ± 0.06	340	
59	98.91	28.77	0.41 ± 0.01	0.86 ± 0.21	340	
60	92.77	36.51	2.18 ± 0.08	0.61 ± 0.07	320	Draco
61	206.54	48.63	1.43 ± 0.02	0.24 ± 0.04	300	
62	267.81	52.66	0.87 ± 0.03	0.62 ± 0.21	290	
63	201.01	56.12	0.47 ± 0.01	0.38 ± 0.12	290	
64	144.67	39.03	2.32 ± 0.09	2.45 ± 0.14	290	
65	112.38	37.04	0.81 ± 0.02	0.32 ± 0.14	290	
66	151.72	37.26	2.83 ± 0.12	2.45 ± 0.15	280	
67	141.84	41.08	2.30 ± 0.03	0.91 ± 0.07	270	
68	142.57	40.02	2.10 ± 0.06	2.25 ± 0.12	270	
69	118.24	40.19	0.25 ± 0.01	1.11 ± 0.35	270	
70	259.42	53.90	0.44 ± 0.01	0.70 ± 0.21	250	
71	196.88	51.28	0.79 ± 0.03	0.28 ± 0.10	250	
72	135.32	36.51	0.96 ± 0.03	0.45 ± 0.12	250	
73	160.69	36.01	1.46 ± 0.05	1.06 ± 0.14	240	
74	115.07	32.64	1.02 ± 0.02	0.44 ± 0.08	240	
75	202.94	67.59	0.54 ± 0.02	0.45 ± 0.12	240	
76	121.95	30.14	4.88 ± 0.18	1.50 ± 0.04	230	
77	160.62	35.32	1.52 ± 0.05	1.13 ± 0.14	230	
78	142.91	39.52	2.06 ± 0.06	3.23 ± 0.11	220	
79	98.79	26.16	0.22 ± 0.01	1.89 ± 0.58	220	
80	116.62	32.51	0.86 ± 0.03	2.27 ± 0.16	220	
81	97.18	26.15	0.39 ± 0.02	1.27 ± 0.43	220	
82	258.67	75.98	1.11 ± 0.02	0.39 ± 0.09	210	
83	106.88	30.43	0.32 ± 0.01	1.49 ± 0.27	210	
84	117.24	35.83	0.46 ± 0.02	0.80 ± 0.17	210	
85	246.08	73.00	0.23 ± 0.03	11.95 ± 0.65	210	
86	208.77	48.29	0.82 ± 0.03	0.38 ± 0.13	200	
87	99.08	27.19	0.25 ± 0.01	2.16 ± 0.39	200	
88	119.03	40.46	0.26 ± 0.01	1.08 ± 0.34	200	
89	267.73	53.09	0.89 ± 0.03	0.66 ± 0.21	200	
90	93.06	23.23	0.81 ± 0.02	0.59 ± 0.09	190	
91	149.84	67.52	0.18 ± 0.01	2.44 ± 0.41	180	
92	113.95	34.60	0.45 ± 0.01	0.53 ± 0.18	170	
93	267.34	81.29	0.71 ± 0.04	0.74 ± 0.19	170	
94	209.89	61.46	0.69 ± 0.02	0.59 ± 0.14	160	IVC 210
95	160.98	61.20	0.97 ± 0.04	0.25 ± 0.08	160	
96	123.78	44.65	0.73 ± 0.03	0.36 ± 0.12	160	
97	119.72	36.83	0.66 ± 0.03	0.50 ± 0.11	160	
98	159.99	35.58	1.52 ± 0.07	1.24 ± 0.18	150	
99	175.05	70.07	0.98 ± 0.04	0.28 ± 0.09	150	

100	150.36	33.57	0.64 ± 0.03	1.04 ± 0.19	140	
101	213.33	43.34	0.47 ± 0.02	0.63 ± 0.17	140	
102	92.22	36.29	1.79 ± 0.08	0.85 ± 0.09	140	Draco
103	254.42	77.07	0.66 ± 0.02	0.45 ± 0.15	140	
104	286.90	52.53	0.90 ± 0.02	1.45 ± 0.13	140	
105	131.12	51.61	0.46 ± 0.02	0.61 ± 0.16	130	IVC 135
106	69.76	55.53	0.36 ± 0.02	0.68 ± 0.21	120	
107	276.27	82.57	0.59 ± 0.04	0.78 ± 0.19	120	
108	129.11	29.25	0.54 ± 0.03	1.09 ± 0.20	110	
109	217.00	39.20	0.81 ± 0.03	0.38 ± 0.15	110	
110	252.95	76.09	0.84 ± 0.02	1.11 ± 0.10	110	
111	116.37	36.01	0.17 ± 0.02	2.21 ± 0.40	110	
112	265.05	79.53	0.29 ± 0.03	1.56 ± 0.40	110	
113	92.71	39.03	1.03 ± 0.05	1.32 ± 0.14	110	Draco
114	97.81	26.03	0.19 ± 0.02	2.66 ± 0.94	110	
115	128.71	29.75	0.34 ± 0.02	1.45 ± 0.32	100	
116	159.04	38.42	1.02 ± 0.08	2.01 ± 0.34	100	
117	259.97	79.03	0.44 ± 0.03	1.12 ± 0.22	100	
118	87.21	57.76	0.21 ± 0.01	1.21 ± 0.31	100	
119	102.42	28.12	0.19 ± 0.02	1.46 ± 0.50	100	
120	118.66	35.26	0.24 ± 0.02	1.38 ± 0.32	90	
121	116.89	35.18	0.49 ± 0.03	0.80 ± 0.20	90	
122	130.37	51.34	0.39 ± 0.02	0.73 ± 0.22	80	IVC 135
123	265.45	80.55	0.48 ± 0.04	0.74 ± 0.31	80	
124	107.14	22.34	4.61 ± 0.44	1.36 ± 0.03	80	
125	105.05	33.98	0.47 ± 0.02	0.90 ± 0.20	70	
126	107.97	28.32	0.36 ± 0.06	3.37 ± 1.61	70	
127	260.51	80.62	0.31 ± 0.05	1.26 ± 0.50	60	
128	113.30	34.79	0.13 ± 0.01	2.25 ± 0.75	60	
129	116.25	56.61	0.43 ± 0.03	0.61 ± 0.23	60	
130	96.01	33.17	0.19 ± 0.02	1.74 ± 0.46	60	
131	113.58	34.01	0.29 ± 0.02	0.76 ± 0.36	50	
132	269.31	60.79	0.17 ± 0.02	1.10 ± 0.42	50	
133	218.55	41.40	0.31 ± 0.03	1.34 ± 0.40	50	
134	208.93	44.60	0.18 ± 0.03	5.47 ± 0.54	50	
135	251.58	74.78	0.32 ± 0.06	9.96 ± 0.89	40	
136	145.71	43.35	0.23 ± 0.06	7.83 ± 1.11	40	
137	150.71	40.31	0.59 ± 0.07	3.63 ± 0.45	40	
138	98.09	21.92	0.35 ± 0.05	3.07 ± 0.30	40	
139	108.35	35.51	0.15 ± 0.01	1.78 ± 0.45	40	
140	209.04	49.60	0.22 ± 0.02	1.24 ± 0.33	30	
141	106.16	21.26	2.08 ± 0.57	3.43 ± 0.06	30	
142	279.11	85.15	0.16 ± 0.03	2.11 ± 0.45	30	
143	108.72	25.41	0.45 ± 0.09	3.24 ± 1.01	30	
144	270.96	75.41	0.09 ± 0.01	5.69 ± 0.82	20	
145	262.53	77.96	0.04 ± 0.02	8.60 ± 2.84	20	
146	258.33	78.12	0.10 ± 0.03	4.96 ± 1.37	20	
147	154.50	32.62	0.15 ± 0.03	22.88 ± 1.13	20	
148	220.60	51.88	0.01 ± 0.03	42.08 ± 14.39	0	
149	122.65	28.97	0.08 ± 0.68	72.07 ± 5.57	0	
150	105.14	21.94	0.00 ± 0.00	0.00 ± 0.00	0	
151	105.57	20.56	0.00 ± 0.00	0.00 ± 0.00	0	
152	133.38	23.43	0.00 ± 0.00	0.00 ± 0.00	0	
153	103.55	22.49	0.00 ± 0.00	0.00 ± 0.00	0	
154	255.59	52.94	−0.01 ± 0.01	28.43 ± 11.68	−10	
155	119.46	34.80	−0.02 ± 0.02	15.36 ± 4.34	−10	
156	145.22	44.35	−0.11 ± 0.06	5.32 ± 1.88	−20	
157	213.46	39.05	−0.12 ± 0.02	2.12 ± 0.69	−20	
158	113.02	34.25	−0.07 ± 0.02	3.14 ± 1.67	−20	
159	251.85	77.94	−0.27 ± 0.02	0.98 ± 0.35	−70	
160	106.91	27.86	−0.38 ± 0.04	2.84 ± 0.92	−90	
161	145.54	39.96	−0.55 ± 0.09	2.43 ± 0.79	−130	
			$v_{\mathrm{LSR}} > +20\,\mathrm{km\,s^{-1}}$			
1	259.71	35.02	0.00 ± 0.00	0.00 ± 0.00	0	

no.	l [deg]	b [deg]	$v_{\mathrm{LSR}}^{\mathrm{sep}}$ [km s^{-1}]	$N_{\mathrm{HI}}^{\mathrm{peak}}$ [10^{20} cm^{-2}]	v_0^{warm} [km s^{-1}]	FWHM$^{\mathrm{warm}}$ [km s^{-1}]	v_0^{cold} [km s^{-1}]	FWHM$^{\mathrm{cold}}$ [km s^{-1}]	f^{cold}	f^{rej}	R [10^{-6}]	ϵ^{LVC} [10^{-26} cm^2]	ϵ^{IVC} [10^{-26} cm^2]	$N_{\mathrm{H_2}}^{\mathrm{peak}}$ [10^{20} cm^{-2}]	$\rho^{\mathrm{LVC}-\tau}$	$\rho^{\mathrm{IVC}-\tau}$	comment
northern Galactic hemisphere																	
3$^-$	278.73	51.45	-17.9	3.6	-27.7 ± 1.0	15.4 ± 0.9	-30.9 ± 0.1	4.4 ± 0.1	58%	43%	0.72 ± 0.01	0.252 ± 0.003	0.445 ± 0.002	1.9 ± 0.1	0.19	0.69	likely
6$^-$	106.97	70.69	-20.5	2.1	-30.0 ± 1.7	17.3 ± 3.0	-29.4 ± 0.1	3.7 ± 0.1	60%	28%	0.013 ± 0.005	0.561 ± 0.008	0.597 ± 0.004	1.1 ± 0.1	0.37	0.87	likely
7$^-$	216.46	37.20	-16.6	2.5	-26.6 ± 0.5	14.0 ± 0.7	-24.7 ± 0.5	3.3 ± 0.7	9%	23%	0.52 ± 0.01	0.882 ± 0.004	0.249 ± 0.006	3.2 ± 0.5	0.49	0.97	possibly
8$^-$	215.06	37.23	-16.6	2.5	-22.5 ± 1.8	22.2 ± 2.8	-20.0 ± 0.5	3.1 ± 0.6	10%	18%	-0.14 ± 0.01	1.06 ± 0.01	0.448 ± 0.007	1.6 ± 0.4	0.75	0.89	possibly
10$^-$	86.99	38.37	-29.5	2.3	-43.5 ± 0.6	5.8 ± 1.2	-43.2 ± 0.2	3.5 ± 0.6	51%	35%	0.210 ± 0.003	0.840 ± 0.002	0.372 ± 0.008	0.9 ± 0.2	0.56	0.83	possibly
12$^-$	203.15	55.01	-15.4	3.0	-42.2 ± 1.2	18.5 ± 1.3	-49.2 ± 0.3	4.6 ± 0.4	25%	23%	-0.192 ± 0.004	1.340 ± 0.003	0.510 ± 0.003	0.6 ± 0.1	0.41	0.82	possibly
13$^-$	112.15	38.58	-23.1	2.4	-28.5 ± 5.5	14.3 ± 5.7	-35.2 ± 0.2	3.6 ± 0.2	71%	30%	-0.183 ± 0.004	0.957 ± 0.004	0.580 ± 0.003	0.8 ± 0.1	0.59	0.82	likely
16$^-$	219.23	43.65	-16.6	2.3	-30.4 ± 0.8	15.4 ± 1.4	-29.5 ± 0.4	4.9 ± 0.6	26%	19%	-0.20 ± 0.01	1.069 ± 0.005	0.492 ± 0.007	0.8 ± 0.3	−0.16	0.39	possibly
17$^-$	101.91	67.43	-15.4	2.6	-28.8 ± 0.9	10.0 ± 1.9	-28.5 ± 0.2	4.2 ± 0.4	54%	22%	0.37 ± 0.01	-0.001 ± 0.011	0.531 ± 0.003	0.6 ± 0.1	0.14	0.72	likely
18$^-$	216.05	39.09	-17.9	2.3	-28.8 ± 2.9	20.2 ± 3.9	-31.2 ± 0.4	4.2 ± 0.6	27%	26%	0.52 ± 0.01	0.922 ± 0.004	0.025 ± 0.005	24 ± 5	0.75	0.51	unclear
19$^-$	215.89	38.13	-15.4	2.4	-26.8 ± 0.5	13.9 ± 0.6	-24.5 ± 0.5	3.1 ± 0.7	8%	23%	0.48 ± 0.01	0.916 ± 0.004	0.131 ± 0.006	6.9 ± 1.1	0.43	0.95	unclear
20$^-$	266.77	52.80	-20.5	3.0	-27.7 ± 1.2	15.0 ± 1.1	-30.9 ± 0.2	4.2 ± 0.3	36%	29%	0.34 ± 0.01	0.477 ± 0.002	0.511 ± 0.002	1.3 ± 0.2	0.66	0.73	possibly
median quantities																	
	215.48	41.37	-17.3	2.5	-28.7 ± 1.1	15.2 ± 1.4	-30.2 ± 0.3	4.0 ± 0.5	32%	25%	0.28 ± 0.01	0.899 ± 0.004	0.470 ± 0.005	1.2 ± 0.2	0.46	0.82	
southern Galactic hemisphere																	
1$^-$	125.21	-20.75	-41.1	3.6	-53.4 ± 2.0	22.9 ± 2.0	-59.2 ± 0.1	5.3 ± 0.1	60%	>72%[a]	1.15 ± 0.02	0.297 ± 0.005	1.125 ± 0.006	0.8 ± 0.1	0.19	0.67	unclear
2$^-$	137.96	-20.37	-42.4	2.1	-51.8 ± 2.2	18.3 ± 2.2	-56.3 ± 0.2	5.0 ± 0.3	50%	>67%[a]	0.45 ± 0.02	0.507 ± 0.006	1.446 ± 0.008	0.3 ± 0.1	0.36	0.81	unclear
6$^-$	126.64	-27.76	-37.3	1.3	-48.7 ± 4.0	17.7 ± 4.0	-52.5 ± 0.5	5.2 ± 0.7	38%	80%	0.64 ± 0.04	0.489 ± 0.010	0.795 ± 0.007	0.5 ± 0.1	0.57	0.38	unclear
mean quantities																	
	129.94	-22.96	-40.3	2.3	-51.3 ± 2.7	19.6 ± 2.7	-56.0 ± 0.3	5.2 ± 0.4	49%	73%	0.75 ± 0.03	0.431 ± 0.007	1.122 ± 0.007	0.5 ± 0.1	0.37	0.62	
1$^+$	257.73	-21.18	20.7	2.5	26.6 ± 0.2	9.6 ± 0.2	–	–	–	36%	-0.92 ± 0.02	1.598 ± 0.008	0.471 ± 0.005	0.8 ± 0.6	0.92	0.87	unlikely
2$^+$	234.52	-32.90	16.8	1.4	18.3 ± 2.8	17.9 ± 3.0	22.1 ± 0.1	3.4 ± 0.2	53%	31%	0.316 ± 0.004	0.588 ± 0.003	1.244 ± 0.005	0.4 ± 0.1	0.40	0.77	possibly
4$^+$	240.19	-20.89	15.6	3.2	15.7 ± 2.6	21.5 ± 2.2	22.0 ± 0.1	4.2 ± 0.1	43%	48%	0.929 ± 0.005	0.458 ± 0.003	0.866 ± 0.003	0.4 ± 0.1	−0.11	0.88	possibly
mean quantities																	
	244.15	-24.99	17.7	2.4	20.2 ± 1.9	16.3 ± 1.8	22.1 ± 0.1	3.8 ± 0.2	48%	38%	0.11 ± 0.01	0.881 ± 0.005	0.860 ± 0.004	0.5 ± 0.3	0.40	0.84	

Table A.2: Derived properties of top-ranked unknown MIVC$^{\pm}$ candidates. The Table is divided into the northern and southern Galactic hemispheres. The columns list from left to right the candidate number from the ranked order (Tables 5.2 and A.1 for the northern, Table 5.4 for the southern Galactic hemisphere), Galactic longitude l, Galactic latitude b, separating velocity $v_{\mathrm{LSR}}^{\mathrm{sep}}$ between LVC and IVC regime, peak IVC HI column density $N_{\mathrm{HI}}^{\mathrm{peak}}$, central velocity v_0^{warm} and width FWHM$^{\mathrm{warm}}$ of the warm gas component, central velocity v_0^{cold} and width FWHM$^{\mathrm{cold}}$ of the cold gas component, cold gas fraction $f^{\mathrm{cold}} = N_{\mathrm{HI}}^{\mathrm{cold}}/(N_{\mathrm{HI}}^{\mathrm{cold}} + N_{\mathrm{HI}}^{\mathrm{warm}})$, fraction of rejected data points f^{rej} during iterative HI-τ fitting, the fitted offset R and dust emissivities for LVCs ϵ^{LVC} and IVCs ϵ^{IVC} of the HI-τ correlation, the inferred peak H_2 column density $N_{\mathrm{H_2}}^{\mathrm{peak}}$, Spearman's rank coefficient $\rho^{\mathrm{LVC}-\tau}$ for $N_{\mathrm{HI}}^{\mathrm{LVC}}$-$\tau$, Spearman's rank coefficient $\rho^{\mathrm{IVC}-\tau}$ for $N_{\mathrm{HI}}^{\mathrm{IVC}}$-$\tau$, and a comment about the validity of the candidate. In the row after all candidates of a given type (north/south, MIVC$^{\pm}$), the median or mean quantities are given. For the northern hemisphere we use the median since there are many candidates.
[a]The fitting threshold is increased to 5×10^{20} cm^{-2}, otherwise most of the data would be omitted for the fit. That is why f^{rej} is larger than the given value.

Candidate no. 6^- All the derived properties of the northern MIVC$^-$ candidates are listed in the upper part of Table A.2 on page 152. The MIVC candidate no. 6^- is connected spectrally to the LVC HI gas (Fig. A.1). South of the candidate, the FIR emission is over-predicted, resulting into negative H_2 column densities. The candidate is associated with FIR excess emission, which is, however, not as strong as compared to other MIVCs. There is a clear association of the IVC with FIR excess emission. The inferred H_2 distribution follows the HI column density distribution of the candidate and the LVC emission is low. The two-component HI profile shows a large contribution of cold gas at the peak location of the cloud. Summarising, candidate no. 6^- is likely a MIVC.

Candidate no. 7^- The MIVC candidate no. 7^- is located in a region with complicated HI spectra showing several different emission peaks at various LVC and IVC velocities (Fig. A.2). In the total HI-τ plot, the data points of the candidate are found slightly above of the general correlation showing a similar behaviour like the LVC gas. The IVC is clearly associated with FIR emission, also the inferred H_2 column densities follow the HI column density distribution. There are several different candidates nearby in projection (candidates nos. 8^-, 18^-, 19^-), apparently belonging to the same IVC structure. However, these individual candidates surround the largest HI peak in three directions and are not located at the peak position. This is likely related to the large LVC HI emission of similar strength towards the IVC emission, which influences the HI-τ correlation and the inferred H_2 column densities. The contribution of the cold component to the total HI line emission strength is small. Summarising, this candidate and its surrounding neighbours are unclear, but they could be part of a larger MIVC structure.

Candidate no. 8^- The MIVC candidate no. 8^- is located in projection very close to candidate no. 7^- and both are part of the same IVC structure (Fig. A.3). In the HI column density map, the candidate cannot be separated from candidate no. 7^-, that is why both have the same peak $N_{\rm HI}$. For candidate no. 8^- we fit a three-component Gaussian fit. The third component is characterised by $v_0 = -45.3 \pm 1.5\,{\rm km\,s^{-1}}$ and FWHM $= 9.5 \pm 1.8\,{\rm km\,s^{-1}}$.

In the IVC contribution to the HI-τ correlation, the candidate shows significant FIR excess emission. However, in the total HI-τ plot the cloud lies on-top of the general correlation showing a similar behaviour like the LVC gas. Visually, the IVC is clearly associated with FIR emission. However, there is LVC HI emission of similar strength towards the IVC emission influencing the HI-τ correlation and the inferred H_2 column densities. The contribution of the cold component to the total HI line emission strength is small. Summarising, this candidate and its surrounding neighbours are unclear, but they could be part of a larger MIVC structure.

Candidate no. 10^- The MIVC candidate no. 10^- is located close to the tip of the MIVC Draco (e.g. Mebold et al. 1985) but not directly associated with it. The velocity separation includes Draco into the LVC gas. Candidate no. 10^- clearly dominates the total HI emission along its lines-of-sight (Fig. A.4). In addition, it is fairly isolated and oddly shaped with two bow-like structures at the southern end. There is also lots of HVC emission within the field.

The cloud itself consists mainly of two different components of cold gas with FWHM $\lesssim 7\,{\rm km\,s^{-1}}$. As compared to Draco, the candidate is much smaller and less bright in the FIR. In the HI-τ plots, the candidate shows only slightly brighter dust emission than the fitted IVC curve, while for the total gas and dust the cloud follows the general correlation. There is a clear association of the IVC with FIR emission. Any excess is weak and may be biased by the bright FIR emission nearby. Summarising, candidate no. 10^- is not clear.

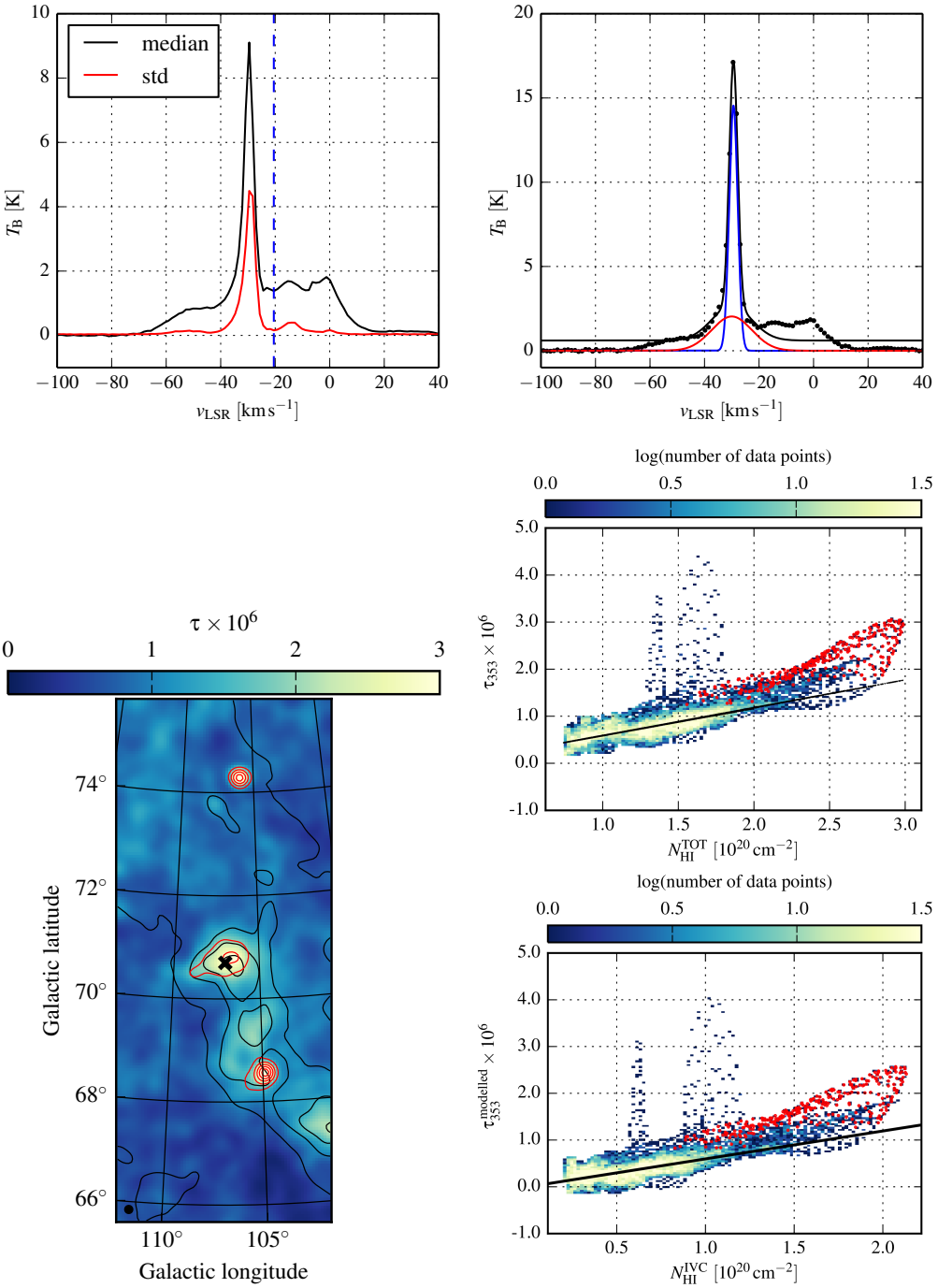

Fig. A.1: Plots for MIVC candidate no. 6^-. The top-left plot shows the velocity separation with the median and standard-deviation spectrum in black and red. The separating velocity is given by the vertical dashed blue line. In the top-right, the two-component Gaussian fit to the peak HI spectrum is presented with the data as black dots and the total Gaussian fit as the black line. The narrow and wide Gaussian components are plotted as the blue and red curves. In the bottom-left, the smoothed τ-map is plotted overlayed with the IVC HI column densities in black and the inferred H_2 column densities in red. Both the HI and H_2 contours start at 0.5×10^{20} cm^{-2} increasing in steps of 0.5×10^{20} cm^{-2}. The position of the candidate is shown by the black cross. The middle-right plot shows the HI-τ plot for the total N_{HI} and total τ. In the bottom-right plot the modelled IVC contribution to τ is given after subtracting the LVC contribution and the constant offset from the total τ. In both HI-τ plots, the red points mark the data points of the MIVC candidate while the black line or black points indicate the modelled HI-τ relation.

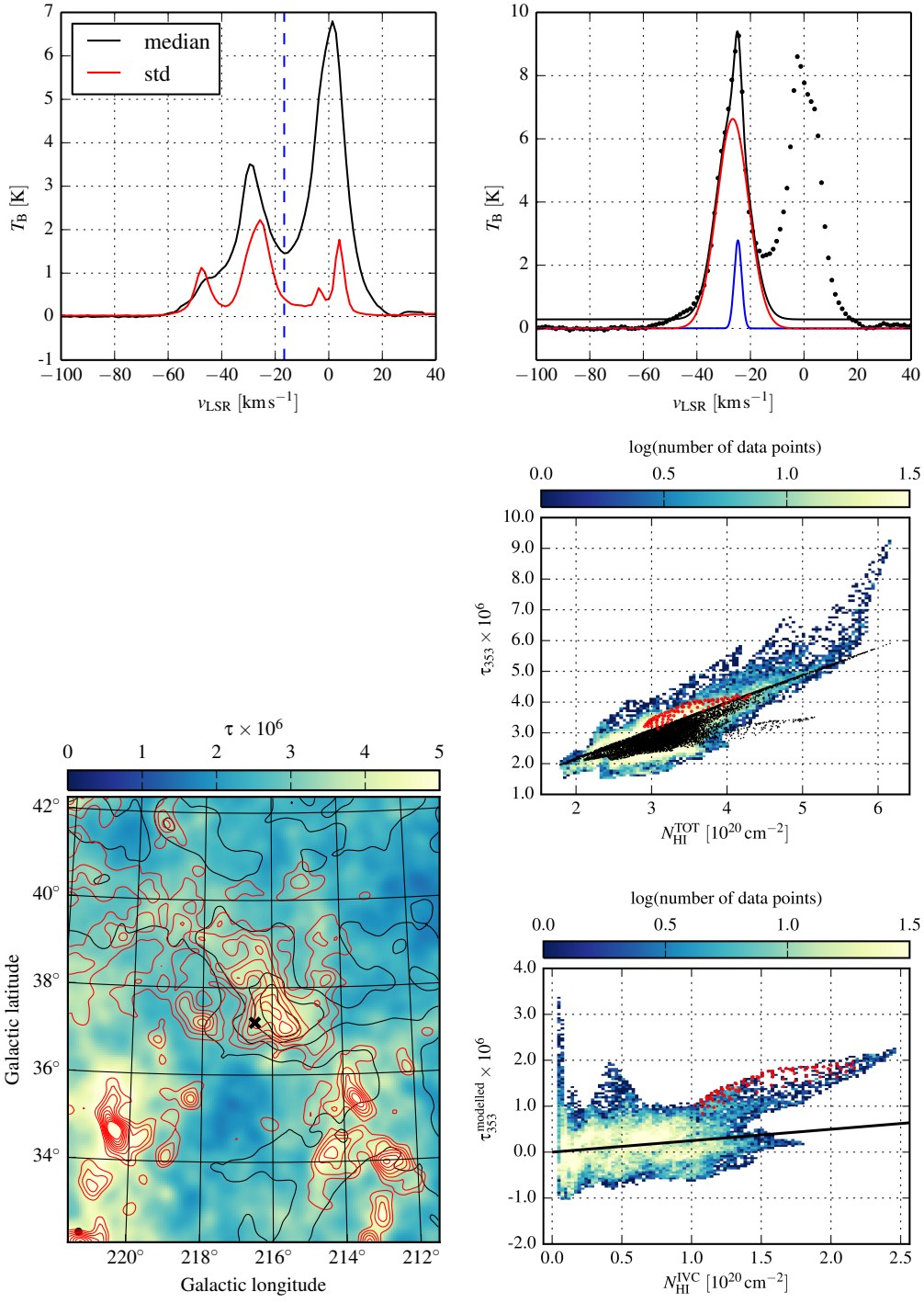

Fig. A.2: Plots for MIVC candidate no. 7$^-$, same as in Fig. A.1.

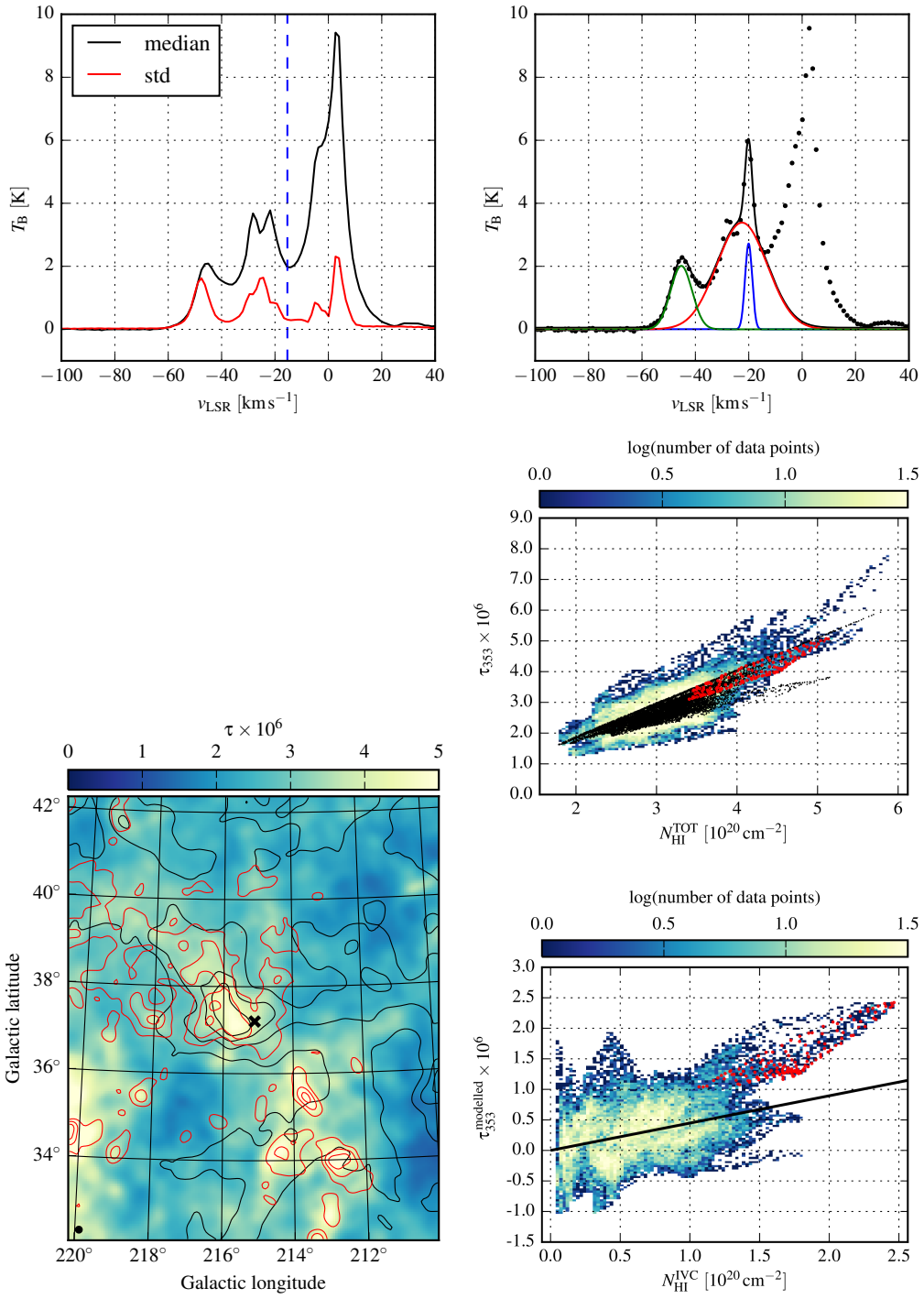

Fig. A.3: Plots for MIVC candidate no. 8$^-$, same as in Fig. A.1. In the HI spectrum (*top-right*), an additional third Gaussian component is fitted, shown as the green line.

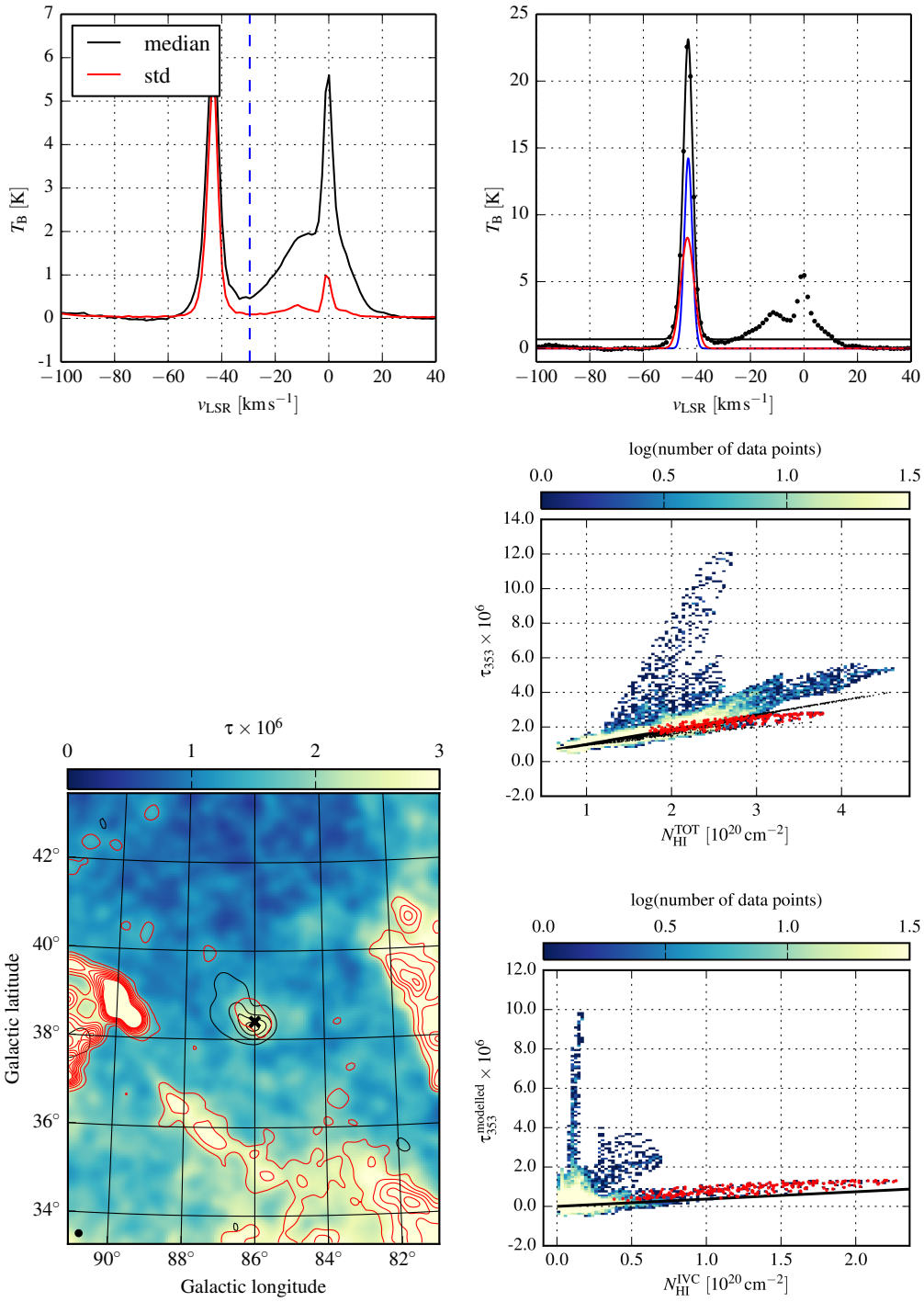

Fig. A.4: Plots for MIVC candidate no. 10⁻, same as in Fig. A.1.

Candidate no. 12^- The MIVC candidate no. 12^- dominates the total HI emission along its lines-of-sight (Fig. A.5). The neighbouring IVC gas consists of distinct clumps that are coherently connected spatially and spectrally. In the HI-τ plots, the candidate shows brighter FIR emission than the other IVC gas. In the total HI-τ plot, the cloud lies just slightly above the IVC points, but below the LVC gas. The candidate is associated with FIR emission. However, the H_2 contribution is relatively small but within the estimated errors significant. Summarising, candidate no. 12^- could be a MIVC.

Candidate no. 13^- The MIVC candidate no. 13^- is found in a region of complicated HI spectra showing numerous LVC, IVC, and HVC components. This does not allow a clear separation between the different velocity components (Fig. A.6). A very large fraction of 71% of the HI is cold. The nearby IVC emission is rather clumpy reflecting the large number of different velocity components in HI emission. In the HI-τ correlation plots, the candidate is brighter in the FIR as compared to the environment. This is true also for the total HI-τ correlation in which the candidate is above the total fit. However, the candidate is still within the scatter of the bulk of data points and no prominent FIR excess is evident.

There is a clear association of the IVCs with FIR emission for several different IVC clumps, although the inferred H_2 distribution does not follow the HI column densities of the IVC gas closely. In general, the field shows a fairly linear HI-FIR correlation. Within small HI peaks in IVC, there appears to be a small FIR excess, which is indicated in both the total and IVC correlation data. Summarising, candidate no. 13^- may be a MIVC.

Candidate no. 16^- The MIVC candidate no. 16^- is located in a region with comparable LVC HI emission (Fig. A.7). A peak $N_{H_2} = 0.8 \pm 0.3 \times 10^{20}\,\mathrm{cm}^{-2}$ is inferred across the IVC, which is not very significant. The candidate shows the largest HI column densities within the field, appearing compatible with the general HI-FIR correlation. Summarising, candidate no. 16^- could be a MIVC.

Candidate no. 17^- The MIVC candidate no. 17^- dominates the HI emission along its lines-of-sight (Fig. A.8). About half of the HI is in the cold component with a small or non-existent shift in velocity relative to the warm component. The estimated LVC dust emissivity is compatible with zero. In the HI-τ plots, the cloud is significantly above the fits for both the IVC contribution and the total correlation. The candidate has a similar behaviour as the candidate no. 6^-, which is also within the field. The candidate is associated with FIR emission and the H_2 column densities nicely follow one HI peak of the IVC. There is a slight FIR excess associated with the candidate, which resembles candidate no. 6^-, but not as prominent. Summarising, candidate no. 17^- is likely a MIVC.

Candidate no. 18^- The MIVC candidate no. 18^- is located very close to candidates nos. 7^-, 8^-, and 19^-, all of which are part of the same IVC structure (Fig. A.9). The peak HI column density of the IVC is less than of the LVCs. The fitted IVC dust emissivity is almost vanishing, resulting in an unrealistic peak $N_{H_2} = 24 \pm 5 \times 10^{20}\,\mathrm{cm}^{-2}$. This shows the difficulties within this field, that are relevant also for the other three candidates nos. 7^-, 8^-, and 19^-. In the HI-τ plots, the candidate shows excess emission relative to the other IVCs. However, in the total HI-τ plot the cloud lies on-top of the general correlation showing a similar behaviour like the LVC gas. Summarising, this candidate and its surrounding neighbours are not clear but they could be part of a larger MIVC structure.

Candidate no. 19^- The MIVC candidate no. 19^- is part of the same IVC structure as candidates nos. 7^-, 8^-, and 18^- (Fig. A.10). In the HI-τ plots, the situation is very similar to the other candidates

nos. 7^-, 8^-, and 18^-, for which FIR excess emission is apparent but with the same behaviour as the LVC gas. Again, the IVC dust emissivity is modelled to be very low which gives the large values and errors on the H_2 column density. Like for the other candidates, the LVC HI emission is of similar strength at the location of the IVC emission, which influences the HI-τ correlation and the inferred H_2. Summarising, this candidate and its surrounding neighbours are not clear but they could be part of a larger MIVC structure.

Candidate no. 20^- Along the lines-of-sight towards the MIVC candidate no. 20^-, the LVC emission has comparable strengths as the IVC with a difficult separation between the LVC and IVC regime (Fig. A.11). The candidate is at the very top of the HI-τ correlation data indicating relatively bright FIR emission. There is a clear association of the FIR emission to the IVC, however, the H_2 column densities are offset south to the HI peaks. There is a complicated and strong LVC foreground near the candidate. However, the H_2 column densities do not follow the foreground either. Summarising, candidate no. 20^- could be a MIVC.

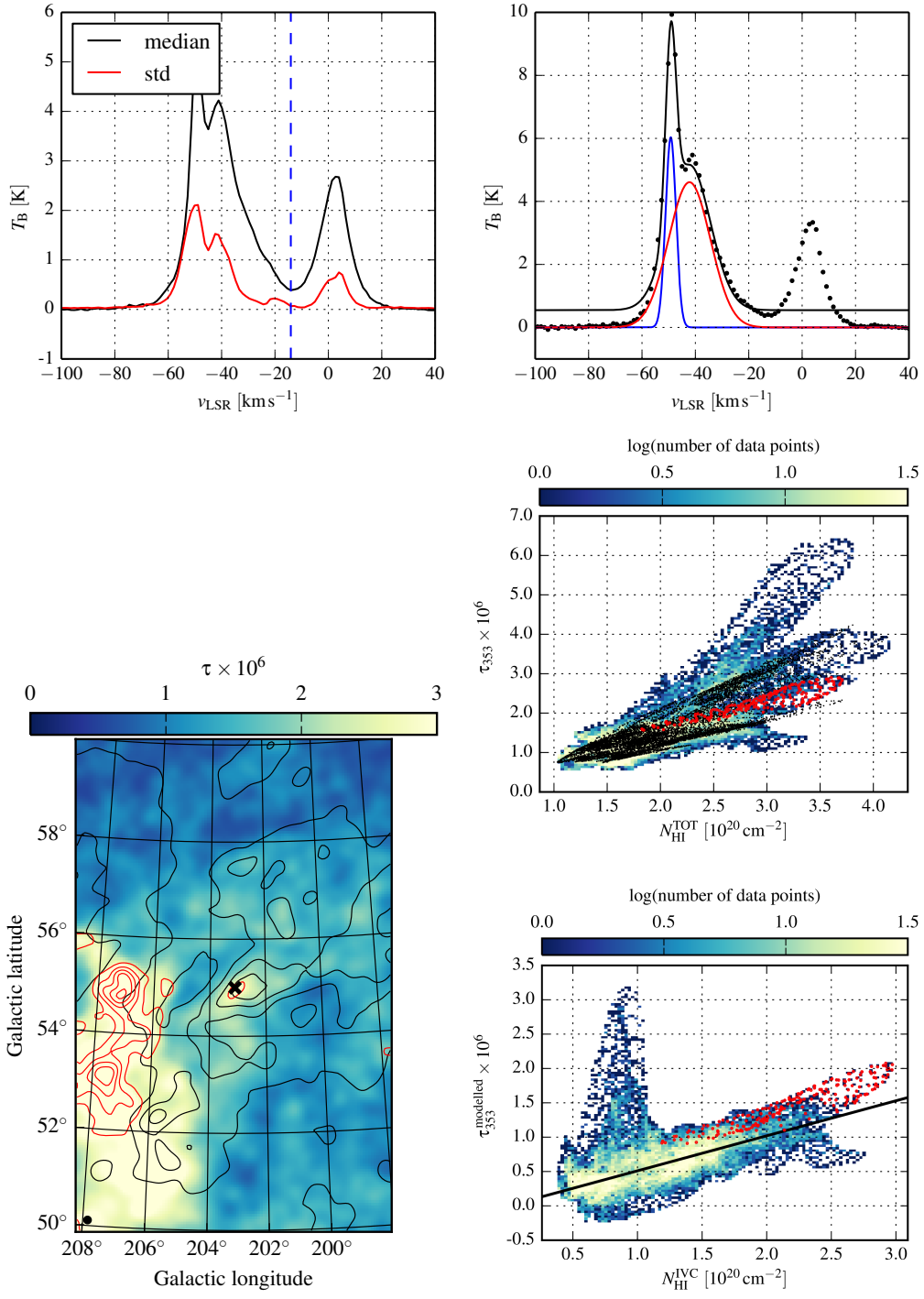

Fig. A.5: Plots for MIVC candidate no. 12$^-$, same as in Fig. A.1.

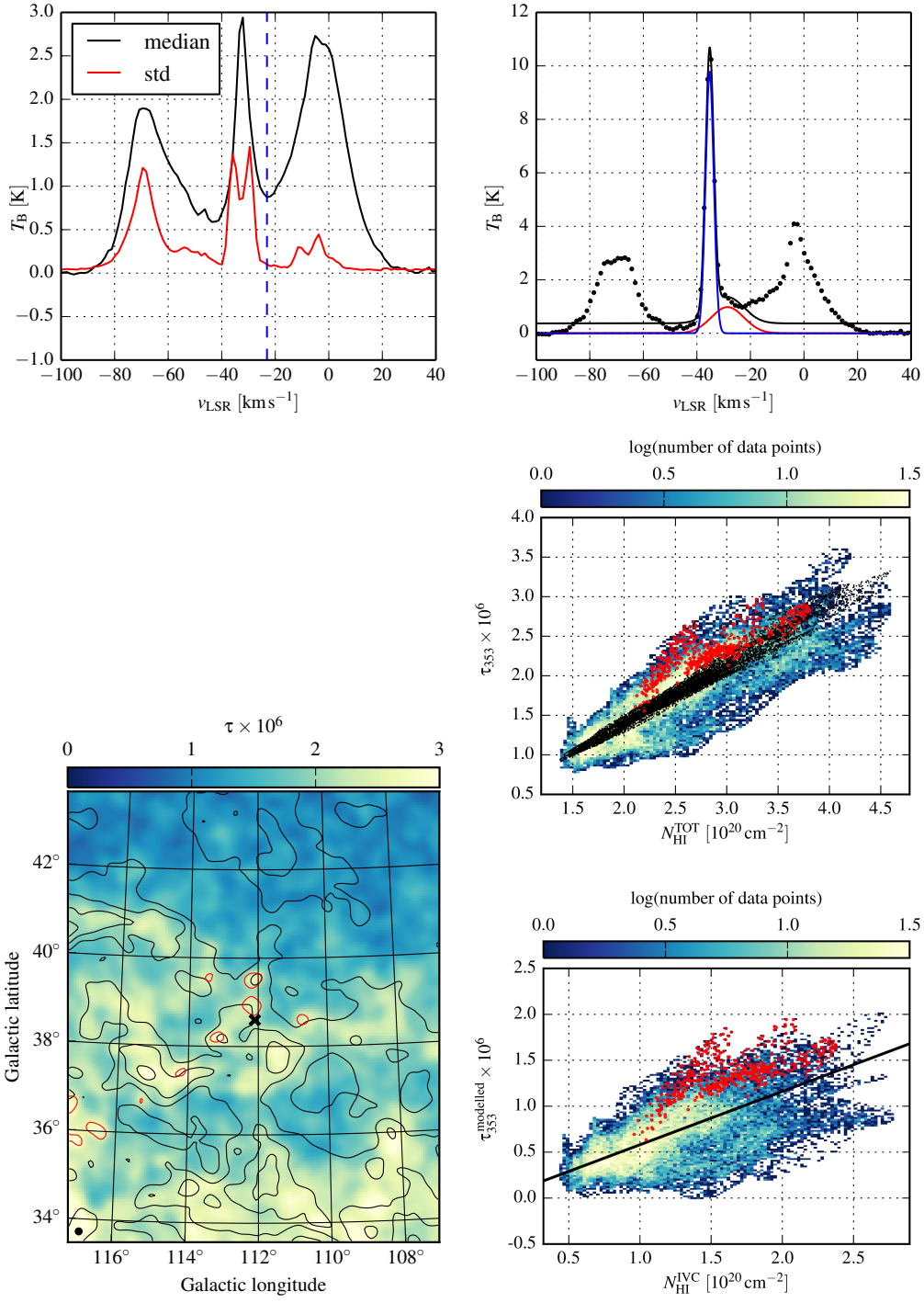

Fig. A.6: Plots for MIVC candidate no. 13$^-$, same as in Fig. A.1.

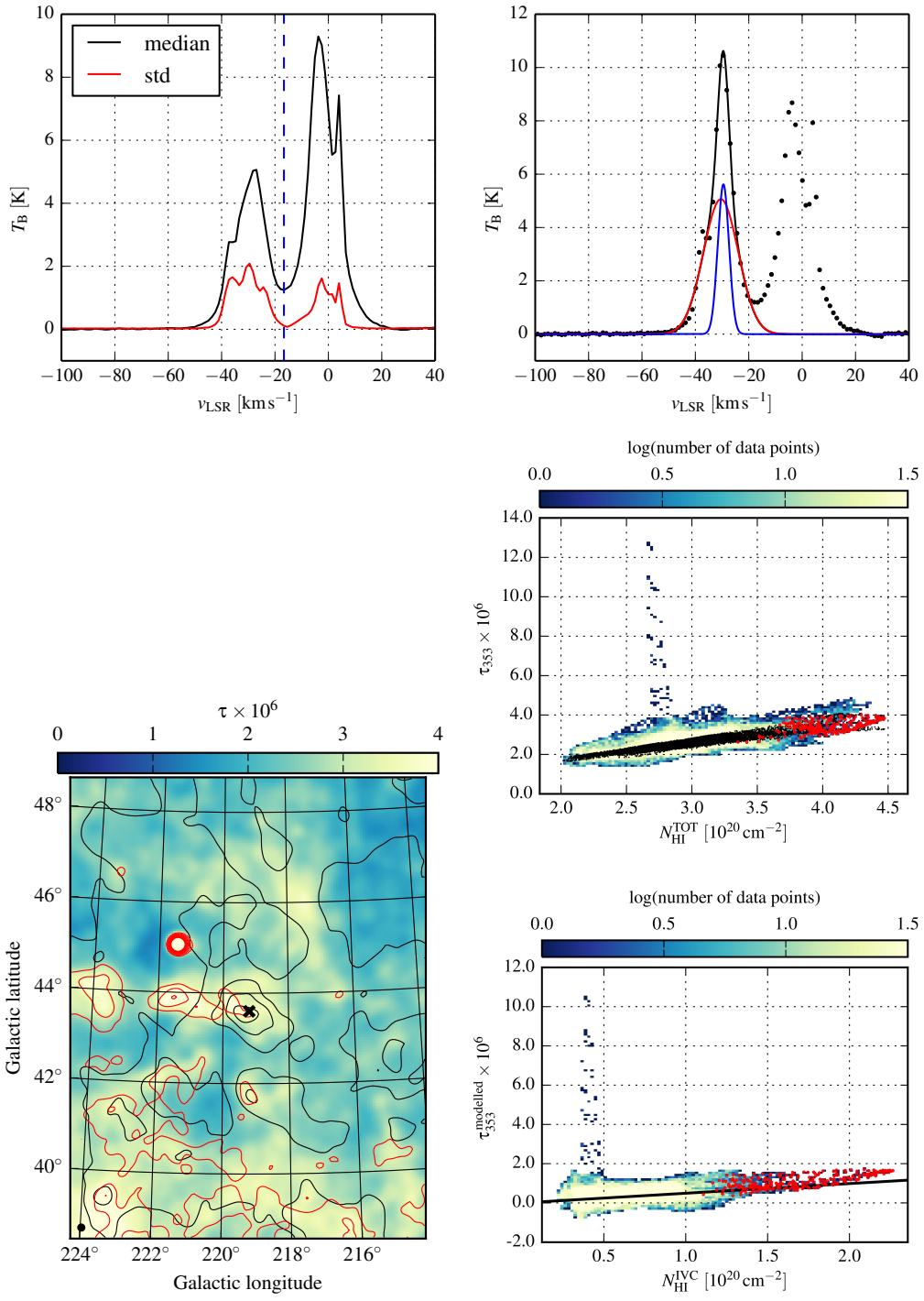

Fig. A.7: Plots for MIVC candidate no. 16$^-$, same as in Fig. A.1.

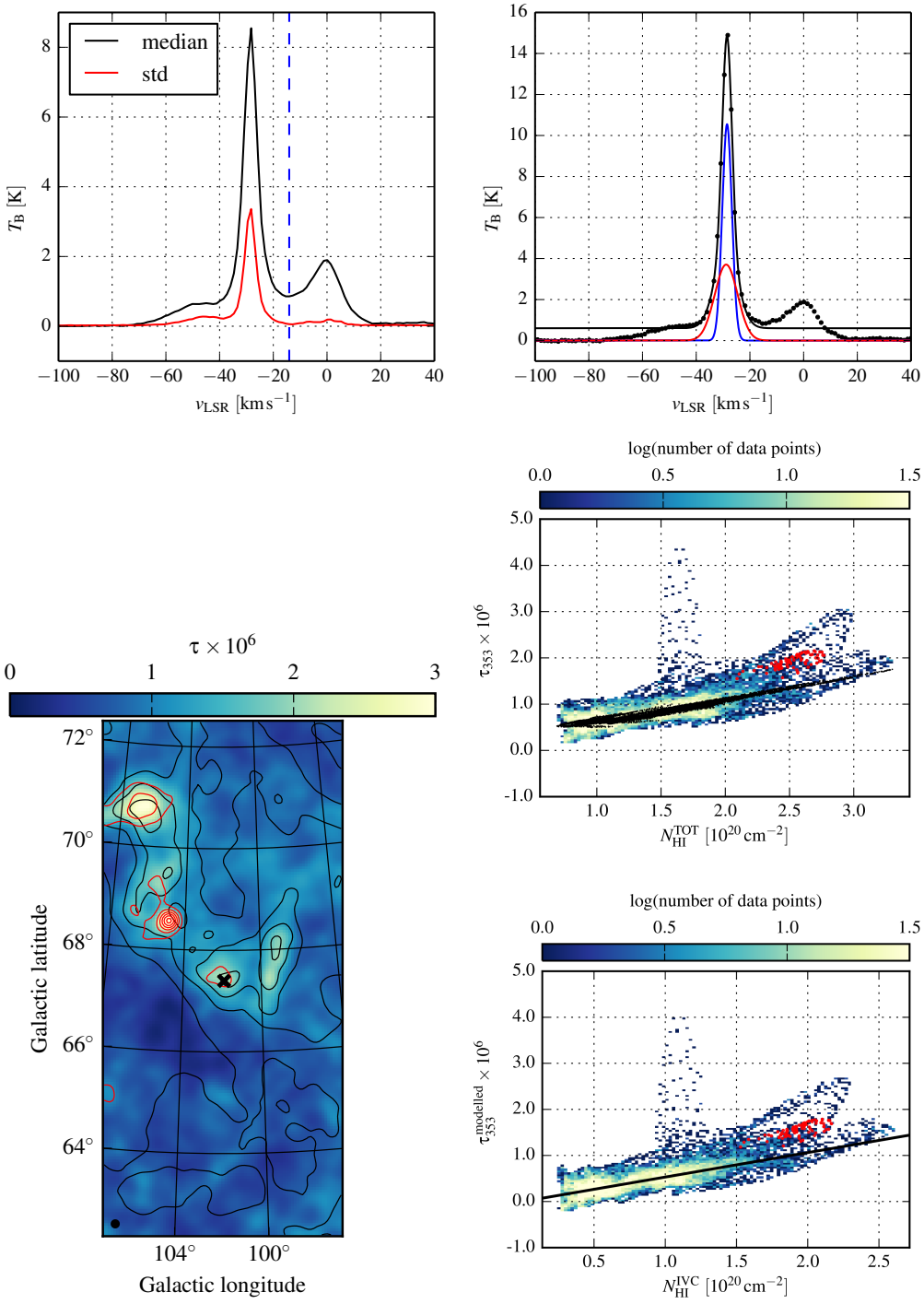

Fig. A.8: Plots for MIVC candidate no. 17$^-$, same as in Fig. A.1.

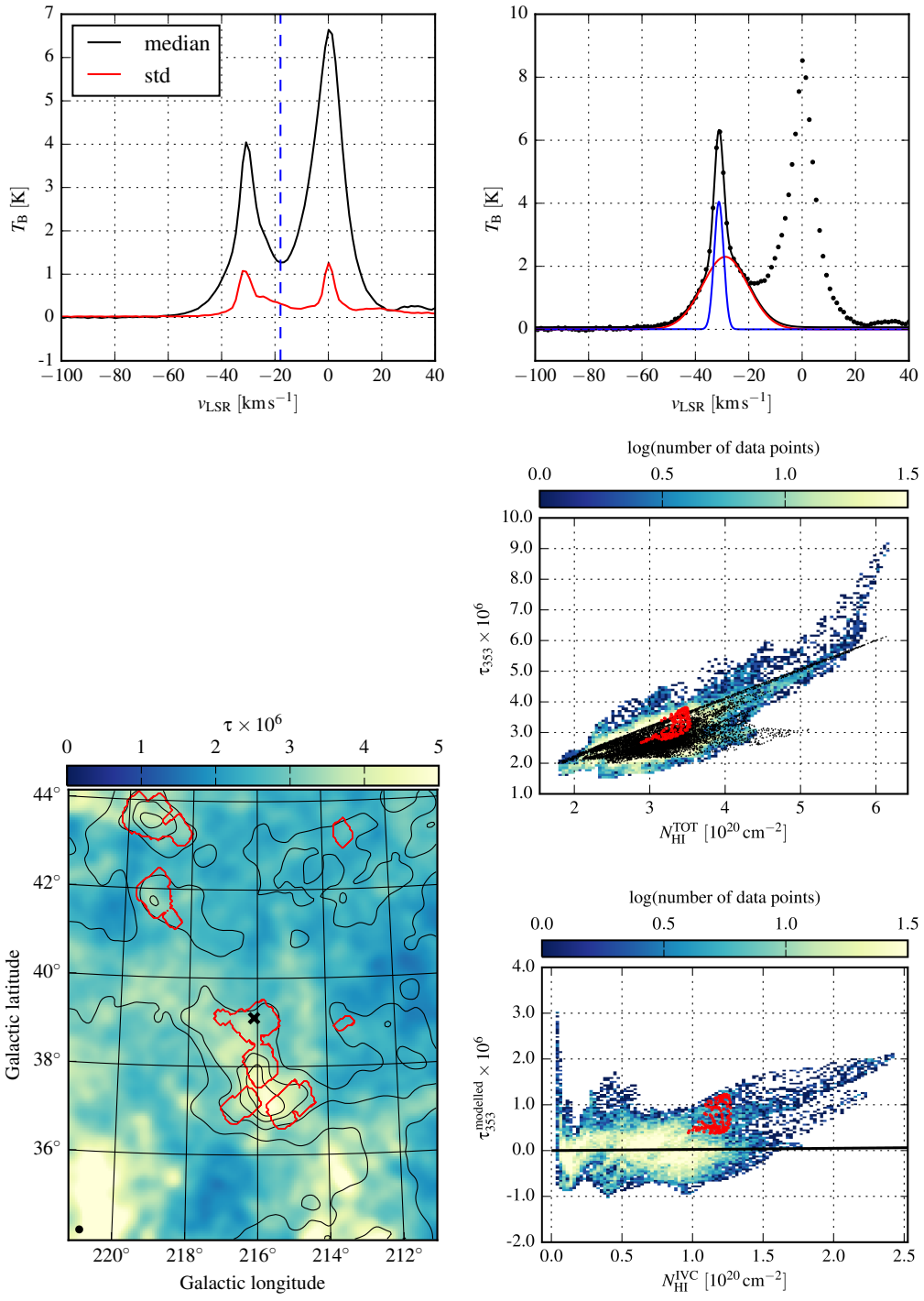

Fig. A.9: Plots for MIVC candidate no. 18$^-$, same as in Fig. A.1.

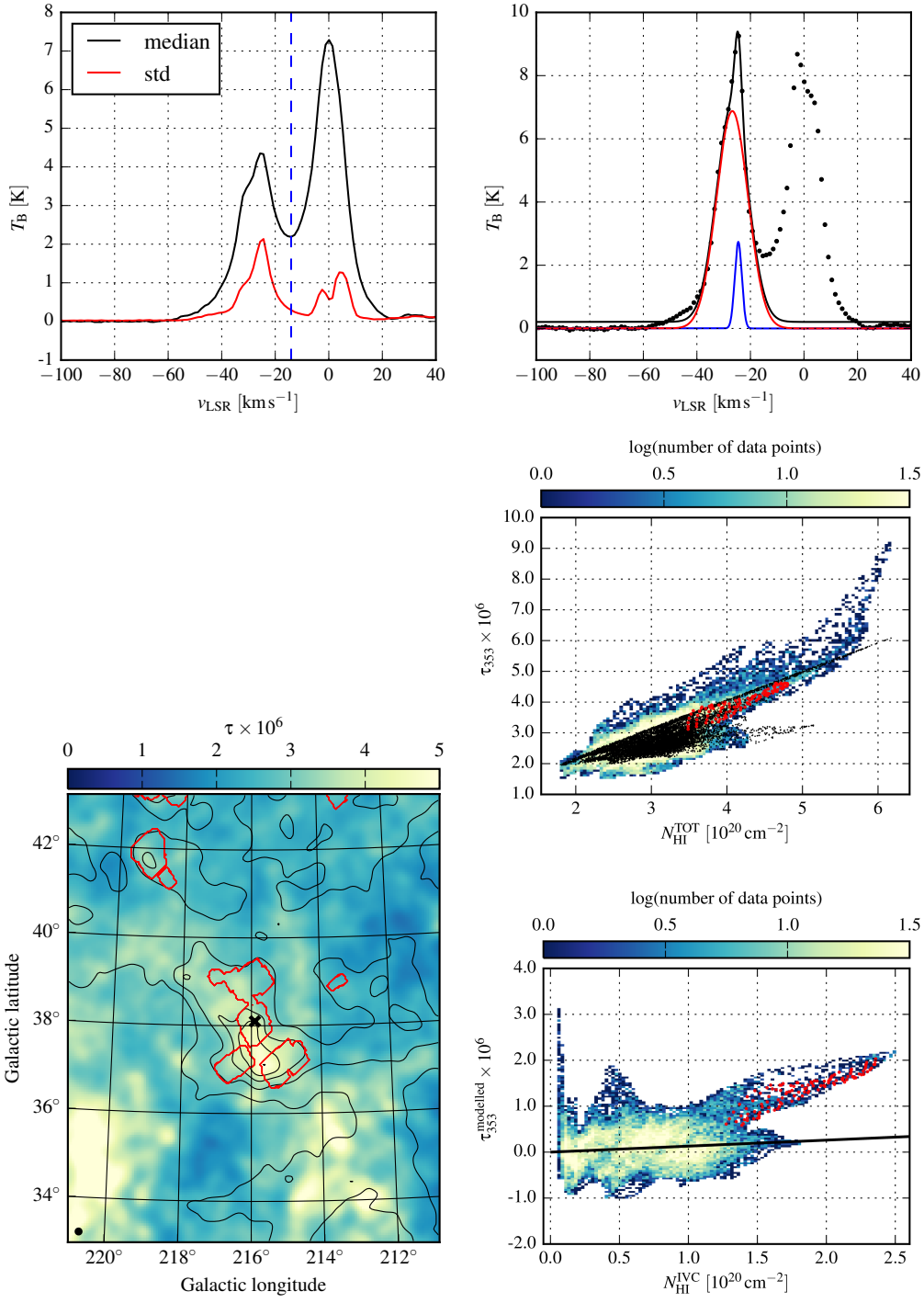

Fig. A.10: Plots for MIVC candidate no. 19$^-$, same as in Fig. A.1.

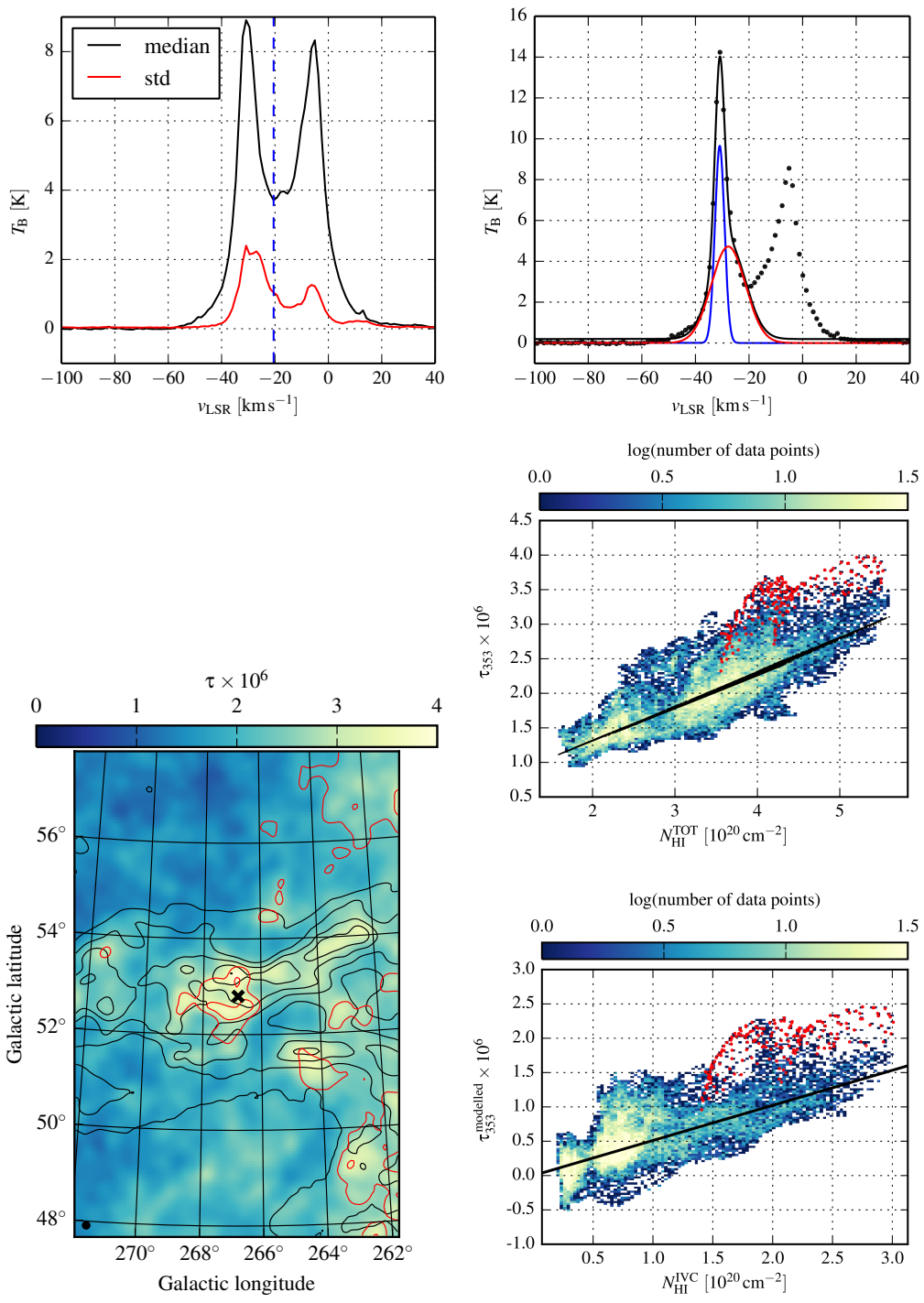

Fig. A.11: Plots for MIVC candidate no. 20$^-$, same as in Fig. A.1.

A.2 Statistical properties of northern IVC+ samples

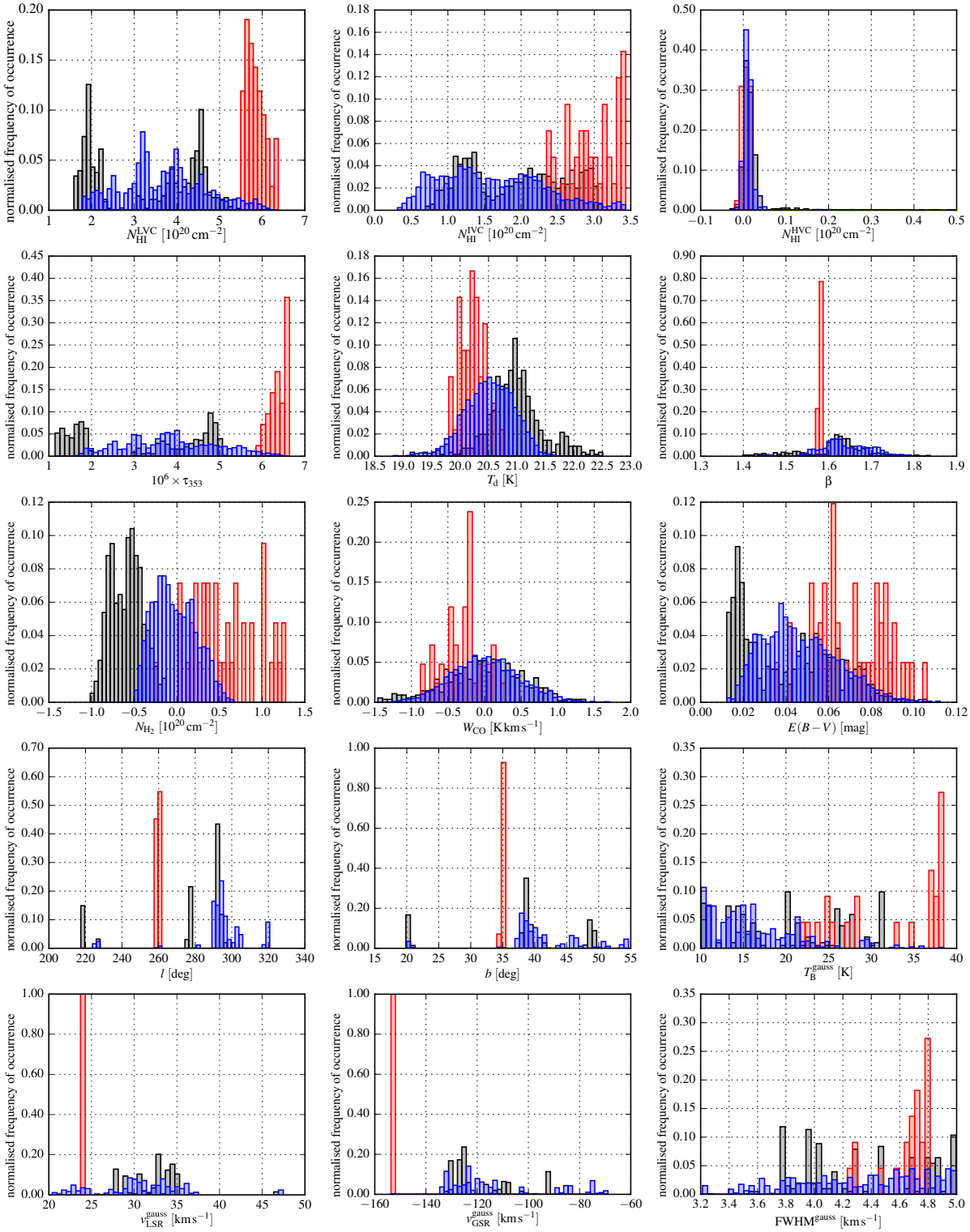

Fig. A.12: Statistical properties of northern AIVC+ (black), MIVC+ (red), and NIVC+ (blue) candidates.

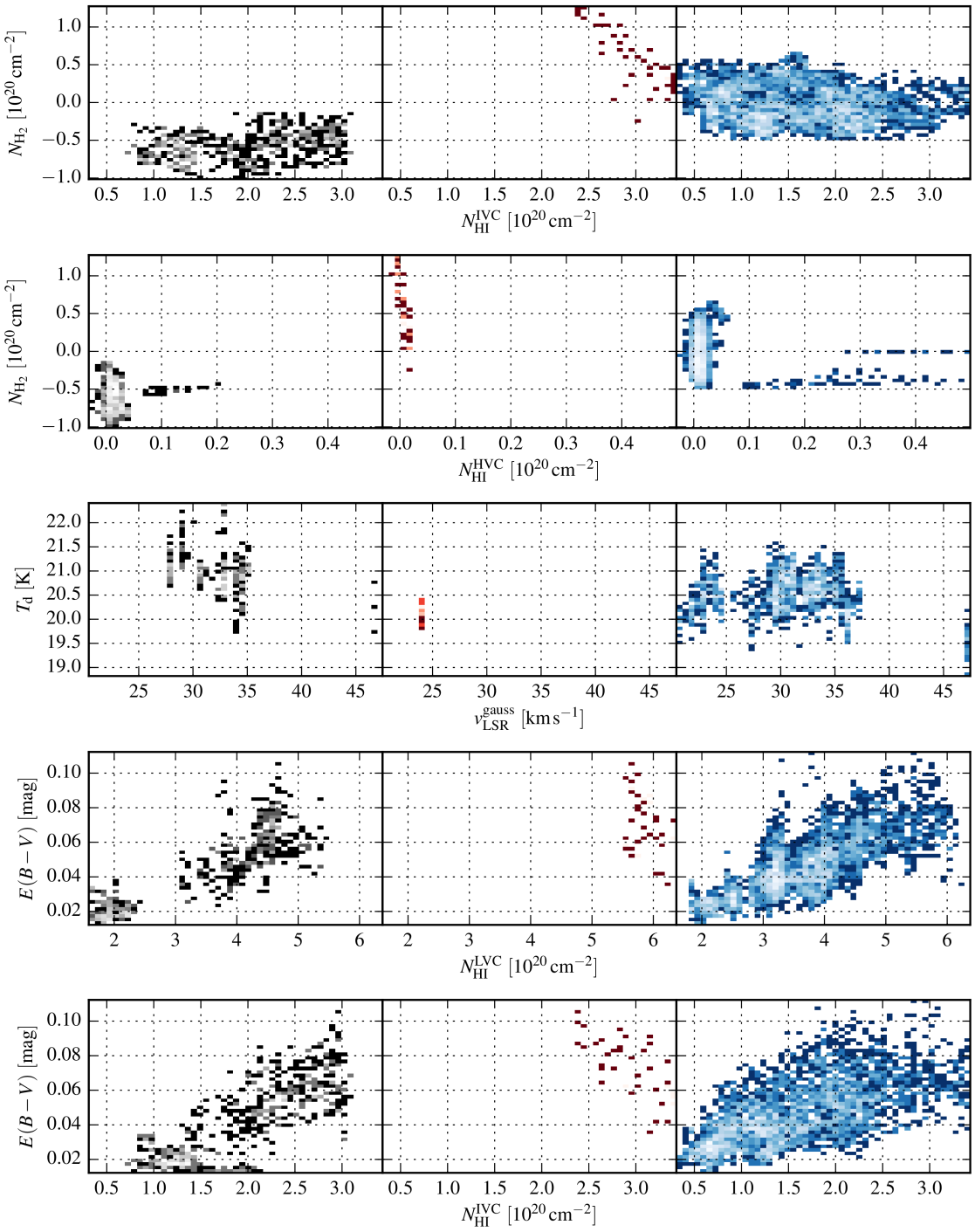

Fig. A.13: Correlation properties of northern AIVC$^+$, MIVC$^+$, and NIVC$^+$ candidates. The left, middle, and right plots show the correlation for the AIVCs$^+$, MIVCs$^+$, and NIVCs$^+$ respectively.

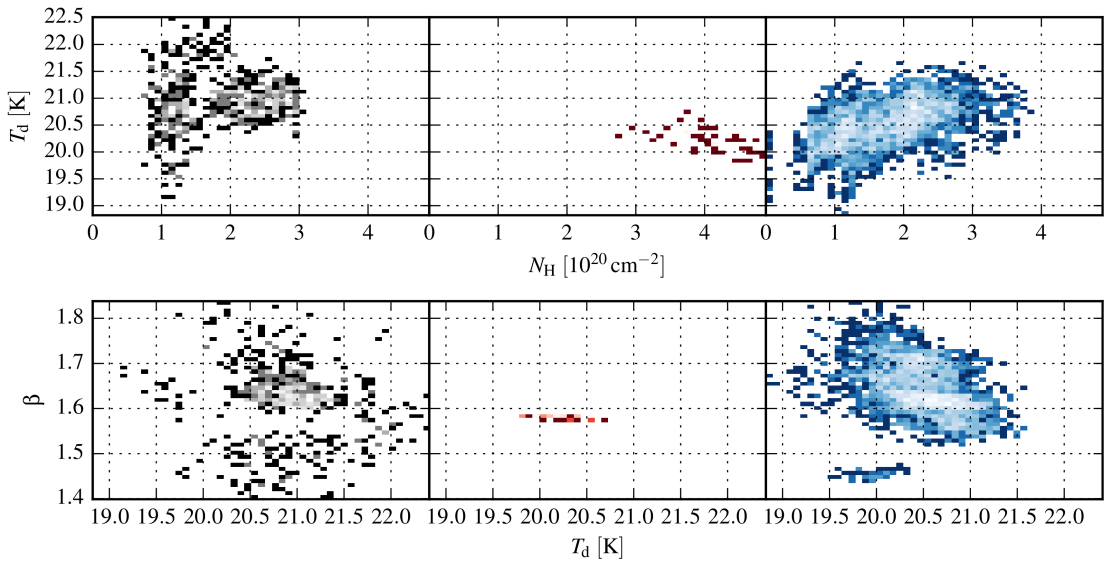

Fig. A.14: Correlation properties of northern AIVC+, MIVC+, and NIVC+ candidates. The left, middle, and right plots show the correlation for the AIVCs+, MIVCs+, and NIVCs+ respectively.

A.3 Southern molecular IVC candidates

Candidate no. 2^- All properties of the southern MIVC$^\pm$ candidates are listed in the lower part Table A.2 on page 152. The MIVC candidate no. 2^- is found towards significant LVC HI emission with at least $N_{\rm HI}^{\rm LVC} \simeq 4 \times 10^{20}\,{\rm cm}^{-2}$. In HI, the candidate cloud is located at the lower latitude end of a large filament that extends up to the border of the data cube at $b = -15°$ (Fig. A.15). For the two-component fit we increase the upper HI column density threshold to $N_{\rm HI} = 5 \times 10^{20}\,{\rm cm}^{-2}$, otherwise the fit would not work because most LVC HI column densities are larger than the usually applied threshold of $N_{\rm HI} = 4 \times 10^{20}\,{\rm cm}^{-2}$.

There is an association of FIR emission to the IVCs within this field, most notably towards this IVC filament. The resulting linear parameters of the HI-τ correlation are peculiar because the dust emissivity is significantly larger for the IVCs than for the LVCs. This apparently leads to the FIR-deficiency of the IVC filament. Also the H_2 column densities are indistinct for this candidate. In the HI-τ correlations the cloud is located on the IVC correlation, which is steeper than for the LVC gas. There is significant LVC emission in this region and also on-top of the candidate. Summarising, candidate no. 2^- is unclear.

Candidate no. 6^- The MIVC candidate no. 6^- is located towards significant LVC HI emission with $N_{\rm HI}^{\rm LVC} \simeq 4 \times 10^{20}\,{\rm cm}^{-2}$. In HI, the candidate cloud is located at the lower latitude end of a large filament that extends up to the border of the data cube at $b = -23°$ (Fig. A.16). The computation of the Spearman's rank coefficients indicate that the LVCs are more related to the dust emission than the IVCs.

There is an association of the FIR emission to the IVC, however, the H_2 column densities do not follow the HI distribution but are located at the edge of the larger IVC filament. In the HI-τ correlations the cloud is located above the general correlation indicating somewhat brighter dust emission than the field, however no apparent FIR excess that steepens for larger HI column densities. Summarising, candidate no. 6^- is unclear.

Candidate no. 2^+ The MIVC candidate no. 2^+ is located towards few LVC HI emission with $N_{\rm HI}^{\rm LVC} \simeq 1 \times 10^{20}\,{\rm cm}^{-2}$. The candidate pixels match the HI IVC distribution very well. In HI the candidate cloud is part of a larger filamentary IVC structure (Fig. A.17).

There is an association of the FIR emission to the IVC and the H_2 column densities follow the HI column densities of the IVC well. However, there is only a slight FIR excess and corresponding low H_2 column densities. In the HI-τ correlations the cloud is located above the general correlation showing a weak FIR excess. Summarising, candidate no. 2^+ could be a MIVC.

Candidate no. 4^+ Candidate no. 4^+ is located close to some large and bright structures, that extend up to the upper boundary of the data cube (Fig. A.18). There is FIR emission associated with the IVC, however, the inferred H_2 column densities are not very significant. In the HI-τ correlations the cloud is located on the general correlation or slightly above, but there is no strong FIR excess associated with the cloud. Summarising, candidate no. 4^+ could be a MIVC.

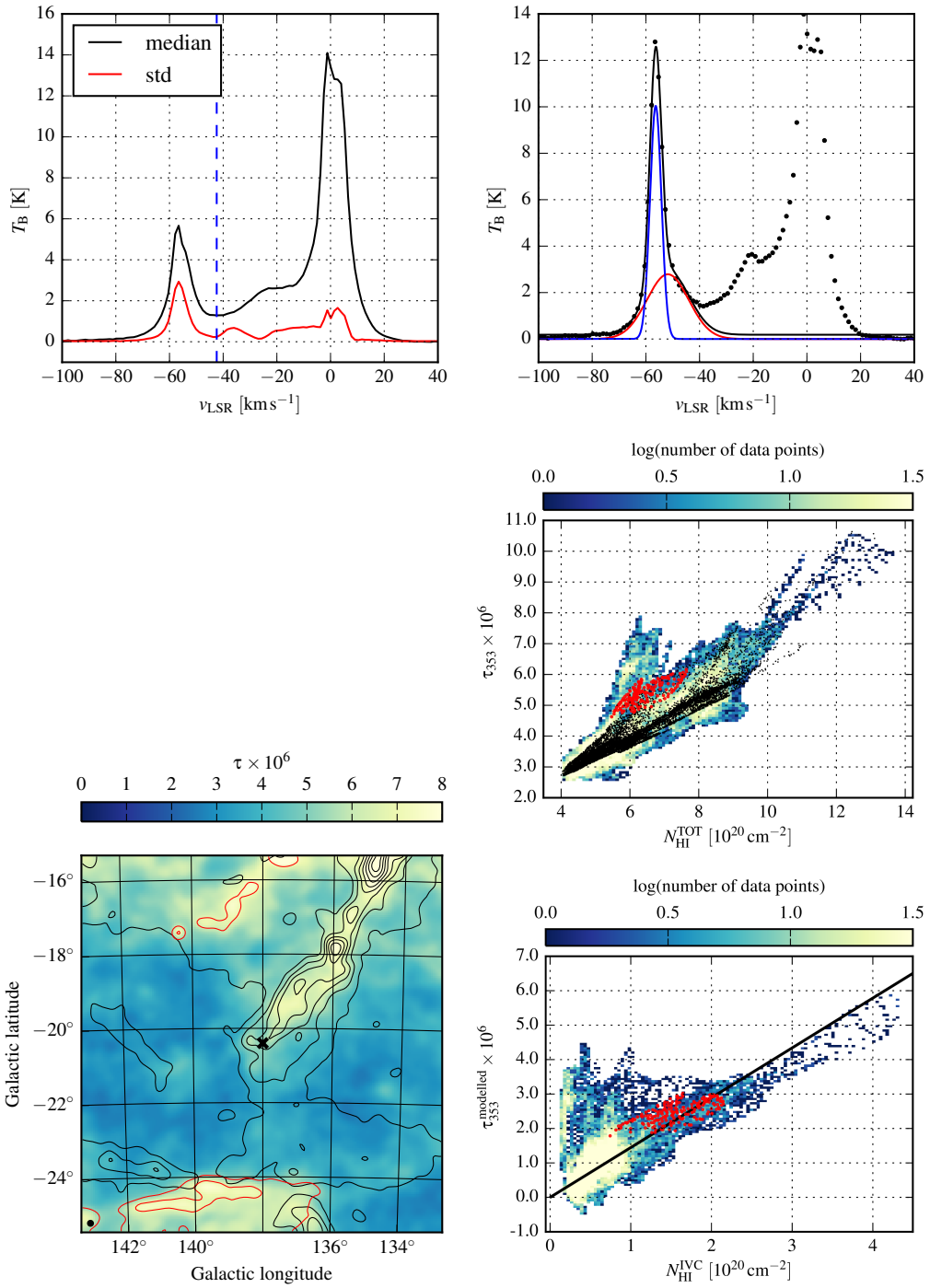

Fig. A.15: Plots for MIVC candidate no. 2$^-$, same as in Fig. A.1.

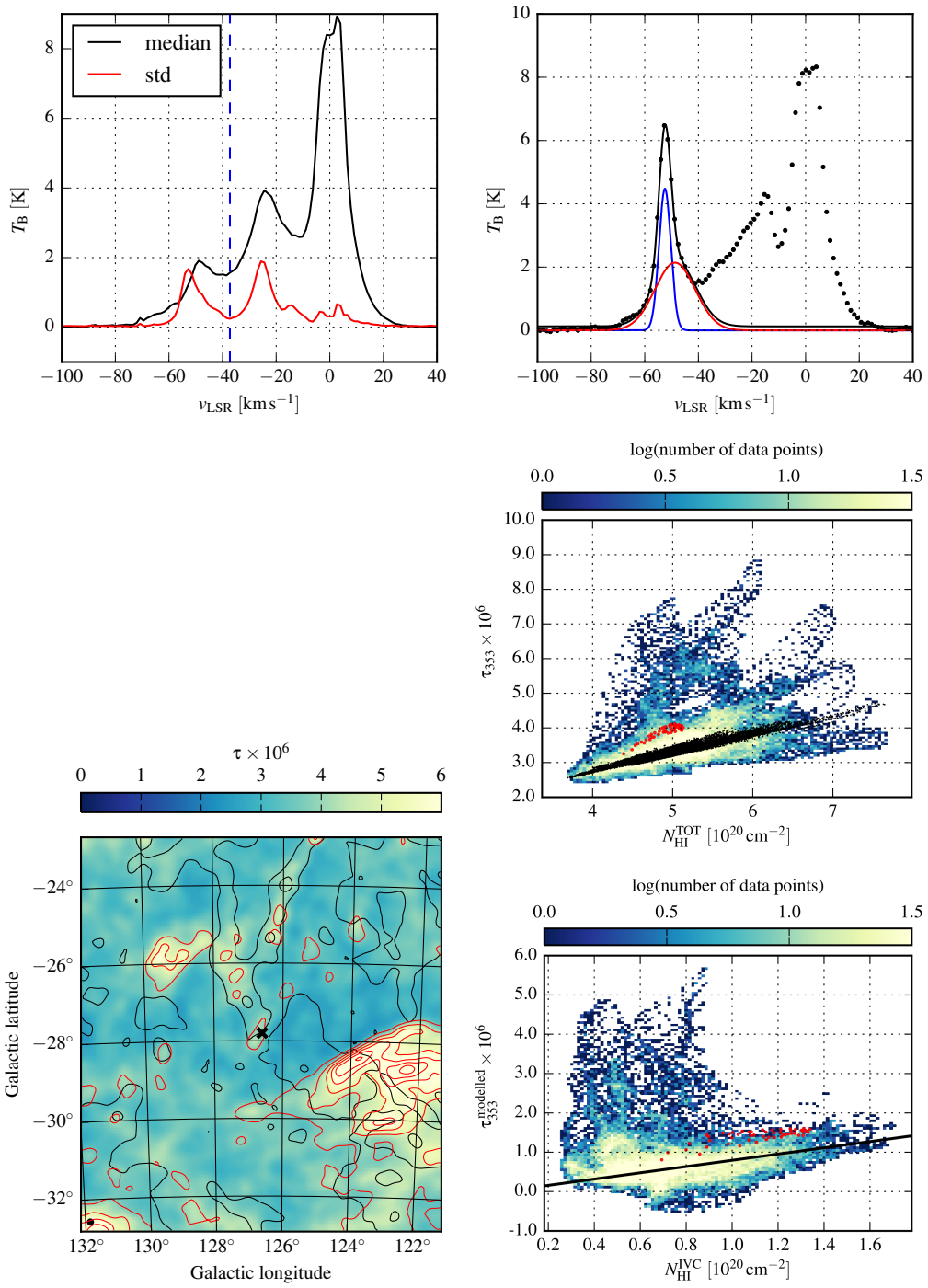

Fig. A.16: Plots for MIVC candidate no. 6$^-$, same as in Fig. A.15. The H_2 contours start at 0.3×10^{20} cm^{-2}, increasing in steps of 0.5×10^{20} cm^{-2}.

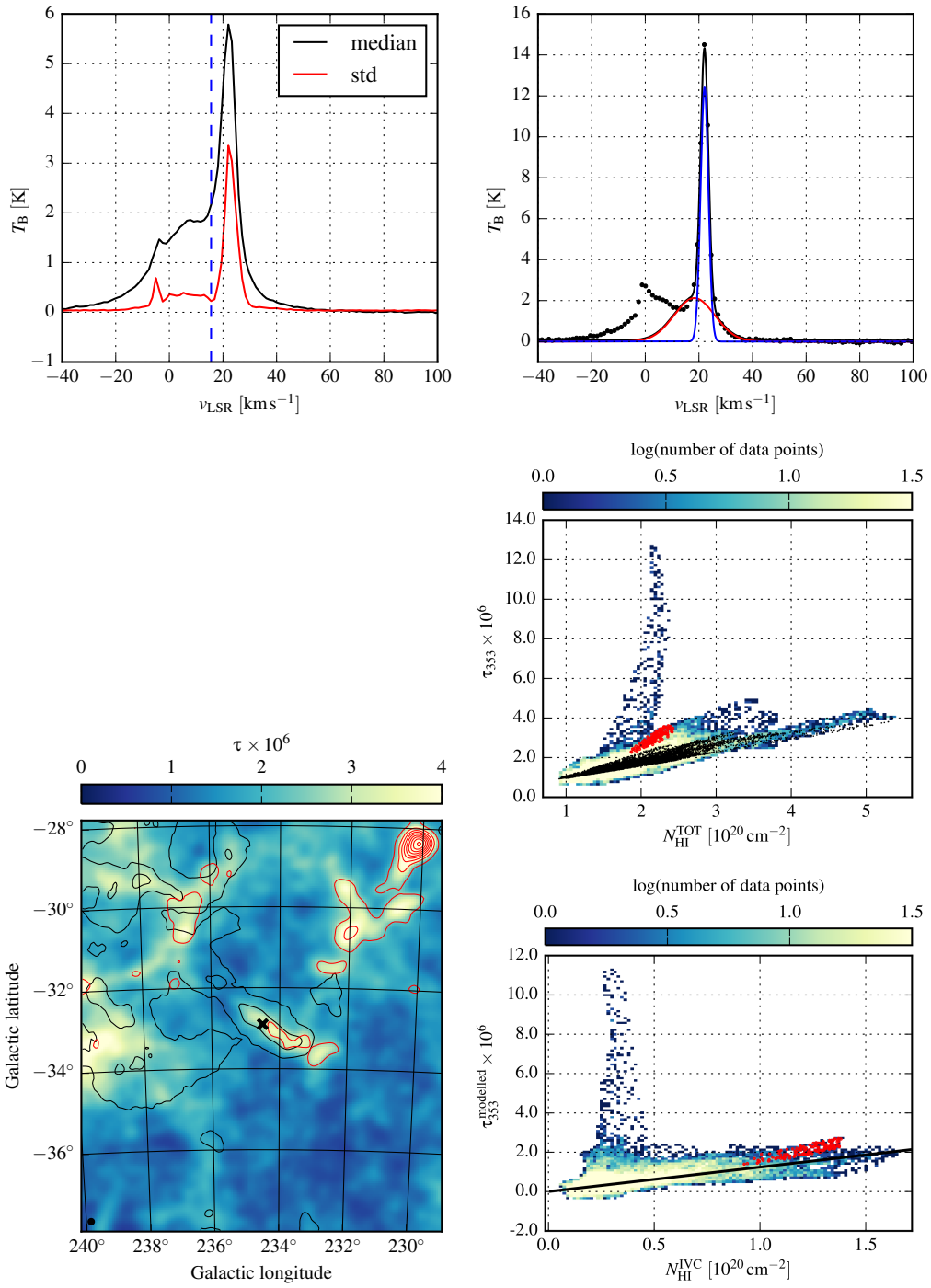

Fig. A.17: Plots for MIVC candidate no. 2^+, same as in Fig. A.15. The H_2 contours start at 0.3×10^{20} cm^{-2}, increasing in steps of 0.5×10^{20} cm^{-2}.

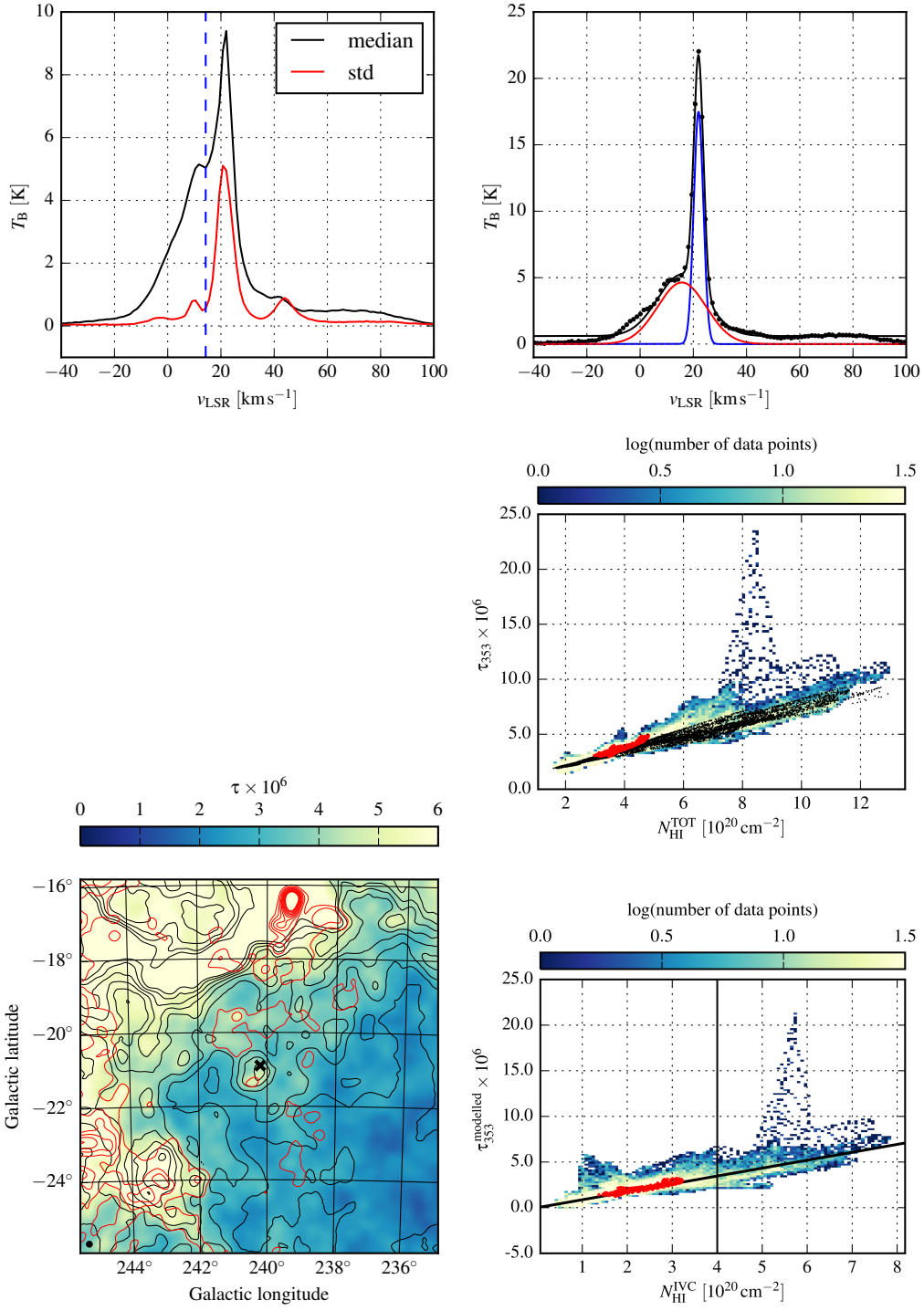

Fig. A.18: Plots for MIVC candidate no. 4^+, same as in Fig. A.15. The H_2 contours start at 0.3×10^{20} cm^{-2}, increasing in steps of 0.5×10^{20} cm^{-2}.

A.4 Statistical properties of southern IVC+ samples

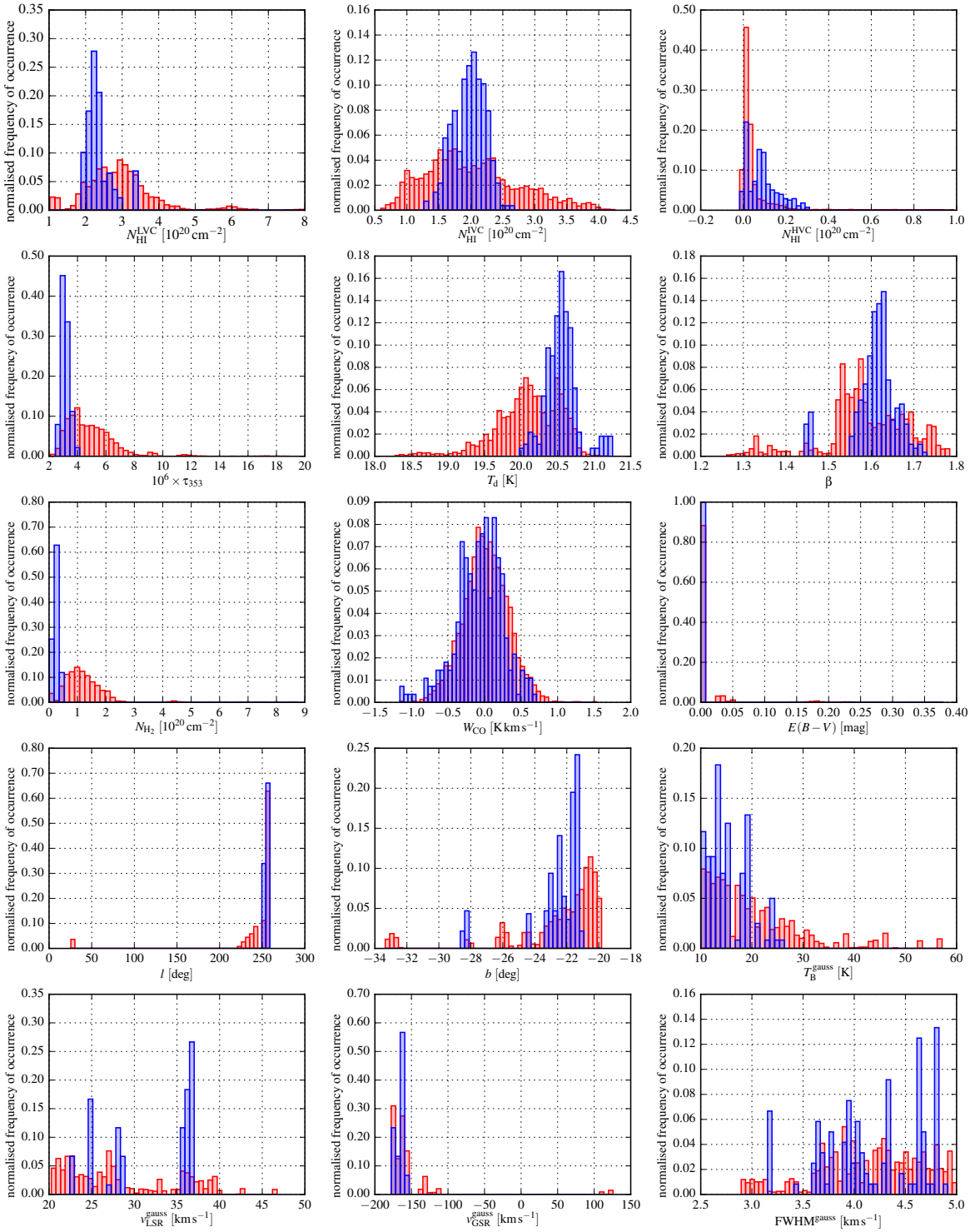

Fig. A.19: Statistical properties of southern AIVC+ (black), MIVC+ (red), and NIVC+ (red) candidates.

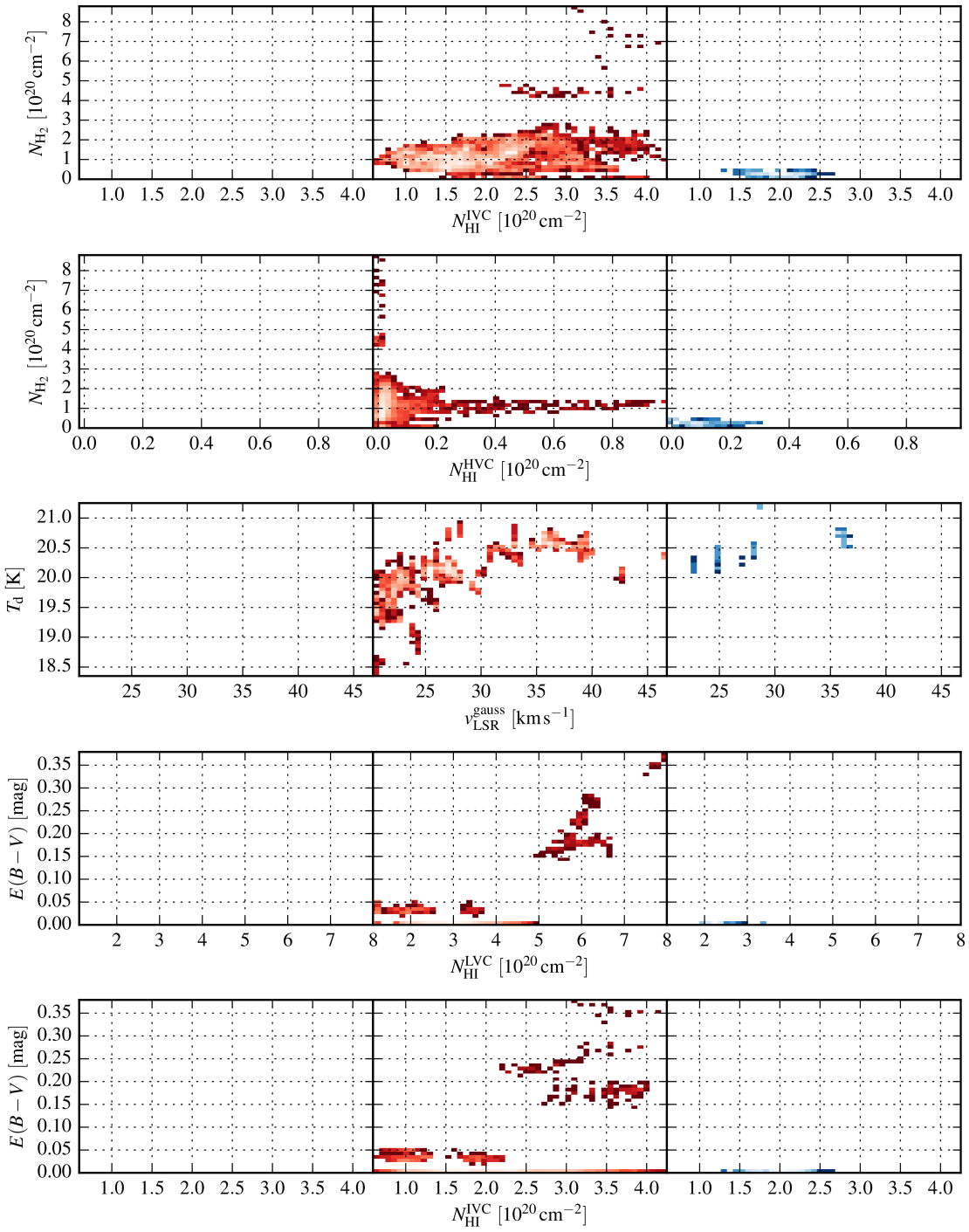

Fig. A.20: Correlation properties of southern AIVC$^+$, MIVC$^+$, and NIVC$^+$ candidates. The left plot (black) shows the AIVCs$^+$, the middle plot (red) the MIVCs$^+$, and the right plot (blue) the NIVCs$^+$.

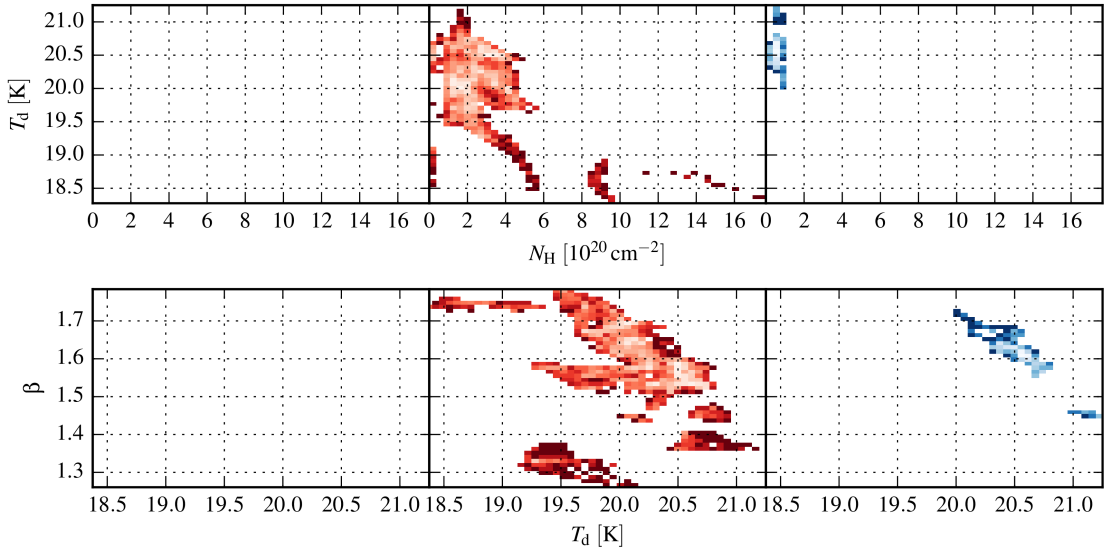

Fig. A.21: Correlation properties of southern AIVC+, MIVC+, and NIVC+ candidates. The left plot (black) shows the AIVCs+, the middle plot (red) the MIVCs+, and the right plot (blue) the NIVCs+.

APPENDIX B

The basics of radio interferometry

In the following the fundamental principles of radio interferometry are explained. These principles are required in order to understand the data product of an interferometer and the different steps in the data reduction process that is described in detail in Sect. 2.5. The following descriptions are based on the NRAO Synthesis Imaging School (Taylor et al. 1999).

B.1 Introduction

The achievable angular resolution of a single-dish telescope with diameter D at observed wavelength λ is given by the Rayleigh-criterion[1]

$$\Delta\alpha = 1.22 \times \frac{\lambda}{D}\,[\mathrm{rad}]. \tag{B.1}$$

Two objects can be spatially resolved by the telescope when they are separated by more than the projected angle $\Delta\alpha$ on the sky. The angular resolution increases with telescope diameter D but decreases for larger wavelength λ.

Radio astronomy measures and analyses radiation of large wavelength. As an example, for the same telescope size, observations of the HI 21 cm line have an angular resolution of a factor $\sim 10^5$ less compared to optical wavelength. It is obvious that single-dish radio-telescopes have to exceed optical telescopes in size by far in order to achieve a sufficiently high angular resolution. However, on earth one cannot build a single radio antenna with arbitrarily large sizes. That is why radio interferometers are built, which consist of a number of antennas that are spread on the ground. The maximum angular resolution of the array is given by the largest separation between individual dishes.

Despite the limited angular resolution of a single-dish telescope, the sensitivity of the instrument is fixed by its collecting area. An interferometer offers the possibility to use the collecting area of many antennas to enhance the sensitivity.

For completeness, we also mention aperture arrays and phased array feeds (PAFs) that are currently in use or in development with the potential to increase the field-of-view and survey speed of radio interferometers largely (e.g. Fisher & Bradley 2000; Hay et al. 2007). Traditional multipixel receivers, like the L-band seven-beam at the Effelsberg 100 m telescope, scan the sky independently with several feed horns. However, this does not sample the focal plane of the telescope fully because the feeds have only small overlaps (compare with Fig. 1 of Winkel et al. 2010). The dense sampling by phased

[1] The theoretical angular resolution as given by Eq. (B.1) is slightly worse than that of an idealised constant-illuminated circular aperture. This is because a tapering-function is assumed that decreases the sensitivity towards the edges of the dish. This taper significantly reduces the side-lobe levels at the cost of angular resolution.

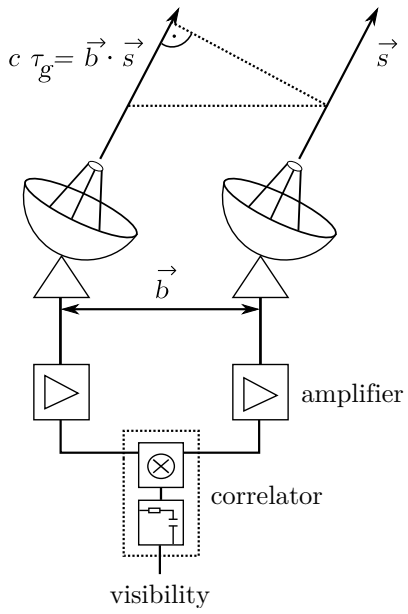

Fig. B.1: Schematic view of a two-element interferometer consisting of two antennas pointing towards $\vec{s}$. The two dishes are separated by the baseline vector $\vec{b}$. There is a geometrical time delay τ_g between the arrival times of the incoming radiation at the two telescopes. The measured signals are amplified and correlated. The correlation consists of multiplication and integration. Reproduced from Taylor et al. (1999).

array feeds (PAFs) allows to form multiple beams on the sky that increase the instantaneous field-of-view significantly. For the Aperture Tile in Focus (Apertif) at the WSRT (Verheijen et al. 2008; Oosterloo et al. 2010), the prototype system increases the number of beams for a single dish from 1 to 37, enlarging the field-of-view from ~0.3 deg^2 to ~8 deg^2. A beam of the PAF is formed digitally as a weighted combination of signals from several array elements. For a full sampling of the focal plane, the array-elements must be spaced with a distance of $\lambda/2$. This cannot be done with traditional feed horns requiring smaller receiving elements.

Aperture arrays rely on the same principles. Lots of simple (dipole) antennas are spread on the ground. By digitally combining the signals from the antennas, one or more beams are formed. By the combination of these individual stations, radio interferometry can be conducted. The Low-Frequency Array (LOFAR, e.g. Stappers et al. 2011) is a working aperture array.

B.2 Two-element interferometer

Any interferometer with its numerous telescopes can be reduced to antenna pairs – the two-element interferometer. Two dishes form a baseline $\vec{b}$ which is the separation of the telescopes projected onto a plane perpendicular to the source direction $\vec{s}$ (Fig. B.1). The two dishes observe the same target simultaneously. We assume that the incoming radiation from the source is a monochromatic plane wave with angular frequency ω. Due to the relative position of the antennas to the source, there is a geometrical time delay τ_g between the arrival times of the signals at the two dishes. At each antenna the incoming signals are transformed into voltages and amplified. After correcting for the geometrical time delay τ_g, the signals are correlated which involves multiplication and integration or time averaging[2].

The incoming monochromatic radiation at antennas 1 and 2 can be written as $U_1 = U\cos(\omega(t-\tau_g))$ and $U_2 = U\cos(\omega t)$ with the geometrical time delay $c\tau_g = \vec{b} \cdot \vec{s}$. After multiplication and time-

[2] There are also additive interferometers, like in the optical.

averaging, the correlator-output is

$$R =< U_1 U_2 >= \frac{U^2}{2} \cos(\omega\tau_g), \tag{B.2}$$

where the amplitude of the cosine is related to the source brightness. The time delay τ_g changes slowly as the source moves on the sky. The fringe phase $\phi = \omega\tau_g$ measures where the source emission is originating from. Depending on the location of the source on the sky, the time-of-arrivals of the signals at the two antennas are different[3]. Hence, the two-element interferometer samples the sky with a cosine-like response pattern. The angular orientation of this cosine on the sky is given by the baseline orientation.

The cosine-like response pattern of a two-element interferometer samples a particular Fourier component of the sky emission. Each unique baseline, in both length and orientation with respect to the source, measures a different Fourier component of the source emission on the sky. The more different and unique baselines the interferometer comprises, the more information about the source intensity distribution is retained. In the limit of infinite baselines, in theory all possible Fourier components of the source distribution are recovered. However, a real radio interferometer offers only a finite number of unique baselines, which results inevitably in incomplete source information.

The longer baselines or larger antenna separations create a rapidly oscillating fringe pattern and sample the sky at a high spatial frequency recovering the information on small angular scales. Likewise the short baselines sample the large scales of the source emission. A problem arises at the smallest baselines since two antennas cannot be positioned arbitrarily close to each other requiring a short-spacing correction (Sect. B.7).

The power dR received from an intensity distribution $I(\vec{s})$ in the solid angle dΩ is given by

$$\mathrm{d}R = A(\vec{s}) I(\vec{s}) \Delta\nu \, \mathrm{d}\Omega \cos(2\pi\nu\tau_g), \tag{B.3}$$

in which the effective collecting area $A(\vec{s})$ and some frequency bandwidth $\Delta\nu$ contribute, given by the specifications of the receiving system. The collecting area $A(\vec{s})$ is not just the sum of the geometrical areas of the individual antennas. The total aperture is reduced in efficiency due to several reasons like the tapering-function, the surface reflection efficiency, or the aperture blockage because of a receiver element in front of the antenna.

The source distribution $I(\vec{s})$ can be understood as the sum of many different point sources if the source itself is spatially incoherent, e.g. the emission is spatially uncorrelated. There is the fundamental mathematical theorem that any function can be decomposed into an even and odd part. This means that we can write $I_\nu(\vec{s}) = I_{\nu,\mathrm{E}}(\vec{s}) + I_{\nu,\mathrm{O}}(\vec{s})$ with the even $I_{\nu,\mathrm{E}}(\vec{s})$ and odd $I_{\nu,\mathrm{O}}(\vec{s})$ component of the source intensity distribution.

We write the "cosine" correlator output as an integral over the entire sphere S:

$$R_{\cos} = \int_S \mathrm{d}\Omega \, A(\vec{s}) I_\nu(\vec{s}) \cos\left(2\pi\nu \vec{b} \cdot \vec{s}\right). \tag{B.4}$$

As an even function this "cosine" correlator output is only sensitive to the even components $I_{\nu,\mathrm{E}}(\vec{s})$ of the source distribution, while the odd components $I_{\nu,\mathrm{O}}(\vec{s})$ are not recovered. We need an additional receiver output that samples the "sines" of the intensity distribution:

$$R_{\sin} = \int_S \mathrm{d}\Omega \, A(\vec{s}) I_\nu(\vec{s}) \sin\left(2\pi\nu \vec{b} \cdot \vec{s}\right). \tag{B.5}$$

[3] This is similar to the ability of the human ears and brain to locate the origin of sounds from the different arrival times of sound waves.

This second correlator is designed with an additional phase shift of 90° to the antenna output.

The Euler relation $\exp(i\phi) = \cos\phi + i\sin\phi$ allows to combine these two correlator outputs into a single complex quantity, the visibility V. We define the complex visibility as

$$V_\nu = \int_S \mathrm{d}\Omega\, A(\vec{s}) I_\nu(\vec{s}) \exp\left(-2\pi i \nu \vec{b}\cdot\vec{s}\right). \tag{B.6}$$

The visibility V_ν is the Fourier transform of the source emission combined with the properties of the telescope.

An interferometric observation is performed such that the source distribution is sampled relative to the phase reference position $\vec{s_0}$ on which the interferometric image is centred. The source position is related to the phase centre by $\vec{s} = \vec{s_0} + \vec{\sigma}$.

A coordinate system is defined in which the visibilities are measured. In the plane of the interferometer, the baseline vector is written with components (u, v, w) where w points toward the phase tracking centre $\vec{s_0}$. These coordinates are given in multiples of wavelength at the centre of the observed frequency band. Sky coordinates are given by (l, m, n), which are direction cosines[4] with respect to (u, v, w). The coordinates (l, m) define a tangent plane perpendicular to the source direction n to which the celestial sphere is projected.

There is an important simplification under the condition of coplanar baselines that is usually fulfilled in the case of small field imaging, e.g. when $|l|$ and $|m|$ are small. Then $w \simeq 0$ and the Fourier transform (Eq. (B.6)) reduces to the two dimensions (u, v):

$$V_\nu(u, v) = \int_{-\infty}^{+\infty}\int_{-\infty}^{+\infty} \mathrm{d}l\,\mathrm{d}m\, A(l, m) I_\nu(l, m)\, e^{-2\pi i(ul+vm)}. \tag{B.7}$$

If the field is too large, phase errors are introduced by omitting the w dependence of the visibilities. In these cases Eq. (B.7) has to be extended to the general three dimensional prescription.

The complex visibilities are the measurements of a radio interferometer. The visibilities are the Fourier transform of the source distribution convolved with the response function of the array. Before an image can be obtained from the visibilities, the data has to be calibrated.

B.3 Calibration

Radio interferometers measure some visibilities $\tilde{V}$, which are related to the true visibilities V by instrumental effects. This relation is in good approximation linear, e.g., the output depends linearly on the input. The visibilities measured by one antenna pair are independent from other measurements of any other baseline.

For the calibration of the science target, one requires calibration sources that have a known spectrum and spatial distribution, for simplicity point-like sources. Usually, several different calibrators are used that are best for a given purpose. For instance, in order to retrieve the bandpass shape, a bright source is best, for which the signal-to-noise ratio is large. Phases are easily calibrated for point-sources in the pointing centre, for which the calibrated phases should be zero. Mathematically speaking, a point-source is a delta-function that is a constant in the Fourier-domain, which is a particular easy case to calibrate on.

[4] Direction cosines are the projections of a coordinate vector (x, y, z) onto the basis vectors (e_x, e_y, e_z) of the coordinate system.

The basic calibration equation is written for an antenna pair ij with time t as

$$\tilde{V}_{ij}(t) = G_{ij}V_{ij}(t) + \epsilon_{ij}(t) + n_{ij}(t). \tag{B.8}$$

The unknown factors are the baseline-based complex gain $G_{ij}(t)$, the baseline-based phase offset $\epsilon_{ij}(t)$ and the complex noise $n_{ij}(t)$. In order to calibrate these time-dependent quantities, one relies on calibration sources that are observed before, after, and during the science observations. The calibration method is an optimisation procedure based on known and measured values for the calibrators.

Bandpass calibration The bandpass is the frequency-dependent response of the receiver system. It is designed to be only sensitive in a certain frequency range in order to suppress strong emission outside the desired bandwidth. Hence, its sensitivity drops to zero at the edges of the band. Within the band the response is also not uniform but depends on frequency. By observing a strong continuum source with a known spectral slope, the bandpass shape is determined. The division by the derived bandpass leads to a flat spectral response, e.g., independent on frequency.

Amplitude calibration After the bandpass calibration the noisy spectrum is centred at an arbitrary value. By observing a calibrator with a known flux density, the spectrum is scaled to a physical meaningful value.

Phase calibration The phases of the visibilities determine where a particular source component is located on the sky with respect to the phase centre. Phases are calibrated by observing a bright known point source, which is defined to be in the phase centre, for which the phase is constant at zero. Also resolved sources with known structures can be used. Phase corrections are applied such that the measured phases match the expected ones.

Phase corrections may depend on time because of fluctuations in the Earth's ionosphere and troposphere. This is especially an issue at higher frequencies where one has to switch continuously between science target and calibrator to capture these changes on a time-scale of minutes. If the science target is sufficiently bright, these measurements themselves can be used for calibration, which is known as self-calibration (Sect. B.6).

B.4 Imaging

The complex visibilities (Eq. B.7), characterised by amplitudes and phases, are the observables of a radio interferometer. They are measured in the (u, v)-plane and are the Fourier transform of the source distribution convolved with the array response. We could just take the inverse Fourier transform and recover the source distribution from the observed data. However, in a real observation the visibilities are not measured in the entire (u, v)-plane but only at discrete sampling points, which are given by the number of available antennas and baselines. An observation only recovers a fraction of the source information. The denser and the more complete the sampling of (u, v)-plane is, the better is the synthesised beam and the observation. We perform the inverse Fourier transformation and introduce the sampling function $S(u, v)$ such that

$$A(l, m)I^{\mathrm{D}}(l, m) = \int_{-\infty}^{+\infty}\int_{-\infty}^{+\infty} \mathrm{d}u\,\mathrm{d}v\, S(u, v)V(u, v)\, e^{+2\pi i(ul+vm)}. \tag{B.9}$$

In the language of radio interferometry, $I^{\mathrm{D}}(l,m)$ is the dirty image. It is related to the true source intensity distribution $I(l,m)$ by a convolution:

$$I^{\mathrm{D}}(l,m) = I(l,m) * B(l,m) = \int_{-\infty}^{+\infty}\int_{-\infty}^{+\infty} \mathrm{d}u\,\mathrm{d}v\, I(u,v)\, e^{+2\pi i(ul+vm)} * \int_{-\infty}^{+\infty}\int_{-\infty}^{+\infty} \mathrm{d}u\,\mathrm{d}v\, S(u,v)\, e^{+2\pi i(ul+vm)} \tag{B.10}$$

where $B(l,m)$ is the synthesised beam, in this case the dirty beam. The synthesised beam is mainly determined by the sampling of the (u,v)-plane. For a single observation of a two-element array of infinitesimal time, the combined aperture consists of two points. This (u,v)-coverage corresponds to a cosine function after Fourier transformation (convolved with the primary beam of an individual antenna, a Gaussian, which is neglected for simplification here). This beam is particularly bad because it has no good directivity and very high side-lobes. By adding more points to the (u,v)-plane, e.g. by using more dishes at different locations creating different projected baselines, the incomplete (u,v)-plane is filled and the interferometer gains a better directivity and a cleaner synthesised beam with lower side-lobes.

The image I^{D} is called the dirty image because of the imaging artefacts that are caused by the convolution of the underlying source emission with the beam response of the interferometer. The dirty image contains strong side-lobes that are the low-order maxima of the beam response of the interferometer caused by a source. This dirty beam is determined by the Fourier transform of the (u,v)-coverage. Negative bowls are present in the dirty image that are caused by the missing of the shortest antenna baselines - the short spacing problem (Sect. B.7). These negative values are a natural result of any interferometric observations.

The dirty image may not be well suited for any scientific analysis because many emission features are not real. Although, when the (u,v)-coverage is very dense, the resulting beam is quite good. Still, a deconvolution of the dirty image is conducted with the aim to remove the side-lobe structures from the dirty image such that the true source distribution is convolved with a Gaussian beam only, the size of which is related to the largest baseline. However, there are in principle an infinite number of solutions to the deconvolution problem. In the following we briefly describe to different deconvolution algorithms, the Maximum Entropy Method (MEM) and the clean algorithm. In our work the clean method is applied.

Maximum Entropy Method The Maximum Entropy Method (MEM, e.g. Cornwell & Evans 1985) finds an image that matches the data within the noise levels and that has maximum entropy. MEM is not a procedure during which a plausible image is reconstructed. Note that this entropy is not the physical entropy from statistical mechanics. Instead it may be understood as a quantity that produces a positive image with a compressed range of pixel values when it is maximised (Taylor et al. 1999, p. 162). In addition, a χ^2 criterion is put in enforcing that the fitted visibility data matches the observed ones closely. In MEM the knowledge of the true source distribution can be put into the maximisation. Generally, MEM algorithms are more difficult to control as compared to a clean algorithm for instance. Deconvolved images with MEM are smooth because neighbouring pixels are coupled together, although the resolution depends on the signal to noise of the data. Often the noise in a MEM image is biased, which is a common problem for any estimator.

Clean algorithm In the iterative cleaning process, one tries to reconstruct the source structure from the dirty image in order to fill in missing information in the (u,v)-plane. This ideally removes the artificial side-lobes and fills up the negative bowls.

A traditional clean algorithm (e.g. Högbom 1974) assumes that the true source distribution can be approximated by a number of point sources. The algorithm takes the brightest emission feature, puts a point source at this location with a fraction of the amplitude in the dirty image, convolves it with

the dirty beam, and subtracts the resulting pattern from the dirty image. This process is repeated until a stopping criterion is reached, like a number of iterations or a chosen residual noise threshold in the cleaned image. During cleaning a model of the true emission is constructed by a number of point sources. From this model and its improved (u, v)-coverage, the clean beam is estimated. The final image is the source model convolved with the clean beam plus the residual emission of the dirty image.

This works well if the source is indeed point-like. However, for extended emission a decomposition into point-sources is not optimal. Multi-scale clean is a different approach better suited for extended emission. In this scheme the source is not modelled with point sources but with 2D Gaussians of various spatial sizes.

There are some issues with a traditional or multi-scale clean approach. First, there are a number of imaging parameters, like threshold value, pixel size, image size, and weighting scheme, which have to be set by the user and which can change the outcome considerably. Moreover, the user has to judge by experience if the result is good or bad. Second, the user has to choose in the first place which structures in the dirty image are real and which are just imaging artefacts. For a complex or unknown source structure this is not trivial. Once image artefacts are cleaned, the model image contains source elements at these locations causing errors in the final image.

Weighting scheme It is possible to modify the properties of the deconvolved image by applying different weighting schemes to the visibilities in the (u, v)-plane. There are basically three different approaches: natural, uniform and super-uniform, and Briggs weighting.

Natural weighting takes the (u, v)-plane and applies a weight to each visibility point that is calculated from the measurement error of that particular visibility. In this way regions of the (u, v)-plane contribute more to the final image that are covered well in the observations because there more (u, v)-points are measured. This is usually the case for the shorter baselines, which are more numerous than the longest ones. Hence, natural weighting reduces the angular resolution of the resulting image, which is more sensitive to extended structures. In addition, the noise is diminished.

Uniform weighting applies weights to the visibilities such that each (u, v)-cell has the same weight. This approach reduces the weights at low (u, v)-distances and increases them at larger ones. This creates a better angular resolution in the final image at the cost of higher noise.

As an alternative to combine both advantages of natural and uniform weighting, the Briggs weighting is introduced (Briggs et al. 1999). This scheme uses the robust parameter to continuously change from natural to uniform weighting. Briggs weighting is the preferred choice because it allows to tune between these two extremes combining advantages of both weighting schemes.

B.5 Aperture synthesis

The dirty beam of the interferometer is basically the Fourier transform of the sampling function of the (u, v)-plane. It is one of the important goals of a radio interferometric observation to fill the (u, v)-plane as completely and homogeneously as possible. One can increase the number of telescopes in the array to sample more regions of the (u, v)-plane. However, there is a natural limitation to this because one cannot build arbitrarily many dishes.

Aperture synthesis is the efficient filling of the (u, v)-plane by the rotation of the Earth during the observation. As the Earth moves, the orientation of all baselines relative to the source changes, which leads to measurements at additional (u, v)-points. Hence, with time the (u, v)-plane is filled more and more because different baselines with different antenna positions and projected baseline-lengths are sampled. If a two-element interferometer observes the north celestial pole for 12 h, the resulting (u, v)-

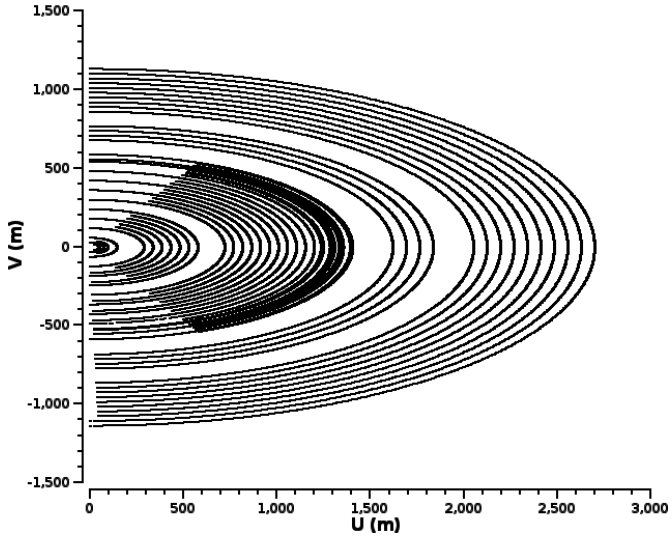

Fig. B.2: (u, v)-coverage of WSRT observations of the molecular cloud (Sect. 2.5). The axes are the baseline coordinates u and v in the plane of the array perpendicular to the source direction. The maximum baseline along u is ~2.7 km. The different tracks show the projected baselines and how they fill the (u, v)-plane during the observation as the Earth rotates. Half of the (u, v)-plane is not plotted, the visibilities are mirrored at the y-axis containing the negative u as well. The regular spacing of the WSRT antennas is reflected by the regular spacings of the (u, v)-tracks. Parts of the (u, v)-tracks in the inner and middle regions appear to be missing, since some semi-ellipses do not start and end at $u = 0$ m. This is likely the result of the shadowing.

coverage would be a circle. With every minute of the observation, the antennas are rotated by the Earth with respect to the north celestial pole, which changes their orientation but not the projected baseline length. If this two-element interferometer would observe a source at lower declination, the (u, v)-coverage turns into an ellipse because the projected baseline length changes over time also.

As an example, for the Westerbork-Synthesis Radio Telscope (WSRT) it is very important to observe over a sufficiently long time. Its antennas are oriented on the east-west axis, which could in an extreme case lead to an elliptical beam with a major axis of infinity in the north-south direction. With aperture synthesis and several hours of observation time, the telescope beam gets more circular. However, only for a source declination of 90° the beam would be fully circular. The obtained (u, v)-coverage for the observations presented in Sect. 2.5 is shown exemplary in Fig. B.2.

B.6 Self-calibration

The final deconvolved images may not be perfect in the sense that there is no white noise around the sources but additional structures and patterns are remaining that cannot be successfully cleaned. On the on hand this may indicate bad data that should be flagged. On the other hand this could be due to residual calibration errors.

There are always residual calibration errors, which are in part simply due to the limited signal-to-noise ratio of the visibility data. Many observations are conducted in the manner that the primary calibrator is observed first, then the target and at the end the secondary calibrator. This is a compromise between time on the target and image quality. For a better calibration continuous switching between calibrator and target would be required to capture variations and fluctuations of the atmosphere and of the instrumental properties like gains or system temperature. For observations at large frequencies, one indeed has to observe a calibrator source repetitively on the time-scale of minutes.

In order to improve the phase calibration, one can calibrate the phases on the science data itself, which is known as self-calibration. In principle this is a normal phase calibration on the shortest possible time-scale to capture any changes in the phases. One has to have a good model for the source, e.g. no false clean components from side-lobe-cleaning. This model is used to calibrate the phases.

For each antenna a phase correction is derived for a chosen time interval. Desirably, this time interval should be as short as possible to capture any phase changes in the system. However, due to a lack

of signal-to-noise, the time interval cannot be arbitrarily reduced. For a reliable self-calibration the signal-to-noise should be three or more.

As in a normal phase calibration one usually uses point-like structures also in self-calibration to improve the phase solutions. In principle one can also calibrate and self-calibrate on extended sources, for which detailed source models are required. For a self-calibration of spectral line observations one often uses unresolved, and thus point-like, continuum sources that are located within the primary beam of the observation. The derived phase solutions over time are applied to the entire visibilities and the data is imaged and deconvolved once more.

B.7 Short spacing problem

There is a minimal baseline length for any radio interferometer. Because of the size of individual antennas, two dishes cannot be put arbitrarily close together. Hence, the smallest baselines are never sampled and the total flux of the source cannot be measured. This information can only be provided by observations of a single-dish telescope. There exist numerous methods how to use single-dish observations in order to fill in these missing spacings, all of which have their own problems. The most widely used method, the feathering, is to Fourier transform the single-dish data and to fill up the (u, v)-plane with these additional measurements. Some weighting factors are applied that match the measured fluxes of interferometer and single dish. Then, the combined data is imaged and cleaned. A different and more linear approach is to combine the science-ready interferometric and single-dish maps directly in the image plane.

The short spacing correction is important for the recovery of the entire source structure. A radio interferometer acts as a Fourier filter because all spatial scales that are not sampled by the array are missing in the final image. Hence, extended and diffuse structures are usually not recovered by an interferometer, especially for objects in the Milky Way. In order to analyse and characterise the target source fully, both interferometric and single-dish observations are required. Otherwise, a significant part of the source structure may be missing.

List of frequently used acronyms

AIVC	Atomic intermediate-velocity cloud
CNM	Cold neutral medium
CO	Carbon monoxide
Decl.	Declination
EBHIS	Effelsberg-Bonn HI Survey
FITS	Flexible Image Transport System
FIR	Far-infrared
FWHM	Full width half maximum
GASS	Galactic All-Sky Survey
GSR	Galactic standard of rest
HEALPix	Hierarchical Equal Area iso-Latitude Pixelization
HI	Atomic hydrogen
H^+	Ionised hydrogen
H_2	Molecular hydrogen
HVC	High-velocity cloud
IR	Infrared
IRAM	Institut de Radioastronomie Millimétrique
IRAS	Infrared Astronomical Satellite
IRIS	Improved Reprocessing of the IRAS Survey
ISM	Interstellar medium
IV	Intermediate-velocity
IVC	Intermediate-velocity cloud
LAB	Leiden-Argentine-Bonn Survey
LSR	Local standard of rest
LVC	Low-velocity cloud
MIVC	Molecular intermediate-velocity cloud
NIVC	Normal intermediate-velocity cloud
OTF	On the fly
PSD	Power spectral density
PV	Position velocity
R.A.	Right Ascension
RFI	Radio frequency interference
SSC	Short spacing correction
WNM	Warm-neutral medium
WSRT	Westerbork Synthesis Radio Telescope

Bibliography

Akaike, H. 1974, Automatic Control, IEEE Transactions on, 19, 716

Albert, C. E. & Danly, L. 2004, in Astrophysics and Space Science Library, Vol. 312, High Velocity Clouds, ed. H. van Woerden, B. P. Wakker, U. J. Schwarz, & K. S. de Boer, 73

Arnal, E. M., Bajaja, E., Larrarte, J. J., Morras, R., & Pöppel, W. G. L. 2000, A&AS, 142, 35

Arzoumanian, D., André, P., Didelon, P., et al. 2011, A&A, 529, L6

Audit, E. & Hennebelle, P. 2005, A&A, 433, 1

Bajaja, E., Arnal, E. M., Larrarte, J. J., et al. 2005, A&A, 440, 767

Barnes, D. G., Staveley-Smith, L., de Blok, W. J. G., et al. 2001, MNRAS, 322, 486

Ben Bekhti, N., Winkel, B., Richter, P., et al. 2012, A&A, 542, A110

Benjamin, R. A., Venn, K. A., Hiltgen, D. D., & Sneden, C. 1996, ApJ, 464, 836

Bergin, E. A., Hartmann, L. W., Raymond, J. C., & Ballesteros-Paredes, J. 2004, ApJ, 612, 921

Berné, O., Marcelino, N., & Cernicharo, J. 2010, Nature, 466, 947

Bertoldi, F. & McKee, C. F. 1992, ApJ, 395, 140

Beucher, S. & Lantuéjoul, C. 1979, Proc. Int. Workshop Image Processing, Real-Time Edge and Motion Detection/Estimation

Blondin, J. M., Wright, E. B., Borkowski, K. J., & Reynolds, S. P. 1998, ApJ, 500, 342

Bobylev, V. V. 2014, Astrophysics, 57, 583

Boggess, N. W., Mather, J. C., Weiss, R., et al. 1992, ApJ, 397, 420

Bolatto, A. D., Wolfire, M., & Leroy, A. K. 2013, ARA&A, 51, 207

Boulanger, F., Abergel, A., Bernard, J.-P., et al. 1996, A&A, 312, 256

Boulanger, F. & Perault, M. 1988, ApJ, 330, 964

Brand, J. & Blitz, L. 1993, A&A, 275, 67

Braun, R. 2012, ApJ, 749, 87

Braun, R. & Burton, W. B. 1999, A&A, 341, 437

Bregman, J. N. 1980, ApJ, 236, 577

Bregman, J. N. 2004, in Astrophysics and Space Science Library, Vol. 312, High Velocity Clouds, ed. H. van Woerden, B. P. Wakker, U. J. Schwarz, & K. S. de Boer, 341

Breitschwerdt, D., Freyberg, M. J., & Egger, R. 2000, A&A, 361, 303

Briggs, D. S., Schwab, F. R., & Sramek, R. A. 1999, in Astronomical Society of the Pacific Conference Series, Vol. 180, Synthesis Imaging in Radio Astronomy II, ed. G. B. Taylor, C. L. Carilli, & R. A. Perley, 127

Brüns, C., Kerp, J., Kalberla, P. M. W., & Mebold, U. 2000, A&A, 357, 120

Brüns, C., Kerp, J., Staveley-Smith, L., et al. 2005, A&A, 432, 45

Burkhart, B., Lazarian, A., Ossenkopf, V., & Stutzki, J. 2013, ApJ, 771, 123

Caimmi, R. 2008, New A, 13, 314

Calabretta, M. R. & Greisen, E. W. 2002, A&A, 395, 1077

Carruthers, G. R. 1970, ApJ, 161, L81

Carter, M., Lazareff, B., Maier, D., et al. 2012, A&A, 538, A89

Chomiuk, L. & Povich, M. S. 2011, AJ, 142, 197

Cleary, M. N., Haslam, C. G. T., & Heiles, C. 1979, A&AS, 36, 95

Coker, C. T., Thompson, T. A., & Martini, P. 2013, ApJ, 778, 79

Comeron, F. & Torra, J. 1992, A&A, 261, 94

Cornwell, T. J. & Evans, K. F. 1985, A&A, 143, 77

Cox, D. P. 2005, ARA&A, 43, 337

Dame, T. M., Hartmann, D., & Thaddeus, P. 2001, ApJ, 547, 792

de Avillez, M. A. 2000, MNRAS, 315, 479

De la Fuente Marcos, R. & De la Fuente Marcos, C. 2008, ApJ, 672, 342

Désert, F.-X., Bazell, D., & Blitz, L. 1990, ApJ, 355, L51

Désert, F. X., Bazell, D., & Boulanger, F. 1988, ApJ, 334, 815

Draine, B. T. 2003, ARA&A, 41, 241

Draine, B. T. 2011, Princeton University Press, ISBN 978-0-691-12214-4

Draine, B. T. & Bertoldi, F. 1996, ApJ, 468, 269

Draine, B. T. & Bertoldi, F. 1999, in ESA Special Publication, Vol. 427, The Universe as Seen by ISO, ed. P. Cox & M. Kessler, 553

Draine, B. T. & Li, A. 2001, ApJ, 551, 807

Draine, B. T. & Li, A. 2007, ApJ, 657, 810

Elmegreen, B. G. 2011, in EAS Publications Series, Vol. 51, EAS Publications Series, ed. C. Charbonnel & T. Montmerle, 19–30

Faridani, S., Flöer, L., Kerp, J., & Westmeier, T. 2014, A&A, 563, A99

Feldmann, R., Gnedin, N. Y., & Kravtsov, A. V. 2012, ApJ, 747, 124

Ferrière, K. M. 2001, Reviews of Modern Physics, 73, 1031

Finkbeiner, D. P. 2003, ApJS, 146, 407

Fisher, J. R. 2002, in Astronomical Society of the Pacific Conference Series, Vol. 278, Single-Dish Radio Astronomy: Techniques and Applications, ed. S. Stanimirovic, D. Altschuler, P. Goldsmith, & C. Salter, 433–445

Fisher, J. R. & Bradley, R. F. 2000, in Society of Photo-Optical Instrumentation Engineers (SPIE) Conference Series, Vol. 4015, Radio Telescopes, ed. H. R. Butcher, 308–318

Ford, H. A., Lockman, F. J., & McClure-Griffiths, N. M. 2010, ApJ, 722, 367

Fraternali, F., Marasco, A., Armillotta, L., & Marinacci, F. 2015, MNRAS, 447, L70

Fraternali, F., Marasco, A., Marinacci, F., & Binney, J. 2013, ApJ, 764, L21

Gentile, G., Józsa, G. I. G., Serra, P., et al. 2013, A&A, 554, A125

Gillmon, K. & Shull, J. M. 2006, ApJ, 636, 908

Gillmon, K., Shull, J. M., Tumlinson, J., & Danforth, C. 2006, ApJ, 636, 891

Giovanelli, R. & Haynes, M. P. 2015, ArXiv e-prints

Girichidis, P., Naab, T., Walch, S., et al. 2015, ArXiv e-prints

Gladders, M. D., Clarke, T. E., Burns, C. R., et al. 1998, ApJ, 507, L161

Glover, S. C. O. 2003, ApJ, 584, 331

Glover, S. C. O. & Clark, P. C. 2012, MNRAS, 426, 377

Glover, S. C. O. & Mac Low, M.-M. 2007, ApJ, 659, 1317

Glover, S. C. O. & Mac Low, M.-M. 2011, MNRAS, 412, 337

Goldsmith, P. F. & Langer, W. D. 1978, ApJ, 222, 881

Górski, K. M., Hivon, E., Banday, A. J., et al. 2005, ApJ, 622, 759

Gould, R. J. & Salpeter, E. E. 1963, ApJ, 138, 393

Grcevich, J. & Putman, M. E. 2009, ApJ, 696, 385

Green, G. M., Schlafly, E. F., Finkbeiner, D. P., et al. 2015, ApJ, 810, 25

Grenier, I. A., Black, J. H., & Strong, A. W. 2015, ARA&A, 53, 199

Grenier, I. A., Casandjian, J.-M., & Terrier, R. 2005, Science, 307, 1292

Guillard, P., Boulanger, F., Pineau Des Forêts, G., & Appleton, P. N. 2009, A&A, 502, 515

Guillet, V., Jones, A. P., & Pineau Des Forêts, G. 2009, A&A, 497, 145

Guillet, V., Pineau Des Forêts, G., & Jones, A. P. 2011, A&A, 527, A123

Hartmann, D. & Burton, W. B. 1997, Cambridge University Press, ISBN 0521471117

Hartmann, D., Magnani, L., & Thaddeus, P. 1998, ApJ, 492, 205

Hartmann, L., Ballesteros-Paredes, J., & Bergin, E. A. 2001, ApJ, 562, 852

Haud, U. 2008, A&A, 483, 461

Haud, U. & Kalberla, P. M. W. 2007, A&A, 466, 555

Hauser, M. G., Arendt, R. G., Kelsall, T., et al. 1998, ApJ, 508, 25

Hay, S., O'Sullivan, J., Kot, J., et al. 2007, in Antennas and Propagation, 2007. EuCAP 2007. The Second European Conference on, 1–5

Heald, G. 2015, in IAU Symposium, Vol. 309, IAU Symposium, ed. B. L. Ziegler, F. Combes, H. Dannerbauer, & M. Verdugo, 69–72

Heald, G., Józsa, G., Serra, P., et al. 2011, A&A, 526, A118

Hearty, T., Fernández, M., Alcalá, J. M., Covino, E., & Neuhäuser, R. 2000, A&A, 357, 681

Heiles, C. & Troland, T. H. 2003, ApJ, 586, 1067

Heitsch, F., Burkert, A., Hartmann, L. W., Slyz, A. D., & Devriendt, J. E. G. 2005, ApJ, 633, L113

Heitsch, F. & Putman, M. E. 2009, ApJ, 698, 1485

Heitsch, F., Slyz, A. D., Devriendt, J. E. G., Hartmann, L. W., & Burkert, A. 2006, ApJ, 648, 1052

Herbst, E. & van Dishoeck, E. F. 2009, ARA&A, 47, 427

Herbstmeier, U., Heithausen, A., & Mebold, U. 1993, A&A, 272, 514

Herbstmeier, U., Moritz, P., & Heithausen, A. 1994, in Astronomical Society of the Pacific Conference Series, Vol. 58, The First Symposium on the Infrared Cirrus and Diffuse Interstellar Clouds, ed. R. M. Cutri & W. B. Latter, 176

Hildebrand, R. H. 1983, QJRAS, 24, 267

Högbom, J. A. 1974, A&AS, 15, 417

Hollenbach, D. & Salpeter, E. E. 1971, ApJ, 163, 155

Hollenbach, D. J., Werner, M. W., & Salpeter, E. E. 1971, ApJ, 163, 165

Howk, J. C. 2012, in EAS Publications Series, Vol. 56, EAS Publications Series, ed. M. A. de Avillez, 291–298

Humphreys, R. M. & Larsen, J. A. 1995, AJ, 110, 2183

International Telecommunication Union - Radiocommunication. 2013, RA Series, RA.2126-1

Jones, A. P. & Nuth, J. A. 2011, A&A, 530, A44

Jones, A. P., Tielens, A. G. G. M., & Hollenbach, D. J. 1996, ApJ, 469, 740

Jones, A. P., Tielens, A. G. G. M., Hollenbach, D. J., & McKee, C. F. 1994, ApJ, 433, 797

Jordan, S. 2008, Astronomische Nachrichten, 329, 875

Joung, M. R., Bryan, G. L., & Putman, M. E. 2012, ApJ, 745, 148

Juvela, M., Padoan, P., & Nordlund, Å. 2001, ApJ, 563, 853

Kalberla, P. M. W. 2003, ApJ, 588, 805

Kalberla, P. M. W., Burton, W. B., Hartmann, D., et al. 2005, A&A, 440, 775

Kalberla, P. M. W. & Dedes, L. 2008, A&A, 487, 951

Kalberla, P. M. W. & Haud, U. 2015, A&A, 578, A78

Kalberla, P. M. W. & Kerp, J. 2009, ARA&A, 47, 27

Kalberla, P. M. W., McClure-Griffiths, N. M., Pisano, D. J., et al. 2010, A&A, 521, A17

Kalberla, P. M. W., Mebold, U., & Reich, W. 1980, A&A, 82, 275

Kelsall, T., Weiland, J. L., Franz, B. A., et al. 1998, ApJ, 508, 44

Kennicutt, R. C. & Evans, N. J. 2012, ARA&A, 50, 531

Kent, S. M., Dame, T. M., & Fazio, G. 1991, ApJ, 378, 131

Kerp, J. 2003, Astronomische Nachrichten, 324, 69

Kerp, J., Winkel, B., Ben Bekhti, N., Flöer, L., & Kalberla, P. M. W. 2011, Astronomische Nachrichten, 332, 637

Klein, B., Hochgürtel, S., Krämer, I., et al. 2012, A&A, 542, L3

Klein, U. 2006, Argelander-Institut für Astronomie, Bonn, Germany, Lecture notes: Radio astronomy: tools, applications and impacts

Kolmogorov, A. N. 1933, Giorn. Ist. Ital. Attuari, 4, 83

Kramer, C. 1997, Calibration of spectral line data at the IRAM 30 m radio telescope, IRAM Memos, Version 2.1

Lagache, G., Abergel, A., Boulanger, F., & Puget, J.-L. 1998, A&A, 333, 709

Lagache, G., Haffner, L. M., Reynolds, R. J., & Tufte, S. L. 2000, A&A, 354, 247

Lagache, G., Puget, J.-L., & Dole, H. 2005, ARA&A, 43, 727

Lamarre, J.-M., Puget, J.-L., Ade, P. A. R., et al. 2010, A&A, 520, A9

Lee, H.-H., Herbst, E., Pineau des Forets, G., Roueff, E., & Le Bourlot, J. 1996, A&A, 311, 690

Lehner, N., Howk, J. C., Thom, C., et al. 2012, MNRAS, 3333

Lenz, D., Flöer, L., & Kerp, J. 2016, A&A, 586, A121

Lenz, D., Kerp, J., Flöer, L., et al. 2015, A&A, 573, A83

Leroy, A. K., Walter, F., Martini, P., et al. 2015, ApJ, 814, 83

Liljestrom, T. 1991, A&A, 244, 483

Liszt, H. S. & Pety, J. 2012, A&A, 541, A58

Liszt, H. S., Pety, J., & Lucas, R. 2010, A&A, 518, A45

Low, F. J., Young, E., Beintema, D. A., et al. 1984, ApJ, 278, L19

Luhman, K. L. 2001, ApJ, 560, 287

Mac Low, M.-M. & Glover, S. C. O. 2012, ApJ, 746, 135

Mac Low, M.-M. & Klessen, R. S. 2004, Reviews of Modern Physics, 76, 125

Madau, P. & Dickinson, M. 2014, ARA&A, 52, 415

Magnani, L., Blitz, L., & Mundy, L. 1985, ApJ, 295, 402

Magnani, L., Hartmann, D., & Speck, B. G. 1996, ApJS, 106, 447

Magnani, L. & Smith, A. J. 2010, ApJ, 722, 1685

Mangum, J. G., Emerson, D. T., & Greisen, E. W. 2007, A&A, 474, 679

Marasco, A. & Fraternali, F. 2011, A&A, 525, A134

Marasco, A., Fraternali, F., & Binney, J. J. 2012, MNRAS, 419, 1107

Marinacci, F., Binney, J., Fraternali, F., et al. 2010, MNRAS, 404, 1464

McClure-Griffiths, N. M., Pisano, D. J., Calabretta, M. R., et al. 2009, ApJS, 181, 398

McGehee, P. M. 2008, Handbook of Star Forming Regions, Volume II, 813

McKee, C. F. & Hollenbach, D. J. 1980, ARA&A, 18, 219

McKee, C. F. & Ostriker, E. C. 2007, ARA&A, 45, 565

McKee, C. F. & Ostriker, J. P. 1977, ApJ, 218, 148

McMullin, J. P., Waters, B., Schiebel, D., Young, W., & Golap, K. 2007, in Astronomical Society of the Pacific Conference Series, Vol. 376, Astronomical Data Analysis Software and Systems XVI, ed. R. A. Shaw, F. Hill, & D. J. Bell, 127

Mebold, U., Cernicharo, J., Velden, L., et al. 1985, A&A, 151, 427

Melioli, C., Brighenti, F., & D'Ercole, A. 2015, MNRAS, 446, 299

Melioli, C., Brighenti, F., D'Ercole, A., & de Gouveia Dal Pino, E. M. 2008, MNRAS, 388, 573

Melioli, C., Brighenti, F., D'Ercole, A., & de Gouveia Dal Pino, E. M. 2009, MNRAS, 399, 1089

Miville-Deschênes, M.-A. & Lagache, G. 2005, ApJS, 157, 302

Moritz, P., Wennmacher, A., Herbstmeier, U., et al. 1998, A&A, 336, 682

Muller, C. A., Oort, J. H., & Raimond, E. 1963, Academie des Sciences Paris Comptes Rendus, 257, 1661

Murray, N., Ménard, B., & Thompson, T. A. 2011, ApJ, 735, 66

Murray, N., Quataert, E., & Thompson, T. A. 2005, ApJ, 618, 569

Murray, N., Quataert, E., & Thompson, T. A. 2010, ApJ, 709, 191

Nath, B. B. & Silk, J. 2009, MNRAS, 396, L90

Neugebauer, G., Habing, H. J., van Duinen, R., et al. 1984, ApJ, 278, L1

Nidever, D. L., Majewski, S. R., & Burton, W. B. 2008, ApJ, 679, 432

Nidever, D. L., Majewski, S. R., Butler Burton, W., & Nigra, L. 2010, ApJ, 723, 1618

Odenwald, S. F. & Rickard, L. J. 1987, ApJ, 318, 702

Onishi, T., Yoshikawa, N., Yamamoto, H., et al. 2001, PASJ, 53, 1017

Oosterloo, T., Fraternali, F., & Sancisi, R. 2007, AJ, 134, 1019

Oosterloo, T., Verheijen, M., & van Cappellen, W. 2010, in ISKAF2010 Science Meeting, 43

Ormel, C. W., Min, M., Tielens, A. G. G. M., Dominik, C., & Paszun, D. 2011, A&A, 532, A43

Osterman, S., Green, J., Froning, C., et al. 2011, Ap&SS, 335, 257

Pardo, J., Cernicharo, J., & Serabyn, E. 2001, Antennas and Propagation, IEEE Transactions on, 49, 1683

Pardo, J. R., Serabyn, E., & Cernicharo, J. 2001, J. Quant. Spec. Radiat. Transf., 68, 419

Peek, J. E. G., Heiles, C., Putman, M. E., & Douglas, K. 2009, ApJ, 692, 827

Pety, J., Bardeau, S., & Reynier, E. 2009, Comparison of ATM versions: Impact on the calibration of IRAM instruments, IRAM Memo 2009-5, Version 1.0

Pineda, J. E., Caselli, P., & Goodman, A. A. 2008, ApJ, 679, 481

Pineda, J. L., Goldsmith, P. F., Chapman, N., et al. 2010, ApJ, 721, 686

Pisano, D. J., Barnes, D. G., Gibson, B. K., et al. 2007, ApJ, 662, 959

Planck Collaboration I. 2011, A&A, 536, A1

Planck Collaboration I. 2014, A&A, 571, A1

Planck Collaboration IX. 2014, A&A, 571, A9

Planck Collaboration VIII. 2014, A&A, 571, A8

Planck Collaboration XI. 2014, A&A, 571, A11

Planck Collaboration XIII. 2014, A&A, 571, A13

Planck Collaboration XIII. 2015, ArXiv e-prints

Planck Collaboration XIV. 2014, A&A, 571, A14

Planck Collaboration XIX. 2011, A&A, 536, A19

Planck Collaboration XVII. 2014, A&A, 566, A55

Planck Collaboration XXIV. 2011, A&A, 536, A24

Planck Collaboration XXVI. 2015, ArXiv e-prints

Planck Collaboration XXX. 2014, A&A, 571, A30

Poelarends, A. J. T., Herwig, F., Langer, N., & Heger, A. 2008, ApJ, 675, 614

Pound, M. W., Wilson, R. W., & Bania, T. M. 1990, ApJ, 351, 165

Predehl, P. & Schmitt, J. H. M. M. 1995, A&A, 293, 889

Puspitarini, L. & Lallement, R. 2012, A&A, 545, A21

Putman, M. E., Peek, J. E. G., & Joung, M. R. 2012, ARA&A, 50, 491

Reach, W. T., Heiles, C., & Bernard, J.-P. 2015, ApJ, 811, 118

Reach, W. T., Koo, B.-C., & Heiles, C. 1994, ApJ, 429, 672

Reach, W. T., Wall, W. F., & Odegard, N. 1998, ApJ, 507, 507

Reid, M. J., Menten, K. M., Zheng, X. W., et al. 2009, ApJ, 700, 137

Richter, P. 2006, in Reviews in Modern Astronomy, Vol. 19, Reviews in Modern Astronomy, ed. S. Roeser, 31

Richter, P., Savage, B. D., Wakker, B. P., Sembach, K. R., & Kalberla, P. M. W. 2001a, ApJ, 549, 281

Richter, P., Sembach, K. R., Wakker, B. P., & Savage, B. D. 2001b, ApJ, 562, L181

Richter, P., Sembach, K. R., Wakker, B. P., et al. 2001c, ApJ, 559, 318

Richter, P., Wakker, B. P., Savage, B. D., & Sembach, K. R. 2003, ApJ, 586, 230

Röhser, T., Kerp, J., Winkel, B., Boulanger, F., & Lagache, G. 2014, A&A, 564, A71

Roshi, D. A. & Perley, R. A. 2003, in Astronomical Society of the Pacific Conference Series, Vol. 306, New technologies in VLBI, ed. Y. C. Minh, 109–121

Roy, N. 2015, Proceedings of the Indian National Science Academy Part A, 81, 583

Sancisi, R., Fraternali, F., Oosterloo, T., & van der Hulst, T. 2008, A&A Rev., 15, 189

Sault, R. J., Teuben, P. J., & Wright, M. C. H. 1995, in Astronomical Society of the Pacific Conference Series, Vol. 77, Astronomical Data Analysis Software and Systems IV, ed. R. A. Shaw, H. E. Payne, & J. J. E. Hayes, 433

Saury, E., Miville-Deschênes, M.-A., Hennebelle, P., Audit, E., & Schmidt, W. 2014, A&A, 567, A16

Savage, B. D., Bohlin, R. C., Drake, J. F., & Budich, W. 1977, ApJ, 216, 291

Savage, B. D. & Sembach, K. R. 1996, ApJ, 470, 893

Schiminovich, D., van Gorkom, J., van der Hulst, T., Oosterloo, T., & Wilkinson, A. 1997, in Astronomical Society of the Pacific Conference Series, Vol. 116, The Nature of Elliptical Galaxies; 2nd Stromlo Symposium, ed. M. Arnaboldi, G. S. Da Costa, & P. Saha, 362

Schwarz, U. J. & de Boer, K. S. 2004, in Astrophysics and Space Science Library, Vol. 312, High Velocity Clouds, ed. H. van Woerden, B. P. Wakker, U. J. Schwarz, & K. S. de Boer, 55

Shannon, C. E. 1949, Proceedings of the Institute of Radio Engineers, 37, 10

Shapiro, P. R. & Field, G. B. 1976, ApJ, 205, 762

Shetty, R., Glover, S. C., Dullemond, C. P., & Klessen, R. S. 2011a, MNRAS, 412, 1686

Shetty, R., Glover, S. C., Dullemond, C. P., et al. 2011b, MNRAS, 415, 3253

Shull, J. M. & Beckwith, S. 1982, ARA&A, 20, 163

Smirnov, N. V. 1936, C. R. Acad. Sci. Paris, 202, 449

Snow, T. P. & McCall, B. J. 2006, ARA&A, 44, 367

Snowden, S. L., Freyberg, M. J., Kuntz, K. D., & Sanders, W. T. 2000, ApJS, 128, 171

Spearman, C. 1904, The American Journal of Psychology, 15, 72

Spearman, C. 1906, British Journal of Psychology, 1904-1920, 2, 89

Stanimirovic, S. 2002, in Astronomical Society of the Pacific Conference Series, Vol. 278, Single-Dish Radio Astronomy: Techniques and Applications, ed. S. Stanimirovic, D. Altschuler, P. Goldsmith, & C. Salter, 375–396

Stanko, S., Klein, B., & Kerp, J. 2005, A&A, 436, 391

Stappers, B. W., Hessels, J. W. T., Alexov, A., et al. 2011, A&A, 530, A80

Stecher, T. P. & Williams, D. A. 1967, ApJ, 149, L29

Strasser, S. & Taylor, A. R. 2004, ApJ, 603, 560

Tauber, J. A., Mandolesi, N., Puget, J.-L., et al. 2010, A&A, 520, A1

Taylor, G. B., Carilli, C. L., & Perley, R. A., eds. 1999, Astronomical Society of the Pacific Conference Series, Vol. 180, Synthesis Imaging in Radio Astronomy II

Terlouw, J. P. & Vogelaar, M. G. R. 2015, Kapteyn Package, version 2.3, Kapteyn Astronomical Institute, Groningen, available from `http://www.astro.rug.nl/software/kapteyn/`

Thilker, D. A., Braun, R., Walterbos, R. A. M., et al. 2004, ApJ, 601, L39

Vallée, J. P. 2008, AJ, 135, 1301

van der Tak, F. F. S., Black, J. H., Schöier, F. L., Jansen, D. J., & van Dishoeck, E. F. 2007, A&A, 468, 627

van Dishoeck, E. F. & Black, J. H. 1988, ApJ, 334, 771

Vázquez-Semadeni, E., Kim, J., Shadmehri, M., & Ballesteros-Paredes, J. 2005, ApJ, 618, 344

Veilleux, S., Cecil, G., & Bland-Hawthorn, J. 2005, ARA&A, 43, 769

Verheijen, M. A. W., Oosterloo, T. A., van Cappellen, W. A., et al. 2008, in American Institute of Physics Conference Series, Vol. 1035, The Evolution of Galaxies Through the Neutral Hydrogen Window, ed. R. Minchin & E. Momjian, 265–271

Wakker, B. P. 1991, A&A, 250, 499

Wakker, B. P. 2001, ApJS, 136, 463

Wakker, B. P. 2004, in Astrophysics and Space Science Library, Vol. 312, High Velocity Clouds, ed. H. van Woerden, B. P. Wakker, U. J. Schwarz, & K. S. de Boer, 25

Wakker, B. P. 2006, ApJS, 163, 282

Wakker, B. P. & Boulanger, F. 1986, A&A, 170, 84

Wakker, B. P., York, D. G., Wilhelm, R., et al. 2008, ApJ, 672, 298

Weiß, A., Heithausen, A., Herbstmeier, U., & Mebold, U. 1999, A&A, 344, 955

Wesselius, P. R. & Fejes, I. 1973, A&A, 24, 15

Westmeier, T. 2007, PhD Thesis, Rheinische Friedrich-Wilhelms-Universität Bonn

Westmeier, T., Braun, R., Brüns, C., Kerp, J., & Thilker, D. A. 2007, New A Rev., 51, 108

Williams, R. J., Mathur, S., Poindexter, S., Elvis, M., & Nicastro, F. 2012, AJ, 143, 82

Wilson, T. L., Rohlfs, K., & Hüttemeister, S. 2009, Tools of Radio Astronomy (Springer-Verlag)

Winkel, B., Kalberla, P. M. W., Kerp, J., & Flöer, L. 2010, ApJS, 188, 488

Winkel, B., Kerp, J., Flöer, L., et al. 2016, A&A, 585, A41

Wolfe, A. M., Gawiser, E., & Prochaska, J. X. 2005, ARA&A, 43, 861

Wolfire, M. G., Hollenbach, D., & McKee, C. F. 2010, ApJ, 716, 1191

Wolfire, M. G., Hollenbach, D., McKee, C. F., Tielens, A. G. G. M., & Bakes, E. L. O. 1995a, ApJ, 443, 152

Wolfire, M. G., McKee, C. F., Hollenbach, D., & Tielens, A. G. G. M. 1995b, ApJ, 453, 673

Wolfire, M. G., McKee, C. F., Hollenbach, D., & Tielens, A. G. G. M. 2003, ApJ, 587, 278

Wong, T. & Blitz, L. 2002, ApJ, 569, 157

Wyse, R. F. G. 2009, in IAU Symposium, Vol. 258, IAU Symposium, ed. E. E. Mamajek, D. R. Soderblom, & R. F. G. Wyse, 11–22

Zschaechner, L. K., Rand, R. J., Heald, G. H., Gentile, G., & Józsa, G. 2012, ApJ, 760, 37

List of Figures

List of Tables

Acknowledgements

During the time of my PhD, many different people have contributed to the success of this effort. I want to sincerely thank everybody who helped me through my PhD.

Most of all, I would like to thank my supervisor P.D. Jürgen Kerp, who gave me the opportunity to do radio astronomy for my Bachelor and Master theses, that lead to my PhD finally. He was patient, supporting, interested, critical, and felt responsible for his students. The large freedom during the daily work was very enjoyable.

Furthermore, I sincerely thank the members of my PhD committee for their time and interest in my work, Prof. Thomas Reiprich, Prof. Peter Schilke, and Prof. Albert Haas.

Over a long period of my PhD, I was a member of the BCGS and IMPRS, from which I had scientific, financial, and social benefits, for which I am grateful. Especially, I would like to thank Prof. Peter Schilke as my BCGS mentor, who helped and guided me through my PhD time.

I very much appreciate the support given by Prof. Michael Kramer during the final levels of my thesis.

One of the reasons for my decision to stay in the group of Jürgen Kerp was the fantastic group: Benjamin, Daniel K., Daniel L., Lars, Milan, Nadya, Peter, Shahram, and Verena. My office colleagues Verena, Daniel K., and Peter made the years pass by way too quickly. Not to mention the many other people of the institute, who made daily lunch and coffee very pleasing.

Special thanks to Benjamin for his time, help, advice, and critical final proof-reading. Discussions with Peter were always insightful, although they often raised more questions than answers. Talking to Daniel K. always gave new ideas, he also helped a lot in the final proof-reading. Thanks to Daniel L. and Lars for their Gaussian decomposition, which was an important ingredient in one of the major chapters of this work. I am very grateful for Jorge L. Pineda for providing data so generously and naturally, and Philipp Schmidt for his initial help with MIRIAD. I express my deep gratitude to all the colleagues and co-workers who helped me in my research.

I would like to express my thanks to Guilaine Lagache and Francois Boulanger from the Planck Collaboration, who gave me the opportunity to do new and exciting research.

I sincerely thank Christina Stein-Schmitz for her continuous support and help in the organisation and administration of contracts, finances, travels, and what ever came along.

Finally, I want to thank my family, most importantly Katharina, who had to endure myself over the last years.